

Prediction of autogenous shrinkage in fly ash blended cement systems

THÈSE N° 7829 (2017)

PRÉSENTÉE LE 3 OCTOBRE 2017
À LA FACULTÉ DES SCIENCES ET TECHNIQUES DE L'INGÉNIEUR
LABORATOIRE DES MATÉRIAUX DE CONSTRUCTION
PROGRAMME DOCTORAL EN SCIENCE ET GÉNIE DES MATÉRIAUX

ÉCOLE POLYTECHNIQUE FÉDÉRALE DE LAUSANNE

POUR L'OBTENTION DU GRADE DE DOCTEUR ÈS SCIENCES

PAR

Zhangli HU

acceptée sur proposition du jury:

Prof. P. Murali, président du jury
Prof. K. Scrivener, Prof. P. Lura, directeurs de thèse
Prof. B. Pichler, rapporteur
Dr M. Vandamme, rapporteur
Prof. V. Michaud, rapporteuse



ÉCOLE POLYTECHNIQUE
FÉDÉRALE DE LAUSANNE

Suisse
2017

“ Direct your eye right inward, and you’ll find
A thousand regions in your mind
Yet undiscovered. Travel them, and be
Expert in home-cosmography ”

— Henry David Thoreau

Acknowledgements

Financial support from the China Scholarship Council is gratefully acknowledged. The doctoral school at EPFL is appreciated for accepting me to be a PhD student.

The four-year PhD study was a great experience in my life: it broadened my horizon, enriched my knowledge and established a firm basis of my future.

I would like to express my appreciation to all the people who ever helped me with my PhD work and supported me in my daily life during the last four years.

First, my special thanks to my supervisor, Prof. Karen Scrivener. She does not only give me the precious opportunity to pursue my study in LMC, but also shows me how to carry out research individually and to explore the truth of science. Without her insightful advices and comments, my research will not have been going on so smoothly. She sent us to conferences and courses to let us get in touch with top scientists and approach advanced knowledge. She is also the person who teaches me what I can do and who I can be in the scientific field as a woman.

My sincere thanks to my co-supervisor, Prof. Pietro Lura, for his great help for my research. He shows his patience and insight during his guidance to me. I cannot count how many days and nights when he helped me for checking and correcting my reports, papers and the thesis. He is my idol for scientific work. I will bear in mind his hardworking, professionalism and attitude in research. Everything I learned from him will forever lead me towards my future work.

I also would like to thank all the jury members: Prof. Véronique Michaud, Prof. Bernhard Pichler and Dr. Matthieu Vandamme and Prof. Muralt Paul, the president of the jury. Thank you all for reading my thesis and giving invaluable comments for improving the final version of the thesis.

Next people on my thank list are my postdocs: Dr. Mateusz Wyrzykowski, Dr. Adrien Hilaire, and Dr. Hadi Kazemi-Kamyab. I feel extremely lucky to have them with me during my PhD. They are my guides and wingmen. They helped me, taught me and checked all the calculations and experimental results with me. They gave me the ability to see my research from different directions. Hadi, special thanks to you, you always encourage me, support me as a brother.

I would like to express my gratitude to Maude, Anne-Sandra and Marie-Alix for their help on administration. They helped us to register courses and conferences, to book hotels and to organize activities for the lab.

I would like to thank Dr. Cyrille Dunant, Dr. Quanghai Do, Dr. Alain Giorla and Prof. Shashank Bishnoi for sharing their programs with me and helping me with coding. Special thanks to Cyrille for being so patient to teach a person who has no experience on programming and providing a lot of precious suggestions.

Acknowledgements

I deeply acknowledge my permanent or temporary officemates and of course also good friends, Francois, Yan, Adrien (Cuban Monkey), Solène and Alain. Special thanks to Francois for this four-year accompany. We started PhD on the same day and shared the office for four years (I guess you will remember my ‘get out of the office’). Special thanks to Yan as well. Even though you just stayed in the lab for one year, we build a really good friendship. I missed all the moments we were together for discussing work, spending spare time and of course enjoying your food.

I would like to thank all my colleagues as well as my friends in the lab: Alex, Julien S, Shiyu, Aurélie, Xuerun, Emmanuelle, Hamed, Franco, Yosra, Hui, Mink, Hong, Aslam, Frank, Anna, Marcelo, Mahsa, Lionel, Joao, Paul, Antonio, Berta, Julien B, Elise, Pawel, Mo, Ruben, Arnaud, Matthieu, Huang and John. Berta and Elise, you two are always so nice to me. I would like to give my special thanks to my dear Viola. She is always supporting me and sharing feelings with me. I am so lucky to have you and all these nice postcards (^-^). I would like to also thank Shiyu, Hui and Xuerun for always pushing me out of the lab, giving me all the nice moments for hotpot, grilling and hiking.

I would like to thank friends I met in Switzerland: Jacky Colliard, Haijuan Zhang, Qin Wu, Yupei Zeng, Xiaoqin Sheng, Peijian Zhou, Anuj, Vineet, Abdel, Amapreet, Carmelo, Fei Yang, Chuanlan Zhang, Minghao Xu, Chaoqun Dong and Wenjiao Xie. Without these friends, my life here will not have been so great. Special thanks to Qin, we have so many similar hobbies and I miss our nice talks.

My deep thanks to my boyfriend, Bingkun. He is my solid backing who always supports me, encourages me and takes care of me. We plan our future together, discuss our work and talk about our ideal life. You make my life colorful.

In the end, I would give my deepest thanks to my parents, my sister Feifei, my uncles and aunts. Without their support, I cannot follow my heart to go abroad and leave them for so many years.

Abstract

Autogenous shrinkage is the unrestrained volume change of cementitious materials occurring at constant temperature without any change in mass. It occurs as a consequence of self-desiccation (decrease of internal relative humidity) and increasing capillary pressure in the pore fluid. In concrete elements hardening in sealed conditions, autogenous shrinkage is critical for crack development, in particular in high performance concrete with low water to cement ratio. Being able to predict autogenous shrinkage can provide insights for the long-term deformation of different concrete mixtures, create a useful database for simulations and ultimately minimize the cracking risks.

The main objective of this thesis is to predict the autogenous shrinkage of fly-ash-blended cement systems by using a quantitative multi-physics approach. In order to reach this goal, a systematic experimental study of autogenous deformation, self-desiccation, microstructure evolution, elastic properties and basic creep of different cementitious systems was first carried out. After having achieved a phenomenological understanding, supported by experimental data, analytical and numerical modeling of autogenous deformation is possible.

In this study, a novel method based on the evolution of microstructure for predicting the self-desiccation was developed. In this method, ^1H nuclear magnetic resonance and mercury intrusion porosimetry were combined to obtain the evolution of the microstructure. This prediction provides another possibility to predict capillary pressure and corresponding autogenous shrinkage of a simulated microstructure.

Prediction of autogenous shrinkage, including poro-elastic and poro-visco-elastic response based on experimental quantities, was accomplished. In the prediction, the poro-elastic deformation of cementitious materials was calculated based on poromechanics. The poro-visco-elastic response was studied with basic creep tests on hardening cementitious materials. Generalized Kelvin-Voigt chains were applied to predict the aging of creep. The prediction matched reasonably well with measured autogenous shrinkage.

Autogenous shrinkage of cementitious materials was also numerically modeled with a microstructure simulation and a finite element method. This part of the work extended existing approaches based mainly on two programming platforms: *μic* platform and Automatic Mechanics for Integrated Experiments (*AMIE*) finite element framework. Average pore pressure load calculated from measured relative humidity, saturation degree and Biot coefficient was imposed into a 3-dimensional microstructure computed with *μic* platform. Based on back-calculated elastic and visco-elastic behavior of C-S-H, an approach for simulating the autogenous shrinkage was demonstrated.

Keywords

Autogenous shrinkage, Fly-ash-blended cement, Self-desiccation, Basic creep, Microstructure evolution, Poromechanical method, Numerical modeling

Résumé

Le retrait endogène est défini comme la variation de volume d'un matériau cimentaire survenant à température constante et sans variation de masse. C'est une conséquence de l'auto-dessiccation et de l'augmentation de la pression capillaire dans le fluide du réseau poreux. Pour des éléments en béton vieillissant en conditions scellées, le retrait endogène est un facteur critique au développement de fissures, en particulier pour les bétons à hautes performances et au faible rapport eau sur ciment. La prédiction du retrait endogène permet un aperçu au long terme des déformations pour différentes compositions de béton et engendre une base de données, pour *in fine* permettre de minimiser le risque de fissuration

L'objectif principal de ce travail de thèse est de prédire le retrait endogène de mélanges cimentaires contenant des cendres volantes en utilisant une approche multi-physique. En ce but, le retrait endogène, l'auto-dessiccation, l'évolution de la microstructure, les propriétés élastiques et le fluage propre ont fait l'objet d'une étude systématique. Après avoir acquis une compréhension phénoménologique des systèmes étudiés grâce aux données expérimentales, des modélisations analytiques et numériques des déformations endogènes sont envisageables.

Dans cette étude, une approche originale basée sur l'évolution de la microstructure est développée pour estimer l'auto-dessiccation. Cette méthode conjugue les mesures de résonance magnétique nucléaire du proton à la porosimétrie au mercure pour obtenir l'état de la microstructure. Ce modèle permet également de prédire, pour une microstructure simulée, la pression capillaire et le retrait endogène associé.

La prédiction analytique du retrait endogène, y compris les réponses élastiques et viscoélastiques, peut être calculée. Dans ce modèle, la déformation élastique des matériaux cimentaires est calculée par une approche poromécanique. La réponse viscoélastique quant à elle est d'abord obtenue par des essais de fluage propre sur des matériaux à différentes époques, puis des chaînes de Kelvin-Voigt correspondantes et le principe de superposition du fluage sont ajoutés au modèle prédictif. Les résultats sont en accord avec les mesures de retrait endogène.

Le retrait endogène est aussi modélisé numériquement, à l'aide d'une microstructure simulée et d'un schéma d'homogénéisation par éléments finis. Cette partie du travail s'inscrit dans la continuité d'approches existantes, basées sur deux plateformes: la plateforme *μic* et l'environnement par éléments finis Automatic Mechanics for Integrated Experiments (*AMIE*). La pression capillaire, elle-même calculée d'après l'humidité relative interne, le degré de saturation et le coefficient de Biot, est imposée à une microstructure simulée par *μic*. Une approche pour simuler le retrait endogène, basée sur un calcul du comportement élastique et viscoélastique du C-S-H, est finalement discutée.

Mots-clés

Retrait endogène, Ciment de cendres volantes, Auto-dessiccation, Fluage propre, Évolution de la microstructure, Approche poromécanique, Modélisation numérique.

Contents

Acknowledgements	v
Abstract.....	vii
Keywords	vii
Résumé	viii
Contents	ix
Glossary	xiv
Chapter 1 Introduction.....	1
1.1 Overview	2
1.2 Statement of problem	4
1.3 Research objectives	5
1.4 Layout of the thesis	6
1.5 References	7
Chapter 2 Materials and phase assemblage	9
2.1 Raw materials	10
2.1.1 Physical properties	10
2.1.2 Chemical properties	11
2.2 Mixtures.....	12
2.3 Assessment of the replacement of fly ash with quartz	14
2.3.1 Isothermal calorimetry	14
2.3.2 Results and conclusion.....	14
2.4 Degree of reaction of fly ash	15
2.4.1 SEM-EDS frequency quantification method	15
2.4.2 SEM-EDS measurement	17
2.4.3 Results and discussion	17
2.5 Phases assemblage.....	19
2.5.1 X-ray diffraction.....	19
2.5.2 Mass balance calculation.....	19

Contents

2.5.3	Results and discussion	20
2.6	References	22
Chapter 3	Autogenous shrinkage and self-desiccation.....	23
3.1	Literature review.....	24
3.1.1	Mechanisms	24
3.1.2	Measurement method.....	30
3.1.3	Errors associated with the measurement of autogenous shrinkage.....	33
3.2	Autogenous shrinkage and self-desiccation	36
3.2.1	Experimental methods.....	36
3.2.2	Autogenous shrinkage.....	38
3.2.3	Self-desiccation.....	41
3.2.4	Relative humidity drop due to salts dissolved in the pore solution.....	42
3.2.5	Relationship between autogenous shrinkage and self-desiccation.....	43
3.3	Summary.....	44
3.4	References	44
Chapter 4	Prediction of internal relative humidity in cementitious materials by ^1H NMR	50
4.1	Literature review.....	51
4.1.1	Application of ^1H NMR in cement	51
4.1.2	Internal RH prediction	54
4.2	The novel method for predicting the Kelvin radius.....	58
4.3	Experimental methods	60
4.3.1	^1H NMR	60
4.3.2	Mercury intrusion porosimetry (MIP).....	61
4.3.3	Chemical shrinkage.....	62
4.3.4	Pore solution extraction	62
4.3.5	Bootstrapping technique	63
4.4	Results	63
4.4.1	RHs.....	63
4.4.2	Chemical shrinkage.....	64

Contents

4.4.3	Degree of hydration	65
4.4.4	Evolution of NMR signal amplitude as function of time	67
4.4.5	Development of cumulative pore volume	68
4.5	Prediction results and discussion	69
4.5.1	Selection of the cut-off sizes	69
4.5.2	Results and discussion	71
4.6	Summary	74
4.7	References	75
Chapter 5	Visco-elastic behavior of cementitious materials	78
5.1	Literature review	79
5.1.1	Mechanism of basic creep	79
5.1.2	Basic creep at early ages	85
5.1.3	Modeling of creep at early ages	88
5.2	Methods	90
5.3	Results	93
5.3.1	Stress applied	93
5.3.2	Apparent creep strain for hardening pastes	93
5.3.3	Instantaneous elastic response	95
5.3.4	Basic creep compliance at different loading ages	97
5.4	Power law expression	101
5.4.1	Kinetics of creep compliance	101
5.4.2	Power law expression	103
5.4.3	Back calculation of the creep compliance	105
5.5	Creep recovery	106
5.6	Rheology modeling	108
5.7	Conclusions	113
5.8	References	114
Chapter 6	Prediction of autogenous shrinkage as poro-visco-elastic deformation....	121
6.1	Literature review	122

Contents

6.1.1	Empirical and semi-empirical models.....	122
6.1.2	Mechanistic prediction methods	124
6.2	Prediction Methods.....	132
6.2.1	Poro-elastic prediction	132
6.2.2	Poro-visco-elastic prediction.....	135
6.3	Parameters from experiments	136
6.3.1	Saturation degree.....	136
6.3.2	Average pore pressure.....	138
6.3.3	Other parameters	138
6.4	Prediction results	141
6.4.1	Prediction of elastic response.....	141
6.4.2	Prediction of the visco-elastic component	144
6.4.3	Prediction of overall autogenous shrinkage	146
6.5	Conclusions	147
6.6	References	148
Chapter 7	Numerical simulation of autogenous shrinkage of cementitious materials	153
7.1	Literature review.....	154
7.1.1	Hydration of cement.....	154
7.1.2	Microstructural modeling of hydration of cement pastes	157
7.2	Simulation methods	163
7.2.1	Microstructure simulation with μic platform.....	163
7.2.2	Finite element method for micro-mechanical simulation of elastic deformation under pore fluid pressure	167
7.2.3	Simulation of the visco-elastic behavior of C-S-H based on non-aging creep	169
7.2.4	Simulation of aging creep	172
7.2.5	Simulation of autogenous shrinkage	174
7.3	Prediction results	175
7.3.1	Simulation of the elastic response of material under capillary pressure..	175
7.3.2	Simulation of the non-aging visco-elastic behavior of C-S-H.....	179
7.3.3	Simulation of aging creep	181
7.3.4	Simulation of autogenous shrinkage	182

7.4	Conclusions	183
7.5	References	184
Chapter 8	Conclusions and perspectives	189
8.1	Experimental investigations	190
8.1.1	Main findings	190
8.1.2	Future perspectives	191
8.2	Analytical prediction part	191
8.2.1	Main findings	191
8.2.2	Future perspectives	192
8.3	Numerical simulation part	192
8.3.1	Main findings	192
8.3.2	Future perspectives	193
8.4	References	193
Appendix A	195
Appendix B	196
Curriculum Vitae	197

Glossary

Notations of cement chemistry

C: CaO (Calcium Oxide) S: SiO₂ (Silicon dioxide) A: Al₂O₃ (Aluminium oxide)
F: Fe₂O₃ (Iron oxide) \$: SO₃ (Sulfate) H: H₂O (Water)

Abbreviations of materials and phases

SCM: Supplementary cementitious material
OPC: Ordinary Portland cement
HPC: High performance concrete
UHPC: Ultra high performance concrete
C₃S: Tricalcium silicate
C₂S: Dicalcium silicate
C₃A: Tricalcium aluminate
C₄AF: Tetracalcium aluminoferrite
C\$H₂: Gypsum
C-S-H: Calcium silicate hydrate
CH: Calcium hydroxide (portlandite)
AFt: Ettringite (Et)
AFm: Monosulfate (Ms)
Hg: Hydrogarnet
SP: Superplasticizer

Abbreviations of techniques

MIP: Mercury intrusion porosimetry
SEM: Scanning electron microscopy
EDS: Energy Dispersive X-ray Spectroscopy
BET: Brunauer-Emmett-Teller
XRF: X-ray Fluorescence
XRD: X-ray diffraction

Glossary

^1H NMR: Proton nuclear magnetic resonance

EMM-ARM: Elastic modulus measurement through ambient response method

CPMG: Carr-Purcell-Meiboom-Gill sequence

QE: Quadrature (solid) echo

LVDTs: Linear variable differential transformers

Abbreviations of others

w/c: water to cement ratio

w/s: water to solid ratio

w/b: water to binder ratio

RH: Relative humidity

PSD: Particle size distribution

CTE: Coefficient of thermal expansion

FEM: Finite element method

AMIE: Automated mechanics for integrated experiments

CVE: Computational volume element

Chapter 1 Introduction

This chapter provides an executive summary of the current state of research on the prediction of autogenous shrinkage. The original motivations and goals for developing quantitative approaches to predict autogenous shrinkage of cement pastes with or without fly ash will be presented. Finally, the structure of this thesis will be presented, including a brief overview of the content of the different chapters.

Contents

1.1	Overview	2
1.2	Statement of problem	4
1.3	Research objectives	5
1.4	Layout of the thesis	6
1.5	References	7

1.1 Overview

Concrete is one of the oldest and most used materials in our daily life, but at the same time it is a material that is not enough fundamentally understood. Increasingly higher amounts of concrete are being manufactured to meet the demands for civil engineering infrastructures, especially in developing countries. For increasing the service-life of concrete infrastructures and decreasing maintenance costs, durability of concrete is key.

Since the late 1970s, high performance concrete (HPC) has been attracting increasing attention, due to its better mechanical properties and enhanced durability compared to traditional concrete [1]. This class of materials should be distinguished from ordinary concrete because of its low water to binder ratio (w/b, an upper threshold of 0.4 is often mentioned), which often requires high amounts of superplasticizer [2]. It also contains special supplementary cementitious materials (SCMs), e.g., silica fume or other type of fine pozzolanic fillers [1].

According to the ACI definition [3], HPC is “*concrete meeting special combinations of performance and uniformity requirements that cannot always be achieved routinely using conventional constituents and normal mixing, placing and curing practices*”. HPC is often used in constructions demanding higher strength, rapid strength development, thin structural elements, tight microstructure for better durability and so on. The outstanding mechanical properties and durability of HPC lead to its common applications to, e.g., skyscrapers, marine structures, pavements and special targeted infrastructures, see some examples in *Figure 1.1*. At the same time, the dramatic increase in practical applications of HPC fueled a wide range of investigations on this class of materials, spanning from the raw material selection to mechanistic modeling of its properties.

However, a very important concern when using HPC is autogenous shrinkage, which is much more pronounced in HPC than in ordinary concrete [2]. Rapid and significant autogenous shrinkage generally occurs in HPC (e.g., [4–6]), due to high capillary pressures that are induced by the fine porosity, small amount of water and rapid hydration of HPC. Contrary to drying shrinkage in ordinary concrete, which proceeds slowly due to evaporation from the exposed surfaces, autogenous shrinkage develops simultaneously in the whole cross-section of the concrete member and may plateau already after several days or weeks at most [7,8]. In addition, in massive concrete members, autogenous shrinkage occurs simultaneously with thermal contraction [9–11]. For these reasons, the deformation caused by autogenous shrinkage should be taken into account and possibly mitigated in HPC, both for in-situ casting and prefabricated elements.

Autogenous shrinkage occurs as a consequence of self-desiccation (decrease of internal relative humidity) and increasing capillary pressure in the pore fluid [8]. The governing parameters are the water to cement ratio (w/c), the chemical shrinkage and the pore structure of the cement paste within the concrete [12]. Autogenous shrinkage, if restrained (which is the typical situation in concrete constructions), will generate eigenstresses within the material [8]. This restraint can happen at the material level (mm- to cm-length scale) by the aggregates or by the reinforcement (internal restraint), or macroscopically by the adjoining structural elements (external restraint) or gradients of deformation throughout the element (self-restraint) [13]. As a result, the buildup of tensile stresses may cause the

formation of micro- or macro- cracks, respectively. These cracks may lead to serious durability problems in the long term, e.g., corrosion of reinforcing steel due to penetration of harmful ions and oxygen into the cracks.

Being able to predict the autogenous shrinkage can provide insights for the long-term deformation of different concrete mixtures, create a useful database for simulations and ultimately minimize the cracking risk. Especially for HPC, successful prediction of autogenous shrinkage will help to remove obstacles to its wider applications.



(a) Burj Khalifa [14]



(b) Donghai Bridge [15]

Figure 1.1 Applications of HPCs

Supplementary cementitious materials (SCMs)

Recent years witness a rising usage of cements containing significant quantities of SCMs. Proper use of SCMs can bring economic and environmental advantages compared to solely ordinary Portland cement (OPC) systems [16], e.g., as an alternative solution for lowering carbon footprint. Note that the manufacture of cement accounts for 5-8 % of the global carbon dioxide production in the world. In HPCs, SCMs such as silica fume, slag and fly ash are used widely since they can enhance the long-term strength and, if applied properly in practical applications, they can also enhance the durability when they partially replace the Portland cement [17].

Portland cement hydration results in phase assemblages that are composed mainly of calcium silicate hydrate (C-S-H) and portlandite [18]. In SCMs-blended cement, however, a much more complicated system with both hydration of cement and pozzolanic reaction of SCMs occurring simultaneously is generated. The ternary diagram [19] in *Figure 1.2* shows the chemical composition of different types of cementitious materials including SCMs. It can be clearly seen that the chemical compositions of SCMs are very different compared to each other or to Portland cement, which affects a number of properties of concrete.

Most of the emphasis for SCMs up to recent times has been on strength development. However, other aspects should also be considered, which can significantly affect the durability of structures, in particular early-age deformations and susceptibility to cracking. Because of the combination of different physical and chemical processes involved, the study of the early-age deformation of these systems is extremely complicated. It is expected that a better general understanding and, most importantly, the ability to make quantitative predictions of the mechanical development and durability response will allow wider use of such blended cements.

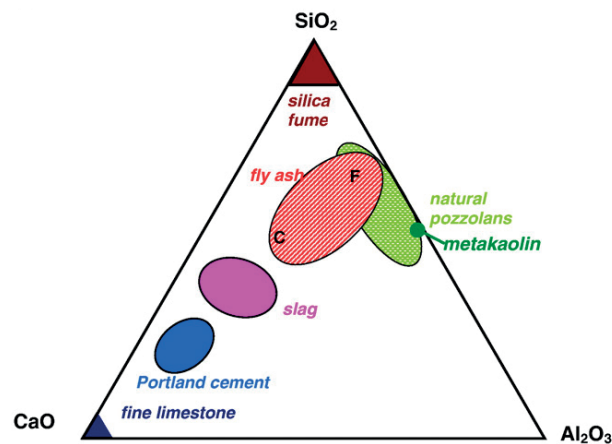


Figure 1.2 $\text{CaO-Al}_2\text{O}_3\text{-SiO}_2$ ternary diagram of Portland cement and common used SCMs, from [19]

Class F fly ash was used in the blended systems studied in this thesis. Fly ash is a by-product of the coal combustion process and the use of it in hydraulic cement can be traced back to the 1930s [20]. Traditionally, replacement of fly ash in structural concrete is limited to 15-25 wt.%. Within the last decade, concretes containing more than 50 % fly ash have been widely and successfully applied [21]. According to previous studies [22,23], fly ash reduced the autogenous shrinkage of concrete effectively when the amount of fly ash was high. This advantage compared to pure Portland cement will increase the use of fly ash in practical applications.

1.2 Statement of problem

Because of the rapid and continuous shrinkage development and the simultaneous action of various driving forces, it is challenging to predict autogenous shrinkage even in pure Portland cement systems. As a rule, in the literature the experimental results and the modeling do not agree. The main reasons for this mismatch between experiments and modeling can be either due to parameters in the models that are not well tuned or to some important thermo-hydro-mechanical aspects that are not considered in the models. In [8], creep has been regarded as an important property that if not consid-

ered in the model can be responsible for the aforementioned difference. Note that creep (time-dependent, supposedly visco-elastic deformation under sustained load) is not taken into account in most studies. A main reason for this exclusion is that it is extremely difficult to separate the relative contributions of creep and elastic shrinkage during shrinkage development.

For SCMs-blended systems, the prediction is further complicated by the need to quantify the effect of SCMs on pore size distribution, internal relative humidity (RH), elastic properties and creep. In order to predict autogenous shrinkage of blended cement systems (in this study represented by fly ash), the aforementioned properties are all needed as inputs.

Although a substantial quantity of studies has focused on the mechanical properties of fly-ash-blended systems, investigations about the effect of fly ash on autogenous shrinkage are scant. The main challenge or difficulty for understanding the mechanisms of autogenous shrinkage in such systems stems from the simultaneous action of hydration reaction of cement and pozzolanic reaction of fly ash, with both processes affecting microstructure development and consequently autogenous shrinkage. Specifically, fly ash changes the volume of gel pores and capillary pores (filler effect), which will affect the autogenous deformation. Moreover, the pozzolanic reaction is an additional source of self-desiccation and therefore shrinkage at later ages.

1.3 Research objectives

The main objective of this thesis is to use a quantitative, multi-physics approach to predict the autogenous shrinkage of fly-ash-blended cement systems. In order to satisfy this objective, several sub-objectives need to be achieved first:

- Reaching a phenomenological understanding, supported by systematic experimental data, of the effect of fly ash and w/c on hydration kinetics, microstructure and elastic properties in order to understand the effect of fly ash on autogenous deformation;
- Based on the development of hydration and microstructure changes, autogenous shrinkage of cementitious systems needs to be predicted by analytical methods using poromechanics;
- Numerical simulation should be done by combining the microstructure simulation platform *μic* and the finite element simulation platform called Automated Mechanics for Integrated Experiments (*AMIE*), both available at EPFL.

Some novel aspects developed in this thesis are expected to achieve a clear impact, both from the theoretical and the applied perspective:

- Quartz as an inert filler with similar particle size as fly ash, is used to substitute fly ash. This approach helps to simulate the filler effect on early hydration properties and autogenous shrinkage;

- Creep is taken into account, which can be regarded as one of the most influential parameters in modeling autogenous shrinkage. In particular, both the contributions of creep and elastic shrinkage is considered during this study;
- The numerical simulation starts from the real particle size distribution (PSD) and is completed with a limited set of fitting parameters.

1.4 Layout of the thesis

The research project is divided into two main parts:

- In the first part, the development of autogenous shrinkage is investigated with the corrugated tubes method, which provides quantitative information about autogenous deformation of different systems. The degree of hydration, the development of the microstructure (solid phases and pore structure) and the mechanical properties (creep and elastic modulus) at early ages are all monitored as a function of time. The data obtained in this experimental section is used as inputs for later modeling;
- In the second part, both analytical and numerical methods are used for the prediction of autogenous shrinkage. The analytical method is based on poromechanical approaches with parameters determined from the experimental section. In the numerical modeling, based on the simulated microstructure with the *μic* modeling platform, the autogenous shrinkage is then computed using finite element method (FEM) with *AMIE*. The inputs for the FEM simulation are voxel files from *μic* and pore pressure calculated from the measured RH evolution¹.

The flowchart of the thesis program, including both the experimental and the numerical part, is shown in *Figure 1.3*. The chapter structure based on the structure of the thesis program is as follows:

Chapter 2 introduces materials, mixtures and hydration properties. Physical and chemical characterization of the materials are presented. The methods for determining the degree of hydration of cement, degree of reaction of fly ash and phase assemblage are explained and the results are discussed. This chapter corresponds to process ① marked in the flow chart.

Chapter 3 presents the experimental results of autogenous shrinkage and self-desiccation, providing the basis of the further prediction. This chapter corresponds to process ② marked in the flow chart.

Chapter 4 shows the prediction of the RH due to the menisci formation in the system with a novel method. The method is based on proton nuclear magnetic resonance (¹H NMR) and mercury intrusion porosimetry (MIP) following the microstructure evolution of the system. The RH is key for determining the driving force of autogenous shrinkage, which is the capillary pressure. This chapter corresponds to process ③ marked in the flow chart.

¹ Pore pressure cannot be computed directly from *μic* due to the limitation of simulating porosity. Detailed explanation for this issue is shown in *Chapter 7*.

Chapter 5 describes the experimental results of uniaxial basic creep of different blended systems. Generalized Kelvin-Voigt chains are used to model the evolution of the basic creep at early ages. This chapter corresponds to process ④ marked in the flow chart.

Chapter 6 presents the analytical prediction of autogenous shrinkage including the visco-elastic response. The prediction is based on poromechanical modeling. Results from different models and parameters are compared. This chapter corresponds to process ⑤ marked in the flow chart.

Chapter 7 presents the simulation of the autogenous shrinkage based on the microstructure model μic and the FEM framework *AMIE*. Simulations of hydration, microstructure, stiffness and visco-elastic response of the systems are shown. This chapter corresponds to process ⑥ marked in the flow chart.

Finally, *Chapter 8* presents the main conclusions and perspectives of this thesis.

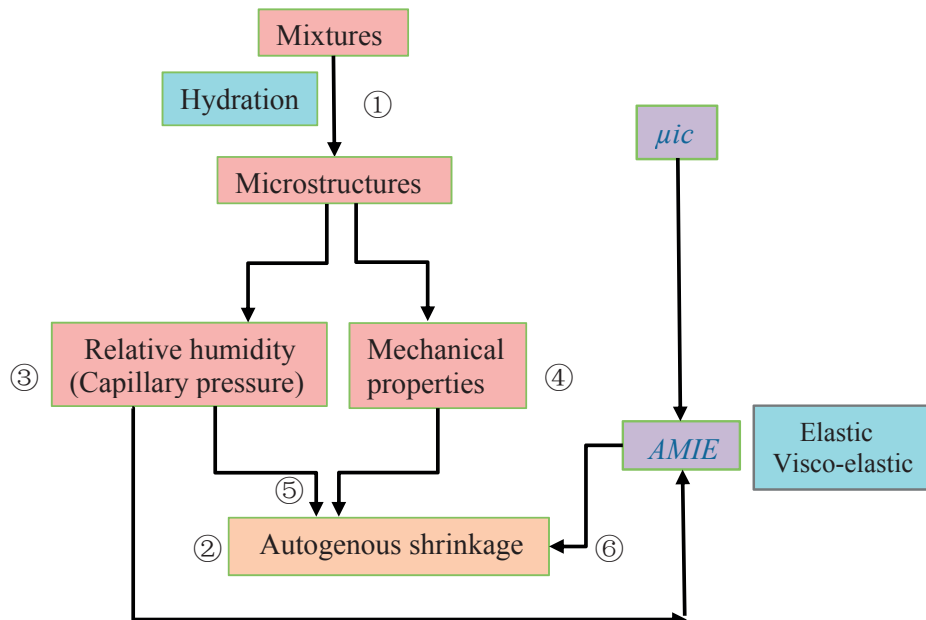


Figure 1.3 Structure of thesis program

1.5 References

- [1] P. C. Aïtcin, High performance concrete, 1998.
- [2] P. C. Aïtcin, The durability characteristics of high performance concrete: A review, *Cem. Concr. Compos.* 25 (2003) 409–420.
- [3] ACI concrete terminology, 2013.
- [4] E. Tazawa, S. Miyazawa, T. Kasai, Chemical shrinkage and autogenous shrinkage of hydrating cement paste, *Cem. Concr. Res.* 25 (1995) 288–292.

-
- [5] O. M. Jensen, P. F. Hansen, Autogenous deformation and change of the relative humidity in silica fume-modified cement paste, *ACI Mater. J.* 93 (1996) 539–543.
- [6] P. Lura, *Autogenous deformation and internal curing of concrete*, Delft, 2003.
- [7] T. Nawa, T. Horita, A mechanism of autogenous shrinkage of cementitious materials, in: *Cem. Comb. Durable Concr.*, Thomas Telford Publishing, 2005: pp. 425–434.
- [8] P. Lura, O. M. Jensen, K. van Breugel, Autogenous shrinkage in high-performance cement paste: An evaluation of basic mechanisms, *Cem. Concr. Res.* 33 (2003) 223–232.
- [9] Ø. Bjøntegaard, T. A. Hammer, E. J. Sellevold, On the measurement of free deformation of early age cement paste and concrete, *Cem. Concr. Compos.* 26 (2004) 427–435.
- [10] P. Mounanga, V. Baroghel-Bouny, A. Loukili, A. Khelidj, Autogenous deformations of cement pastes: Part I. Temperature effects at early age and micro–macro correlations, *Cem. Concr. Res.* 36 (2006) 110–122.
- [11] H. Chen, *Autogenous and Thermal Deformations and Their Interaction in Early Age Cementitious Materials*, EPFL, 2013.
- [12] O. M. Jensen, P. F. Hansen, Autogenous deformation and RH-change in perspective, *Cem. Concr. Res.* 31 (2001) 1859–1865.
- [13] P. Lura, O.M. Jensen, J. Weiss, Cracking in cement paste induced by autogenous shrinkage, *Mater. Struct.* 42 (2009) 1089–1099.
- [14] The Skyscraper Center, (n.d.). <http://skyscrapercenter.com/>.
- [15] Donghai Bridge, (n.d.). https://en.wikipedia.org/wiki/Donghai_Bridge.
- [16] M. Narmluk, T. Nawa, Effect of fly ash on the kinetics of Portland cement hydration at different curing temperatures, *Cem. Concr. Res.* 41 (2011) 579–589.
- [17] C. S. Poon, L. Lam, Y. L. Wong, A study on high strength concrete prepared with large volumes of low calcium fly ash, *Cem. Concr. Res.* 30 (2000) 447–455.
- [18] J. E. Rossen, *Stability of C-A-S-H in pastes of alite and cement blended with supplementary cementitious materials*, EPFL, 2014.
- [19] B. Lothenbach, K. Scrivener, R.D. Hooton, Supplementary cementitious materials, *Cem. Concr. Res.* 41 (2011) 1244–1256.
- [20] ACI Committee 232, *Use of Fly Ash in Concrete*, American Concrete Institute, 2003.
- [21] G. Hannesson, K. Kuder, R. Shogren, D. Lehman, The influence of high volume of fly ash and slag on the compressive strength of self-consolidating concrete, *Constr. Build. Mater.* 30 (2012) 161–168.
- [22] Y. Li, J. Bao, Y. Guo, The relationship between autogenous shrinkage and pore structure of cement paste with mineral admixtures, *Constr. Build. Mater.* 24 (2010) 1855–1860.
- [23] P. Termkhajornkit, T. Nawa, M. Nakai, T. Saito, Effect of fly ash on autogenous shrinkage, *Cem. Concr. Res.* 35 (2005) 473–482.

Chapter 2 Materials and phase assemblage

This chapter describes in detail the characteristics of the raw materials, the mixture design and the phase assemblage of pastes used in this thesis. The PSD was measured with laser diffraction and the specific surface area with the Brunauer-Emmett-Teller (BET) method. The composition of the materials, both as oxide and as mineral components, was analyzed with X-ray Fluorescence (XRF) and X-ray diffraction (XRD). The degree of reaction of fly ash was determined from a method based on scanning electron microscopy and energy dispersive X-ray spectroscopy (SEM-EDS). Phase assemblage was calculated from mass balance.

Contents

2.1	Raw materials.....	10
2.1.1	Physical properties.....	10
2.1.2	Chemical properties.....	11
2.2	Mixtures	12
2.3	Assessment of the replacement of fly ash with quartz.....	14
2.3.1	Isothermal calorimetry.....	14
2.3.2	Results and conclusion	14
2.4	Degree of reaction of fly ash.....	15
2.4.1	SEM-EDS frequency quantification method.....	15
2.4.2	SEM-EDS measurement.....	17
2.4.3	Results and discussion	17
2.5	Phases assemblage	19
2.5.1	X-ray diffraction	19
2.5.2	Mass balance calculation	19
2.5.3	Results and discussion	20
2.6	References.....	22

2.1 Raw materials

Portland cement CEM I 42.5N supplied by Holcim (Siggenthal), quartz powder fillers and Class-F fly ash were used in this thesis. The fly ash is expected to show “filler effect” at early ages (i.e., the fly ash particles will initially not react themselves but influence cement hydration by serving as nucleation sites, increasing the effective w/c and changing the particle packing [1,2]). The pozzolanic reaction of silicate in the pozzolanic materials and calcium hydroxide to form C-S-H will occur at later ages. The C-S-H formed will have a lower Ca/Si compared to C-S-H from cement reaction [3]. The main motivation for using fly ash in this study is to develop models to predict autogenous shrinkage including the pozzolanic reaction. The quartz powder filler was used to replace the same volume of fly ash in the systems with the purpose of both checking the effect of w/c and separating the physical and chemical effect of fly ash.

2.1.1 Physical properties

The particle size of the powders used in cementitious systems has a significant influence on the workability, on the hydration kinetics and on the mechanical properties, including autogenous shrinkage. Therefore, PSD of the raw materials was investigated with laser diffraction (see *Figure 2.1*). Quartz filler with the closest particle size to fly ash was selected among three different kinds of quartz filler (of mean diameter 4 μm , 8 μm and 12 μm , respectively, not shown here). The fineness of the cement particles is between that of the fly ash and of the quartz fillers. The D_{50}^2 of the three powders is shown in *Table 2.1*. Cement, fly ash and quartz fillers have mean diameters of about 13 μm , 16 μm and 12 μm , respectively. The fly ash contains coarser particles than other two powders, but at the same time also more small particles.

Other physical properties such as the BET specific surface area and density of the powders are also shown in *Table 2.1*. The density of the materials was measured by using an Erlenmeyer flask with turpentine (density of 0.86-0.87 g/cm^3) serving as the liquid in the measurement. The density measurement was based on the Swiss standard SN 215 [4]. The specific surface area of these three powders is very similar. The measured density of the fly ash and the quartz filler is close.

² D_{50} is the equivalent spherical diameter for which 50% of the particles are smaller than the equivalent diameter, respectively.

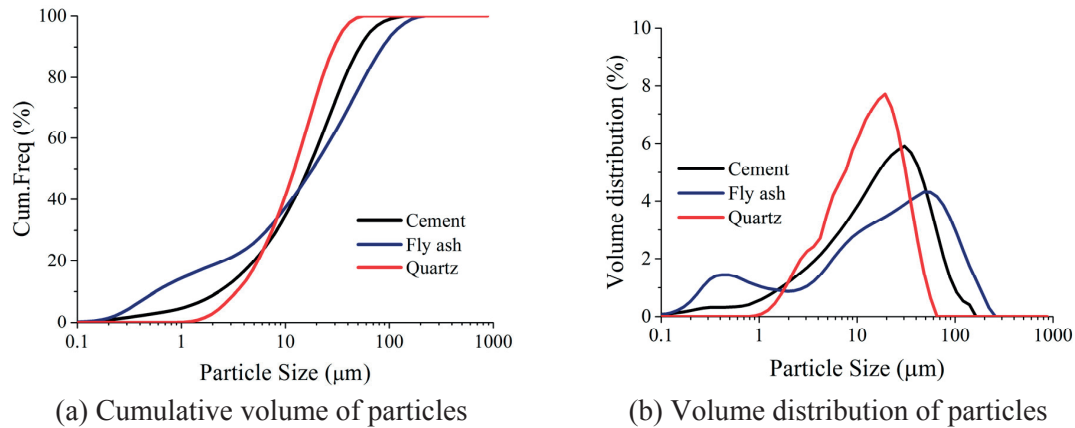


Figure 2.1 Particle size distribution of the three powders

Table 2.1 Physical properties of the three powders

Materials	D ₅₀ (μm)	Specific surface area (m ² /g)	Density (g/cm ³)
Cement	13	1.15	3.12
Fly ash	16	1.16	2.17
Quartz filler	12	1.17	2.63

2.1.2 Chemical properties

The oxide composition (measured with XRF) of the three powders is listed in *Table 2.2*. In addition, the mineral composition of cement and fly ash (measured with XRD and quantified by Rietveld analysis) is presented in *Table 2.3*.

Table 2.2 Oxide composition of the three powders from XRF (wt.%)

Composition	Cement	Fly ash	Quartz filler
SiO ₂	20.45	69.67	99.83
Al ₂ O ₃	4.39	23.8	-
Fe ₂ O ₃	3.01	2.39	0.03
CaO	64.48	0.1	0.02
MgO	1.66	0.2	-
SO ₃	2.83	0.004	-
Na ₂ O	0.24	0.09	-
K ₂ O	0.89	0.61	0.05
TiO ₂	0.34	1.51	0.02
P ₂ O ₅	0.28	0.14	-
Mn ₂ O ₃	0.05	0.05	-
ZrO ₂	-	-	0.01
Loss	1.3	0.95	0.02

Table 2.3 Mineral composition of cement and fly ash from XRD (wt.%)

Phases	Cement	Phases	Fly ash
Alite C_3S	69.0	Mullite	20.2
Belite $\beta-C_2S$	8.3	Quartz	13.2
C_3A cube	6.7	Magnetite	0.2
C_4AF	8.2	Amorphous	66.4
Gypsum	4.3	-	-
Bassanite	2.8	-	-
Anhydrite	0.8	-	-

2.2 Mixtures

Portland cement pastes with w/c of 0.30 and 0.35 by mass (referred as Cement-0.3 and Cement-0.35 later) were prepared as reference systems. By keeping the water to solid ratio (w/s) constant, part of the cement was replaced with fly ash (at substitution levels 20% and 40% by mass of cement, referred to as CFA20-0.3, CFA40-0.3, CFA20-0.35 and CFA40-0.35). Fly ash was then replaced by quartz powder by keeping the same volume fraction (pastes referred to as CQZ20-0.3, CQZ40-0.3, CQZ20-0.35 and CQZ40-0.35 later), described in *Figure 2.2*. In order to adjust the workability (same slump for all the pastes), pastes with w/s of 0.30 were mixed with polycarboxylate-ether type superplasticizer (SP, solid content 37%) at rate 0.3% by mass of cement. The detailed mixture composition is given in *Table 2.4*.

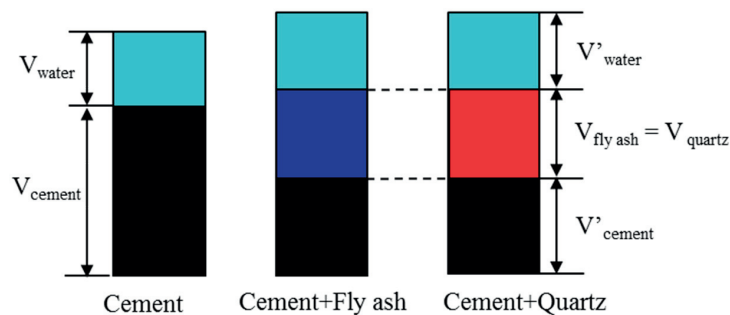


Figure 2.2 Schematic picture of the designed mixtures

Replacing cement with quartz filler allowed mixing stable pastes of relatively high w/c (up to w/c 0.63) that would otherwise experience segregation. The reason for keeping the volume fraction of fly ash and quartz fillers constant in the system is because the volumetric composition is paramount for the volume changes (in this case, for the autogenous shrinkage). The w/c ranges from 0.3 to 0.63 and

the initial porosity (water to paste ratio by volume) was only slightly different (from 44% to 52%) in different systems, as shown in *Table 2.4* (assuming the total mass of the solids is 100 g).

In order to remove the air bubbles in the specimen as many as possible, the pastes were prepared in a vacuum mixer (see *Figure 2.3*). The mixing process was two-minutes mixing at speed of 450 rpm after low speed premixing at 200 rpm for twenty seconds. Different procedures for sample storage and preparation were used for the different experimental methods, as specified in the description of each method in the following chapters. The influence of the air voids in experiments will be examined as well.

Table 2.4 Mixture design and initial porosities for ten systems

Materials	w/c	Cement (g)	Fly ash (g)	Quartz fillers (g)	Water (g)	SP (g)	Initial porosity
Cement-0.3	0.30	100	-	-	29.79	0.3	0.48
Cement-0.35	0.35	100	-	-	35	-	0.52
CFA20-0.3	0.37	80	20	-	29.83	0.24	0.46
CFA40-0.3	0.50	60	40	-	29.87	0.18	0.44
CFA20-0.35	0.44	80	20	-	35	-	0.50
CFA40-0.35	0.58	60	40	-	35	-	0.48
CQZ20-0.3	0.39	76.92	-	23.08	29.84	0.23	0.47
CQZ40-0.3	0.54	55.25	-	44.75	29.88	0.17	0.46
CQZ20-0.35	0.46	76.92	-	23.08	35	-	0.51
CQZ40-0.35	0.63	55.25	-	44.75	35	-	0.50



Figure 2.3 Vacuum mixer used in this investigation

2.3 Assessment of the replacement of fly ash with quartz

2.3.1 Isothermal calorimetry

Isothermal calorimetry was used to evaluate the replacement of fly ash with the type of quartz filler selected. The measurements at $20 \pm 0.1^\circ\text{C}$ were performed on mixtures with w/s of 0.3 with a TAM Air calorimeter. The calorimeter was placed in a temperature-controlled room to enhance the stability of the baseline. After mixing in a vacuum mixer, approximately 10 g of paste were placed in a glass ampoule with a diameter of 24.9 mm. The exact weight was precisely measured for each sample for the normalization. After gently tapping, the ampoule was sealed with vapor-tight caps and inserted into the calorimeter, where the measurements lasted for 7 d. All the experiments were performed in duplicate for each system and the results presented are the average of the two specimens. The difference in cumulative heat release between duplicate specimens at 7 d was on average less than 1 J/g. The obtained data was normalized per gram of cement.

2.3.2 Results and conclusion

Figure 2.4 shows the heat flow released during hydration of cementitious systems with w/s of 0.3. In Figure 2.4, it also shows the linear part of the acceleration period in the heat of hydration of the different systems (solid line) to easily compare the slope.

According to literature [5,6], due to presence of the inert particles (fly ash and quartz), the hydration of cement is promoted by higher effective w/c (relatively more available space for the formation of hydrates) and additional nucleation sites (highly depending on the distance between particles due to enhance the shearing condition and fineness of the filler due to the extra surface area provided).

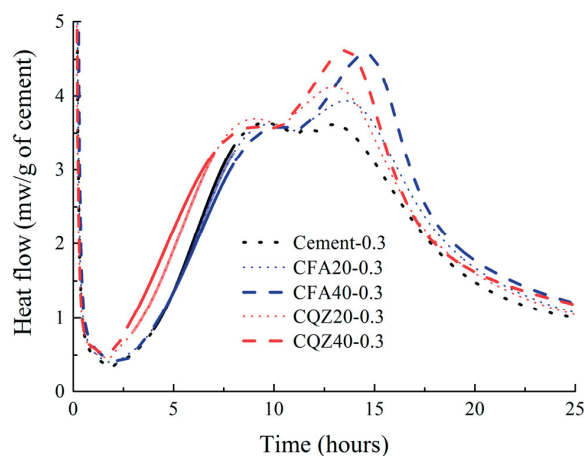


Figure 2.4 Hydration heat flow of systems with w/s of 0.3

When cement was replaced by quartz, higher slope of the heat flow during the acceleration period was attained compared to the pure cement paste, which signifies an acceleration of cement hydration in quartz-blended systems. The same effect can be seen in fly-ash-blended system, but it was not as significant as in the quartz systems. In addition, fly ash or quartz-blended systems had higher intensity of the peak of aluminum (the peak occurred at around 13-15h which is due to renewed aluminate reaction to form ettringite) compared to Cement-0.3. The more cement was replaced by fly ash or quartz, the higher was the intensity of the aluminum peaks. With the same substitution level, the intensity effect was similar in both fillers. The effect is related mainly to depletion rate of sulfate [6].

For the same volume fraction of quartz and fly ash, the total heat of the systems at 7 days was similar, as shown in *Figure 2.5*. These results indicate that the selected quartz was a good replacement for the fly ash at early ages, since they had similar effect on the hydration of cement at early ages. However, since the finer part of the fly ash and quartz are not exactly the same, a different impact on the refinement of the pore structure can be expected, which has to be taken into consideration in later studies. Theoretically, capillary stresses due to self-desiccation occur in pores within the 0.005-0.05 μm range [5].

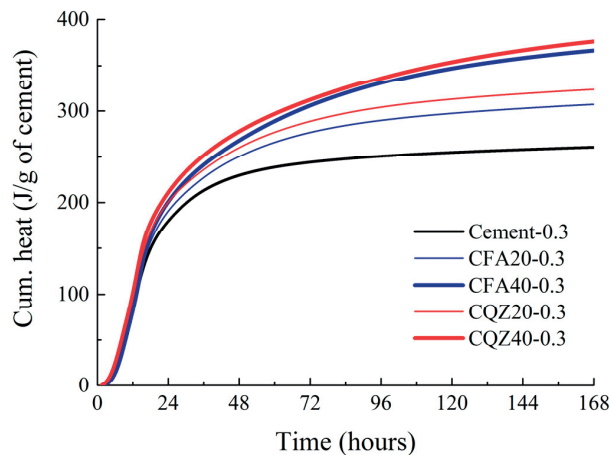


Figure 2.5 Cumulative heat release of blended systems with w/s of 0.3

2.4 Degree of reaction of fly ash

2.4.1 SEM-EDS frequency quantification method

The difficulty for quantifying the degree of reaction of fly ash in blended systems has been addressed in previous studies [7]. The big challenge for applying normal quantification methods, e.g., XRD, is due to the high amount of amorphous phase presented in fly ash. Other methods such as selective dissolution and grey level histogram based on backscattered electron image analyses have been found not giving results with enough accuracy. Comparison among different methods for quantifying the

siliceous fly ash is shown in [7]. Therefore, a novel approach recently developed by Durdzinski et al., [8] based on SEM-EDS was used in this thesis for quantifying the degree of reaction of fly ash. The systems with w/c of 0.35 are the ones which have been focused on in later prediction and simulation. The degree of reaction of the fly ash in two systems, CFA20-0.35 and CFA40-0.35, was quantified in this section.

The key of this method is to plot the element composition of numerous pixels of specimens from EDS in a ternary frequency diagram. Different glass components of fly ash are then grouped and analyzed. By comparing the volume fraction of different glass groups in raw fly ash and hydrated systems, the degree of reaction of fly ash can be determined based on the calculated consumption of glass groups individually. The entire procedure for the quantification can be seen in a schematic representation in *Figure 2.6*.

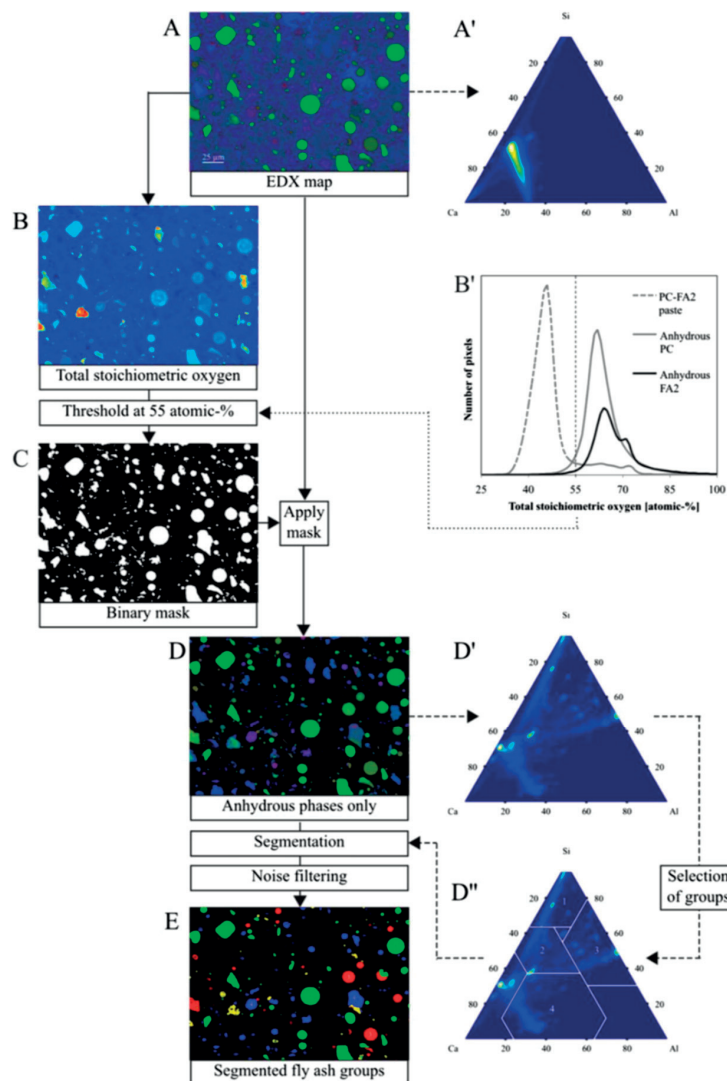


Figure 2.6 Flow chart of the method with SEM-EDS for quantifying the degree of reaction of fly ash in hydrated systems, from [8]

Basically, this approach can be summarized into the following steps:

(1) EDS element mapping is carried out on selected number of frames. Element components are collected with the information of atomic percentage, process A in *Figure 2.6*.

(2) The element components of each pixel are then plotted in so-called ‘blobs’ in a ternary frequency diagram (Al-Si-Ca is selected for fly ash), process B and C in *Figure 2.6*. For raw fly ash, direct plot can be possible while for hydrated systems, a mask has to be first applied to filter hydrates out. This filtering is for differentiating components from anhydrates and hydrates by considering the content of oxides.

(3) Differentiate and analyze glass groups based on the ternary frequency diagram of only anhydrates, see process D and D’ in *Figure 2.6*. As a result, the range of the chemical composition of each glass group can be determined and used for the quantification of its volume.

A more detailed explanation of the method can be seen in [8].

2.4.2 SEM-EDS measurement

Sample preparation

Hydrating samples were cut into slices with the thickness of 2 mm with a diamond saw at desired ages (3, 7, and 28 d). Hydration was stopped with solvent exchange method. Isopropanol used during stopping the hydration was changed at 1 h, 1 d and 3 d after the slices being cut. The sample was dried for more than 7 d in a desiccator and broken into small pieces (size of around 5 mm). The selected piece of the sample was then impregnated under vacuum with an epoxy resin and polished using four diamond grain sizes (9, 3, 1 and $\frac{1}{4}$ μm). The polished sample was coated with a conductive layer of carbon before putting under the microscope.

SEM-EDS

FEI Quanta 200 electron microscope was used for SEM investigation. The working distance of 12.5 mm and operating voltage of 15 kV were set. Backscatter electron image was taken and analyzed with EDS element mapping. In total, 8 frames were used for obtaining millions of data points (pixels). Atomic percentages of elements (Al, Si, Ca, Mg, Fe, K, Na, Ti, P and S) in each pixel were quantified.

2.4.3 Results and discussion

The ternary frequency diagram of CFA40-0.35 at 28 d is plotted in *Figure 2.7*. As a siliceous fly ash, only two groups of glass can be identified: glass 1: silicates; glass 2: aluminosilicates with low to moderate calcium. The segmentation criteria for each glass is shown in the ternary frequency diagram. Each segmented glass group can be visualized in the microstructure image from EDS mapping, on the right side of *Figure 2.7*. The chemical components of each glass are shown in *Table 2.5*. The glass 1 contains high amount of Si with a small amount of Al while the glass 2 contains higher amount of Al.

After quantifying the volume fraction of each glass group, the degree of reaction of fly ash α_{FA} is calculated based on the reaction of both glasses, see equation as follows:

Equation 2.1

$$\alpha_{FA} = \frac{V_{g1}^{raw} + V_{g2}^{raw} - (V_{g1}^{hyd} + V_{g2}^{hyd})}{V_{flyash}^{raw}}$$

where: V_{g1}^{raw} and V_{g2}^{raw} are volume fraction of the initial glass 1 and glass 2 in the total paste (age 0), V_{g1}^{hyd} and V_{g2}^{hyd} are volume fraction of the unreacted glass 1 and glass 2 in the hydrated pastes. V_{flyash}^{raw} is volume fraction of fly ash in paste at initial time.

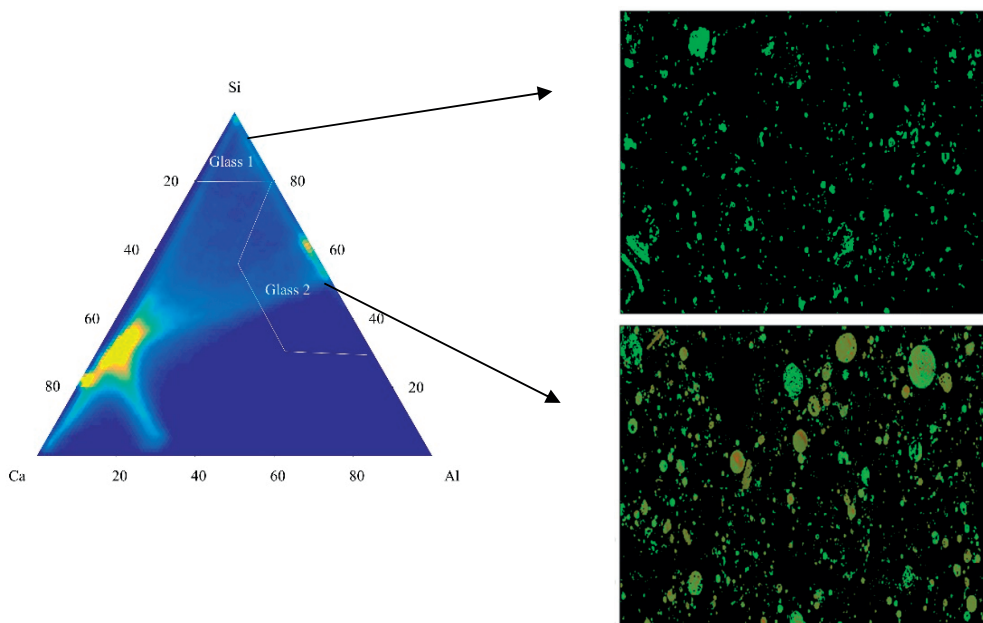


Figure 2.7 Glass groups for fly ash identified from the ternary frequency diagram of CFA40-0.35 at 28 d

Table 2.5 Chemical composition of the glasses in fly ash investigated

Type of glass	CaO	SiO ₂	Al ₂ O ₃
Glass 1	0.4	85.6	14.0
Glass 2	0.5	71.1	28.4

The volume fraction (normalized to total glass phases in fly ash powders) of unreacted two glass groups and the degree of reaction of fly ash calculated are both shown in *Figure 2.8*. As indicated in the figure, the fly ash investigated in this study was not very reactive with the total degree of reaction of 35 % and 25 % in CFA20-0.35 and CFA40-0.35 at 28 d, respectively. It is normal to see higher reaction degree found in systems with lower substitution level of fly ash. It is due to higher pH and

higher supply of Ca in the pore solution in CFA20-0.25. The glass 1 in both system was less reactive than the glass 2. The glass 2 contributed more to the total reaction of fly ash. The reaction rate was gradually evolving as the hydration time.

According to the round robin test on the degree of reaction of fly ash in blended systems in [7], SEM-EDS method overestimated the reaction of siliceous fly ash due to the smaller cross-sections of 3-dimensional features in microscope.

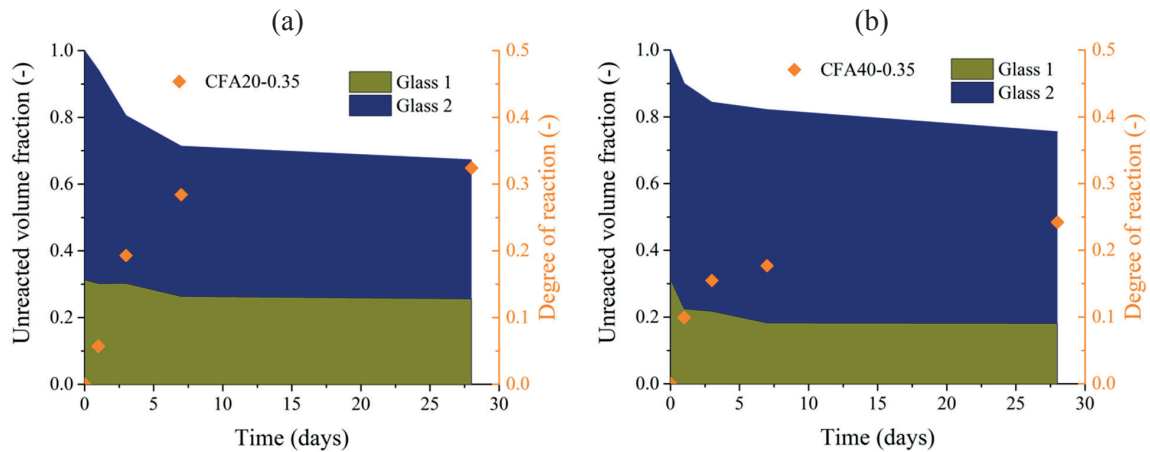


Figure 2.8 Unreacted volume fraction³ of glassy phases and degree of reaction of fly ash

2.5 Phases assemblage

2.5.1 X-ray diffraction

Samples were prepared and cast into plastic vessels. The vessels were sealed with a screwed cap and a layer of paraffin film. All specimens were sealed stored at 20 ± 0.1 °C before testing. XRD measurements were performed on freshly sliced samples (thickness of around 2 mm) at 1, 3, 7, 14 and 28 d. The specimens were cut with a diamond saw at desired ages and put into the XRD chamber immediately. The patterns of the hydrated samples were recorded using an X-ray diffractometer (CuK α radiation, 45 kV, 40 mA) in the scanning range of 5-70 °. The applied testing rate was 0.02 °/s for all specimens.

2.5.2 Mass balance calculation

In order to quantify also the amount of amorphous phases, such as C-S-H, mass balance calculation was applied in this section. Mass balance calculation for quantifying the phase assemblage followed the same procedure as in [9], see *Figure 2.9*.

³ The specific error is 3 vol.% according to [8]

The principle of mass balance is calculating the hydrates based on the consumed oxides composition from anhydrides assuming the equivalent elements during chemical reactions. In the process, the quantity of clinker phases and ettringite was determined from XRD. Free water was calculated by subtracting the water bound in hydrates from the initial water in mixtures. The water bound in C-S-H was calculated based on the ^1H NMR test in [10]. As a result, the water molecules to unit of Si and Al ratio is kept as 4 in C-S-H chain [10]. For CFA40-0.35, the reactive phases in fly ash were obtained from the SEM-EDS method for considering two glass phases.

Since the fixed composition of hydrates is needed in the mass balance calculation, SEM-EDS analysis was applied to C-S-H for obtaining the ratio of chemical compositions of C-S-H, namely Ca/Si and Al/Si. This quantification was done with EDS spots analysis. Only inner C-S-H was considered in the calculation of the element ratios due to it is less affected by intermixing with other phases.

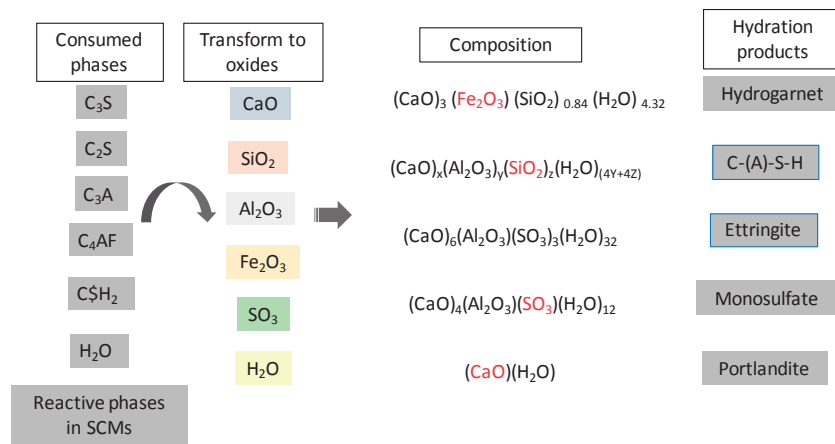


Figure 2.9 Schematic representation of mass balance method (oxides marked as red are the composition for calculating specific hydration product)

2.5.3 Results and discussion

The chemical composition of C-S-H in three systems was investigated: Cement-0.35, CFA40-0.35 and CQZ40-0.35. These three systems are the systems used for later prediction and simulation in Chapter 6 and Chapter 7. Si/Ca and Al/Ca of C-S-H in three systems are plotted at 28 d in Figure 2.10. A higher Si/Ca can be found in CQZ40-0.35 and CFA40-0.35 than in Cement-0.35. The composition of C-S-H should not change by adding quartz in the system [12]. However, higher Si/Ca in CQZ40-035 found here may be due to higher w/c in the system than in Cement-035 which promotes the dissolution of Si and Ca. Ca is later consumed by the formation of portlandite while Si goes to C-S-H only.

Higher Al/Ca can be observed in CFA40-035 than two other systems. The higher Al/Ca and Si/Ca in CFA40-0.35 are mainly from the supply of Al and Si in fly ash [2]. The pozzolanic reaction increased two ratios in C-S-H of CFA40-0.35. The higher Si/Ca can be partly due to also the filler effect as explained for CQZ40-0.35.

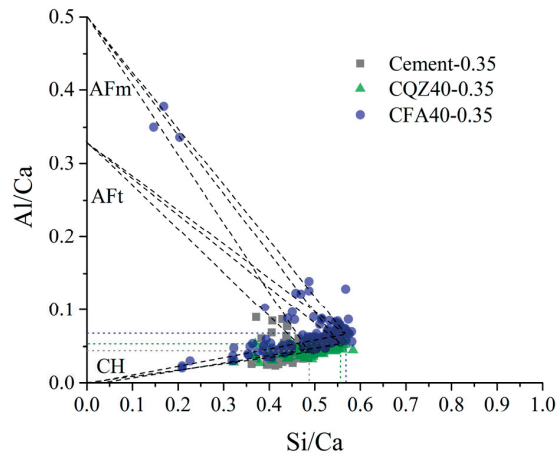


Figure 2.10 Comparison of the chemical composition of C-S-H in three systems at 28 d (Cement-0.35, CQZ40-0.35 and CFA40-0.35)

Phase assemblage for three systems at 3 d and 28 d is shown in Figure 2.11. The volume of the main phases appeared in each system was normalized to the volume of the paste. Higher water and less amount of C-S-H was found in blended systems. The amount of portlandite in CFA40-0.35 was lower than that in two other systems due to the pozzolanic reaction of fly ash. The volume of water + air can be compared with the porosity determined from experiments in later chapters. The volume of different phases is helpful for verifying the microstructure simulation in Chapter 7.

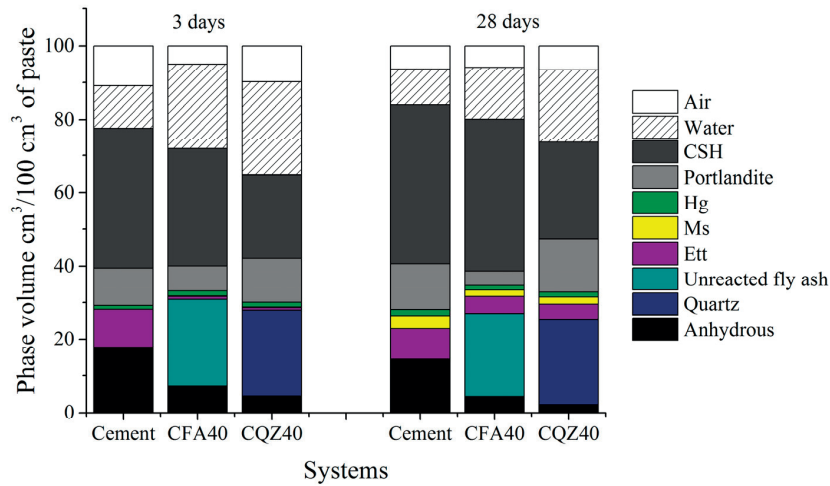


Figure 2.11 Phases assemblage from mass balance method

2.6 References

- [1] B. Lothenbach, K. Scrivener, R. D. Hooton, Supplementary cementitious materials, *Cem. Concr. Res.* 41 (2011) 1244–1256.
- [2] F. Deschner, F. Winnefeld, B. Lothenbach, S. Seufert, P. Schwesig, S. Dittrich, et al., Hydration of Portland cement with high replacement by siliceous fly ash, *Cem. Concr. Res.* 42 (2012) 1389–1400.
- [3] H. F. W. Taylor, *Cement chemistry*, Thomas Telford Publishing, 1997.
- [4] Norm suisse SIA 215 Liants minéraux, 1990.
- [5] M. Namluk, T. Nawa, Effect of fly ash on the kinetics of Portland cement hydration at different curing temperatures, *Cem. Concr. Res.* 41 (2011) 579–589.
- [6] E. Berodier, K. Scrivener, Understanding the filler effect on the nucleation and growth of C-S-H, *J. Am. Ceram. Soc.* 97 (2014) 3764–3773.
- [7] P. T. Durdziński, M. Ben Haha, S. A. Bernal, N. De Belie, G. Elke, B. Lothenbach, et al., Outcomes of the RILEM round robin on degree of reaction of slag and fly ash in blended cements, *Mater. Struct.* 50:135 (2017).
- [8] P. T. Durdziński, C. F. Dunant, M. Ben Haha, K. L. Scrivener, A new quantification method based on SEM-EDS to assess fly ash composition and study the reaction of its individual components in hydrating cement paste, *Cem. Concr. Res.* 73 (2015) 111–122.
- [9] P. T. Durdziński, M. Ben Haha, M. Zajac, K. L. Scrivener, Phase assemblage of composite cements, *Cem. Concr. Res.* 99 (2017) 172–182.
- [10] A. C. A. Muller, K. L. Scrivener, A. M. Gajewicz, P. J. McDonald, Use of bench-top NMR to measure the density, composition and desorption isotherm of C-S-H in cement paste, *Microporous Mesoporous Mater.* 178 (2013) 99–103.

Chapter 3 Autogenous shrinkage and self-desiccation

This chapter reviews the mechanisms and the procedures for measuring autogenous shrinkage as well as the experimental factors influencing the accuracy of autogenous shrinkage measurement. In addition, the experimental results of autogenous shrinkage and self-desiccation (i.e., of the development of the internal RH) in cement pastes with different w/cs and different amounts of quartz filler and fly ash are presented.

Contents

3.1	Literature review.....	24
3.1.1	Mechanisms	24
3.1.2	Measurement method	30
3.1.3	Errors associated with the measurement of autogenous shrinkage.....	33
3.2	Autogenous shrinkage and self-desiccation	36
3.2.1	Experimental methods.....	36
3.2.2	Autogenous shrinkage.....	38
3.2.3	Self-desiccation.....	41
3.2.4	Relative humidity drop due to salts dissolved in the pore solution.....	42
3.2.5	Relationship between autogenous shrinkage and self-desiccation.....	43
3.3	Summary.....	44
3.4	References	44

3.1 Literature review

Autogenous shrinkage is, as stated in [1] ‘*the bulk deformation of a closed, isothermal, cementitious material system not subjected to external forces*’. While autogenous shrinkage is much lower than drying shrinkage in traditional concrete, it is more pronounced for HPC and UHPC with high cement content and low w/c [2,3]. It may lead to serious durability problems, as mentioned in *Chapter 1*. Methods for reducing shrinkage based on avoiding moisture loss or wet external curing are not effective against autogenous shrinkage, because avoiding moisture loss does not influence self-desiccation and the distance of water penetration from the surface is limited due to the low porosity of HPC [4]. Therefore, internal water curing was developed for HPC, in which internal water reservoirs are embedded into the fresh concrete with the aim of gradually releasing the water they contain during cement hydration, thereby mitigating autogenous shrinkage. For a deeper discussion on internal curing method, see reference [4]. In this thesis, measurements and predictions of autogenous shrinkage are only performed in systems without internal curing.

This literature review aims at bringing together the recent discussions and contributions about clarifying the mechanisms and demonstrating testing methods of autogenous shrinkage.

3.1.1 Mechanisms

Autogenous shrinkage is caused by chemical shrinkage (the volume occupied by the products of the hydration reaction is smaller than that of the reactants [5]) and self-desiccation as a consequence of cement hydration [6]. The self-desiccation and self-desiccation deformation are also manifestations of the chemical shrinkage, see *Figure 3.1*. Empty pores are generated due to chemical shrinkage and as a result, the radius of the water menisci is decreased (*Figure 3.1(a)*), inducing the self-desiccation and self-desiccation deformation (*Figure 3.1(b)*) [1].

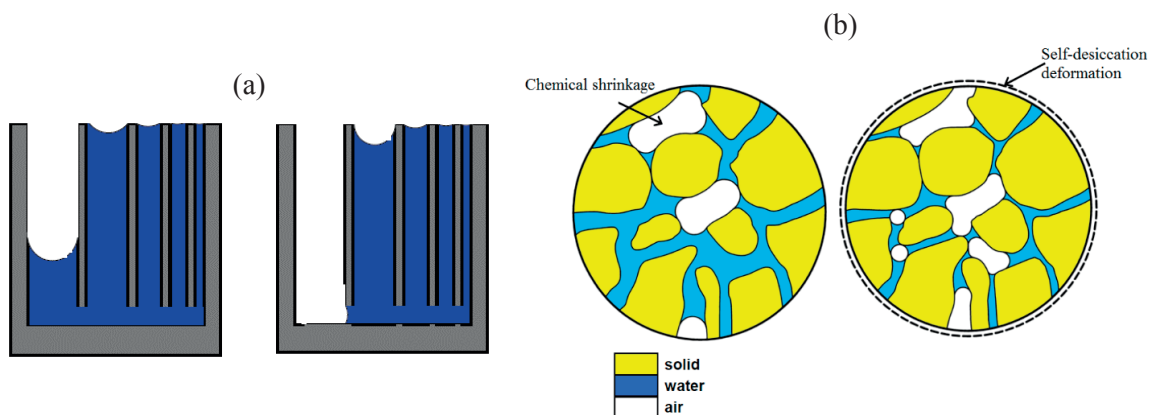
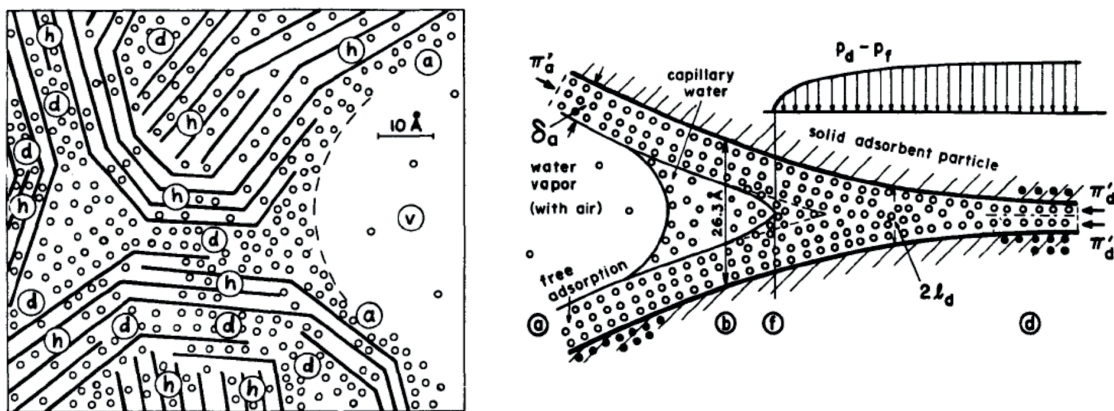


Figure 3.1 Schematic representation of self-desiccation ((a), cylinder pore walls and pore water is shown as dark blue) [10] and self-desiccation deformation (b) [1]

The bulk deformation of a cement-based system (an unsaturated, porous body) is a result of the chemical and physical interaction between the solid skeleton and the pore solution. With the progress of cement hydration, cementitious materials experience several volume deformation processes. Before setting, when concrete is still plastic, chemical shrinkage causes a bulk volume reduction (no voids created) without the buildup of stress [1]. After setting, the solids form a solid skeleton and chemical shrinkage leads to the desaturation of pores and formation of water-air menisci [7,8]. Around set time, the multiplication of connected paths with further cement hydration leads to a rapid increase of elastic modulus, while later the increasing of elastic modulus slows down as the connections broaden [9]. After all the solids become connected, the stiffness of the systems increase is limited and the volume deformation therefore is more modest.

Consensus that self-desiccation is the primary cause of the autogenous shrinkage has been reached; however, the real driving force is still being debated. The proposed mechanisms are necessarily related to the proposed models of microstructure, with characteristic pore classes and water populations occupying these classes [11]. The following discussion of the mechanisms of autogenous shrinkage is based on the classical model of microstructure and pore water by Powers [12]. The schematic *Figure 3.2(a)* shows the interaction of water and microstructure.

According to the available literature, the proposed driving forces for autogenous shrinkage are mainly: changes in the surface tension of the solid gel particles, disjoining pressure, and capillary tension [1]. The last two are favored by most of researchers, while the surface tension of solid gel particles is commonly considered to have minor influence on autogenous shrinkage. *Figure 3.2(b)* shows the water air menisci and the corresponding stress [11]. The explanation of the figure, along with the definition and description of three driving forces and the focus of the debate are presented below:



(a) Model microstructure of cement paste with different types of water (b) Model of a hindered water adsorption layer with transition into a macropore

Figure 3.2 Sketch of solid and water states in cement paste [11]: (d), interlayer water (h), physically adsorbed water (a), capillary water (c) and empty pores (v)

Surface tension:

The surface tension of a solid is the tangential stress (force per unit length) in its surface layer [13,14]. The adsorption of a liquid onto any solid leads to a decrease of surface tension and thereby to swelling. In *Figure 3.2(b)*, the surface tension is shown as the force marked with π . The self-desiccation changes the thickness of the water layer adsorbed onto the cement gel solid (as proven by a study using BET isotherm measurement, the lower RH results to smaller thickness of the adsorbed water layer as shown in [15]), which basically leads to an increase of the surface energy and surface tension [14]. Therefore, changes in the surface tension acting on the C-S-H are considered as one possible reason for shrinkage (or for swelling when the RH is increasing and the thickness of the adsorbed water layer is increasing).

A relationship between the adsorbed layer and the surface tension of the solids was examined by Bangham et al. [16]. The Gibbs' adsorption isotherm was applied to derive *Equation 3.1* [17]. However, the calculation was found to be not accurate enough, especially at lower vapor pressure. Later on, they proposed *Equation 3.2* to relate changes of the surface tension of the solids with expansion/shrinkage by combining the Laplace equation and *Equation 3.1* (Powers [18] also established a principally similar equation). This famous equation was then used for modeling both swelling and autogenous shrinkage [14,19].

However, according to most authors, the surface tension should not play a dominant role as a driving force of autogenous shrinkage due to following reasons:

In a sealed condition, the range of RH change is from 100% to 75% since hydration of cement stops when the RH becomes lower than about 75% [20–22]. In this range, the water and solid status are very similar as presented in *Figure 3.2 (b)* where the adsorbed water layer [14] is rather thick. Based on the equation proposed by Badmann et al. [15], the thickness of the water layer is related to the RH, resulting to around 3-4 water molecule layers after 7 d of hydration for cement paste with w/c 0.4. Powers and Brownyard [23], by using the BET isotherm, calculated that a monomolecular water layer would complete at RH of 12% and a bimolecular water layer would complete at RH of 51%. The surface tension will be reduced significantly with the first layer of water molecule absorbed, but the change declined to almost negligible levels for the third or fourth layers [7]. This is mainly because of the relatively weaker chemical bound forces between the outer layers and the surface of the solid. Only when the RH is lower than about 30%, surface tension can outweigh the cohesive forces between water molecules [11]. In some papers, RH of 50% can be found instead of 30% [24]. However, the agreement is that, when the RH is below 30%, the van der Waals attraction is the dominating force in the system. Another reason could be that the surface tension acts only on the solids alone and not directly on the entire porous body, therefore it should not be an important reason for the apparent deformation [25].

Equation 3.1

$$\pi = \frac{R \cdot T}{V_m \cdot O} \int_0^P \frac{V}{P} dP = -\Delta F$$

where: R [J/mol·K] stands for ideal gas constant, T [K] stands for the absolute temperature, V_m [m³/mol] stands for the molar volume of water and O [m²/kg] stands for the specific surface area of

the inner part of the solids. V [m³] is the volume of water layer adsorbed and P [Pa] is the vapor pressure. ΔF is the decrease of the surface energy [J/m²].

Equation 3.2

$$\frac{\Delta l}{l} = \lambda(F_0 - F) = \lambda(\gamma_0 - \gamma)$$

where: $\Delta l/l$ [m/m] stands for the linear shrinkage because of a variation in surface energy, λ is a constant linked with elastic properties of the solids, can be expressed with O , elastic modulus E [Pa] (or bulk modulus of porous materials K [Pa]) and density ρ [kg/m³] of solids, see *Equation 3.3* [26,27] (the assumption behind the second equal sign is the Poisson's ratio of 0.25). F and F_0 is surface energies with and without the adsorbed water layer, respectively. γ and γ_0 [N/m] are the surface tension with and without the adsorbed water layer.

Equation 3.3

$$\lambda = (O \cdot \rho) / (3 \cdot E) = (2 \cdot O \cdot \rho) / (9 \cdot K)$$

Disjoining pressure:

Disjoining pressure describes the complex interactions between the solid walls and the pore fluid and it is highly sensitive to the ion concentration in the pore fluid, see *Equation 3.4* [28–30]. The disjoining pressure is called P_d in this thesis, while in some papers the Greek letter Π can be found instead. In other words, as shown in *Figure 3.2 (b)*, the action of the disjoining pressure region is in the areas of hindered absorption, between (f) to (d), where the space between the two solid surfaces, $2l_d$ (pore size), becomes less than the two times the thickness of the free adsorbed layers, about 10 water molecules (26.3Å) [24].

Equation 3.4

$$P_d = P_m + P_e + P_s$$

where: P_m is the attractive dispersive force (primarily the van der Waals forces), P_e stands for the repulsive force due to the diffuse electric double layer and P_s is defined as the properties of water and its ability to form solvation or the hydration shells (it can lead to high repulsive forces) [28].

Beltzung and Wittmann [24,31] performed a separation test between two quartz glass and mica surfaces which were attracted by van der Waals forces in the dry condition. They noticed that, when the RH was increased to around 55%, the disjoining pressure overcame the van der Waals attraction (which is weakened when the absorbed water increases) and began to separate the quartz surfaces. The disjoining pressure was considered to be closely linked with RH and to act also at high RH, so that it could be a driving force of autogenous shrinkage. After Wittmann and his coworkers, some more studies, e.g., modeling of autogenous shrinkage based on the mechanism of disjoining pressure (often with capillary pressure together) were published [32]. Besides the direct measurements of separating quartz and mica surfaces [24], there are further, some research supporting this mechanism. According to them, two main points were focused: 1) pore fluid at a scale of a few nanometers cannot

generate capillary pressure, however, in the cement paste, large amount of pores are nano-pores [33]; 2) shrinkage is reduced by changing the chemical compositions (ion concentration) in the pore fluid. This behavior is typical when disjoining pressure is the mechanism of autogenous shrinkage [24]. However, both of them are lack of evidences and are still being questioned. For the first point, the water in the nano-pores should have the same stress state as the capillary water. Additionally, the menisci have been physically observed and the Kelvin equation proven valid for pore radii of 4 nm [34]. For the second point, the properties of the materials would be completely changed after adding the alkali.

To calculate the disjoining pressure, the aforementioned three terms in *Equation 3.4* should be determined with the distance of two solid interphases, see [28]. However, with the help of proposed balance under gravitational potential of the disjoining pressure between helium and glasses, the volume changes caused by disjoining pressure can be calculated in the cementitious materials [35], see *Equation 3.5*.

Equation 3.5

$$\frac{dV_d}{V} = \frac{w \cdot \Delta P_d}{-K}$$

where: V_d/V is the dimensional change of the materials due to disjoining pressure variation, w is the volumetric water content at certain temperature.

There is no doubt that disjoining pressure has its primary effect when the RH is above 50%. However, the main argument raised by some researchers is the influence of disjoining pressure when the internal RH changes from 100% to 70-80%. According to [7], the disjoining pressure stays practically constant at that RH range because the number of adsorbed water layers in this region changes very sharply. The value of disjoining pressure has been reported in [24] to be of the order of magnitude of a couple of MPa.

Capillary tension:

The capillary tension in the pore solution is related to the water-air menisci formed in the partly empty pores [2]. As expressed with the Young-Laplace equation in *Equation 3.6* with the assumption of cylindrical pores, the capillary tension in cementitious materials can be defined as the pressure difference between the vapor above the meniscus and the liquid in the system. Its effect should dominate in the upper RH range, above about 45% RH (correspond to pore radii of 2 nm) because at lower RH the menisci burst and cannot exist anymore [14]. The relationship between capillary tension and RH has been shown in *Equation 3.7*. According to most researchers (e.g., [7,36,37]), the capillary tension is regarded as the main driving force of autogenous shrinkage. Due to the formation of menisci at the pore fluid-vapor interfaces, capillary tension in the pore fluid and compression in the solid skeleton develop.

Equation 3.6

$$P_c = P_g - P_l = -\frac{2\gamma_w \cos(\theta_w)}{r}$$

where: P_c [Pa] is the capillary tension (negative value), P_g [Pa] is the gas pressure above the menisci, P_l [Pa] is the saturated vapor pressure, γ_w is the surface tension of the liquid in the inner walls of capillary (for pure water, the value equals to 7.28×10^{-2} N/m at 20 °C, this can be used also for the pore solution since the influence of ions in the pore solution is small but the surfactant have a large effect on this value), θ_w [°] denotes the contact angle between the pore fluid and the pore walls.

Equation 3.7

$$P_c = \frac{R \cdot T}{V} \ln(RH)$$

With the assumption that cementitious materials behave as elastic and isotropic porous solids, it is possible to predict the linear autogenous shrinkage based on the capillary tension mechanism using different approaches based on poromechanics [38–40].

The constitutive equation shown below (*Equation 3.8*) for linear deformation of porous materials is on the basis of the *Biot-Bishop approach* [41]:

Equation 3.8

$$\frac{\Delta l}{l} = -\frac{1}{3} \cdot P_c \cdot S \cdot b / K = -\frac{1}{3} \cdot P_c \cdot S \cdot \left(\frac{1}{K} - \frac{1}{K_s} \right)$$

where: K [Pa] is bulk modulus of the porous system and K_s [Pa] is the bulk modulus of the solid skeleton. S [-] represents the saturation fraction or saturation degree of the system. b is the Biot coefficient. The saturation degree and the capillary tension together are named as average pore stress ($P_c \cdot S$) [40].

Notice the use of saturation degree here is actually a proxy for Bishop's parameter χ [-]. This parameter χ is reflecting the contact area between the pore solution and the solid and is often expressed as a function of saturation degree ($\chi = \chi(S)$) [42]. Since S is easier to measure than χ and they should not be very different (at full saturation and at zero saturation they are equal) [43], in the range of saturation degrees covered in self-desiccation, we can assume that $S \sim \chi$. Therefore, to simplify, S is used in the equation for replacing χ .

The *Biot-Bishop approach* was first proposed by Biot in 1941[44] by extending *Hooke's law* for the consolidation of a porous body, which reads the deformation of the materials equals to the fluid pore pressure (P) divided by the bulk modulus (K). Biot and Willis [45] introduced the Biot coefficient ($b = 1 - K/K_s$, K_s is the bulk modulus of the solid skeleton) into the initial equation from Biot. By considering also the relationship between S and χ , the average pore pressure can be described as $S \times P_l + (1-S) \times P_g$ (P_l and P_g stand for the pressure of the pore water and the gas) [46]. *Equation 3.8* can be obtained by introducing the $P_c = P_g - P_l$ (neglecting the change of gas pressure) into the equation for volumetric displacement of the material (assume the isotropy of the material, thus linear deformation is calculated as 1/3 of the volumetric deformation) [47].

This equation has been used widely for modeling autogenous shrinkage considering only the elastic response of porous cementitious materials under the capillary stress. It is noteworthy to differentiate

and integrate *Equation 3.8*, with considering K , K_S and S (and not only P_c) vary during hydration to model autogenous deformation.

On the basis of the *Biot-Bishop approach*, *Coussy model* [38] was proposed by considering the effect of the interface energy in addition to the effect pressure, then *Vlahinić model* [42] was proposed by considering the weakening of the porous skeleton due to the desaturation of the material. From the literature, models including the *Biot-Bishop approach* [41], *Coussy model* and *Vlahinić model* can be found, which generally yield similar results when the RH is higher than 50% [48].

Summary

All these three driving forces mentioned above can be calculated based on knowledge of the internal RH of the system. It is noted that, it may be difficult or impossible to distinguish and separate the effect of different mechanisms involved in autogenous shrinkage; this is in particular true for capillary tension and disjoining pressure (due to the linear momentum conservation between hindered adsorption water and capillary water, these two forces should be in equilibrium [48]). The changes of the pore pressure either due to capillary tension or disjoining pressure is associated to the RH based on *Kelvin-Laplace equation* [39] (*Equation 3.7*). A recent published paper [49] used thermodynamic method to clarify the mechanism of autogenous shrinkage. In [49], the authors are against that disjoining pressure being the primary mechanism since it keeps in constant in the bulk liquid stress during desiccating. From a theoretical point of view and based on its formal equivalence with the disjoining pressure approach [48], the capillary pressure can be considered as the most important driving force for autogenous shrinkage.

However, the observed early-age expansion cannot be explained by the capillary pressure evolution which should be increasing (considering the absolute value) all the time. This measured expansion is associated to reabsorption of bleed water [50] (in this case, the expansion is following a shrinkage deformation, discussed in *section 3.1.3*) or an higher crystallization pressure caused by the portlandite oversaturation level in solution [51,52] or the ettringite formation at high RH [50].

This thesis work will be based on the capillary pressure mechanism as a framework for carrying out all the investigations. Therefore, whenever studying autogenous shrinkage, precise knowledge of the evolution of the porosity and pore network, the state of water in the capillary pores, the chemical potential of the pore solution and of the mechanical properties of the solid skeleton as hydration proceeds are necessary.

3.1.2 Measurement method

Drying shrinkage or thermal deformations may occur in cement systems at early ages together with autogenous shrinkage. Choosing a proper measuring technique to investigate autogenous shrinkage is essential for distinguishing it from other different deformations [53].

The evolution of autogenous shrinkage typically shows a very high strain rate as soon as the measurements are started. The reason is that before set time, the cementitious material cannot sustain internal voids and autogenous deformation is equal to chemical shrinkage. As this deformation happens

in the liquid stage and is not stress-inducing, taking it into account would result in mistaken conclusions. Therefore, a reference time also referred to as *time-zero* (the time at which the autogenous deformation should be zeroed), is a key factor in determine autogenous shrinkage, as extensively discussed in the literature (e.g., [54,55]). Using a wrong or unreasonable *time-zero* or reference time during the experiments will lead to completely opposite conclusion for the deformation, no matter what kind of methods is used.

Traditional methods for measuring autogenous deformation include both volumetric and linear methods. Buoyancy methods were first used to measure volumetric autogenous shrinkage by Yates in the 1940s [56]. Generally, in volumetric measurements, fresh cement pastes or mortars are filled in a flexible plastic membrane (or a rubber bag), after which the membrane is sealed and immersed in water or oil (see *Figure 3.3*). The change of weight of the immersed sample is recorded over time, and thus the volumetric deformation can be obtained via Archimedes' principle.

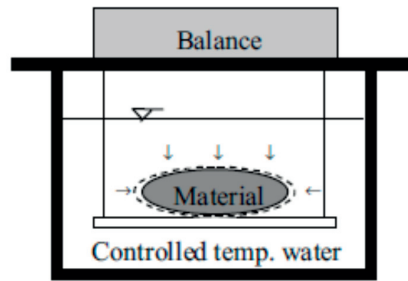


Figure 3.3 Measurement of autogenous shrinkage using rubber bags [57]

The most critical points which researchers need to note are the permeation of water through the membrane (rubber membranes are usually not watertight and the water activity is different inside and outside of the membrane due to the dissolved ions), absorption of the oil by the membrane during the measurements (paraffin oil is often used, expansion of the rubber occurs when oil is adsorbed) and the problem with bleeding water being reabsorbed by hardening paste [58,59]. All have a strong impact on the final results of the autogenous deformation. For the problem of permeation of water and adsorption of oil, membranes made with different types of materials, e.g., latex or polyurethane have been compared in the literature [59]. Another problem with the volumetric measurement is the possible loss of contact between the membrane and the hardening specimens [58]. If a larger sample is used, the deformation caused by the temperature gradient from the surface to the sample core needs to be taken into the consideration [60]. In practice, attention should be paid to the occurrence of temperature gradients as the exterior of the cementitious material equilibrates gradually to the external temperature. This temperature gradient will possibly lead to self-restraint due to the non-uniform thermal deformations within the materials [61].

Linear methods have also been applied to measure autogenous shrinkage for decades. There are primarily three categories of testing setups:

The first type of setup is where samples are measured after demolding and sealing by e.g., the measurement based on the ASTM C157 [62], standard length change measurement for mortar and concrete. Linear variable differential transformers (LVDTs) have been used to measure the deformation after demolding [63]. The main disadvantage of this type of method is the late starting time, since samples need to become strong enough to be demolded. Note that autogenous shrinkage is remarkably pronounced at early ages due to high proceeding rate of hydration and self-desiccation [53]. Therefore, it is of crucial importance to start to measure the deformations as early as possible.

Another type of methods for the deformation is based on measurements in the mold, e.g., Japan Concrete Institute (JCI) setup, with LVDTs that measure the movement of studs that are positioned within the fresh concrete [64–66], see *Figure 3.4*. The LVDTs are placed through holes on the side of the molds. The disadvantages of these methods are: a) the difficulty of sealing (the sample is cast into the mold from the top, it cannot be perfectly encased and it is difficult to control the mass loss of the sample); b) friction with the mold. Even when using Teflon sheets or two foils with lubrication or either sheets of Mylar [58] in between, the concrete might get stuck because the sides are never perfectly smooth; c) the studs might move in the fresh concrete due to the vertical forces exerted by the settling materials [66].

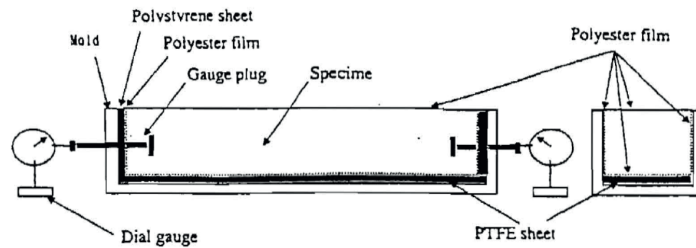


Figure 3.4 Setup based on JCI method [65]

Corrugated tubes method is one of the most widely used methods to measure linear evolution of autogenous shrinkage of cementitious materials from the time of casting, which was first proposed by Jensen and Hansen [67] and later developed into the ASTM C1698-09 method [68]. In this method, a plastic corrugated tube (*Figure 3.5*) which is much stiffer in the radial than in the longitudinal direction is used. This corrugated tube filled with cement paste is then sealed and placed horizontally on a metal frame. The tubes are further placed in a temperature controlled oil bath (a water bath should not be used because the tubes might be permeable to water). This implementation allows control of the temperature and further limits the evaporation through tube [53]. Then the linear shrinkage is obtained by following the displacement of the ends of the tubes. While in ASTM C1698-09, this is done by placing the samples manually on a measuring bench and measuring the length change with a comparator. For higher accuracy and simplicity, the displacement can be measured continuously with transducers attached to the ends of the sample (either both ends or one end with the other end fixed is possible), e.g., [12].

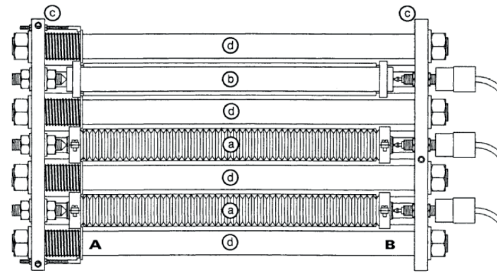


Figure 3.5 Schematic figure of corrugated tubes for autogenous shrinkage measurement [67]

The advantage of using manual measurement in the ASTM standard is that only one transducer is demanded. However, samples should be ensured to be stiff enough to be relocated. Note that any damaging of the fragile sample during handling may in the end give invalid measurements [53].

It has been shown that, assuming isotropy of autogenous deformation, the two types of methods (volumetric and linear method) can provide equivalent results when sources of error and measurements artefacts (e.g., avoid penetration of liquid through the membrane) are eliminated [58,59].

3.1.3 Errors associated with the measurement of autogenous shrinkage

The most significant factors that may influence the measurements are identified: temperature effects, bleeding and reference time. These factors not only influence the measurements performed with corrugated tubes, but also other approaches mentioned above. We published a paper [53], in which we carried out a systematic study quantifying the precision of the autogenous shrinkage measurement, mainly focusing on all these aforementioned factors on the measured deformation.

Deformation due to temperature change

The hydration of cementitious materials is exothermic, which causes the temperature of the system to increase, due to their rather low thermal conductivity. The increase of the temperature when the rate of the heat release exceeds the rate of the heat dissipation leads to the expansion of the cementitious materials. The potential of the deformation of materials due to temperature change can be described as the coefficient of thermal expansion (CTE). This thermal expansion in the cementitious materials encompasses two mechanisms: 1) the direct thermal dilation occurred immediately with the increased temperature [69]; 2) an increase of RH caused by the increase of the temperature [70] (hygro-thermal mechanism, referred as $\Delta RH/\Delta T$ in the Figure 3.6 [71]). The typical CTE measured is about $10 \times 10^{-6} \mu\text{m}/\text{m}/^\circ\text{C}$ for hardened concrete and is about $20 \times 10^{-6} \mu\text{m}/\text{m}/^\circ\text{C}$ for cement pastes [70].

This expansion may happen even when the temperature of ambient is controlled during the experiments, due to self-heating of the samples caused by exothermic hydration reaction; this problem becomes especially important when using samples with rather large sizes and with low w/c [72]. Therefore, poor control of the temperature may cause misleading results. In [53], it was found that for cement paste with w/c of 0.30, the maximum temperature difference between the surrounding and

inside the corrugated tubes could be 3.5 °C (air-storage) or 0.6 °C (oil-bath cured), resulting in 56 $\mu\text{m}/\text{m}$ or 9.6 $\mu\text{m}/\text{m}$ thermal strain (assuming CTE is 16 $\mu\text{m}/\text{m}/^\circ\text{C}$).

It was also found that there was a higher temperature increase in the samples in Vicat tests compared to the samples in corrugated tubes, leading to an underestimation of the set time and therefore an overestimation of the autogenous shrinkage deformation [53]. Because of the faster hydration of the cement pastes in the Vicat test, consequently faster setting occurred comparing to that in the corrugated tubes (30 minutes' delay of the set time corresponds to a strain of 60 $\mu\text{m}/\text{m}$) [53].

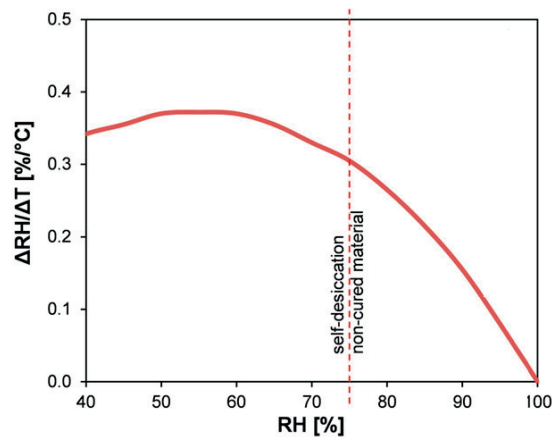


Figure 3.6 Schematic representation of the evolution of $\Delta RH/\Delta T$ as a function of RH [71]

Bleeding

Bleeding can be observed quite frequently in specimens, mainly due to the mix design (e.g., w/c, dosage of SP and admixtures) or the original properties of cement particles and the PSD. Bleeding was declared in the ASTM standard [68] as a possible source of error. However, this impact should be negligible for cement pastes or mortars with w/c lower than 0.40 as stated in [68].

When bleeding happens, there is a lower initial w/c of the system under the layer of bleed water first experience a shrinkage. Then the reabsorption of the layer of water from the surface (similar as external curing) back into the specimen occurs gradually, keeping the RH high and suppressing shrinkage [50].

Expansion caused by bleeding can be minimized by rotating the sample before the set time. As seen in Figure 3.7, the result of autogenous deformation showed expansion at early ages and then continued the shrinkage [53]. Higher shrinkage and slope of shrinkage were observed from the rotated samples compared to non-rotated samples. This was also observed in [50]. Rotation altered not only the initial swelling behavior, but also the subsequent shrinkage. The influence of rotation was much higher in the systems with higher w/c. Bleeding can also influence the initial shrinkage (see Figure 3.7) even when the w/c is 0.30, however, this effect maybe more significant before final setting [53].

Note that rotation may have an effect (especially with fast rotation) on the microstructure, but it ensures that a paste/mortar with the actual w/c is tested.

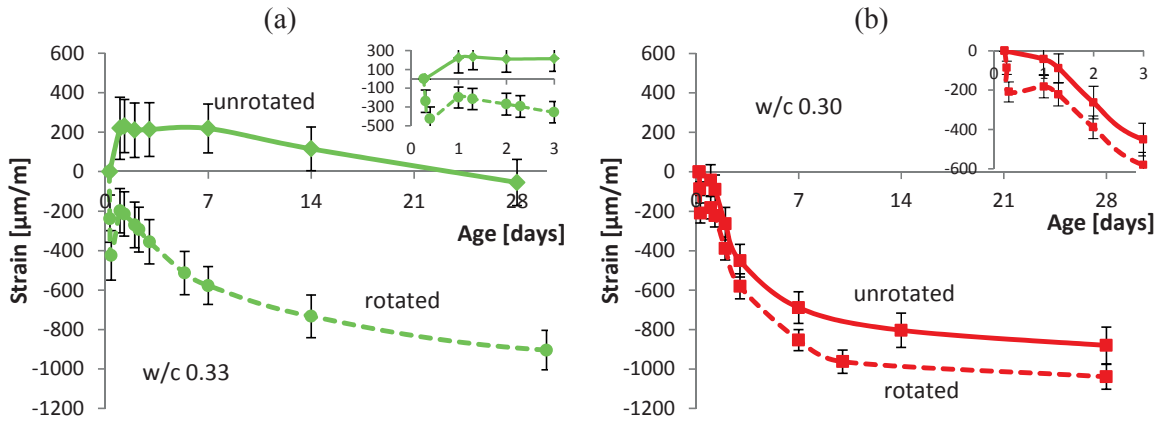


Figure 3.7 Influence of rotation on the autogenous shrinkage results ((a): system with w/c of 0.33, (b): system with w/c of 0.30) [53]

Reference time

The necessity of using the reference time was addressed in *section 3.1.2*. In addition, higher scatter was found when the measurement was started too early (before final set) [53,67].

There are several ways for determining *time-zero*: 1) final set time from Vicat needle test [68], reflecting the transition from fluid to solid (the time is also referred as fluid-to-solid transition time). This method is simple and convenient but there is the issue about the temperature change; 2) the time when the rate of the shrinkage changes significantly [54]. This method is suitable for excluding the initial stage with sharply increasing of the autogenous shrinkage. However, if there is expansion preceded as well, it is difficult to define one single change in the rate of shrinkage; 3) the time for meniscus depression generating [73] (simultaneously with the evolution of RH), which does not always agree well with the initial and final set time depending on systems; 4) the start point of the drop of RH as a new way for determining the reference time is proposed by Huang and Ye [74]. This method may need to be re-examined since on the one hand this time is much later than the final set time, on the other hand they may mistake the stabilization of the sensor as a phenomena associated to the chemical effects.

Indeed, using the fluid-to-solid transition time as *time-zero* has more physical meaning. The volumetric deformation and the creation of vapor is found to correspond well with the development of a stress-resisting network of solids by comparing different techniques (acoustic emission measurements, electrical conductivity and ultrasonic pulse conduction) [75]. This fluid-to-solid transition is also close to the final set time (method 1)) [75]. Thus in this thesis, final set time from Vicat needle test will be used as *time-zero*.

3.2 Autogenous shrinkage and self-desiccation

3.2.1 Experimental methods

Vicat needle test

Set time including initial or final set time was measured by using an automatic Vicat needle (setup shown in *Figure 3.8*). The measurement method followed in general the ASTM standard [76], with a modification concerning covering of the samples with stretched food-wrap during the tests. The principle of this standard measurement is to estimate set time from the depth of penetration of a steel needle into a hardening cement paste. The final set time was considered as the moment when the needle could not penetrate into the sample any more. The needle was automatically dropped with intervals of 10 min.



Figure 3.8 Setup for Vicat needle test

Autogenous shrinkage

The linear autogenous shrinkage strains were measured using corrugated tubes (*Figure 3.9*) with 29 mm diameter and length of 425 mm based on ASTM C1698-09 [68]. Before being filled, each tube was closed at one end with a polyethylene plug of 19 mm length and diameter of 21 mm-24 mm (truncated cone). Then it was placed vertically in a steel pipe which was fixed to a vibrating table to provide support during filling. Right after mixing, around 500 g of fresh paste was poured into the corrugated tube within about 2 minutes. Vibration was applied to ensure good filling and partially remove air voids. The corrugated tubes filled with paste were sealed with another plug. Then the tubes were submerged into a silicon oil bath to limit drying through the tubes/plugs and to control efficiently the temperature to be at 20 ± 0.1 °C.

The reference length bar of 425 mm length made of INVAR steel was used for calibrating the measuring bench. The measurement started approximately 1 h after casting. Results of duplicated samples are shown, in which the duplicate samples came from independent mixings. No penetration of the oil into the tubes could be observed, and no considerable mass increase of the samples occurred through the measurement time.



Figure 3.9 Setup for autogenous shrinkage measurement

Relative humidity

Water activity probes type HC2-AW-(USB) (Rotronic) were used to monitor the internal RH (*Figure 3.10*). The accuracy of the sensors at 23 °C is $\pm 0.5\%RH/\pm 0.1\text{ K}$. At approximately 20 h after casting in a plastic vessel, the samples were quickly crushed into pieces of up to 5 mm size and put inside hermetic sample holders. Before and after each experiment, the sensors were calibrated with four different saturated solutions of salts (potassium sulfate, potassium nitrate, potassium chloride and sodium chloride) in the equilibrium RH range of 75-98 %RH. The RH readings were logged at 5 min interval during one month of hydration. After testing for one month, the average drift of the sensors is about $\pm 1.0\%RH$ compared to the beginning of the tests (obtained from before and after calibration); the effect of this drift was partially compensated by calibrating with the average readings from before- and after-calibration. The measurements were performed under controlled temperature of $20\pm 0.1\text{ }^\circ\text{C}$, maintained by circulating tempered water in the casings of the sample holders.

In order to quantify the effect of ions presented in pore solution on the measured RH, the RH of pore solution of systems with w/s of 0.35 was measured. A hydraulic press was used to extract the pore solution from the samples at the ages of around 1, 3, 7, 14 and 28 d. The procedure described in the work of Barneyback and Diamond [77] was followed in this study, while altering the pressure applied (500 MPa). Samples for pore solution extraction were mixed with a vacuum mixer and cast into plastic cylinder containers. Before the extraction, samples were stored in a temperature-controlled room. Right before the extraction, the plastic containers were quickly removed and the samples were placed in the sealed chamber with the water-activity sensor to measure the corresponding RH.



Figure 3.10 Setup for internal relative humidity measurement

3.2.2 Autogenous shrinkage

The autogenous shrinkage development of systems until 28 days with two different w/s is presented in *Figure 3.11* and *Figure 3.12*, respectively. The autogenous shrinkage at time t can be calculated with *Equation 3.9*:

Equation 3.9

$$\varepsilon_{as} = \frac{l(t) - l(t_s)}{l(t_s)} \cdot 10^6 \mu\text{m} / \text{m}$$

where: $l(t)$ [m] is the length of the specimen at time t which can be determined with *Equation 3.10*; t_s is the final set time.

Equation 3.10

$$l(t) = l_{ref} + R(t) - 2 \cdot l_{plug}$$

where: l_{ref} [m] is the length of the reference bar; $R(t)$ is the reading from the gauges linked with LVDTs; l_{plug} [m] is the average length of the plugs on the end of the corrugated tubes.

The results shown here were zeroed at the final set time (*Table 3.1*). The setup gives good repeatability of the measurements for duplicate samples with the maximum difference of the strain of 100 $\mu\text{m}/\text{m}$ (the slopes of duplicate samples are the same). The development of autogenous shrinkage after final set time could be roughly separated into three stages: in the first stage, a small swelling was observed for all systems with w/s of 0.35. During the second stage, a rapid development of autogenous shrinkage was observed. At this stage, the stiffness of the specimen was very low and therefore the sample likely deformed considerably even at low capillary pressures. During the last stage, the autogenous shrinkage slowed down but kept increasing with different rates for different systems due to different hydration processes until the end of the experiments at 28 d. The exception is the autogenous shrinkage of CQZ40-0.35, in which a gradual expansion happened after 3 d due to its rather high

effective w/c, followed by a plateau after 7 d. This may be due to segregation occurred, giving unreliable results, which can be seen from the faster increasing of autogenous shrinkage than Cement-0.35.

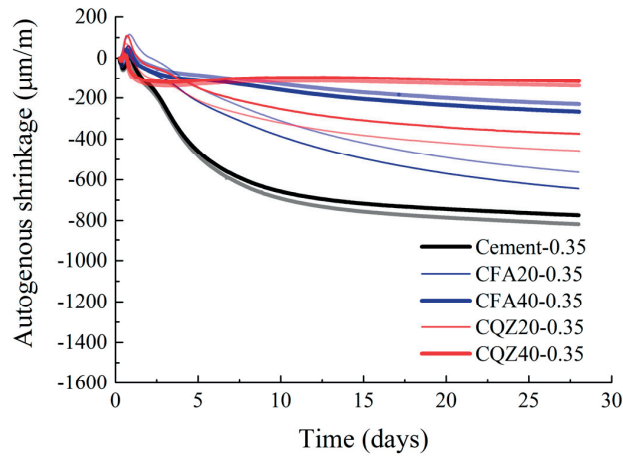


Figure 3.11 Autogenous shrinkage results of cementitious systems with w/s of 0.35

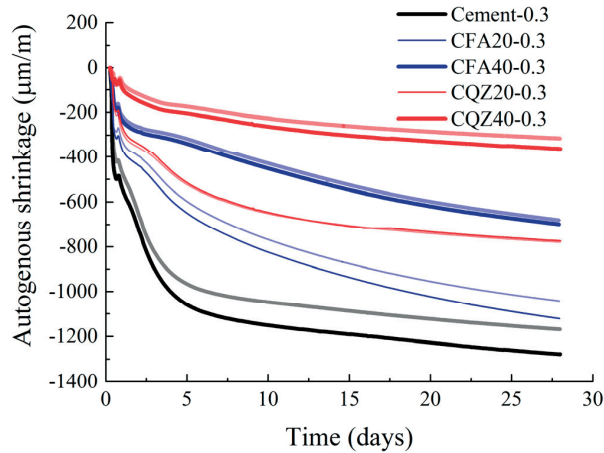


Figure 3.12 Autogenous shrinkage results of blended systems with w/s of 0.30

Table 3.1 Set time of different systems (hours)

Initial set time	Cement	CFA20	CFA40	CQZ20	CQZ40
w/s = 0.35	5.1	4.8	4.7	4.6	4.6
w/s = 0.30	4.2	3.3	5.0	4.8	3.9
Final set time	Cement	CFA20	CFA40	CQZ20	CQZ40
w/s = 0.35	6.1	5.8	6.8	7.3	7.5
w/s = 0.30	5.4	5.3	7.2	7.2	6.2

Comparing the two different w/s considered in this study, the lower the w/s of the system, the higher the autogenous shrinkage. For the total autogenous shrinkage of systems of w/s of 0.35 after 28 d, Cement-0.35 had the highest autogenous shrinkage because of the lowest w/c. With the same volume fraction of fly ash and quartz in the systems, fly-ash-blended systems showed higher autogenous shrinkage. But both of them had much less autogenous shrinkage than cement system (3-4 times less) after 3 d. The trend is the same for w/s of 0.30 and these results also agree with [78], where it was found that the presence of fly ash decreased the autogenous shrinkage. Relating the effective w/c (see *Table 2.4* in *Chapter 2*) to the autogenous shrinkage, the higher self-desiccation can be found due to lower initial water in the systems (the lower relative humidity in the system, the higher the capillary pressure).

The effect of fillers on autogenous shrinkage for both w/s can be separated into four contributions: 1) increase w/c at the same solid content of the pastes; 2) high specific surface resulting in water adsorbed onto the surface of the fillers (which in part compensates effect 1)); 3) different initial pore structure depending on the packing of the particles; 4) restraint to deformation offered by the unaltered filler particles [4]. For point 1), the behavior of the autogenous shrinkage will be the same as the evolution of degree of hydration due to w/c.

For the same substitution level, the divergence of the autogenous shrinkage between quartz-blended systems and fly-ash-blended systems occurred at different ages for different w/s. In w/s of 0.35, the differences between two systems were not very large (particularly at substitution level of 40%, the difference was less than 100 $\mu\text{m}/\text{m}$) and the curves diverged at around 10 d. Whereas at w/s of 0.30, the difference can be as high as 300 $\mu\text{m}/\text{m}$ and the results diverged earlier, around 5 d. Before 5 days, fly-ash-blended and quartz-blended systems with the same substitution levels presented a striking similarity in slopes.

The effect of the pozzolanic reaction (typically in systems with fly ash, slag and silica fume) on the autogenous shrinkage has been extensively studied, e.g., [79–81]. The main effect at early ages will be the dilution of the clinker phases and the impact of clinker granulometry in such systems [82]. At later ages, the effect of the proper pozzolanic reaction should in addition be taken into consideration. The reduction of autogenous shrinkage of fly-ash-blended systems comparing to cement systems could be related to the filler effect at early-ages. However, the reduction highly depends on the average particle size and shape of the fly ash (retain more water) [80]. Termkhajornkit et al. [78] also proposed that lower autogenous shrinkage rates were measured when the SO_3 content in the fly ash was increased. They suggested the process of autogenous shrinkage to be divided into four stages. In the first two stages (possibly correspond to plastic stage), the autogenous shrinkage was mainly caused by the movement of particles due to gravity. In the third stage, the hydration of cement and the reaction of the C_3A to form ettringite was proposed as the dependence of the evolution autogenous shrinkage. In the last stage, autogenous shrinkage slowed down and it seemed to depend mainly on the pozzolanic hydration of the fly ash after 56 days. However, the higher slope of autogenous shrinkage of fly-ash-blended systems shows that fly ash also has a special effect as a pozzolan especially after several days of hydration (degree of reaction of fly ash was around 20%-30% in systems with w/s 0.35). In [6], they mentioned the autogenous shrinkage was enhanced by the pozzolanic reaction of silica fume by removing the stressed portlandite crystals and forming amorphous phase. The same consumption of portlandite crystals happens with fly ash in this case.

3.2.3 Self-desiccation

The experimental results about the evolution of the internal RH in the specimens up to 28 d for systems with w/s of 0.35 and up to 7 d for systems with w/s of 0.30 are presented in *Figure 3.13* and *Figure 3.14*, respectively. Each plot of the curves shows the average result of duplicate samples (two measurements in the systems are close). The fast evolution of RH observed before 3 d in all systems was due to rapid hydration in this period. At the start of the measurements at the age of about 1 d, the internal RH in all specimens was around 96 to 98 %, which is mainly because of the RH drop due to dissolved salts in the pore solution. In moisture-sealed, isothermal conditions, the reduction of internal RH in cementitious systems depends on two major mechanisms: desaturation of pores due to chemical shrinkage (RH_K) and water activity of the pore solution [7]:

Equation 3.11

$$RH = RH_S \cdot RH_K$$

where: the RH_S term (range from 0 - 1) depends on the water activity in the pore solution. RH_S varies continuously with the change of the concentration of the pore solution.

For specimens with different w/s at the same age, as expected, the lower the w/s, the more pronounced the internal RH drop. For the highest w/c tested (CQZ40-0.35 and CFA40-0.35), the RH drop seems to take place mostly due to the effect of dissolved ions in the pore solution, especially at early ages (before about 7 days).

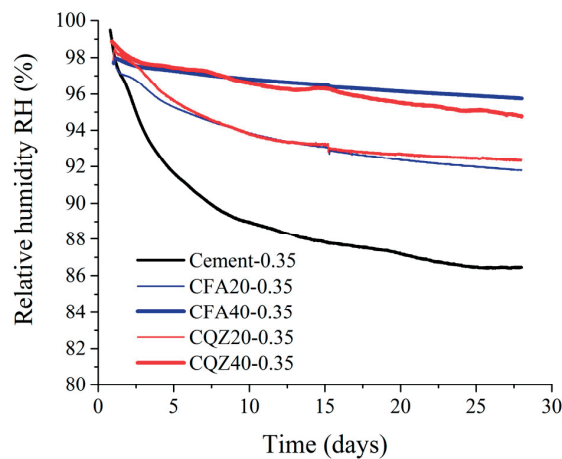


Figure 3.13 Measured RH of blended systems with w/s of 0.35 until 28 d

For the RH drop of fly-ash-blended systems and quartz-blended systems, in the case of higher w/s, the difference between these two systems was limited. Strictly speaking, the slope of autogenous shrinkage in the fly-ash-blended systems was slightly higher than that in quartz blended systems. This indicated that the differences in autogenous shrinkage (in any case small at this w/s) between these two systems were not caused by changes in the RH but possibly rather by the different stiffness of the fillers. In the case of lower w/s, even only up to 7 d, the difference between the two different

filler-blended systems was clear. The RH curves diverged at around 3-5 d after casting, which corresponded to the divergence time of autogenous shrinkage of these systems.

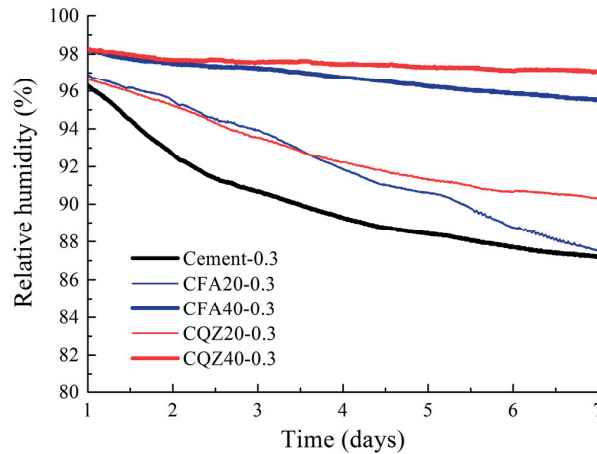


Figure 3.14 Measured RH of blended systems with w/s of 0.30 until 7 d

3.2.4 Relative humidity drop due to salts dissolved in the pore solution

In order to investigate in depth the relationship between the RH_K and autogenous shrinkage, RH_s was measured with the pore liquid extracted from the samples with w/s of 0.35 at different ages, shown in Figure 3.15. Based on the results presented in this figure, dissolved ions have a really minor effect on the total relative humidity, never higher than about 3 %-4 % in the studied systems. As expected, at 28 d the lowest RH_s in the studied systems was around 96 % in Cement-0.35.

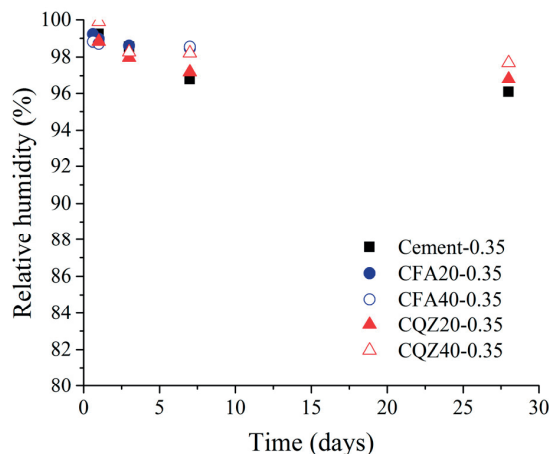


Figure 3.15 Measured RH_s of systems with w/s of 0.35

The RH_S are expected to be lower in the systems with lower w/c, since the ionic concentrations in the solutions are higher for lower water contents. However, this trend is not completely evident in the measurements, possibly due to the insufficient accuracy of the RH sensors in this high RH range. From the figure, the RH_S in all the systems was quite similar. Relatively lower RH_S can still be found at lower w/c (e.g., in CFA20-0.35, CQZ40-0.35).

3.2.5 Relationship between autogenous shrinkage and self-desiccation

In *Figure 3.16*, the relationship between autogenous shrinkage and the calculated RH_K (based on *Equation 3.11*) was presented for the systems with w/s of 0.35. The regular “S shape” curves were shown in Cement and quartz-blended systems but approximately linear relationships were found for fly-ash-blended systems. The curve for CQZ40-0.35 was not exactly following the same trend as other systems, possibly due to the large expansion happening after 3 d. Comparing the slopes, the curves of the fly-ash-blended systems with two different substitution levels showed almost the same slope, while the slopes of the pure cement and quartz-blended systems were similar. Apparently, the fly-ash-blended systems show higher slope than other systems, which means that for the same drop of RH, the fly-ash-blended systems have consistently higher deformation.

From the modeling point of view (using e.g., the *Biot-Bishop approach* [41]), the shape of the curves is also reasonable. Combining *Equation 3.7* and *Equation 3.8*, the RH_K can be linked to the autogenous deformation (note that the saturation degree was also linked with the RH, e.g., by sorption isotherm). Assuming that the bulk modulus evolved with the degree of hydration (in *Chapter 5* and *Chapter 6*, detailed studies about the elastic modulus and Poisson’s ratio development will be shown), almost linear relationship between the capillary pressure and RH was found in this RH range, thus the curves should follow the same trend as the relationship between saturation degree and RH which is almost S shape according to sorption isotherm measurement [83].

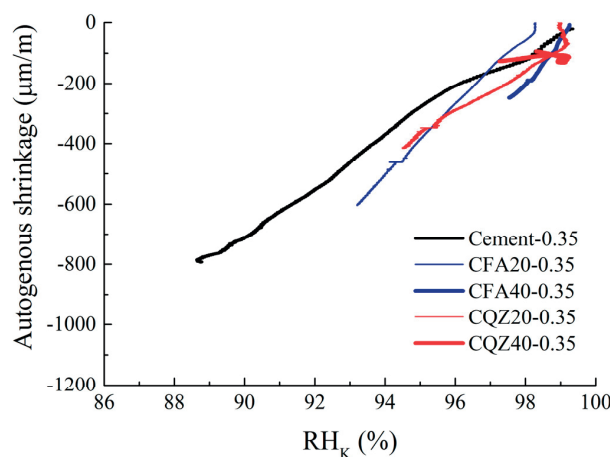


Figure 3.16 Relationship between RH_K and autogenous shrinkage of systems with w/s of 0.35

3.3 Summary

This chapter is the experimental basis of the whole thesis:

In the first part of this chapter, state of the art for the mechanisms associated with autogenous shrinkage, experimental methods presented in literature (volumetric and linear method) and possible errors induced during the experiments were presented.

In the second part, an experimental investigation on autogenous shrinkage measurements and self-desiccation was performed with pure cement and blended systems with w/s of 0.30 and 0.35. The lower w/s results in higher autogenous shrinkage, which corresponds well with the RH evolution of the systems. Further, for a given w/s (0.30 or 0.35), for decreasing amount of filler, increases the amount of cement, and consequently, the w/c decreases (since the volume of the solid is constant); this also leads to higher autogenous shrinkage.

The differences between autogenous shrinkage of fly-ash-blended systems and of quartz-blended systems was bigger in lower w/s. The effect of fly ash on the higher w/s for reducing the autogenous shrinkage was mainly due to the filler effect and slightly due to the pozzolanic reaction.

The measured RH of fly-ash-blended systems and quartz-blended systems at 0.35 were similar, which indicates that the effect of the pozzolanic reaction of fly ash is more due to the change of stiffness rather than the microstructure of the system. The measured degree of reaction of fly ash was around 23% and around 33% in CFA40-0.35 and CFA20-0.35, respectively, see *Chapter 2*. Higher reaction degree of fly ash leads to steeper slope of the curve linking RH_K and autogenous shrinkage. Moreover, in the low w/s, the effect of fly ash for pozzolanic reaction seemed more pronounced. The pozzolanic reaction influenced the autogenous shrinkage as well as the RH.

The RH decrease due to the ion dissolved in the pore solution is below 3% and the system with higher w/c experienced lower RH change. Taking the RH_S into consideration, the relationship between the RH_K and autogenous shrinkage at w/c of 0.35 depends on the studied systems. The slope of the linear part of the curve of fly-ash-blended systems was steeper than the ones in cement and quartz-blended systems.

3.4 References

- [1] O. M. Jensen, P.F. Hansen, Autogenous deformation and RH-change in perspective, *Cem. Concr. Res.* 31 (2001) 1859–1865.
- [2] F. de Larrard, G. Ithurrealde, P. Acker, D. Chauvel, High-performance concrete for a nuclear containment, *Spec. Publ.* 121 (1990) 549–576.
- [3] H. Justnes, E.J. Sellevold, G. Lundevall, High strength concrete binders part a: reactivity and composition of cement pastes with and without condensed silica fume, 2 (1992).
- [4] P. Lura, Autogenous deformation and internal curing of concrete, Delft, 2003.

- [5] H. L. Chateliter, Sur les changements de volume qui accompagnent le durcissement des ciments, 1900.
- [6] O. M. Jensen, P. F. Hansen, Autogenous deformation and change of the relative humidity in silica fume-modified cement paste, *ACI Mater. J.* 93 (1996) 539–543.
- [7] P. Lura, O. M. Jensen, K. van Breugel, Autogenous shrinkage in high-performance cement paste: An evaluation of basic mechanisms, *Cem. Concr. Res.* 33 (2003) 223–232.
- [8] O. M. Jensen, P. F. Hansen, Influence of temperature on autogenous deformation and relative humidity change in hardening cement paste, *Cem. Concr. Res.* 29 (1999) 567–575.
- [9] G. Ye, P. Lura, K. van Breugel, L.A. Fraaij, Study on the development of the microstructure in cement-based materials by means of numerical simulation and ultrasonic pulse velocity measurement, *Cem. Concr. Compos.* 26 (2004) 491–497.
- [10] J. Weiss, P. Lura, F. Rajabipour, G. Sant, Performance of shrinkage-reducing admixtures at difference humidities and at early ages, *ACI Mater. J.* 105 (2008) 478–486.
- [11] Z. P. Bažant, Thermodynamics of interacting continua with surfaces and creep analysis of concrete structures, *Nucl. Eng. Des.* 20 (1972) 477–505.
- [12] T. C. Hansen, Physical structure of hardened cement paste. A classical approach, *Mater. Struct.* 19 (1986) 423–436.
- [13] Shuttleworth. R, The surface tension of solids, in: *Proceedings Phys. Soc.*, 1950: pp. 444–457.
- [14] F. Wittmann, Surface tension shrinkage and strength of hardened cement paste, *Mater. Struct.* 1 (1968) 547–552.
- [15] R. Badmann, N. Stockhausen, M. J. Setzer, The statistical thickness and the chemical potential of adsorbed water films, *J. Colloid Interface Sci.* 82 (1981) 534–542.
- [16] D. H. Bangham, R. I. Razouk, Adsorption and the wettability of solid surfaces, *Trans. Faraday Soc.* 33 (1937) 1459–1463.
- [17] F. Wittmann, Interaction of hardened cement paste and water, *J. Am. Ceram. Soc.* 56 (1973) 409–415.
- [18] T. C. Powers, The thermodynamics of volume change and creep, *Matériaux Constr.* 1 (1968) 487–507.
- [19] E. A. B. Koenders, K. van Breugel, Numerical modelling of autogenous shrinkage of hardening cement paste, *Cem. Concr. Res.* 27 (1997) 1489–1499.
- [20] O. M. Jensen, Thermodynamic limitation of self-desiccation, *Cem. Concr. Res.* 25 (1995) 157–164.
- [21] R. J. Flatt, G. W. Scherer, J. W. Bullard, Why alite stops hydrating below 80% relative humidity, *Cem. Concr. Res.* 41 (2011) 987–992.
- [22] M. Wyrzykowski, P. Lura, Effect of relative humidity decrease due to self-desiccation on the hydration kinetics of cement, *Cem. Concr. Res.* 85 (2016) 75–81.
- [23] T. C. Powers, T. L. Brownyard, Studies of the physical properties of hardened Portland cement paste, *J. Am. Concr. Inst.* 43 (1946) 101–132.
- [24] F. Beltzung, F. H. Wittmann, Role of disjoining pressure in cement based materials, *Cem. Concr. Res.* 35 (2005) 2364–2370.
- [25] T. C. Powers, Mechanisms of shrinkage and reversible creep of hardened cement paste, in: *Int.*

- Conf. Struct. Concr. Sect. G, 1965: pp. 319–344.
- [26] Yates. D.J.C, Molecular specificity in physical adsorption, in: *Adv. Catal.*, 1960.
- [27] T. L. Hill, *Theory of Physical Adsorption*, in: 1952: pp. 211–258.
- [28] M. J. Setzer, The solid-liquid gel-system of hardened cement paste, *Restor. Build. Monum.* 14 (2008) 259–270.
- [29] B. V. Derjaguin, N. V. Churaev, V. M. Muller, *Disjoining pressure*, in: *surf. forces*, Springer US, Boston, MA, 1987: pp. 25–52.
- [30] P. B. Balbuena, D. Berry, K. E. Gubbins, Solvation pressures for simple fluids in micropores, *J. Phys. Chem.* 97 (1993) 937–943.
- [31] C. F. Ferraris, *Mechanismes du retrait de la pate de ciment durcie*, 1986.
- [32] T. Lu, E. Koenders, Modeling and analyzing autogenous shrinkage of hardening cement paste, in: *1st Int. Conf. Aging Mater. Struct.*, Delft, The Netherlands, 2014: pp. 155–162.
- [33] F. H. Wittmann, F. Beltzung, T.J. Zhao, Shrinkage mechanisms, crack formation and service life of reinforced concrete structures, *Int. J. Struct. Eng.* 1 (2009) 13.
- [34] L. R. Fisher, J. N. Israelachvili, Experimental studies on the applicability of the Kelvin equation to highly curved concave menisci, *J. Colloid Interface Sci.* 80 (1981) 528–541.
- [35] I. Maruyama, Origin of drying shrinkage of hardened cement paste: hydration pressure, *J. Adv. Concr. Technol.* 8 (2010) 187–200.
- [36] D. P. Bentz, E. J. Garboczi, D. A. Quenard, Modelling drying shrinkage in reconstructed porous materials: application to porous Vycor glass, *Model. Simul. Mater. Sci. Eng.* 6 (1999) 211–236.
- [37] C. Pichler, R. Lackner, H. A. Mang, A multiscale micromechanics model for the autogenous-shrinkage deformation of early-age cement-based materials, *Eng. Fract. Mech.* 74 (2007) 34–58.
- [38] O. Coussy, The equivalent pore pressure and the swelling and shrinkage of cement-based materials, *Mater. Struct.* 37 (2003) 15–20.
- [39] Z. C. Grasley, C. K. Leung, Desiccation shrinkage of cementitious materials as an aging, poroviscoelastic response, *Cem. Concr. Res.* 41 (2011) 77–89.
- [40] D. Gawin, F. Pesavento, B. A. Schrefler, Modelling creep and shrinkage of concrete by means of effective stresses, *Mater. Struct.* 40 (2007) 579–591.
- [41] A. W. Bishop, G. E. Blight, Some aspects of effective stress in saturated and partly saturated soils, *Géotechnique.* 13 (1963) 177–197.
- [42] I. Vlahinić, H. M. Jennings, J. J. Thomas, A constitutive model for drying of a partially saturated porous material, *Mech. Mater.* 41 (2009) 319–328.
- [43] J. M. Pereira, O. Coussy, E. E. Alonso, J. Vaunat, S. Olivella, Is the degree of saturation a good candidate for Bishop's χ parameter, in: *Proc. Fifth Int. Conf. Unsaturated Soils*, Barcelona Spain, 2010: pp. 913–919.
- [44] M. A. Biot, General theory of three dimensional consolidation general theory of three-dimensional consolidation, *J. Appl. Phys. Addit. Inf. J. Appl. Phys. J. Homepage.* 12 (1941).
- [45] M. A. Biot, D. G. Willis, The elastic coefficients of the theory of consolidation, *J. Appl. Mech.* (1957) 594–601.

- [46] R.W. Lewis, B. A. Schrefler, *The finite element method in the deformation and consolidation of porous media*, John Wiley and Sons Inc., New York, 1987.
- [47] M. Wyrzykowski, C. Di Bella, P. Lura, Prediction of drying shrinkage of cement-based mortars with poroelastic approaches – A Critical Review, in: 6th Biot Conf. Poromechanics, Paris, 2017.
- [48] C. Di Bella, M. Wyrzykowski, P. Lura, Evaluation of the ultimate drying shrinkage of cement-based mortars with poroelastic models, *Mater. Struct.* (2017).
- [49] S. F. Rahman, Z. C. Grasley, The significance of pore liquid pressure and disjoining pressure on the desiccation shrinkage of cementitious materials, *Int. J. Adv. Eng. Sci. Appl. Math.* (2017).
- [50] B. J. Mohr, K. L. Hood, Influence of bleed water reabsorption on cement paste autogenous deformation, *Cem. Concr. Res.* 40 (2010) 220–225.
- [51] G. Sant, A. Kumar, C. Patapy, G. Le Saout, K. Scrivener, The influence of sodium and potassium hydroxide on volume changes in cementitious materials, *Cem. Concr. Res.* 42 (2012) 1447–1455.
- [52] G. Sant, B. Lothenbach, P. Juilland, G. Le Saout, J. Weiss, K. Scrivener, The origin of early age expansions induced in cementitious materials containing shrinkage reducing admixtures, *Cem. Concr. Res.* 41 (2011) 218–229.
- [53] M. Wyrzykowski, Z. Hu, S. Ghourchian, K. Scrivener, P. Lura, Corrugated tube protocol for autogenous shrinkage measurements: review and statistical assessment, *Mater. Struct.* (2017) 50–57.
- [54] G. Sant, A discussion of analysis approaches for determining “time-zero” from chemical shrinkage and autogenous strain measurements in cement paste, in: *Int. RILEM Conf. Vol. Chang. Hardening Concr. Test. Mitig.*, RILEM Publications, 2006: pp. 375–383.
- [55] J. Weiss, Experimental determination of the “Time Zero”, t_0 (‘Maturity-Zero’, M_0), in: *RILEM Publications SARL*, n.d.: pp. 195–206.
- [56] J. C. Yates, Effect of calcium chloride on readings of a volumeter including Portland cement pastes on linear changes of concrete, *Highw. Res. Board Proc.* 21 (1942).
- [57] H. Justnes, A. Van Gemert, F. Verboven, E. J. Sellevold, Total and external chemical shrinkage of low w/c ratio cement pastes, *Adv. Cem. Res.* 8 (1996) 121–126.
- [58] G. Sant, P. Lura, J. Weiss, Measurement of volume change in cementitious materials at early ages - Review of testing protocols and interpretation of results, *Transp. Res. Rec. C* (2006) 21.
- [59] P. Lura, O. M. Jensen, Measuring techniques for autogenous strain of cement paste, *Mater. Struct.* 40 (2007) 431–440.
- [60] A. Loukili, D. Chopin, A. Khelidj, J.-Y. Le Touzo, A new approach to determine autogenous shrinkage of mortar at an early age considering temperature history, *Cem. Concr. Res.* 30 (2000) 915–922.
- [61] H. Chen, *Autogenous and Thermal Deformations and Their Interaction in Early Age Cementitious Materials*, EPFL, 2013.
- [62] ASTM C157 Length change of hardened hydraulic/cement mortar and concrete, ASTM. (2014).

- [63] A. Loukili, A. Khelidj, P. Richard, Hydration kinetics, change of relative humidity, and autogenous shrinkage of ultra-high-strength concrete, *Cem. Concr. Res.* 29 (1999) 577–584.
- [64] Japan Concrete Institute, *Autogenous shrinkage of concrete*, CRC Press, 1998.
- [65] M. Mazloom, A. A. Ramezani-pour, Setting times and autogenous shrinkage before demoulding of high-strength concrete, in: *27th Conf. Our World Concr. Struct.*, Singapore, 2002.
- [66] M. N. Amin, J.-S. Kim, T. T. Dat, J. Kim, Improving test methods to measure early age autogenous shrinkage in concrete based on air cooling, *IES J. Part A Civ. Struct. Eng.* 3 (2010) 244–256.
- [67] O. M. Jensen, P. F. Hansen, A dilatometer for measuring autogenous deformation in hardening Portland cement paste, *Mater. Struct.* 28 (1995) 406–409.
- [68] ASTM, ASTM C1698-09: Standard test method for autogenous strain of cement paste and mortar, (2009) 1–8.
- [69] Z.P. Bažant, Delayed thermal dilatations of cement paste and concrete due to mass transport, *Nucl. Eng. Des.* 14 (1970) 308–318.
- [70] E. J. Sellevold, Ø. Bjøntegaard, Coefficient of thermal expansion of cement paste and concrete: Mechanisms of moisture interaction, *Mater. Struct.* 39 (2006) 809–815.
- [71] M. Wyrzykowski, P. Lura, Controlling the coefficient of thermal expansion of cementitious materials – A new application for superabsorbent polymers, *Cem. Concr. Compos.* 35 (2013) 49–58.
- [72] M. Wyrzykowski, P. Lura, Moisture dependence of thermal expansion in cement-based materials at early ages, *Cem. Concr. Res.* 53 (2013) 25–35.
- [73] J.-P. Liu, T. Qian, S. Wei, M. Chang-Wen, T. Ming-Shu, Study on the self-desiccation effect in early-age concrete and the determination of “time-zero” of self-desiccation shrinkage, in: *Int. RILEM Conf. Vol. Chang. Hardening Concr. Test. Mitig.*, Lyngby, 2006.
- [74] H. Huang, G. Ye, Examining the “time-zero” of autogenous shrinkage in high/ultra-high performance cement pastes, *Cem. Concr. Res.* 97 (2017) 107–114.
- [75] G. Sant, M. Dehadrai, D. Bentz, P. Lura, C. F. Ferraris, J. W. Bullard, J. Weiss, Detecting the fluid-to-solid transition in cement pastes, *ACI Comm.* 236. (2009) 53–57.
- [76] American Society for Testing and Materials, ASTM C191-13: Standard test method for time of setting of hydraulic cement by Vicat needle, *ASTM Stand. B. i* (2014) 1–8.
- [77] R. S. Barneyback, S. Diamond, Expression and analysis of pore fluids from hardened cement pastes and mortars, *Cem. Concr. Res.* 11 (1981) 279–285.
- [78] P. Termkhajornkit, T. Nawa, M. Nakai, T. Saito, Effect of fly ash on autogenous shrinkage, *Cem. Concr. Res.* 35 (2005) 473–482.
- [79] E. Tazawa, S. Miyazawa, Autogenous shrinkage of cement paste with condensed silica fume, 4th CANMET-ACI Int. Conf. Fly Ash, Silica Fume, Slag Nat. Pozzolans Concr. 13 (1992) 875–894.
- [80] B. G. Kim, K. M. Lee, H. K. Lee, Autogenous shrinkage of high-performance concrete containing fly ash, *Mag. Concr. Res.* 55 (2003) 507–515.
- [81] Y. W. Chan, C. Y. Liu, Y. S. Lu, Effect of slag and fly ash on the autogenous shrinkage of

- high performance concrete, in: Proc. Intern. Work. Autogenous Shrinkage Concr., 1998: pp. 221–228.
- [82] F. Deschner, F. Winnefeld, B. Lothenbach, S. Seufert, P. Schwesig, S. Dittrich, F. Goetz-Neunhoeffler, J. Neubauer, Hydration of Portland cement with high replacement by siliceous fly ash, *Cem. Concr. Res.* 42 (2012) 1389–1400.
- [83] V. Baroghel-Bouny, Water vapour sorption experiments on hardened cementitious materials, *Cem. Concr. Res.* 37 (2007) 414–437.

Chapter 4 Prediction of internal relative humidity in cementitious materials by ^1H NMR

This chapter describes a novel method based on pore volumes evolution by using ^1H NMR and pore sizes using MIP to obtain the Kelvin radius. The internal RH was then calculated based on Kelvin-Cohan equation by taking also the water activity of the pore solution into consideration. The uncertainty of the new prediction depending on various parameters was studied by means of a parametric bootstrapping technique. This chapter was written based on the paper recently submitted to Cement and Concrete Research.

Contents

4.1	Literature review	51
4.1.1	Application of ^1H NMR in cement	51
4.1.2	Internal RH prediction	54
4.2	The novel method for predicting the Kelvin radius	58
4.3	Experimental methods.....	60
4.3.1	^1H NMR.....	60
4.3.2	Mercury intrusion porosimetry (MIP)	61
4.3.3	Chemical shrinkage	62
4.3.4	Pore solution extraction	62
4.3.5	Bootstrapping technique	63
4.4	Results	63
4.4.1	RHs	63
4.4.2	Chemical shrinkage	64
4.4.3	Degree of hydration	65
4.4.4	Evolution of NMR signal amplitude as function of time	67
4.4.5	Development of cumulative pore volume	68
4.5	Prediction results and discussion	69
4.5.1	Selection of the cut-off sizes	69
4.5.2	Results and discussion	71
4.6	Summary	74
4.7	References	75

4.1 Literature review

4.1.1 Application of ^1H NMR in cement

Proton NMR relaxometry is a method that allows studying the relaxation time of the hydrogen nuclei particles after their initial excitation with an externally applied pulse [1]. The spin nuclei ^1H can exist in two different spin states: “up” and “down”. When the nuclei are exposed to a static magnetic field, the distribution between the two spin states is described with Boltzmann distribution [2]. This causes a distribution of spins between the “up” and “down” states according to the relaxation which is the reverse process of spins return to their original equilibrium state in the static magnetic field after the excitation from the fluctuating magnetic field [3]. The relaxation time (both the spin-lattice or longitudinal relaxation time T_1 and the spin-spin or transverse relaxation time T_2) depends strongly on the physical and chemical environment [1]. Of particular interest for studying water in porous systems is that the relaxation times are shorter the stronger the interactions of nuclei with the solids. With ^1H NMR, it is possible to detect and quantify a wide range of the water states or pore networks down to nano-meter level (theoretically it can probe water in pores of any size) without pre-drying the specimens, since water acts as a probe itself [4,5]. Therefore, the method allows for finding quantities of water and estimating the averaged sizes of pores, in which it is contained in a non-destructive, in-situ way (this feature is very attractive in cement study since removing the water in other methods, e.g., microscopy or mercury intrusion porosimetry, may cause damage of the pore structure).

The application of ^1H NMR to study water populations in hydrating cementitious materials can be traced back to the 1980s [6]. Recent years, the application of this technique in cement domain is becoming more solid and mature [2], e.g., it has been successfully used for pore size distribution quantification [5], specific surface area measurement [7], quantifying the densification of C-S-H [8] and determining the adsorption isotherm [4], and the results have been validated in aforementioned studies by comparing them with other traditional techniques. However, in practice, the application is limited to mainly white cement due to the paramagnetic impurities (such as Fe^{3+}) that are present in grey cement generating too fast pore water relaxation [1].

In the following years, several models were developed to distinguish between different water populations and study their state in the pore structure [1,9,10]. With different pulse sequences, ^1H NMR relaxation data can be interpreted in terms of different water populations [7]. The pulse sequences commonly used for resolving T_2 of water in the specimen is the co-called Carr-Purcell-Meiboom-Gill (CPMG) sequence (proposed by Carr and Purcell [11] and Meiboom and Gill [12], detailed scheme is presented in *Figure 4.1*) and quadrature (solid) echo measurement (QE) (first proposed by Powles and Strange [13], presented in *Figure 4.2*).

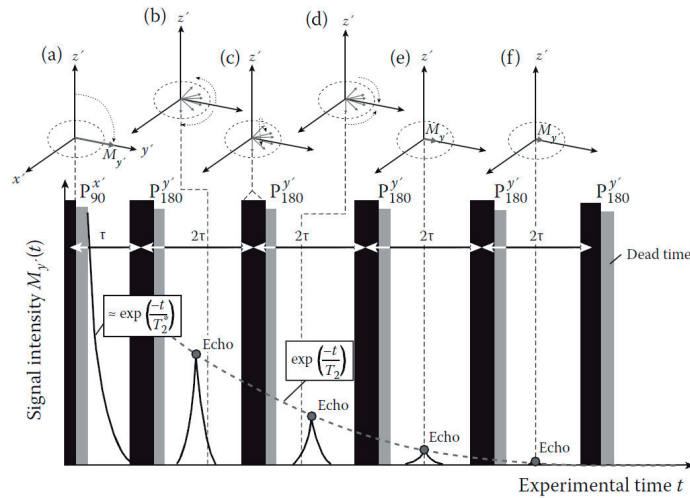


Figure 4.1 Schematic figure of CPMG pulse sequence with the spins state from [3]

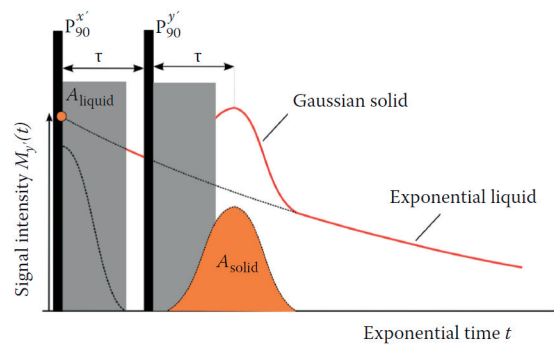


Figure 4.2 Schematic figure of QE pulse sequence from [3]

Basically, after inverting the measured signal of T_2 from the CPMG measurement with the inverse Laplace transform [14], and by fitting the signal from the QE measurement with Gaussian fits, four components of the total signal are distinguished, forming four separate peaks in the inverted spectrum. These four components are assigned to different water populations in cement paste. The fastest relaxing component at T_2 of $\sim 10 \mu\text{s}$ [7] corresponds to ^1H chemically combined in crystalline phases, e.g., CH and ettringite (signal detected from QE), referred to as ‘solid water’. Longer relaxation times are due to mobile water components detected in the CPMG experiment: interlayer, gel and capillary water (the latter comprising both the interhydrate water [8] and water in large capillaries and voids or cracks) correspond to the signals at T_2 of around 80-120, 300-500 and thousands of μs , respectively, an example for the evolution of NMR signal during hydration of white cement with w/c of 0.4 is shown in Figure 4.3 from [7].

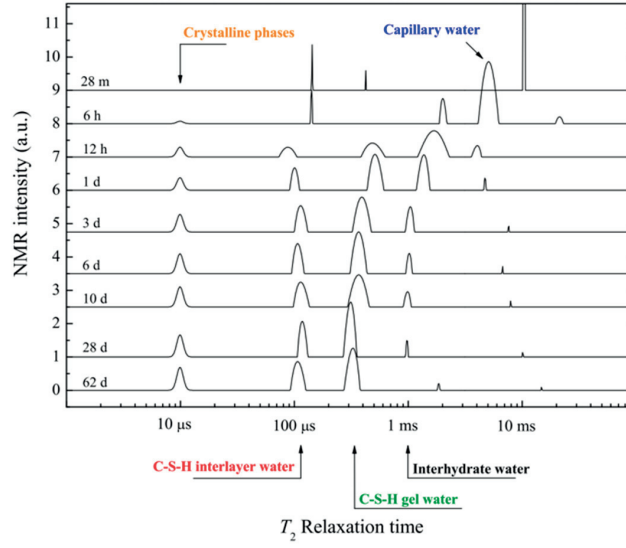


Figure 4.3 Evolution of NMR signals during hydration of white cement with w/c of 0.4 from [7]

Fast exchange model (fast diffusion model) [15] has been well accepted and applied successfully into cement domain (first by Halperin et al [16]). It, as one of the two main models relating the relaxation rate R ($R=1/T_{1,2}$) from ^1H NMR with pore sizes, proposes two types of distinct magnetic species: the pore surface sites and bulk liquid [15]. As shown in Equation 4.1, the global relaxation rate is a weight average of the relaxation rate of the aforementioned two types: the relaxation rate of a water molecule adsorbed on the pore surface and the relaxation rate of the bulk liquid. The former is much higher than the latter (T_2 relaxation time of former is of the order of microseconds while that of the latter is of the order of seconds) [2]. Therefore, the global relaxation rate can be approximated only with relaxation rate of the surface water molecule. According to the model, the scale of the measured relaxation is linked with the characteristic pore sizes, e.g., the pore surface area (S_p) relates with the amount of water molecules adsorbed and the pore volume (V_p) relates with number of water molecules within the pores.

Equation 4.1

$$\frac{1}{T_2} = \frac{\varepsilon \cdot S_p}{V_p} \cdot \frac{1}{T_2^{surface}} + \left(1 - \frac{\varepsilon \cdot S_p}{V_p}\right) \cdot \frac{1}{T_2^{bulk}} \approx \frac{\varepsilon \cdot S_p}{V_p} \cdot \frac{1}{T_2^{surface}} \quad (\text{since } T_2^{surface} (\mu\text{s}) \ll T_2^{bulk} (\text{s}))$$

where: ε [nm] is the thickness of the adsorbed water layer.

With an assumption of planar pores, the surface area equals to twice of area A ($S_p=2 \times A$) and the pore volume equals to cross area times pore width d ($V_p=A \times d$). Thus S_p/V_p will be replaced by $2/d$, relating the pore size with the T_2 with another unknown $\varepsilon/T_2^{surface}$ which is the so-called surface relaxivity [8]. As calculated in [7], the surface relaxivity obtained as 3.73×10^{-3} nm/ μs .

4.1.2 Internal RH prediction

A part of initial water in the cementitious materials is consumed by cement hydration ending up with two-fold formats (rest of free water stays similar to bulk water): a portion of water binds into hydration products and another portion is adsorbed on surfaces of solids. Since the volume of hydration products is smaller than the volume of reactants (dry cement binders and water), empty voids are created in the hydrating microstructure and the porous systems becomes partly saturated (non-saturated). This phenomenon is referred to as chemical shrinkage. Due to this formation of capillary menisci at the pore fluid-vapor interfaces, capillary tension in the pore fluid, the driving force of autogenous shrinkage (see *Chapter 3*), and compression in the solid skeleton develop. The capillary pores are continuing to be emptied as cement hydration proceeds, resulting in the air-water menisci to be gradually smaller. At the same time, the development of the menisci leads to a decrease of RH, so-called self-desiccation [17,18]. The phenomenon becomes more pronounced with decreasing w/b, due to small amounts of water and finer microstructures created.

The relationship of the capillary pressure and Kelvin radius with the RH variation is shown in *Figure 4.4* reproduced from [19]. In the self-desiccation condition, the range of the RH is from 100% to 75% (explained in *Chapter 3*, presented as red line range in the figure). The link between the internal RH decrease in the pores and changes of pressure exerted on the skeleton by the pore fluids is expressed by the Kelvin-Laplace equation ($P_c = R \times T / V \times \ln(RH_K)$, Equation 3.7) [20].

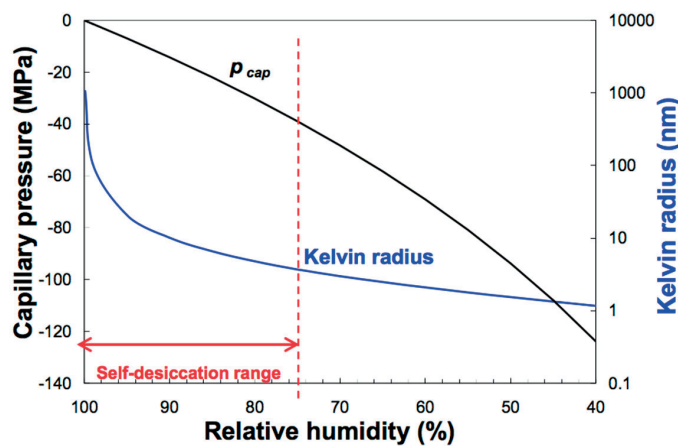


Figure 4.4 Evolution of capillary pressure and Kelvin radius as function of RH, from [19]

Hua et al. [21] first suggested that the Kelvin radius, a key parameter for calculation of the internal RH according to the Kelvin equation ($RH_K = \exp(-2 \gamma_w \cos \theta_w V / (r R T))$), can be estimated based on the pore size distribution as measured with MIP. The basic assumption in their approach was that a volume intruded at a certain intrusion pressure, and therefore through a certain size of pores by mercury in MIP measurement is equal to the volume of pores larger than that certain size that empty of water during desaturation, which means $\Delta V(t_0)$ in *Figure 4.5(a)* and *(b)* are the same. Therefore, knowing the volume of emptied porosity during desaturation, one could relate it to the volume of

mercury entrained during MIP and find corresponding intrusion radius. Next, using the Kelvin-Laplace equation, RH occurring up such desaturation can be calculated. The volume of emptied pores during hydration driven by desaturation was determined with chemical shrinkage. The calculation can be conveniently performed with the following equation:

Equation 4.2

$$P_c(\Delta V(t_0)) = \frac{\gamma_w \cdot \cos \theta_w}{\gamma_{Hg} \cdot \cos \theta_{Hg}} \cdot P_{Hg}(\Delta V(t_0))$$

where: γ_w [N/m] and γ_{Hg} [N/m] are the surface tension of water/water vapor and mercury/vacuum, respectively; θ_w [°] and θ_{Hg} [°] are the contact angle of the water and mercury with the solids. P_c [Pa] and P_{Hg} [Pa] are the depression and intrusion pressure; $\Delta V(t_0)$ is the corresponding volume of the pressure.

In moisture-sealed, isothermal conditions, the reduction of internal RH in cementitious systems depends on two major mechanisms: desaturation of pores due to chemical shrinkage and water activity of the pore solution, $RH = RH_K \times RH_S$ [17,22]. The RH_K term is due to the curvature effects of the menisci at the interface of vapor and pore solution and can be described with the Kelvin equation. The RH_S varies continuously with the change of concentration of pore solution. It can be measured directly by water activity sensors (shown in Chapter 3) or approximated using Raoult's Law based on composition of pore solution [17] (Equation 4.3).

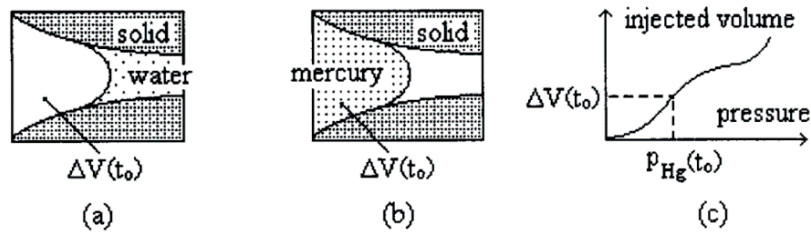


Figure 4.5 Schematic figure of evacuation of pore solution under depression (a) and intrusion of mercury under pressure in MIP (b) and (c) [21]

Equation 4.3

$$RH_S = \frac{n_{H_2O}}{n_{solution}}$$

where: n_{H_2O} [mmol/l] and $n_{solution}$ [mmol/l] are the number of moles of water and the total number of moles in the solution (including solute), respectively. Note that this equation is based on an ideal solution (the equilibrium RH relies on the molar fraction of water in the pore solution) [22,23].

The approach originally presented by Hua et al. [21] approach was recently extended to account for the adsorbed water effects on Kelvin radius r [nm] (see Figure 4.6) and validated with RH measurements by Chen et al. [23]. The extension of the Kelvin equation to take into account the presence of

an adsorbed water layer of thickness t [nm] on the surface of the pore wall is referred to as the Kelvin-Cohan equation (with the Kelvin radius $r=r_p-t$ [nm], r_p [nm] is the pore radius) [23,24]:

Equation 4.4

$$RH_K = \exp\left(-\frac{2\gamma_w \cos(\theta_w)M_w}{(r_p - t)RT\rho_w}\right)$$

The thickness of the adsorbed liquid layer can be empirically described based on a formula proposed by Badmann et al. [25] with the values of the fit parameters determined in [25] as $K_1=0.385$ and $K_2=0.189$:

Equation 4.5

$$t = K_1 - (K_2 \cdot \ln(-\ln(RH)))$$

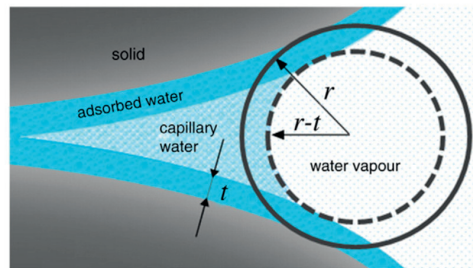


Figure 4.6 Schematic figure of the capillary pores with the adsorbed water and capillary water [26]

It has shown from their simulation, however, that this t , at the range of interest (rather high RH, and therefore very large r), has minor effect. It starts being important only at low RH, where r has similar size as t [26].

Obtaining the Kelvin radius based on Hua's approach (further referred to as "chemical shrinkage-MIP method") is based on the following approximations:

- 1) the volume of pores filled by water in the saturated samples during chemical shrinkage is the same as the chemical shrinkage (empty pores) in the sealed samples;
- 2) all pores in a cementitious material are connected to the surface, and therefore accessible in the MIP measurement;
- 3) pore sizes are obtained based on a model of capillary tubes (Washburn model) [27];
- 4) the pores are emptied from the larger size to the smaller size during hydration and each class of pore sizes can only be either fully emptied or fully saturated [28];
- 5) the so-called *ink-bottle effect* [29] is neglected (see discussion in [23,30]).

This method has been shown to be able to successfully estimate the evolution of internal RH in self-desiccating samples [23]. However, one important uncertainty of the prediction with this method limitation stems from the approximation 1). In fact, the degree of hydration of saturated samples is higher than that of sealed samples at the same age, especially for low w/c [31,32]. As shown in [31], by comparing the heat release of sealed and saturated samples with w/c of 0.3 and 0.5, the difference was larger in samples with lower w/c. Consequently, the difference of chemical shrinkage between saturated and sealed samples is higher the lower their w/c.

This problem can be corrected by using the degree of hydration instead of hydration time when combining chemical shrinkage and MIP (see also *Figure 4.7*). A similar method was already mentioned and quantified with one single system in reference [23]. To express the chemical shrinkage as a function of the degree of hydration, in this chapter the degree of hydration of saturated and sealed samples is measured by XRD and quantified with Rietveld analysis method. By bridging the chemical shrinkage and the degree of hydration of saturated samples, the chemical shrinkage of sealed samples at a desired degree of hydration can be estimated and a final prediction can be made according to the updated chemical shrinkage results.

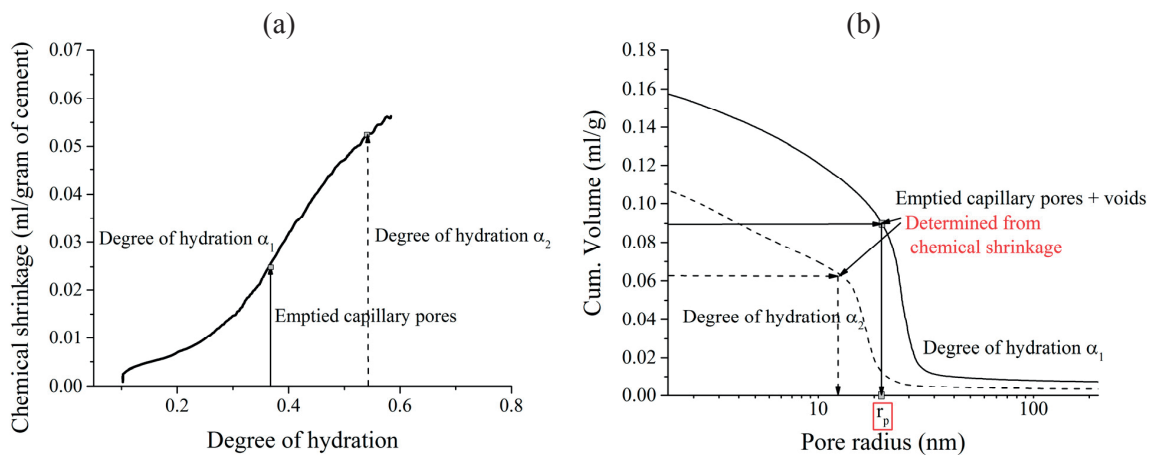


Figure 4.7 Schematic diagram of the principle of the chemical shrinkage - MIP approach to obtain the pore radius r_p . (a) is the chemical shrinkage data, providing the volume of pores emptied; (b) is the cumulative pore size distribution from MIP during hydration

Note that the difference between sealed and saturated samples varies with different thickness of the samples as well [23,32–34]. The latter is due to inaccessibility of part of sample's volume by water during chemical shrinkage measurement caused by low permeability of pastes at low w/c. Since water acts as a probe in chemical shrinkage measurement, inaccessibility leads to underestimated chemical shrinkage.

This chapter aims at evaluating and predicting evolution of the internal RH in cementitious materials with different w/c based on a knowledge of the pore size distribution and its evolution. In the present work, the volume of pores filled with pore solution is obtained by ^1H NMR measurements on sealed samples, and then combined with MIP for estimating the Kelvin radius. The predictions are compared

to measurements of RH evolution in autogenous conditions (self-desiccation) and also the chemical shrinkage-MIP approach.

4.2 The novel method for predicting the Kelvin radius

Changes of pressure exerted on the skeleton by the pore fluid can be linked with the internal RH decrease in the pores as expressed by the Kelvin-Laplace equation [20]. Thus, being able to predict the internal RH evolution is key in understanding the development of autogenous shrinkage and finding more reliable ways to estimate the risk of cracking and ultimately prevent cracking. In particular, predicting RH evolution in self-desiccating materials based solely on the microstructural data and evolution of hydration degree can constitute a basis for extending the application of microstructural models of hydration to the macroscopic level, where deformations are considered. Second, the presented experimental and modeling data can be considered as a direct evidence of the mechanisms proposed in the literature to be responsible for self-desiccation [17,35].

The previously-reported method (shown in *section 4.1.2*) using MIP combined with chemical shrinkage [23] is based on estimating the radius of pores corresponding to the volume of capillary pores of a given size *already emptied* of pore solution during hydration at a given hydration stage [21]. The novel approach proposed here is using ^1H NMR combined with MIP to estimate the size of pores corresponding to the volume of capillary pores *still filled* with pore solution at a given hydration stage. A fundamental difference is that, in the former method, the emptied pores were measured in water-saturated conditions, while in the method proposed here the amount of water-filled pores is measured during self-desiccation (autogenous conditions).

The novel method for obtaining the Kelvin radius proposed is based on calculating the size of the capillary pores filled with pore solution by combining data from ^1H NMR and MIP (further referred to the NMR-MIP method). One advantage of the new method is the fact that the ^1H NMR and MIP samples are maturing in the same, sealed conditions. The assumptions 2), 3), 4) and 5) mentioned in *section 4.1.2* still apply due to the use of MIP to measure the pore size distribution.

The evolution of the ^1H NMR signal amplitude of the different mobile water populations is calculated from the area of each signal peak in the inverted CPMG data and it can be transformed to the water mass or volume present (with the assumption that the density of all types of water is the same) in the system at a desired hydration time (*Figure 4.8(a)*). The pore sizes can also be estimated based on the relaxation times T_2 , see *section 4.1.1* [16]. However, the models for the pores are different in the assumption of MIP method (cylinder) and the ^1H NMR (planar) in the calculation. Secondly, the pores inside of the cement paste are not any kind of model but shape varied. The obtained pore size from the ^1H NMR is only the average pore size [5]. For this reason, the relaxation time cannot provide precise information on the size of the largest water-filled pore in a capillary pore system. Hence, this pore size of different water populations cannot be used directly to obtain the Kelvin radius. In fact, since the pore sizes within one pore population correspond to a certain spans of sizes, this approach would yield a systematic underestimation of the Kelvin radius.

Considering that ^1H NMR provides only water-filled porosity, it is assumed that the emptied pore volume is equal to the total pore volume minus the volume of pores containing mobile water (or rather pore solution) as detected by ^1H NMR:

Equation 4.6

$$V_{\text{emptied pore volume+voids}} = V_{\text{total pores}} - V_{\text{solution filled pores}}$$

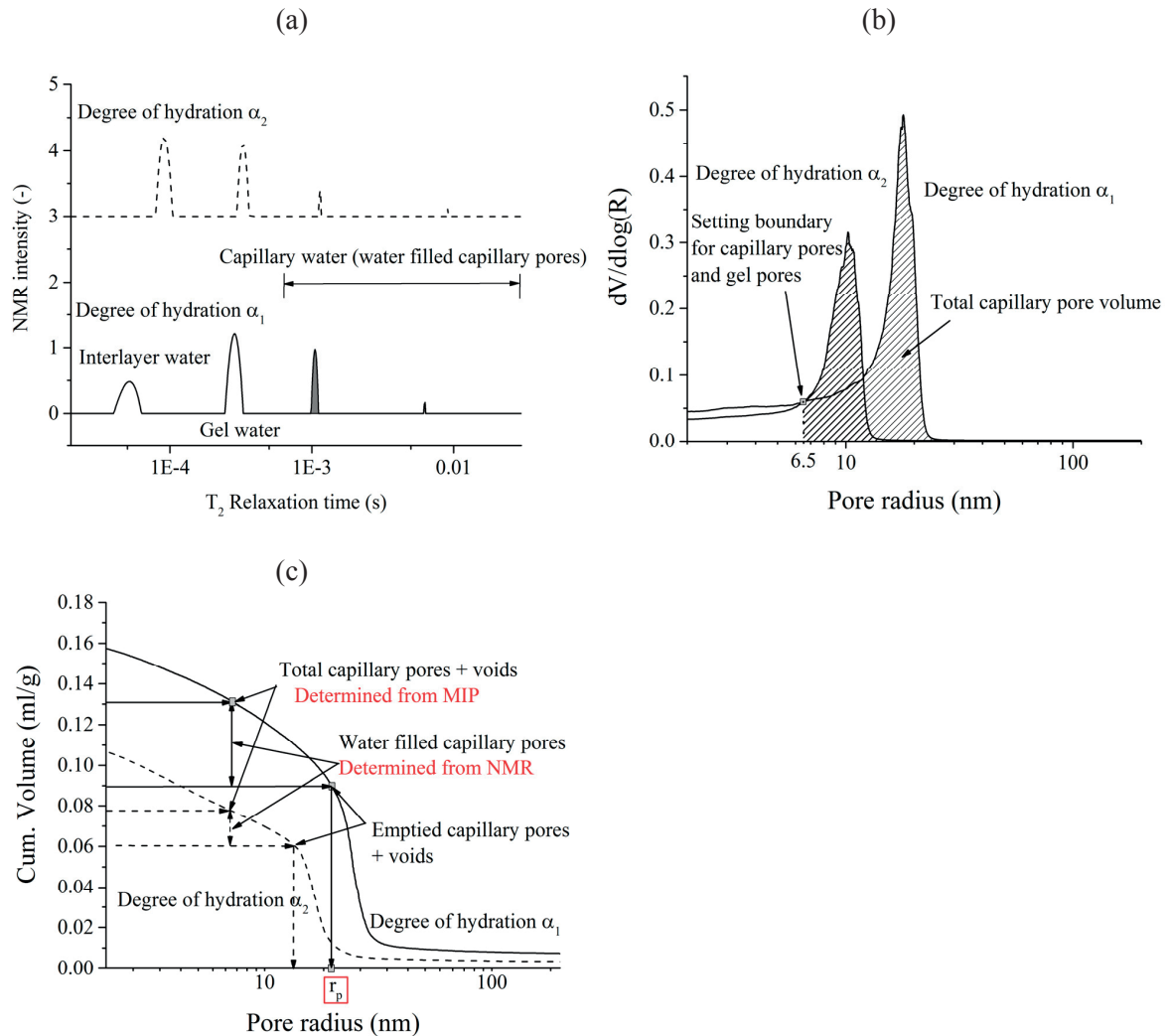


Figure 4.8 Schematic diagram of the principle of the new approach to obtain the pore radius r_p (a) Water populations from ^1H NMR, providing information about the volume of water-filled capillary pores at different ages (size of shaded area), signals due to hydrogen in the solid part are not presented; (b) Pore size distribution from MIP, providing information about the volume of total capillary pores and voids (as an example, size of shaded area with the assumption of cut-off size between gel pores and capillary pores at 6.5 nm); (c) Cumulative pore size distribution from MIP during hydration

In terms of pore size distributions obtained from MIP, however, it needs to be realized that only part of the pore volume can be accessed by mercury at the pressure of 400 MPa as applied here, which corresponds to pores with equivalent radii larger than about 1.2 nm (for contact angle of mercury assumed as 120°). Considering pore sizes and volumes revealed by the ^1H NMR (see *section 4.1.1*), it can be the pores resolved by MIP capillary pores and part of gel pores (see [5]). For predicting the internal RH, the gel pores are not taken into consideration, as the assumption is that these pores are always saturated with water at the RH considered here (not lower than 80%, the corresponding Kelvin-radius should be around 6.7 nm) according to the Kelvin equation. Therefore, instead of using the whole MIP curve of the cumulative pore volume, only the part corresponding to the capillary pores is employed here. The boundary between gel water and capillary water (also called cut-off size of the capillary pores) was assumed at the lower end of the main capillary peak in the differential MIP curve (see *Figure 4.8(c)*). The radius corresponding to the boundary varies from system to system and an average cut-off size was selected (in the schematic *Figure 4.8(b)*, an exemplary cut-off radius of 6.5 nm is shown). A detailed reasoning about the choice of cut-off size is reported in *section 4.5.1*. Using the selected radii allowed estimating the effect of the assumed size on the calculated Kelvin radius. Considering explicitly the capillary pores, *Equation 4.6* can be replaced with:

Equation 4.7

$$V_{\text{emptied pore volume+voids}} = V_{\text{total capillary pores+voids}} - V_{\text{solution filled capillary pores}}$$

Then, using this volume as input in the cumulative pore volume curves from MIP, the Kelvin radius is calculated as the radius of the corresponding volume (*Figure 4.8 (c)*).

4.3 Experimental methods

As mentioned in *section 4.1.1*, magnetic impurities in the materials often render ^1H NMR method not feasible; this was the case for the systems containing fly ash. Therefore, in this chapter, only pastes with pure Portland cement and quartz blended systems were prepared including Cement-0.35, CQZ20-0.35, Cement-0.3 and CQZ20-0.3 (shown as w/c in the figures in order to see the effect of w/c clearly). The mixture design has been given in *Chapter 2*. The inert quartz filler is not expected to influence the development of the Kelvin radius since the Kelvin radius will be mostly influenced by pores within the hydration products that are much smaller than the spaces between the grains.

4.3.1 ^1H NMR

A Bruker Minispec benchtop NMR spectrometer with operating frequency of 7.5 MHz and temperature controlled at 20 ± 0.5 °C by using water circulation for ^1H NMR measurements (*Figure 4.9*). A more detailed discussion of the method for acquiring different water populations can be found in reference [8]. Basically, CPMG echo measurements were performed to obtain signals of capillary

water, gel water and interlayer water (all comprising ‘mobile’ water), while quadrature echo measurements were performed for chemically bound water (associated with portlandite and ettringite, referred to as ‘solid’ water). The number of scans in CPMG experiment increased from 512 to 1024 as the decrease of the relaxation time and signal-to-noise ratio. The signal-to-noise ratio was typically 500:1. Each scan comprised 256 log-spaced echoes in the range $6\ \mu\text{s}$ -12 ms. For the QE experiment, 128 scans were recorded before 12 h, 192 scans from 12 h to 24 h and 256 scans after 24 h. The solid echo was recorded with the pulse gap of the range $\tau = 15\text{-}45\ \mu\text{s}$.



Figure 4.9 Bruker Minispec NMR spectrometer

In this study, samples of around 10 mm height were cast into dedicated NMR glass tubes with internal $\text{Ø}8$ mm and 180 mm length and sealed with two layers of paraffin film to eliminate water evaporation to the ambient. Continuous measurements were performed for 3 days after casting and discrete measurements were carried out at 7, 14 and 28 d (the samples enclosed directly in the sealed dedicated NMR glass tubes were stored in a room with controlled temperature of $20 \pm 0.5\ ^\circ\text{C}$). For discrete measurements, the results are shown as the average of at least four CPMG and QE scans each (collected over about 1-2 h each).

4.3.2 Mercury intrusion porosimetry (MIP)

Pascal 140 and 440 porosimeters by POROTEC were used for mercury intrusion porosimetry. Maximum pressures of 150 kPa and 400 MPa were reached in the low pressure (Pascal 140, used for filling the sample with mercury) and high pressure (Pascal 440) chambers, respectively. The MIP samples were cast in cylindrical plastic containers hermetically sealed and kept at constant temperature of $20 \pm 0.3\ ^\circ\text{C}$. At specific ages (1, 3, 7, 14 and 28 d), one or two slices of the cylindrical samples were cut with a diamond saw with water as lubricant and immersed in isopropanol for 7 days to exchange the pore solution and facilitate drying [36]. The isopropanol was renewed after 1 h, 1 d and 3 d. Then, the slices were stored in desiccators over silica gel for at least 7 days. The dried samples were broken with pincers into 5 pieces of about 3-5 mm size and the total weight of each sample was

around 1.5 g. These pieces were inserted into the CD3 dilatometer and the MIP measurements followed. For the calculation of pore sizes, the Washburn model based on cylindrical pores was used. The contact angle of mercury on the cement paste was assumed to be 120°, whilst 140°, 130° (120-140° cover the normal range of contact angles used in the literature [30,37,38]) were used as well to assess sensitivity of the prediction methods. The surface tension of mercury was assumed to be 0.48 N/m.

4.3.3 Chemical shrinkage

The chemical shrinkage can be measured as the volume of water absorbed by a paste during hydration to maintain its saturation. The protocol used to measure chemical shrinkage was in accordance with procedure A described in the ASTM C 1608-07 standard [39]. Approximately 2 g of a paste (two systems: Cement-0.3 and CQZ20-0.35) were cast into a transparent glass vials with internal Ø20 mm and 60 mm height and tapped gently afterwards to remove the air bubbles from the paste. 2 g of paste correspond to about 3 mm of sample thickness in the vials. The thickness of the specimen should be selected based on the properties of the system and the desired experimental duration [34]. It has been reported in numerous studies, e.g., [33,34] that for increasing sample thickness, the resolved chemical shrinkage decreases, since lower regions of the sample are not readily accessible by water acting as a probe, see also [32]. This is especially important for low w/c cement pastes with low permeability. On the other hand, too thin a sample would lead to high error in the measurements, especially if long-term measurements are performed with small volumes of chemical shrinkage at later ages. In order to check the effect of sample thickness on the measured chemical shrinkage, results from two different thicknesses were compared: 3 mm and 5 mm. The vials were filled up with de-aired deionized water. A capillary tube with a rubber plug was mounted on the top of the vial in a way that the water from a vial entered the capillary. Blue-coloured oil was added on top of the water layer in the capillary tubes to easily follow the decrease of water level as the hydration develops. The vial was then inserted into a temperature-controlled water-bath at 20±0.1 °C. A webcam connected to a desktop computer was used to take images of the water level (with coloured oil on top) in the tube every 10 min. The images were analysed to determine the decrease of the fluid level in the tube.

4.3.4 Pore solution extraction

The procedure for extracting the pore solution was described in *Chapter 3*. The pore solution of two systems (0.35 and 0.49) was filtered with a nylon filter (0.45 µm) and then diluted 3 times (8 M nitric acid and deionized water) and 10 times (with deionized water) and sealed to avoid precipitation or carbonation. After this, the concentration of different ions (Ca²⁺, Na⁺, K⁺ and SO₄²⁻) was measured by using inductively-coupled plasma mass spectrometry (ICP-MS). The concentration of OH⁻ was obtained by measuring the pH of the solution. The average error of ICP-MS measurement for all the ions is about 10 %. The extraction and the analysis of the pore solution composition were performed in order to compare the results from the direct RH measurement on pore solutions with the predictions according to Raoult's law.

4.3.5 Bootstrapping technique

To estimate the propagation of uncertainty in the RH predictions with the novel method, uncertainties from experimental measurements such as RH_s and scatter between the duplicate samples of MIP and NMR were considered. The propagation of these uncertainties is estimated with a bootstrapping technique [40] for the two systems with w/c: 0.30 and 0.46. Bootstrapping is a statistical method that can be used for estimation of the propagation of uncertainty. According to the parametric bootstrapping technique used here, the data on scatter of the experimentally determined data (MIP, NMR and RH_s) were used to generate the simulated dataset (composed of 9999 replicates) obtained by sampling with repetitions from the original data (for RH_s , non-parametric approach) or by sampling from the assumed normal distributions (with average and standard deviation estimated from the NMR and MIP experiments, parametric approach). Next, the sampled data was used for prediction of the RH. From the set of 10000 predicted RH (9999 simulated + average measured), the 95% confidence intervals were next obtained and are presented as error bars later in *section 4.5.2*.

4.4 Results

4.4.1 RH_s

The ion composition of pore solution of two systems (w/c=0.35 and 0.46) is shown in *Table 4.1*. As liquid water is consumed during hydration in both systems, the concentration of ions like K^+ , Na^+ and OH^- increased with time. Ions such as Ca^{2+} and SO_4^{2-} started to decrease after an initial increase at very early ages and stabilized afterwards mainly due to dissolution and reaction of gypsum and C_3A [41] (Ca^{2+} was always decreasing in the concentration presented in *Table 4.1*, because no measurements were made before 15 h). The decrease of ion concentration leads to higher water activity in the system [23]. In higher w/c, theoretically, the ions concentration is lower, which can be linked to the initial water content in the system. When considering ion adsorption on the solid surfaces as well, however, the picture is complicated by differences in the available surface area. Based on a simple calculation to estimate the effect of w/c on the ion concentration (see [23]), the ion concentration in a system with w/c of 0.35 is expected to be 18% higher than in a system with w/c of 0.46. However, for the measured K^+ and Na^+ , concentrations, this difference is larger (see *Table 4.1*). As also indicated in *Table 4.1*, for different ions the concentrations did not vary in a systematic manner between the two systems. The RH_s calculated with Raoult's law is depending on the overall ions concentration.

The RH_s of pore solutions of systems with different w/c are obtained both from calculations with Raoult's law (two systems) and measurements performed directly on the extracted pore solutions (results of systems with w/s of 0.35 from *Chapter 3*). The results are presented in *Figure 4.10 (a)* and *(b)* respectively.

The RH_s decreased with hydration time from about 98.5 % at 3 days to 97 % at 28 days. The RH_s are expected to be lower in the systems with lower w/c, since the ionic concentrations in the solutions are higher due to the lower water contents. However, this trend is not directly evident in the measurements, possibly due to the insufficient accuracy of the RH sensors in this high RH range. According

to the comparison between the measurements and the predictions, the latter gives higher RH_S than the measured results after 3 days. The difference is however at most 0.8 % RH. Since the data on pore solution is available only for part of the systems, the measured RH_S is used instead of Raoult's law in further predictions of the overall RH; it should be noted that application of Raoult's law can be useful if one needs to predict the overall RH depression based only on, e.g., simulated pore solution composition and pore structure.

Table 4.1 Measured pore solution composition for two systems

Systems	Time	Ca^{2+} (mmol/l)	K^+ (mmol/l)	Na^+ (mmol/l)	SO_4^{2-} (mmol/l)	OH^- (mmol/l)
w/c=0.35	15h	3.4	290.5	64.4	7.2	262
	1d	2.4	327.6	71.6	5.5	327
	3d	2.3	427.9	123.3	16.9	385
	7d	1.5	483.2	116.2	10.7	602
	28d	1.1	536.5	147.5	5.4	787
w/c=0.46	15h	4.1	223.4	51.6	34.1	437
	1d	3.3	360.3	78.4	6.7	438
	3d	2.5	309.5	79.5	2.1	741
	28d	1.2	366.5	112.6	1.6	792

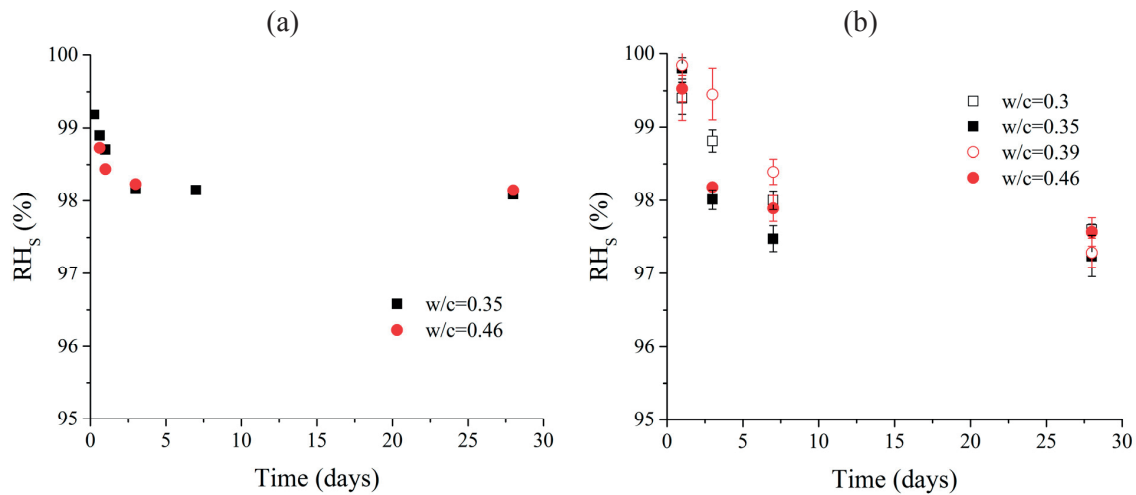


Figure 4.10 Relative humidity of pore solution of cementitious materials: (a) Relative humidity of pore solution calculated based on Raoult's law; (b) Relative humidity of pore solution measured by RH sensors

4.4.2 Chemical shrinkage

The results presented in Figure 4.11 are normalized per gram of cement. The first measurements were

taken 30 min after start of mixing. The results were zeroed at final set since the volume reduction occurring before final set (determined by Vicat needle test, see *Chapter 3*) is supposed to results all in collapse of the paste (bulk volume change) rather than in emptying of the pores [23,42].

Previous studies of chemical shrinkage highlighted the importance of sample thickness [3,34]. In this study, samples of 3-mm and 5-mm thickness were compared. Considering the small differences between the two thicknesses tested, the 3-mm thickness was chosen for the internal RH simulations.

The results show that most of the chemical shrinkage of the two extreme systems (w/c of 0.30 and 0.46) happened in the first 5-7 days. While the rate of chemical shrinkage slowed down after the first week, the chemical shrinkage increased steadily during the whole measurement period, i.e. until 28 days. The two systems had similar chemical shrinkage up to around 4 days, after this the measurements diverged with higher chemical shrinkage measured at higher w/c. Very good repeatability was observed between the duplicate samples. Note that, since the pastes were hydrating under saturated conditions, both their chemical shrinkage (or degree of hydration) is higher than for the same pastes under sealed conditions, especially in systems with lower w/c (lower than about 0.40-0.42) [31,32]. In reference [31] by comparing the heat of hydration and the chemical shrinkage in sealed and saturated samples with w/c 0.30, their chemical shrinkage diverged at around 26 h, whereas no difference was observed for higher w/c of 0.5.

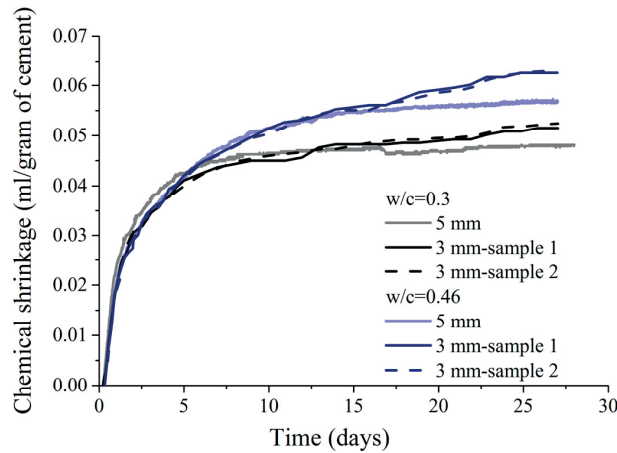


Figure 4.11 Chemical shrinkage measurements on cement pastes with different w/c (results for duplicate samples).

4.4.3 Degree of hydration

The degree of hydration of specimens (cured under water and sealed) of the two extreme systems (w/c 0.30 and 0.46, the same systems as for chemical shrinkage tests) during the first 28 days obtained from XRD analysis is shown in *Figure 4.12*. As mentioned in the previous section, the results clearly indicate that samples cured under water had higher degree of hydration compared to sealed samples. As expected, the difference between the degree of hydration of sealed and saturated samples is higher for the lower w/c.

Figure 4.13 shows the chemical shrinkage as a function of the degree of hydration. There is a clear linear relationship between the two quantities, which in addition does not appear to depend significantly on the w/c. Chemical shrinkage measurement requires that the systems are saturated. However, assuming the linear dependence of chemical shrinkage vs. hydration degree also for the sealed systems, the chemical shrinkage of the latter system could be estimated from their measured hydration degree evolution.

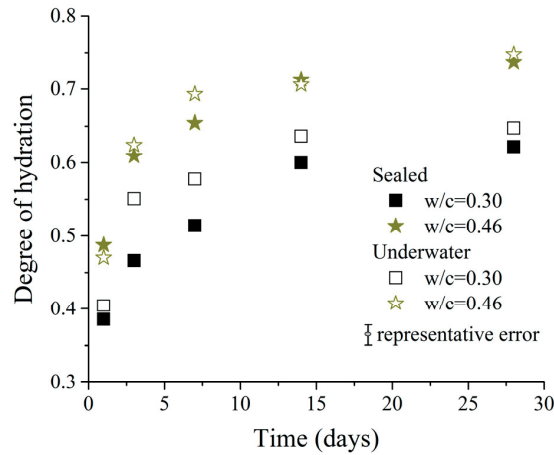


Figure 4.12 Degree of hydration of two systems under two curing conditions (either sealed or saturated), duplicate samples were tested for the w/c 0.30 system; the representative error refers to the maximum difference between the duplicate samples.

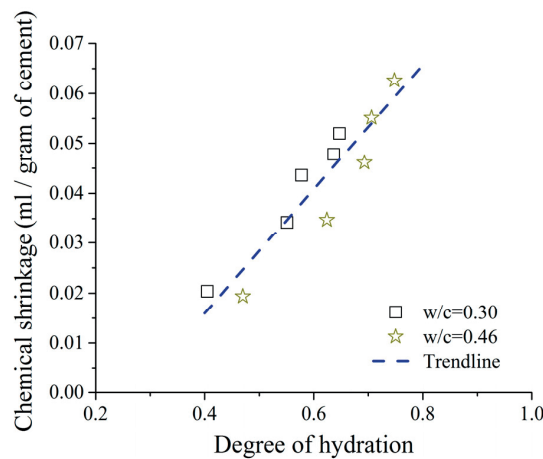


Figure 4.13 Chemical shrinkage vs. degree of hydration of two systems under saturated conditions

4.4.4 Evolution of NMR signal amplitude as function of time

The evolution of NMR signal amplitude of different water populations for different systems is presented in *Figure 4.14*. The signal of solid water obtained from QE measurement is taken into consideration and used to calibrate the total liquid water signal from CPMG measurements (for sealed pastes, signal fraction of capillary water + gel water + interlayer water + solid water = 1) [8]. The volume of water populations can be calculated from the signal fraction (assuming a density of all water populations equal to that of bulk water). Duplicate samples (individual mixing, measured on different days) were tested for the w/c of 0.35; the largest difference in signal fraction is about 0.05 (see *Figure 4.15*). From the data of samples with w/c of 0.35, the average noise level was around 3-4 % of the total signal. In *Figure 4.14*, only the average signal of samples with w/c of 0.35 was shown. Therefore, when the signal of a single water population is close to the noise level, the quantification is prone to high error.

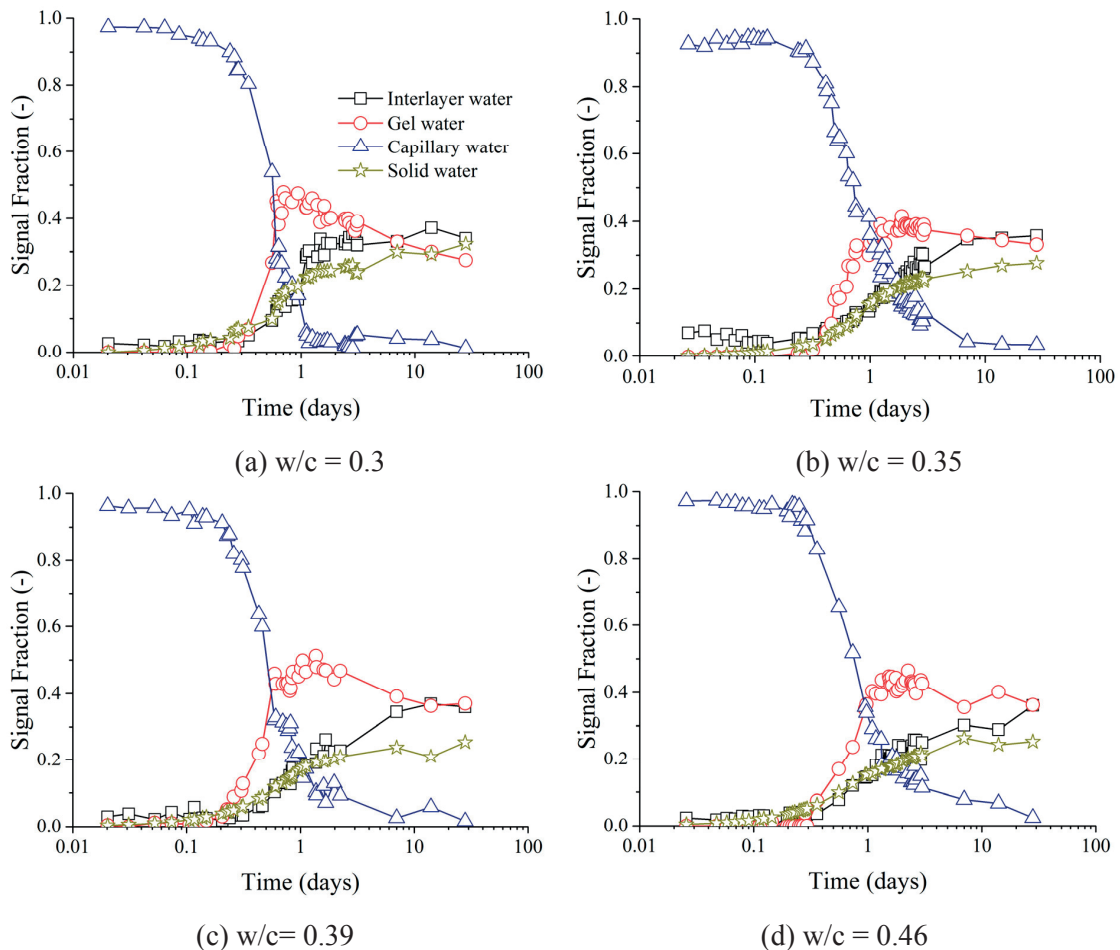


Figure 4.14 Signal amplitude of different water populations in cementitious materials from NMR

In the case of the sample with w/c of 0.30, the amount of capillary water (free water) remained constant in the first few hours, then decreased rapidly during the first day and continued decreasing at much slower rate later on. The reason for this rapid decrease of capillary water is due to the consumption of water during early-age hydration (corresponding to the main hydration peak); this results in accordance with the previous studies on evolution of water populations during hydration, see [7]. The rate of the decrease in the signal fraction of capillary water depends on the w/c of the system. Comparison between systems shows that the higher the w/c , the later the drop of the signal and the higher the final capillary water amount. During the first two days, the signals associated with gel, interlayer and solid water all increased, while the amount of capillary water steadily decreased.

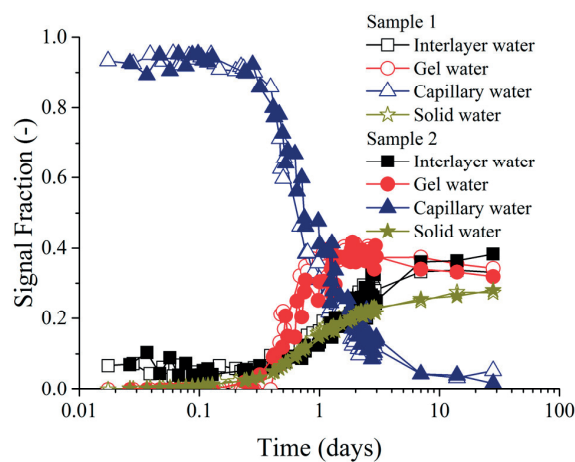


Figure 4.15 Signal amplitude of different water populations from duplicated samples of Cement-0.35

4.4.5 Development of cumulative pore volume

Figure 4.16 shows the relationship between pore radius and porosity of all systems as determined with MIP. It can be seen that microstructural changes during the experiments are related to hydration time and w/c . For all w/c , the total porosity decreased as function of hydration time and the pores were progressively refined. As a result of rapid hydration in the first 3 days, the most significant changes in the porosity and pore size distribution happened during this time.

As expected, the total porosity is higher for systems with higher w/c as well as the threshold pore entry radius and the critical pore entry radius are observed to be larger in pastes with higher w/c at all ages. The threshold pore entry size (the intersection between the two tangents of the cumulative pore volume curve) ranged from about 10 nm to about 100 nm, while the critical pore radius (pore size corresponds to the steepest slope of the cumulative pore volume curve) ranged from 10 nm to around 30 nm. Results of duplicate samples are shown for the system with w/c of 0.30, in which the difference in the total porosity was around 2.5%.

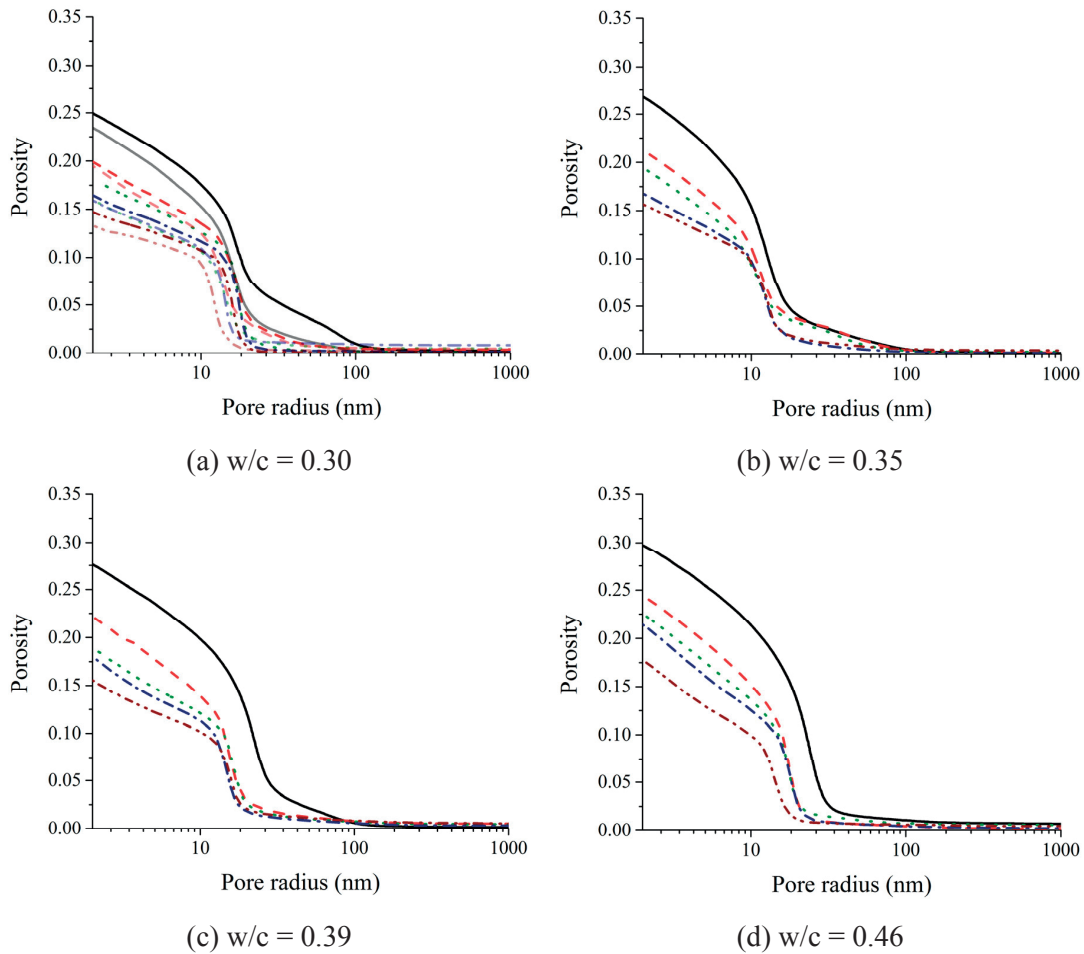


Figure 4.16 Evolution of porosity as function of pore radius at different ages in all systems

4.5 Prediction results and discussion

4.5.1 Selection of the cut-off sizes

With the objective of identifying different pore classes, the differential pore size distribution measured by MIP is shown in *Figure 4.17*. In [5] and [30], the total pore volume minus the fraction within the C-S-H peak was assigned to the capillary pores. This operation was possible since two main peaks (associated to gel pores and capillary pores) could be separated in pastes made with white Portland cement [5]. The results, in terms of both pore volumes and pore sizes, were in good agreement with NMR data. However, in the pastes made with ordinary (grey) Portland cement examined in the present study, no clear gel pore peak could be seen in the differential pore size distribution and the approach described above could not be applied. Therefore, a cut-off radius was used as stated in *section 4.2*.

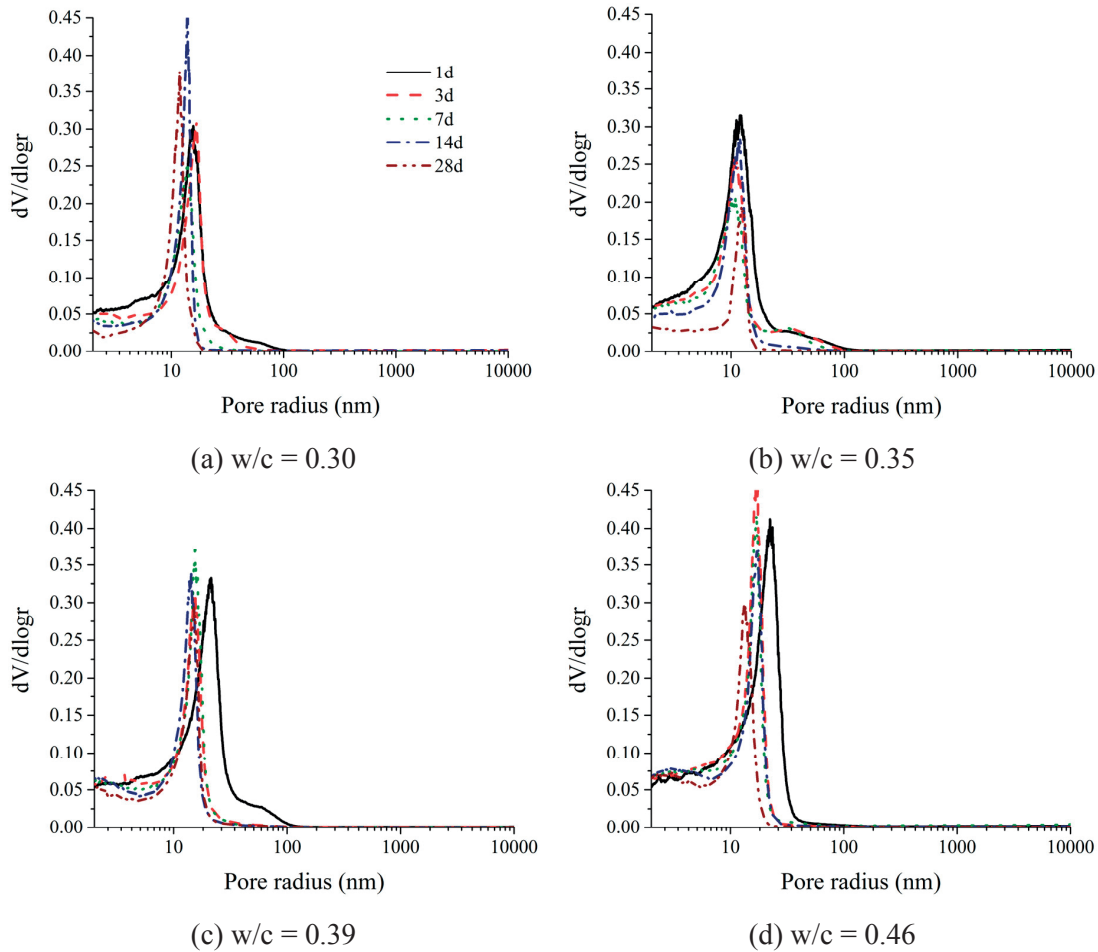


Figure 4.17 Pore size distribution from MIP for four systems

The cut-off radius was assumed in the present study as the point at which the peak in the MIP differential curve flattens. The estimations for all systems and ages are presented in *Table 4.2*. It can be seen that, except for the w/c 0.35 paste at 1 d, all other estimates fall in the range 6-7 nm, and the average radius was 6.5, with a relatively narrow confidence interval of ± 0.5 nm (95 % confidence interval based on t-distribution). Considering the relatively narrow confidence interval of the estimated cut-off radii, one single averaged value was used for all the calculations, while the boundary values were additionally checked with sensitivity analysis in *Figure 4.20*. Since the found radius was relatively constant through different systems and ages, it appears to be an inherent feature of the pore structures studied here and is therefore assumed to be the cut-off radius between the gel and capillary pores.

The estimated cut-off radii were further validated with the NMR-based estimations of pore sizes. It should be noted that NMR allows estimating only average, or dominant pore sizes, and not the smallest sizes of a given water population (here, for the capillary pores, being the cut-off radii), since it resolves a bulk of water in a given population of pores. The estimation can be performed using the fast exchange model [43], Assuming cylindrical geometry of the capillary pores, with surface-to-

volume ratio $S_p/V_p=2/r$, and adopting the surface relaxivity equal to $\lambda=3.73 \cdot 10^{-3}$ nm/ μ s [4], the average pore radii of the capillary pores are estimated to be in the range 8-12 nm. After assuming spherical geometry, with $S_p/V_p=3/r$, the estimate changes to 12-18 nm. These values for the average radii agree reasonably well with the position of the peaks in the MIP curves in *Figure 4.17*, especially at later ages, and are consistent with the MIP-based estimation of the smallest radii (cut-off radii) equal to about 6.5 nm.

Table 4.2 Cut-off sizes for all systems (nm)

Systems	1 d	3 d	7 d	14 d	28 d
w/c = 0.30	7.3	7.1	6.0	6.4	6.2
w/c = 0.35	4.4	5.7	5.4	5.2	8.0
w/c = 0.39	6.9	6.0	8.2	7.8	7.9
w/c = 0.46	6.6	6.5	7.1	5.5	6.6

4.5.2 Results and discussion

The calculated RH (based on *Equation 4.4*, with contact angle of 120°) from the novel approach for all systems with different w/c are shown in *Figure 4.18* alongside the RH measured. The predictions show a reasonable agreement with the experimental values. The agreements are better for w/c 0.30 and 0.39 than for w/c 0.35 and 0.46. It is intrinsic to the calculations that there are several sources of error from the experiments. To investigate how these errors cumulate, a bootstrapping technique was used for the two systems (the approach is explained in *section 4.3.5*). This approach results in the error bars as shown in the figure. Generally speaking, the experimental values are within the errors of the prediction. The scatter of the MIP, NMR and *RH_s* measurements was larger in the system with low w/c, leading to a 95 % confidence band of maximum about 8 % RH.

In the case of the w/c 0.30 paste, the measured RH lies within the bootstrapping 95 % confidence intervals of the simulated RH. However, this is not the case for the w/c 0.46, where although the uncertainty resulting from the errors of the MIP, NMR and *RH_s* measurements was smaller, the simulated confidence intervals of the prediction did not encompass the measured RH.

As the deviation between experiments and prediction does not follow an obvious trend, it is difficult to identify the factors responsible for the smaller or larger deviations. However, it is clear that larger deviations may arise when the pore radii estimated based on chemical shrinkage or NMR-determined volumes lie on the flatter part of the MIP curve (see *Figure 4.8*).

The Kelvin radii predicted from both methods (i.e., chemical shrinkage-MIP method and NMR-MIP method) together with the one calculated based on the experimental RH results for the lowest and highest w/c are presented in *Figure 4.19*. The Kelvin radii predicted according to both methods show a good agreement with the calculation from the experimental RH results at low w/c, while the agreement in the higher w/c range is less satisfactory, especially at early ages.

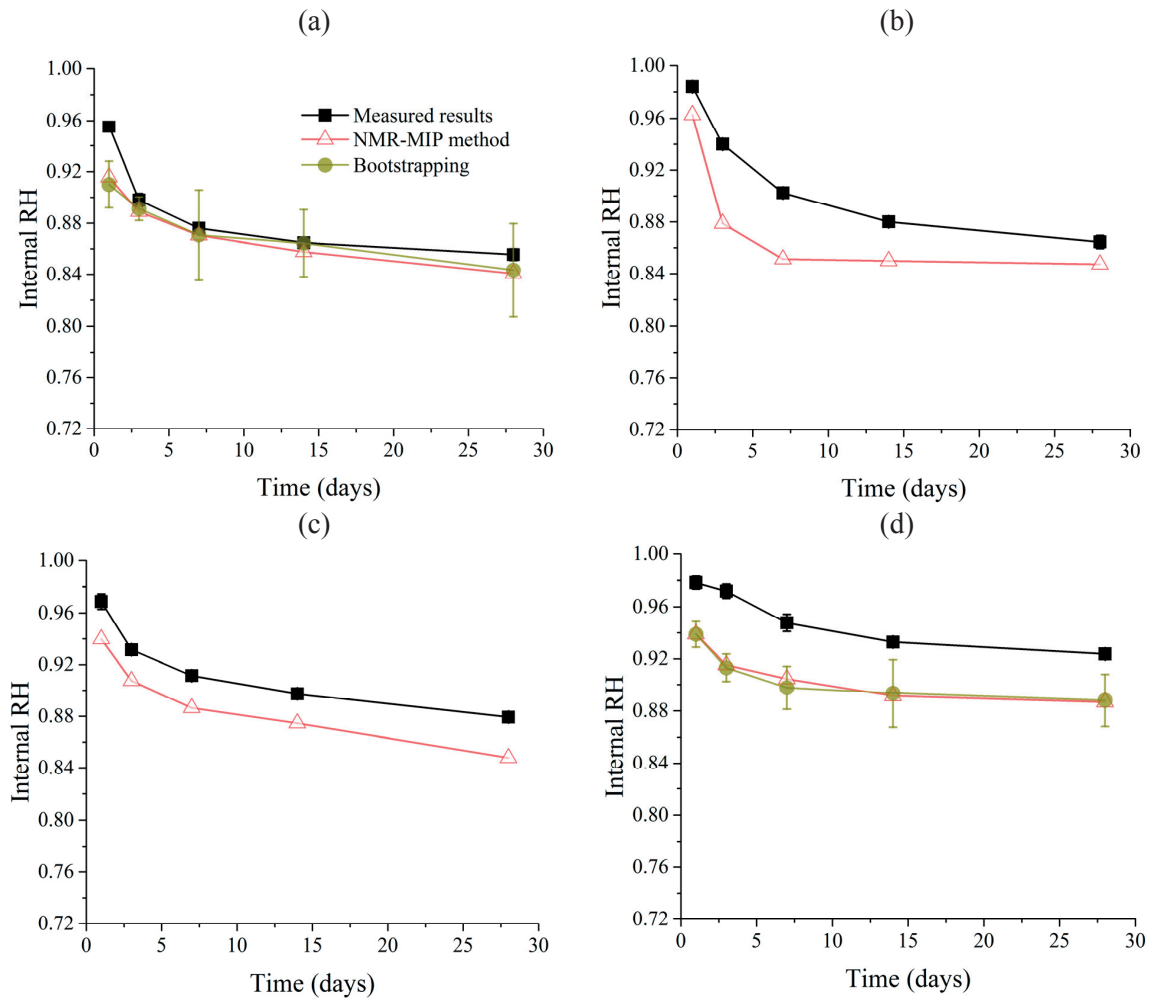


Figure 4.18 Comparison between predicted (with contact angle of 120°) and measured RH based on NMR-MIP method ((a): w/c of 0.30; (b): w/c of 0.35; (c): w/c of 0.39; (d): w/c of 0.46). Error bars refer to 95% bootstrap confidence intervals calculated

One of the reasons for the lower Kelvin radii estimated here with the two methods could be due to a systematic bias towards smaller pores in the pore size distribution measured by MIP (see the discussion in [23]). This effect should however be of minor importance in this study, since the Kelvin radii calculated from RH are smaller than the critical pore entry sizes in all cases after 1 d.

Another hypothesis is that the contribution of RH_s to the internal RH may be systematically overestimated. Indeed, Figure 4.10 shows large scatter in particular in the first days and unsystematic dependence on w/c, which might depend on the uncertainty of measurements on pore solutions in the high RH range. Since the RH_s term is more important for high w/c, errors in this term will have a larger impact on the calculated Kelvin radii for pastes of higher w/c.

Comparing the predictions of the previous and novel methods, it can be seen that results are very close in both cases. However, the previous method (Chemical shrinkage-MIP) seems to systemati-

cally give higher values than the new method (NMR-MIP). This trend may be explained by the presence of entrapped air. For samples hydrating with water curing with no imposed water pressure, air voids may remain empty and would therefore not be resolved in the chemical shrinkage measurement. On the other hand, air voids would be intruded by mercury in MIP measurements, they would end up contributing to the volume of capillary voids and would also shift the pore size distribution toward larger sizes [44]. On the other hand, the NMR measurements should not be prone to this artefact since they estimate the volume of the filled capillaries only. Consequently, the Kelvin radius determined may have been overestimated with both methods due to this artefact, but to a higher extent with the Chemical shrinkage-MIP method.

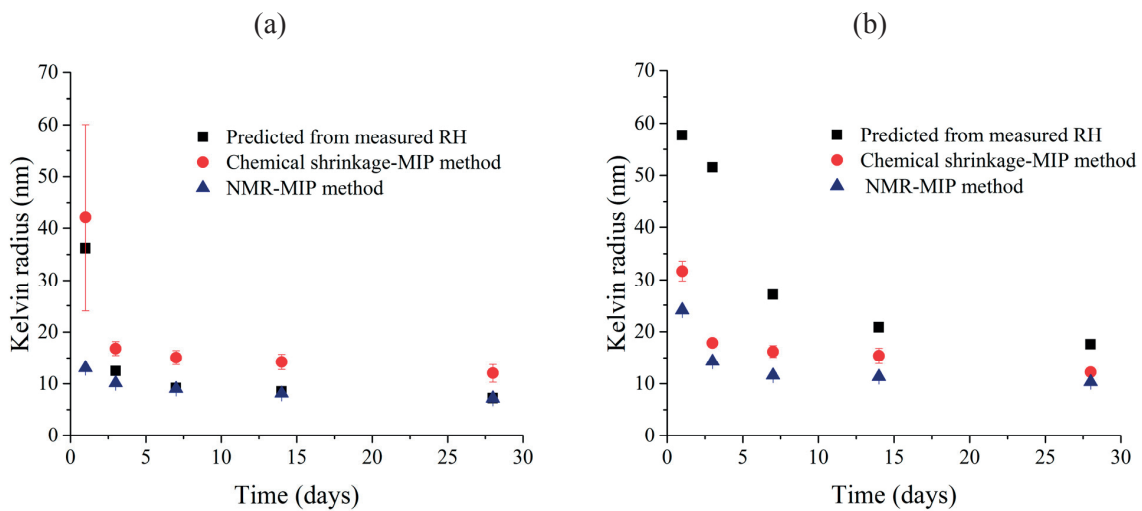


Figure 4.19 Comparison between predicted Kelvin radii $r=(r_p-t)$ with the two different approaches ((a), w/c of 0.30, (b), w/c of 0.46)

A possible source of error could also be systematic differences in the chemical shrinkage between water saturated and sealed samples, due, e.g., to effects on the density of the C-S-H phase. Further, chemical shrinkage could be possibly overestimated if leaching occurred in samples exposed to water during the test, as the leached out volume might be erroneously resolved as chemical shrinkage, leading in consequence to underestimations of the Kelvin radius. From the NMR side, errors may originate from assuming the same density of 1 g/cm^3 for all types of water when the capillary water amount from NMR is converted into pore volume of mm^3 per mm^3 sample.

In order to test the sensitivity of the prediction to different values of the assumed parameters, i.e. contact angles (140° , 130° and 120°) and cut-off radii (6, 6.5 and 7 nm), a comparison of the results with different values is shown in Figure 4.20. The lowest cut-off size was selected on one hand according to the lowest RH found for the range of MIP curve shape and on the other hand due to the RH needed for continuing the hydration in cementitious materials (around 75% RH according to [32]), while the highest cut-off size was selected due to range of cut-off sizes reported in Table 4.2 in section 4.5.1. It can be seen that in the method based on NMR proposed here, the contact angle has a

negligible influence on the predicted RH. With larger contact angles, slightly higher RH was predicted especially at ages up to 3 d. The tested boundaries of the cut-off radii (6 and 7 nm based on the determined confidence intervals) correspond to differences of the predicted RH at a level of about 2%. The difference becomes especially visible for lower cut-off radii assumed (6 nm), leading to lower predicted RH, especially at later ages.

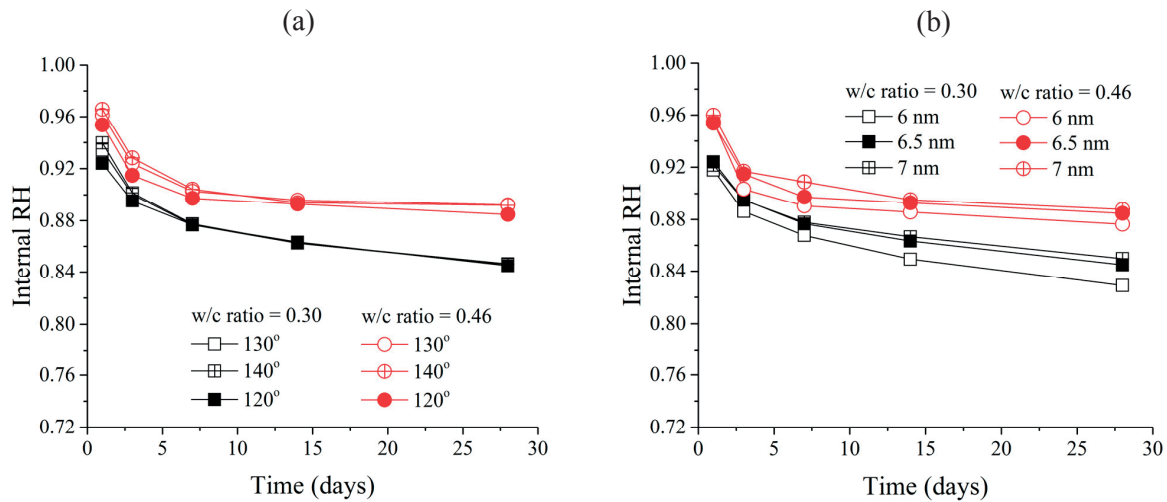


Figure 4.20 Sensitivity analysis, (a): effect of contact angle; (b): effect of cut-off sizes

4.6 Summary

In this chapter, the internal RH was measured and predicted for cementitious materials with w/c in the range 0.30 to 0.46. The predictions were based on a novel method to estimate the evolution of the Kelvin radius based on combining the volume of water-filled pores obtained by ^1H NMR with a pore size distribution measured by MIP, at given hydration stages. This new method was compared with a previously-published method that is based on finding the volume of empty pores due to chemical shrinkage and combining it with the pore size distribution measured by MIP.

According to the results, the new method proposed here agreed reasonably well with the measured decrease of RH for the pastes at w/c of 0.30-0.46. At low w/c the new method provided better agreement than the previous method, whereas for the higher w/c both methods performed in a similar way, overestimating the RH depression as compared to the experimental data. The differences between the predicted and measured values may originate from the effect of air voids and the errors of the experimental input, while the ink-bottle effect is not expected to have a pronounced impact on the results.

The major advantage of the method proposed here is that it uses as input only data obtained from sealed samples, both for the determination of the pore solution volumes as well as for pore size distributions. On the contrary, the previous method employed saturated samples for the chemical shrinkage measurements, which are incompatible with the sealed conditions of self-desiccation.

Propagation of uncertainty of the experimentally-determined data was assessed by means of the bootstrapping technique, yielding relatively high uncertainty of the predictions, up to $\pm 4\%$. Additionally, the effect of parameters assumed in calculations was studied. The assumed contact angle of mercury was found as having a negligible influence on the predicted results, while the choice of the cut-off radius had a slightly higher impact, resulting in differences of the predictions of up to 2% RH.

4.7 References

- [1] P. J. McDonald, J.-P. Korb, J. Mitchell, L. Monteilhet, Surface relaxation and chemical exchange in hydrating cement pastes: a two-dimensional NMR relaxation study., *Am. Phys. Soc.* 72 (2005) 11409-1-11409-9.
- [2] A. Valori, P. J. McDonald, K. L. Scrivener, The morphology of C-S-H: Lessons from ^1H nuclear magnetic resonance relaxometry, *Cem. Concr. Res.* 49 (2013) 65–81.
- [3] K. Scrivener, R. Snellings, B. Lothenbach, *A practical guide to microstructural analysis of cementitious materials*, 2016.
- [4] A. Gajewicz, *Characterisation of cement microstructure and pore – water interaction by ^1H nuclear magnetic resonance relaxometry*, University of Surrey, 2014.
- [5] A. C. A. Muller, *Characterization of porosity & C-S-H in cement pastes by ^1H NMR*, EPFL, 2014.
- [6] L. J. Schreiner, J. C. Mactavish, L. Miljkovic, M. M. Pintar, R. Blinc, G. Lahajnar, D. Lasic, L. W. Reeves, NMR line shape-spin-lattice relaxation correlation study of Portland cement hydration, *J. Am. Ceram. Soc.* 68 (1985) 10–16.
- [7] A. C. A. Muller, K. L. Scrivener, A. M. Gajewicz, P. J. McDonald, Use of bench-top NMR to measure the density, composition and desorption isotherm of C-S-H in cement paste, *Microporous Mesoporous Mater.* 178 (2013) 99–103.
- [8] A. C. A. Muller, K. L. Scrivener, A. M. Gajewicz, P. J. McDonald, Densification of C-S-H measured by ^1H NMR relaxometry, *J. Phys. Chem.* 117 (2013) 403–412.
- [9] D. D. Lasic, M. M. Pintar, R. Blinc, Are proton NMR observations supportive of the osmotic model of cement hydration?, *Philos. Mag. Lett.* 58 (1988) 227–232.
- [10] L. Monteilhet, J. P. Korb, J. Mitchell, P. J. McDonald, Observation of exchange of micropore water in cement pastes by two-dimensional T_2 - T_2 nuclear magnetic resonance relaxometry, *Phys. Rev. E - Stat. Nonlinear, Soft Matter Phys.* 74 (2006) 1–9.
- [11] H. Y. Carr, E. M. Purcell, Effects of diffusion on free precession in nuclear magnetic resonance experiments, *Phys. Rev.* 94 (1954) 630–638.
- [12] S. Meiboom, D. Gill, Modified spin-echo method for measuring nuclear relaxation times, *Rev. Sci. Instrum.* 29 (1958) 688–691.
- [13] J. G. Powles, J. H. Strange, Zero time resolution nuclear magnetic resonance transient in solids, *Proc. Phys. Soc.* 82 (1963) 6–15.
- [14] L. Venkataramanan, Y. Q. Song, M. D. Hürlimann, Solving Fredholm integrals of the first kind with tensor product structure in 2 and 2.5 dimensions, *IEEE Trans. Signal Process.* 50

- (2002) 1017–1026.
- [15] K. R. Brownstein, C. E. Tarr, Importance of classical diffusion in NMR studies of water in biological cells, (n.d.).
- [16] W. P. Halperin, J.-Y. Jehng, Y.-Q. Song, Application of spin-spin relaxation to measurement of surface area and pore size distributions in a hydrating cement paste, *Magn. Reson. Imaging*. 12 (1994) 169–173.
- [17] P. Lura, O. M. Jensen, K. van Breugel, Autogenous shrinkage in high-performance cement paste: An evaluation of basic mechanisms, *Cem. Concr. Res.* 33 (2003) 223–232.
- [18] O. M. Jensen, P. F. Hansen, Influence of temperature on autogenous deformation and relative humidity change in hardening cement paste, *Cem. Concr. Res.* 29 (1999) 567–575.
- [19] P. Lura, M. Wyrzykowski, M. Griffa, Handout of the course: shrinkage and cracking of concrete: mechanisms and impact on durability, (2013) 1–16.
- [20] J. C. Melrose, Model calculations for capillary condensation, *AIChE J.* 12 (1966) 986–994.
- [21] C. Hua, P. Acker, A. Ehrlacher, Analyses and models of the autogenous shrinkage of hardening cement paste, *Cem. Concr. Res.* 25 (1995) 1457–1468.
- [22] H. Köhler, The nucleus in and the growth of hygroscopic droplets, *Trans. Faraday Soc.* 32 (1936) 1152.
- [23] H. Chen, M. Wyrzykowski, K. Scrivener, P. Lura, Prediction of self-desiccation in low water-to-cement ratio pastes based on pore structure evolution, *Cem. Concr. Res.* 49 (2013) 38–47.
- [24] L. H. Cohan, Sorption hysteresis and the vapor pressure of concave surfaces, *J. Am. Chem. Soc.* 60 (1938) 433–435.
- [25] R. Badmann, N. Stockhausen, M. J. Setzer, The statistical thickness and the chemical potential of adsorbed water films, *J. Colloid Interface Sci.* 82 (1981) 534–542.
- [26] H. Chen, Autogenous and Thermal Deformations and their interaction in early age cementitious materials, EPFL, 2013.
- [27] E. W. Washburn, Note on a method of determining the distribution of pore sizes in a porous material, *Proc. Natl. Acad. Sci. U. S. A.* 7 (1921) 115–116.
- [28] P. Lura, O. M. Jensen, J. Weiss, Cracking in cement paste induced by autogenous shrinkage, *Mater. Struct.* 42 (2009) 1089–1099.
- [29] S. Diamond, The patch microstructure in concrete: The effect of superplasticizer, *Cem. Concr. Res.* 36 (2006) 776–779.
- [30] A. C. A. Muller, K. L. Scrivener, A reassessment of mercury intrusion porosimetry by comparison with ¹H NMR relaxometry, *Cem. Concr. Res.* (2016) submitted.
- [31] P. Lura, F. Winnefeld, S. Klemm, Simultaneous measurements of heat of hydration and chemical shrinkage on hardening cement pastes, *J. Therm. Anal. Calorim.* 101 (2010) 925–932.
- [32] M. Wyrzykowski, P. Lura, Effect of relative humidity decrease due to self-desiccation on the hydration kinetics of cement, *Cem. Concr. Res.* 85 (2016) 75–81.
- [33] G. Sant, D. Bentz, J. Weiss, Capillary porosity depercolation in cement-based materials: Measurement techniques and factors which influence their interpretation, *Cem. Concr. Res.* 41 (2011) 854–864.
- [34] M. Geiker, T. Knudsen, Chemical shrinkage of Portland cement pastes, *Cem. Concr. Res.* 12

- (1982) 603–610.
- [35] O. M. Jensen, P. F. Hansen, A dilatometer for measuring autogenous deformation in hardening Portland cement paste, *Mater. Struct.* 28 (1995) 406–409.
- [36] J. Zhang, G. W. Scherer, Comparison of methods for arresting hydration of cement, *Cem. Concr. Res.* 41 (2011) 1024–1036.
- [37] D. Shi, D. N. Winslow, Contact angle and damage during mercury intrusion into cement paste, *Cem. Concr. Res.* 15 (1985) 645–654.
- [38] R. A. Cook, K. C. Hover, Mercury porosimetry of hardened cement pastes, *Cem. Concr. Res.* 29 (1999) 933–943.
- [39] ASTM, Standard C1608-12: Standard test method for chemical shrinkage of hydraulic cement paste, in: 2014: pp. 1–5.
- [40] B. Efron, Bootstrap methods: another look at the Jackknife, *Stat. Math.* 7 (1979) 1–26.
- [41] D. Rothstein, J. J. Thomas, B. J. Christensen, H. M. Jennings, Solubility behavior of Ca-, S-, Al-, and Si-bearing solid phases in Portland cement pore solutions as a function of hydration time, *Cem. Concr. Res.* 32 (2002) 1663–1671.
- [42] P. Lura, O. M. Jensen, Measuring techniques for autogenous strain of cement paste, *Mater. Struct.* 40 (2007) 431–440.
- [43] P. J. McDonald, V. Rodin, A. Valori, Characterisation of intra- and inter-C–S–H gel pore water in white cement based on an analysis of NMR signal amplitudes as a function of water content, *Cem. Concr. Res.* 40 (2010) 1656–1663.
- [44] M. Wyrzykowski, R. Kiesewetter, J. Kaufmann, R. Baumann, P. Lura, Pore structure of mortars with cellulose ether additions – Mercury intrusion porosimetry study, *Cem. Concr. Compos.* 53 (2014) 25–34.

Chapter 5 Visco-elastic behavior of cementitious materials

This chapter aims at elucidating the effect of hydration on visco-elastic behavior of cementitious materials, focusing on uniaxial basic creep tests under different loading ages (from 20 h to 28 d). The validity of the power law expression and of the parameters describing the evolution of the visco-elastic behavior of cementitious systems were evaluated. In the last section, generalized Kelvin-Voigt chains were used to model time-dependent creep. The main aim of the results presented in this chapter is to establish the experimental basis to calculate the visco-elastic response in the autogenous shrinkage predictions (see *Chapter 6*).

Contents

5.1	Literature review.....	79
5.1.1	Mechanism of basic creep.....	79
5.1.2	Basic creep at early ages.....	85
5.1.3	Modeling of creep at early ages.....	88
5.2	Methods.....	90
5.3	Results.....	93
5.3.1	Stress applied.....	93
5.3.2	Apparent creep strain for hardening pastes.....	93
5.3.3	Instantaneous elastic response.....	95
5.3.4	Basic creep compliance at different loading ages.....	97
5.4	Power law expression.....	101
5.4.1	Kinetics of creep compliance.....	101
5.4.2	Power law expression.....	103
5.4.3	Back calculation of the creep compliance.....	105
5.5	Creep recovery.....	106
5.6	Rheology modeling.....	108
5.7	Conclusions.....	113
5.8	References.....	114

5.1 Literature review

Concrete shows pronounced visco-elastic behavior, especially at early ages, under sustained loads/deformations, which manifests either as creep (increasing strain at constant load) or stress relaxation (decreasing stress at constant strain). This visco-elastic behavior needs to be precisely known, since it has a substantial impact on the long-term deformation of concrete members in compression and bending [1]. In extreme cases, creep might even be a part of the reasons of the structural collapse, e.g., in the famous case of the failure of the Koror-Babeldaob Bridge in Palau [2]. The visco-elastic response is also a cause of loss of prestress in prestressed concrete elements and structures [3]. However, creep is not always harmful. On the positive side, the visco-elastic behavior of concrete influences the buildup and development of stresses due to restrained shrinkage and thermal gradients and contributes to reduce the risk of cracking at early ages [4]. Therefore, the visco-elastic behavior of cementitious materials has attracted massive attention for almost a century in all its aspects, including the study of its fundamental mechanisms, establishment of experimental databases and simulation approaches.

Basic creep (creep of sealed specimens [5]) will be the only concern in this thesis since the original objective for carrying out the creep tests is for providing the visco-elastic response for autogenous shrinkage (no external drying). In terms of the significance of investigating basic creep, on the one hand, drying creep is also of lower importance at early ages (except for very thin samples), especially in the first few days. In fact, drying is a slow phenomenon and larger concrete members will experience relatively little drying (in any case in their bulk) within the first few days to weeks after casting [6]. On the other hand, dealing with basic creep avoids the complications connected to the effect of drying and shrinkage gradients in the specimens.

This section briefly reviews the literature dedicated to mechanisms, experimental characterization and modeling of basic creep particularly at early ages.

5.1.1 Mechanism of basic creep

It has been found that among all anhydrous and hydrated phases in cement pastes, only the hydration product C-S-H appears to show non-negligible visco-elastic behavior [7]. Water, especially gel and interlayer water may also play a fundamental role in the creep response [8]. With respect to the exact mechanisms of creep, even though some promising research findings were published recently [9–14], no consensus has been reached yet with the available experimental data. In other words, the role of water and C-S-H and the precise mechanisms that lead to creep continue to be questioned [13,15,16].

Role of water on the mechanism of basic creep

The importance of water in the mechanisms of basic creep is still under debate [15,17,18]. The most important observation supporting the significance of water is that fully dried specimen have been found to have insignificant basic creep, e.g., [19,20]. However, there are also some conflicting conclusions from other published studies, according to which water only has a minor effect on creep,

especially on basic creep, since creep in the study of Tamtsia and Beaudoin [18] was significant even after D-drying⁴. A systematic literature review has been published particularly on the role of water in creep [21]. Therefore, only the important and more recent mechanisms are presented in this section.

Different populations of water (the classification of different types of water can be seen in *Chapter 4*), or more specifically the interactions between water and solids, may impact creep in different ways.

The capillary water can take up loads in the very short term and then transfer them to the solid skeleton [21]. It moves in the microstructure due to pressure differences. However, capillary water should not be involved as a primary factor in the creep mechanisms. The main reasoning behind this conclusion is that macro-diffusion of pore water from macro-pores to macro-pores needs to take place through the micro-pores, but the diffusing fraction is found to be small, particularly when the w/c is low and the pores are most emptied [17] (see macro-diffusion in *Figure 5.1* under external load).

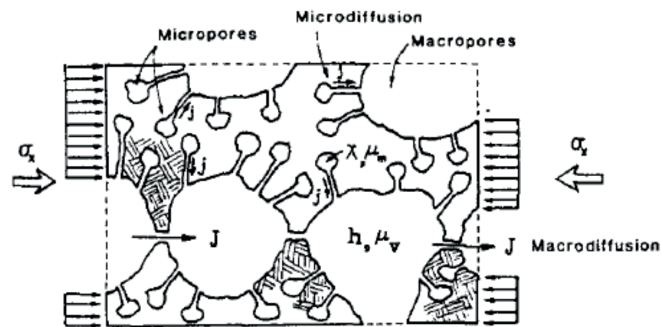


Figure 5.1 Schematic representation of diffusion process in cement paste under applied stresses, from [17]

The role of gel water, interlayer water and adsorbed water has been intensively studied, especially after publications by Powers [22,23]. Powers put forward the concept of the redistribution of water from gel pores to adjacent larger pores caused by the mechanical stressed applied and by the preexisting disjoining pressure. In Powers' hypothesis, due to the redistribution of water (see *Figure 5.2*), the decreased volume of gel water explains the (basic) creep [22]. In a sealed specimen, the redistributed water remains in the system, either situated in unhindered films or to be as capillary water, which increases the internal RH. In an open specimen, an additional drying is induced by losing the redistributed water [22]. Subsequently, when L'Hermite and Mamillan [24] measured the mass evolution differences of samples (drying samples, these experiments did not specifically target basic creep) with two conditions, under-load and load-free, negligible differences were found. Therefore, they drew the conclusion that water is not been squeezed out from the pores (i.e., cement paste does not behave like a 'sponge'). However, this result does not represent strong evidence against redistribution between different types of water.

⁴ D-drying is a vacuum drying method (the pressure of the vacuum pump is maintained at 15×10^{-3} Torr or 30×10^{-3} Torr) performed in a trap connected to a dry ice bath with temperature of -78.5 °C [109].

Indeed, Powers' hypothesis is difficult to test due to the complexity of the hygro-mechanical response of cementitious materials. Therefore, the mechanism has not been experimentally demonstrated until recently, when Wyrzykowski and Lura [12,25] observed the water redistribution in low w/c mortar samples under either tension or compression, with an increase of the internal RH up to about 2% when a compressive stress level of 30% of the compressive strength was applied. The RH change occurred immediately or almost immediately, within several seconds. However, these experiments cannot ascertain whether the water redistribution is caused by micro-diffusion or sliding and rearrangement of the C-S-H (explained in the next section).

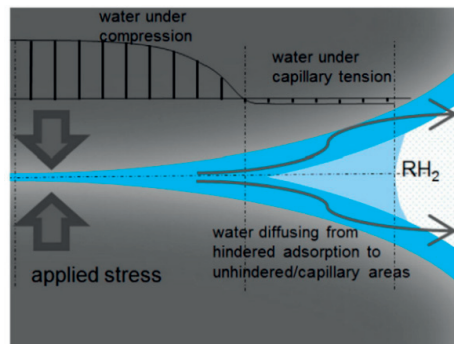


Figure 5.2 Schematic representation of water redistribution from hindered adsorption areas in gel pores into unhindered area, e.g., larger gel pores or capillary pores, from [12]

Bažant proposed micro-diffusion of the local water as the mechanism for short-term creep [26]. The micro-diffusion happens as water transport between a macro-pore and an adjacent micro-pore under externally applied stresses [17] (see Figure 5.1). Note that only micro-diffusion from load-bearing micro-pores to macro-pores (see Figure 5.1) would increase creep. Two hypotheses were proposed for the mechanism related to micro-diffusion of water: 1) the micro-diffusion of water (volumetric) disrupts the microstructure of cement by causing dissolution of bonds and formation of new bonds within the C-S-H structure or sliding of the C-S-H sheets (deviatoric) [17,27]; 2) the micro-diffusion alone is the dominating reason also for longer-term creep, manifesting within a few days to a few weeks or years [7]. Bažant and Chern [17] opposed the second hypothesis because micro-diffusion is supposed to be a rather fast process (according to the calculation provided in [17], this process may be completed in just over 1.4 s).

The role of the interlayer water in the so-called dissolution-precipitation mechanism was discussed in [11,28,29]. According to these studies, either hydration or the local stress state affects the chemical potential of the solids and therefore the solubility of C-S-H in the pore solution is increased. Due to diffusion of ions, precipitation of C-S-H occurs on unstressed C-S-H, causing a strain accommodation [11]. The process was first put forward for gypsum plaster and then adapted for hydrated cement pastes [28]. A schematic representation of the mechanisms behind pressure solution creep is shown in Figure 5.3. The redistribution of the solution is consistent with the previously-mentioned experimental support in [12,25]. Since it links the chemical processes to creep, this mechanism allows to explain the aging effect of creep. However, Grasley and Lange [27] argued that concerning long-term

creep without reaction, dissolution-precipitation alone is not sufficient to explain the entire creep behavior. Indeed, the C-S-H in matured samples would still dissolve where under high stress and reform elsewhere. This effect does not necessarily to be linked with the rate of hydration of cement.

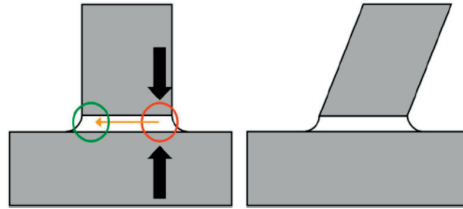


Figure 5.3 Schematic representation of the process of the so-called pressure solution creep (the red circle shows the area under stress, the green circle shows the stress-free area, the arrow shows the dissolution and precipitation direction), from [28]

Role of C-S-H on the mechanism of basic creep

Several hypotheses about the driving mechanisms of creep relevant to C-S-H have been put forward, even no universal agreement has yet been reached [15]. The interactions between water and C-S-H should be also taken into consideration. Both the atomic structure [30] (see Figure 5.4) and the nanoscale morphology of C-S-H are expected to be the reason for manifesting visco-elastic behavior. The structure of C-S-H may be either layered (lamellar) or granular (colloid) according to different models proposed in the literature (see Figure 5.5), while the morphology at the nanoscale is of needle-shaped clusters [31,32].

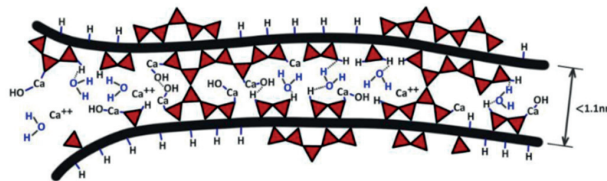


Figure 5.4 Schematic presentation of C-S-H gel structure, from [30]

The mechanisms of creep associated to C-S-H were reviewed in an old but rigorous paper [39] as well as in a recent paper [21]. The primary interpretations of the C-S-H models and the visco-elastic behavior including aging are listed as follows:

1. Sliding between C-S-H sheets caused by the stress leads to breaking and reconstitution of hydrogen bonds (see Figure 5.4) [8,40]. During the sliding process, pore water (more specifically C-S-H inter-layer water) may be necessary as lubricant. As also shown in the microprestress-solidification theory (refined solidification theory) [41], the long-term creep is a result of a quasi-dislocation of adjacent particles resulting through a shear slip mechanism [13] (see Figure 5.6 based on the model of Figure 5.5 (b) and Figure 5.7 based on the model of Figure 5.5 (d)). Jennings [42] specified two mechanisms

for young and matured cementitious systems: due to sliding between C-S-H, hydrogen bonds or other weak bonds are broken in the former case (see *Figure 5.7 (a) and (b)*), while no bonds break but the pore space is rearranged by the movement of particles in the latter case (see *Figure 5.7 (c) and (d)*).

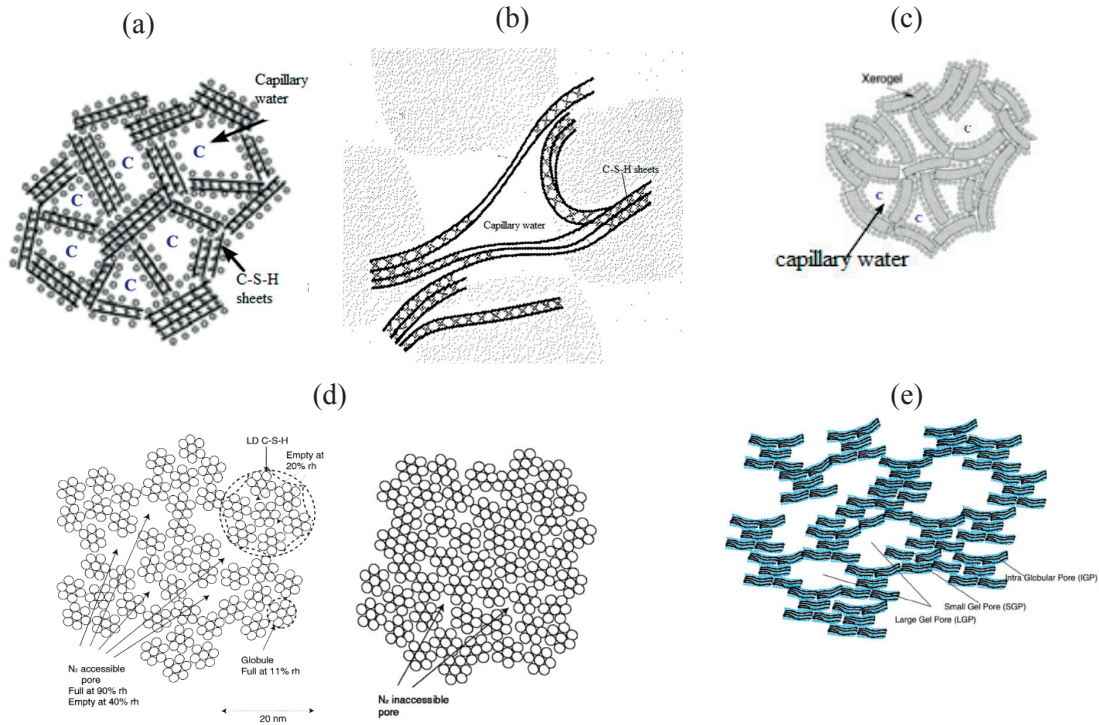
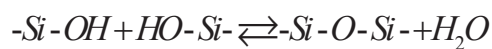


Figure 5.5 C-S-H models: (a) colloid model from Powers and Brownyard [33], figure from [34]; (b) layered model from Feldman and Sereda [35], clay-like structure with interlayer water between layers; (c) colloid model by Wittmann [36], so-called Munich model, ‘xerogel’ is used for open structures that have dried out; (d) colloid model by Jennings for both low density C-S-H and high density C-S-H [37]; (e) refined colloid model by Jennings [38]

2. Rearrangement between C-S-H particles in a shearing process, e.g., silica polymerization (counts for aging, for a simplified expression of this process see *Equation 5.1*) or interlayer consolidation [43,44]. Aging is defined as a process that induces ‘changes over time that are unrelated to the hydration reactions’ [45], in which the number of bonds between the C-S-H layers or globules increases. Silica polymerization of C-S-H induced by external loading or drying process was a mechanism for long-term creep [44]. The interlayer consolidation theory claims that creep is a result of the aging of a layered C-S-H due to external stress (drying is another source of consolidation, due to capillary stresses) [46].

Equation 5.1



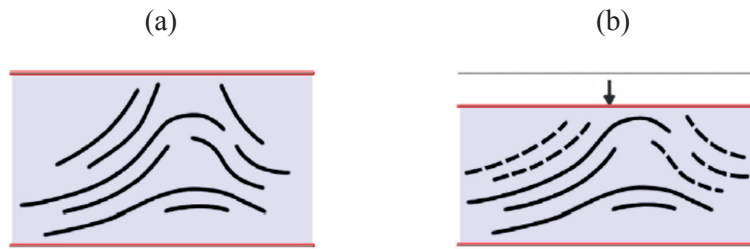


Figure 5.6 Schematic diagram of the creep mechanism due to the sliding of layers (dashed lines) based on the model of figure 5.5 (b), from [13]

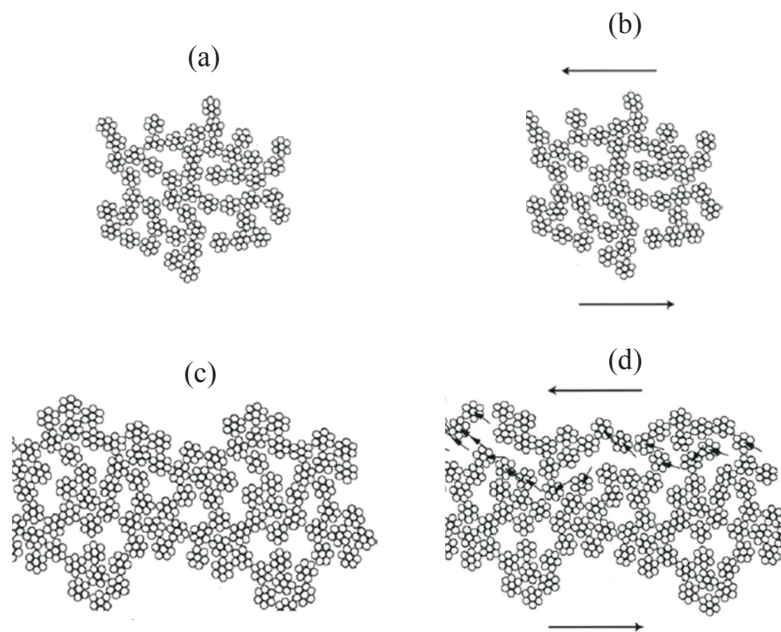


Figure 5.7 Schematic diagram of the creep mechanism due to the sliding of colloid particles ((a) and (b) for hydrating systems before and after sliding, the change of the surface area is small in this case; (c) and (d) for matured systems before and after sliding) based on the model of Figure 5.5 (d), increase of the surface area in this case [42]

To clarify the mechanism, at the C-S-H level, few fundamental investigations have ever been carried out and most of them employed the nanoindentation (or microindentation) technique, where a nano-indenter (or micro-indenter) is pressed into the surface of a hydrated cement paste specimen or compacts, providing a record of penetration depth vs. time measurements at a constant force, which allows assessing, e.g., the creep response. In nanoindentation measurements on cement paste, C-S-H shows, after a short initial transition period, logarithmic creep with time [9,10]. However, these measurements are questionable for a number of reasons: 1) the influence volume of nanoindentation (the portion of paste of which the mechanical properties are measured) covers a couple of μm and may include other phases and porosity besides C-S-H [47,48]; 2) the small volumes under investigation cannot be representative for the cement paste, mainly due to large local variations of porosity that are

intrinsic in cement paste [47,48]; 3) the stresses applied during nanoindentation are very high compared to typical stress levels during the macroscopic creep tests and a high degree of sample damage is likely to occur [49]; 4) while both traditional creep tests and nanoindentation show logarithmic creep, their time scale is not comparable [10]; 5) sample preparation for nanoindentation includes lengthy polishing of the surface of the sample (a virgin sample, without drying and epoxy impregnation), which will inevitably cause damage [50]. One way of overcoming the aforementioned limitations of the nano-scale tests of C-S-H creep would be to test the macroscopic creep response of pure C-S-H. Very few published papers measured the visco-elastic properties on compacts of synthesized C-S-H with macro-mechanical tests. The relaxation measurements in [13], however, were limited to comparatively small samples ($12.8 \times 55.9 \times 1 \text{ mm}^3$) and did not succeed in proving a clear dependence between structural changes in the C-S-H and its visco-elastic behavior. In summary, the visco-elastic behavior of pure C-S-H constitutes a serious gap in the current state of understanding of creep mechanisms of cement-based materials.

5.1.2 Basic creep at early ages

Basic creep, especially at early ages, appears to be of crucial importance for the behavior of concrete in the case of restrained shrinkage accompanied with thermal stresses. Since early-age creep may influence the whole service-life time (through its impact on the risk of cracking), it becomes more and more important for both field applications and research. Few, mostly phenomenological observations about basic creep of hardening cementitious materials are reported in the literature.

In this thesis, only the linear basic creep (in which the creep deformations are proportional to the applied stress) will be discussed and studied since the stress level due to capillary pressure would fall in the linear range. According to the literature, the linear visco-elastic behavior of cementitious materials ends above a stress to compressive strength of the specimens at the load age ratio of about 0.4, see *Figure 5.8*). Even if this is sometimes not mentioned, most of the studies and models in the literature concern the linear creep region.

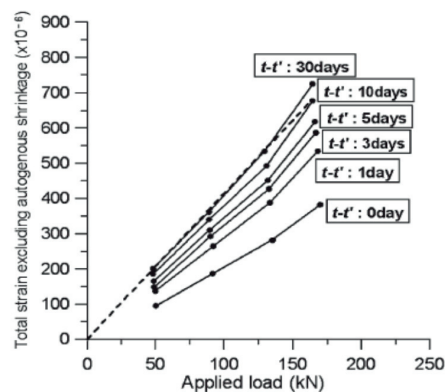


Figure 5.8 Relationship between basic creep strain and applied loads at different loading ages (the four dots correspond to applied loads of 0.1, 0.2, 0.3 and 0.4 of the compressive strength at the time of loading), from [51]

Basic creep and creep kinetics at early ages

Creep is noticed to be even more sensitive to the degree of hydration than other mechanical properties, e.g., the strength and the elastic modulus [52]. In particular, the degree of hydration at the time of loading is one of the major parameters affecting the creep. Plotted in log-log, the evolution of kinetics of basic creep compliance was found to be linear respect to time or age, e.g., the creep rate evolution in [53], see *Figure 5.9*. It has been found that, when fitting the compliance rate with a power law, the exponent should be a range of 0.9 to 1.0 for concrete [54,55] (this corresponds to the slope of the linear relationship in *Figure 5.9*).

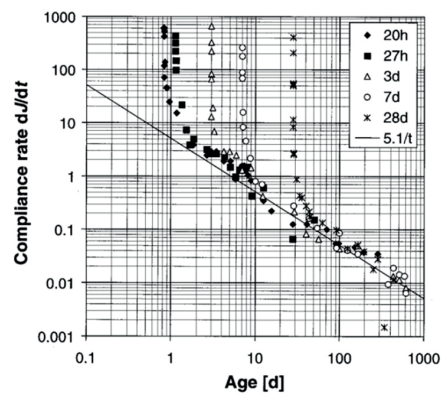


Figure 5.9 Creep compliance rate as a function of age, plotted in log-log, from [53]

The amplitude of the creep compliance is decreasing with increasing loading ages because of increasing hydration degree and this trend is more obvious for specimen with lower w/c [56–58]. The dependence of creep upon the degree of hydration is basically linked to the evolution of porosity, hydration products (C-S-H) and elastic constants.

According to Delsaute et al. [59], the kinetics of the basic creep coefficient did not change after the first two hours and moreover changes in the creep amplitude were associated with the porosity, in particular with the volume fraction of the large capillary pores. Ghodousi et al. observed age-dependent behavior of the creep compliance before the first month, while it vanished after around 100 d [58].

Short-term and long-term creep

The majority of researchers agree that different behavior and mechanisms apply to short-term creep and long-term creep, based on their different kinetics [60,61]. Generally, short-term creep is believed to be associated to a dilating behavior, which lasts from several days to weeks [60]. It means that the short-term creep is associated to volume changes. However, in recent research, one single power-law creep was found for hydrates (C-S-H) [63]. The long-term creep is believed to be volume-constant with a much longer duration [60]. It appears that the short-term creep can be described with a power law, while long-term creep is logarithmic [62]. Short-term creep has been attributed to micro-diffusion within the capillary pores (however, this process should be very fast, see the discussion above),

while long-term creep has been attributed to sliding between C-S-H sheets [8,40]. Yet, the differentiation between them is unclear, as no clear boundary exists between the two regimes in experimental creep curves.

Creep under different loading types

Due to the multi-scale heterogeneity of the system, the stress state of cementitious materials is rather complex. At early ages, tensile stresses induced by the restrained shrinkage (including thermal contraction and autogenous shrinkage) could result in cracks [64]. However, the differences between creep in uniaxial compression (the classical way to perform these tests, which covers the majority of the literature) and creep under uniaxial tension (where it is difficult to fix the specimens and avoid bending moments, cementitious materials are brittle and strains are mostly too small for accurate measurements) is still not clear. A comparison between creep in tension and compression can be found in [65].

Relationship between basic creep and autogenous shrinkage

Apart from the external load, in self-desiccating conditions experienced by cementitious systems with low w/c, the rapid shrinkage of the solid skeleton induced by increasing pore pressure likely also includes a creep component [66,67]. While this insight represents a breakthrough for the prediction of autogenous shrinkage, the description of the problem becomes very challenging, particularly due to lack of understanding on the exact action of basic creep during autogenous shrinkage [68]. There is no doubt that a visco-elastic response will occur because of the internal stress on the solid skeleton caused by the capillary pressure. However, the quantification of the effect of the internal stress on creep is not straightforward, since no convincing experimental evidence about the coupling between autogenous shrinkage and basic creep has been published yet [69–71]. On the other hand, this coupling was approached from the modeling point of view, e.g., by Gawin et al. [72,73]. The coupling problem is illustrated in *Figure 5.10*.

The most logical and robust approach to interpret basic creep measurements appears to be subtracting the measured free strain (autogenous shrinkage) from the total basic creep [71,74], as is conventionally done with drying shrinkage and drying creep. However, the existence of the coupling shown in *Figure 5.10* would imply that the conventional subtraction approach is not correct to access basic creep. Considering micro-cracks occurring during loading, autogenous shrinkage in load-free samples and samples under-loaded is assumed to be different [75,76]. The work of Wei et al. [77] concluded that it was justify to decouple autogenous shrinkage and tensile creep strain by using the conventional subtraction approach, since no difference in the RH evolution was observed in loaded and unloaded samples in tension. In my opinion, however, one point is noteworthy here: even though no RH evolution difference, it is insufficient to prove the uncoupling between autogenous shrinkage and creep strain since RH is only a part of all the parameters for creep and autogenous shrinkage. Based on the observations in the literature, it seems necessary to separate the loading conditions and measure in both tension and compression when studying the coupling in the future.

A further complication of this approach is brought about by the fact that self-desiccation and autogenous shrinkage are evolving very rapidly at early ages, so that all care needs to be taken that both loaded and unloaded specimens follow exactly the same curing regime.

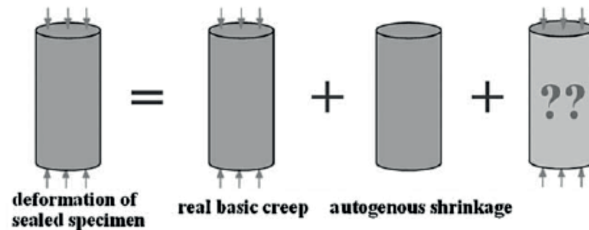


Figure 5.10 Schematic diagram for the possible coupling between autogenous shrinkage and basic creep and the influence on the total creep deformation [51]

Basic creep of cement paste blended with SCMs

The effect of SCMs on the visco-elastic behavior of concrete, which is vital for modern concrete structures in which blended cements are the standard binder, has however received only limited attention in most studies about creep at early ages. Among the few studies that exist, fly ash, slag and silica fume are the mostly investigated SCMs focusing the impact of them on the basic creep compliance. The main observation is that concrete with different mineral additives experiences different creep behavior, especially for the very early ages under loading [78,79]. With the presence of silica fume, for example, the early age creep was found to be increased proportionally to the degree of cement replacement by silica fume. The addition of fly ash also enhanced the development of compliance function [58]. This was not the case for the replacement of cement with slag, which had no significant effect on the development of the compliance function in compression (in tension, higher creep compliance was found also in slag concrete) [58]. This conclusion might be however questioned, since they included also the instantaneous strain reflecting elastic properties (which vary for different SCMs-blends) into account. On the contrary, in reference [57] the basic creep compliance was reduced by the presence of fly ash and slag but not by silica fume and the explanation was the different reactivity of different SCMs. For lack of comprehensive investigations, no clear evidence of the influence of SCMs on the basic creep compliance is available, let alone any credible explanation for their influence. All effects found in the literature were simply and roughly interpreted as originating from the microstructure, the strength or the interfacial properties of the SCMs, without any specific evidence.

5.1.3 Modeling of creep at early ages

Existing models for early age creep

Since the driving mechanism of creep is unclear and fundamental tests are missing, modeling of creep and creep recovery remains extremely challenging. In most common phenomenological models (an-

alytical or rheological), some free parameters in the constitutive equations are derived by fitting experimental creep curves [56,80,81]. Regarding the numerical models, if these are to be built starting from the C-S-H level, they have to currently rely on assumptions and also need a certain degree of fitting. Therefore, it is paramount to establish a model that: 1) has a clear physical meaning for all involved parameters and 2) can be verified with reliable experimental data at the C-S-H level (these data are still missing, as stated in *section 5.1.1*).

The most challenging part for modeling creep at early ages is finding a way to deal with aging. Basically, both phenomenological models and models based on actual physical mechanisms developed in the last decades were trying to account for aging following different approaches. In the phenomenological category models (numerical or rheological models), the shape of the creep curve is the most important concern; in these models, some free parameters in the constitutive equations are always obtained by fitting. Models like power law [80], double power law [82], log-double power law [83] and linear logarithmic law [84] use a parameter which is as a function of loading time or degree of hydration to consider the aging effect, even if most of them were established originally for mature concrete. The general method used for taking the effect of age on the basic creep into account is by expressing the material parameters in the model as functions of the degree of hydration [6]. Time is also being used in some models, but it is not as good as the degree of hydration, because the latter has a clear physical meaning and it is directly related to the material properties of the concrete.

The rheological models such as Kelvin-Voigt, Maxwell chain (including the generalized Kelvin or Maxwell chain) and the Burgers model, usually use aging spring stiffness and dashpot viscosities units that both depend also on either loading time or degree of hydration to introduce the age or time dependency into these models [56,64,81]. The difference between different rheological models is the way to arrange the spring and the dashpot. Naturally, the rheological models are only mathematical approximations of the visco-elastic behavior, without any attempt at simulating the chemical or physical processes of the materials. Some work has been done to identify the stiffness and visco-elastic response of the different components in the cement paste, in order to link the phases properties and the modeling parameters together, giving a physical meaning to the model [85,86]. In [86], the parameters in the Kelvin-Voigt model were related to the interfacial density, interfacial radii and interfacial viscosities. Generalized Maxwell and Kelvin-Voigt models can be transformed into each other with mathematical operations [85], which gives the freedom for selecting any model. Conventionally, Kelvin-Voigt models are easier to use for creep while Maxwell models have advantages when used for relaxation.

Among the models based on actual physical mechanisms, solidification theory [87] (see *Figure 5.11*) and later microprestress-solidification [41] is used widely. The solidification theory ignores the aging effect on creep but considers the volume growth of a non-aging, visco-elastic constituent [62]. An improvement of this theory was obtained by using a flow term in the creep model for dealing with the aging effect [88].

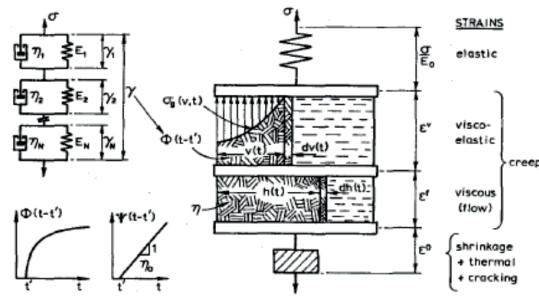


Figure 5.11 Modeling based on solidification theory [87]

Superposition method and incremental method

The superposition method was proposed by McHenry in 1943 [50] for understanding creep of concrete under varying stress. The principle of the method is regarding the reduction in the compressive stress as unloading of compressive stress when estimating creep instead of the application of a tensile stress; it is the most often used method in the literature due to the simplicity of application [89,90]. It is found to underestimate the creep compliance when the applied load is high and to overestimate the creep recovery, because of the assumption that the loading history does not affect the creep compliance rate change [91]. Other useful methods are incremental methods such as the equivalent time method and the fictitious time method [91,92]. These methods were used in the fundamental basic creep model (in [91], a power-law model was used with parameters determined by fitting the experimental data), in which either equivalent time or degree of hydration based formulations were applied. Nevertheless, neither of them is able to successfully predict the creep compliance under successive loading, especially for loading at very early ages [56].

5.2 Methods

Elastic modulus

Elastic modulus tests are used to verify the instantaneous strain part of the creep experiments. At early ages (before 10 d), the Young's modulus was measured continuously with the Elastic Modulus Measurement through Ambient Response Method (EMM-ARM) which was developed by Azenha et al. [93] to follow the kinetics of the elastic modulus development. A hollow tubular beam made of acrylic glass with length of 550 mm, outer diameter of 20 mm and inner diameter of 16 mm was used. The tubes were sealed with polypropylene caps after being filled with fresh paste and placed in a temperature-controlled room at 20 ± 0.3 °C (see Figure 5.12). Then one end of the composite beam was fixed in the horizontal position with a metal clamp, operating as a cantilevered structural system with a span of 450 mm. Afterwards, a lightweight accelerometer (mass and sensitivity equal to 23.25 g and 1 V/g, respectively) was attached to the free end of the cantilever beam. A fan was placed on one side of the beam to increase the amplitude of the vibration.

Quasi-static elastic modulus measurements were performed based on the Swiss standard [94] at specific ages (1, 3, 7, 14, and 28 d) on prismatic samples of size $40 \times 40 \times 160 \text{ mm}^3$ to verify the accuracy of the immediate deformation measured in the creep setups. After demolding at 1 d, the samples were wrapped with multiple, vapor-tight paraffin films and stored in a room with $20 \pm 0.3 \text{ }^\circ\text{C}$ and RH of 90%. A stress-strength ratio of 0.3 was used during the tests and the final results came from the average of two samples.



Figure 5.12 Setup of EMM-ARM

Compressive strength test

The compressive strength of the paste was measured to determine the stress to be applied during the creep measurements. The tests were done on three samples at desired ages (1, 3, 7, 14, and 28 d). Prismatic samples with size of $40 \times 40 \times 160 \text{ mm}^3$ were cast and cut into $40 \times 40 \times 40 \text{ mm}^3$ cubic samples with a diamond saw after sealed curing for one day. All samples were sealed cured in a temperature-controlled chamber ($20 \pm 0.3 \text{ }^\circ\text{C}$) after demolding.

Uniaxial compressive creep

Uniaxial compressive creep tests were performed on pastes using creep frames made of steel and equipped with a lever mechanism, as shown in the schematic diagram in *Figure 5.13*. Specimen of $25 \times 25 \times 80 \text{ mm}^3$ were cast and demolded after 19 h (leaving one hour for the sample preparation before the experiments). They were sealed afterwards with polyethylene film (first layer, in contact with the sample) and self-adhesive aluminum foil (second layer, applied over the plastic film). The samples were labelled and weighed before and after loading, to make sure that negligible weight loss occurred (the average mass loss was less than 0.1 %). Two loading plates (cells) helped to fix the position of the specimen and of the LVDTs. Two small steel balls on each plate allowed to distribute uniformly the load to the loading plates. Three LVDTs are positioned to monitor the displacement of two loading plates before testing (a 2-dimensional simulation with CAST 3M was used to compare the elastic modulus obtained from the displacement between the steel plates and the one of the sample, see *Appendix A*). The load system with dead weights was added manually at the other end of the frame.

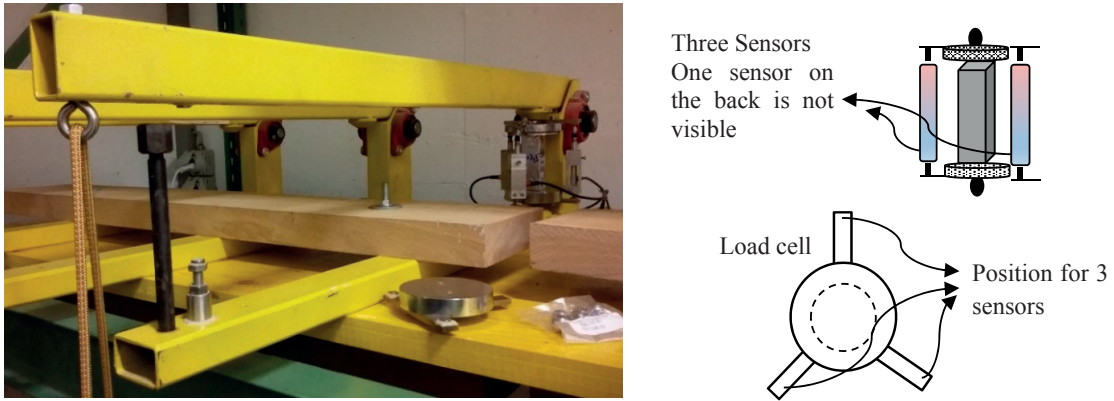


Figure 5.13 Schematic diagram for uniaxial compressive creep tests (left: creep setup for cementitious materials; right: loading cell and samples, side and top view)

Two loading processes were applied in this study: stepwise and constant loading. In the stepwise loading process, the initial load was added at 20 h and successive loads were added onto the same sample at desired ages. In the constant loading process, loads were added only once and removed at desired ages on different samples. The detailed loading steps are shown in Figure 5.14. At each loading time, a total load corresponding to stress-strength ratio of 0.1 was imposed on the samples. The data was logged at the interval of 1 s in the first 15 min during each loading step and 2 min afterwards. Two specimens were used for each loading step to check the repeatability and the sensitivity of the test. The test was performed in a temperature (20 ± 0.7 °C) and relative humidity ($75 \% \pm 1.0$ %) controlled room.

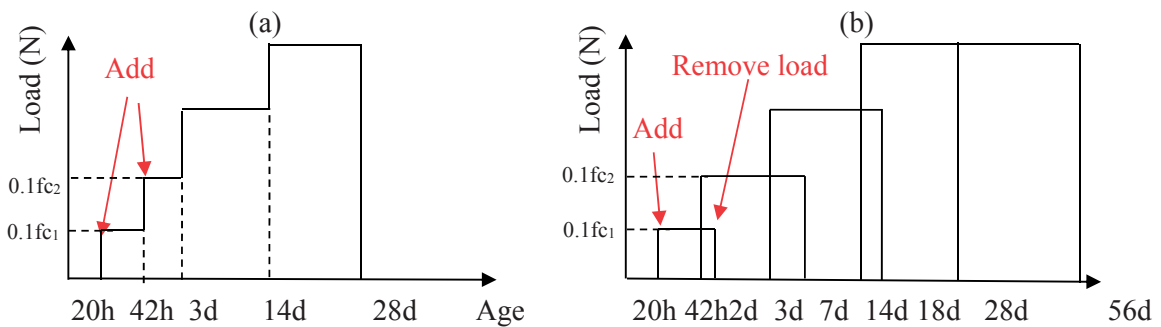


Figure 5.14 Schematic representation of loading steps for different loading histories ((a): stepwise loading process; (b): constant loading process)

5.3 Results

5.3.1 Stress applied

The mean values of three specimens used for each system in a single compressive strength test are presented in *Table 5.1*, together with the standard deviation. The replacement of cement with quartz fillers and fly ash dramatically reduced the compressive strength. While the compressive strength of the two blended systems were almost identical up to 1 week of age, CFA40-0.35 achieved higher compressive strength at later ages. The average standard deviation of all the results is less than 2 MPa. The stress⁵ applied on different systems at different loading time, corresponding to 10% of the compressive strength is then calculated.

Table 5.1 Compressive strength results of three systems

Compressive strength (MPa)	1 d	3 d	7 d	14 d	28 d
Cement-0.35	38.3±0.7	59.3±1.4	71.7±2.0	84.6±2.8	90.3±2.7
CFA40-0.35	16.4±1.7	33.5±2.9	46.4±1.1	53.7±1.2	70.3±1.4
CQZ40-0.35	18.9±0.5	33.9±1.2	44.5±2.1	47.1±1.4	53.6±1.0

5.3.2 Apparent creep strain for hardening pastes

The measured apparent uniaxial creep strain for the three systems at different loading ages is plotted as a function of hydration time in *Figure 5.15*. For each measurement, the overall repeatability between the two measured specimens was considered satisfactory in all cases. The maximum percentage of strain difference between two identical samples was 7 %. Thanks to enough data points, two distinct stages can be distinguished in the curves, with an initial very rapid deformation phase that is usually ending several seconds after loading. These two stages can be associated to the instantaneous elastic (the immediate, linear response of the cement paste to the load) and the visco-elastic part (starting at the end of the elastic part). It is noteworthy that it is not possible to separate completely these components, both because of theoretical and practical issues. First of all, creep already manifests even at the elastic stage, as has been shown in [14]. Secondly, the separation was done manually, such that it may induce a time error of several seconds to several minutes, which is however of minor importance for the final value and for the kinetics of the basic creep compliance.

The rate of apparent creep strain development at different loading ages (20 h, 42 h, 3 d, 14 d and 28 d) varied during the loading process, which is attributable to the hydration process and to the presence of autogenous shrinkage. Note that the autogenous shrinkage was not yet subtracted from these

⁵ The stress calculated at 20 h and 42 h was an approximation from the whole curve of the compressive strength, with the assumption that the compressive strength of the specimens at 0 time equals to zero. It will be more reasonable to assume the compressive strength of the specimens at time of setting equals to zero. In this case, the calculated stress applied will be around 0.3 MPa larger than the stress calculated with previous assumption.

curves, this will be considered later in the calculation of the kinetics of the basic creep compliance. This is also the reason for the reduced creep recovery in Cement-0.35 when unloading the specimen at 2 d, while this effect is not very obvious in the blended systems due to the rather lower autogenous shrinkage comparing to that of the pure cement paste (see *Chapter 3*). The higher total strain of the Cement-0.35 sample is also due to its higher compressive strength, which means higher stress to which these samples are loaded. Besides, the rate of creep strain in CQZ40-0.35 was much flatter than that of the other two systems.

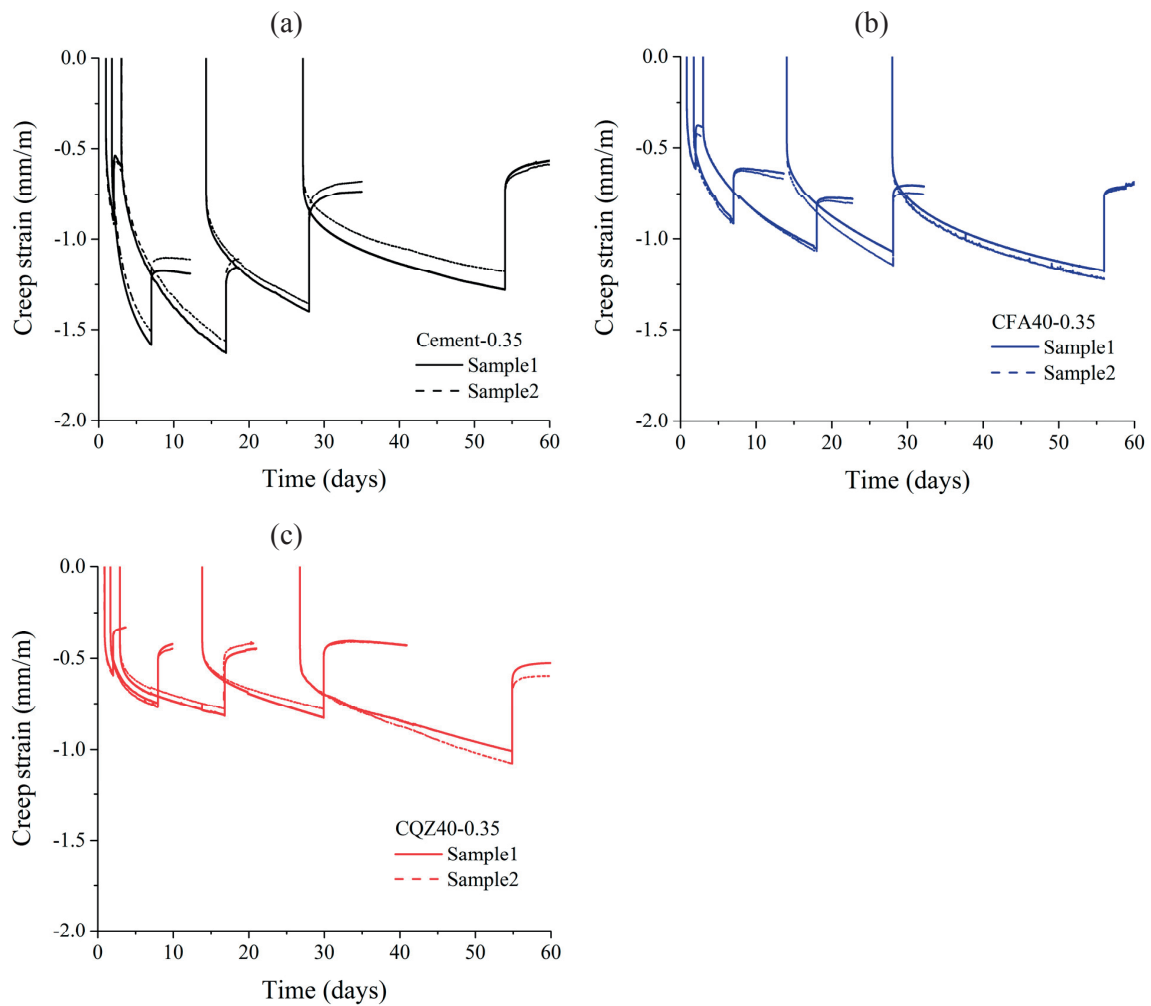


Figure 5.15 Apparent creep strain (including instantaneous strain part) of different systems ((a): Cement-0.35; (b) CFA40-0.35; (c) CQZ40-0.35)

The measured apparent uniaxial creep strain for the three systems under stepwise loading was also plotted as a function of hydration time in *Figure 5.16*. During this loading process, the creep strain was also lower with later loading ages. It is clear from this plot that the strain evolution was gentler

in CQZ40-0.35. The creep recovery was much less than the creep strain in all systems (the residual strain was rather high).

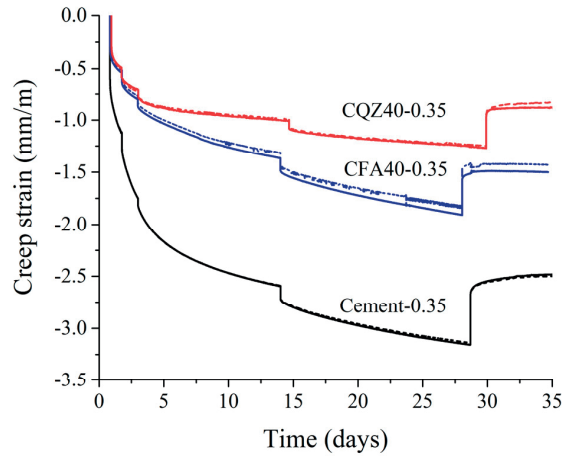


Figure 5.16 Apparent creep strain of specimens under stepwise loading

5.3.3 Instantaneous elastic response

The elastic modulus was calculated based on the instantaneous strain and the applied stress by using the equation below:

Equation 5.2

$$E(t') = \frac{\sigma}{\varepsilon_a}$$

in which $E(t')$ is the elastic modulus, ε_a is the instantaneous strain and σ is the stress applied to the sample. In this study, the elastic modulus calculated based on the instantaneous strain from the creep tests, both under loading and unloading, was compared with the measured elastic modulus from the static elastic modulus tests, as shown in *Figure 5.17*.

The elastic modulus increased as a function of time (i.e., with the hydration process), with high rate at early ages, and it slowed down gradually. For Cement-0.35, the elastic modulus was almost stable after 7 d. For CFA40-0.35 and CQZ40-0.35, a continuous increase of elastic modulus up to 28 d was measured. It is widely accepted that the elastic modulus (similarly to the compressive strength) depends on first approximation on the porosity, while other effects are only secondary, e.g., the degree of hydration of the systems and the amount of the hydration products formed [81]. As evident in *Figure 5.17*, the samples under constant loading showed an average higher consistency as those under stepwise loading. This could be expected, because under the stepwise loading regime, progressively smaller loads are added at later ages, with the consequence of a decrease in the accuracy. For cement paste, the elastic modulus calculated under both constant and stepwise loading is close to or a bit lower than the quasi-static elastic modulus results.

Theoretically, the elastic modulus measured from the instantaneous strain in the creep tests may differ from the quasi-static modulus because: 1) the measured deformation is the displacement of the loading plates, rather than the deformation of the samples (the influence of this point was estimated in *Appendix A*). Specifically, the steel plate will slightly deform due to the central loading. This effect leads to lower deformation of the cement paste samples, since the sensors were placed on the side of the steel plate. The last two reasons will cause higher strain to be recorded; 2) the determination of the end point of instantaneous strain part is not trivial. Part of the visco-elastic deformation may have often incorrectly taken into account for the calculation of the elastic modulus, which results lower elastic modulus calculated out of the instantaneous strain.

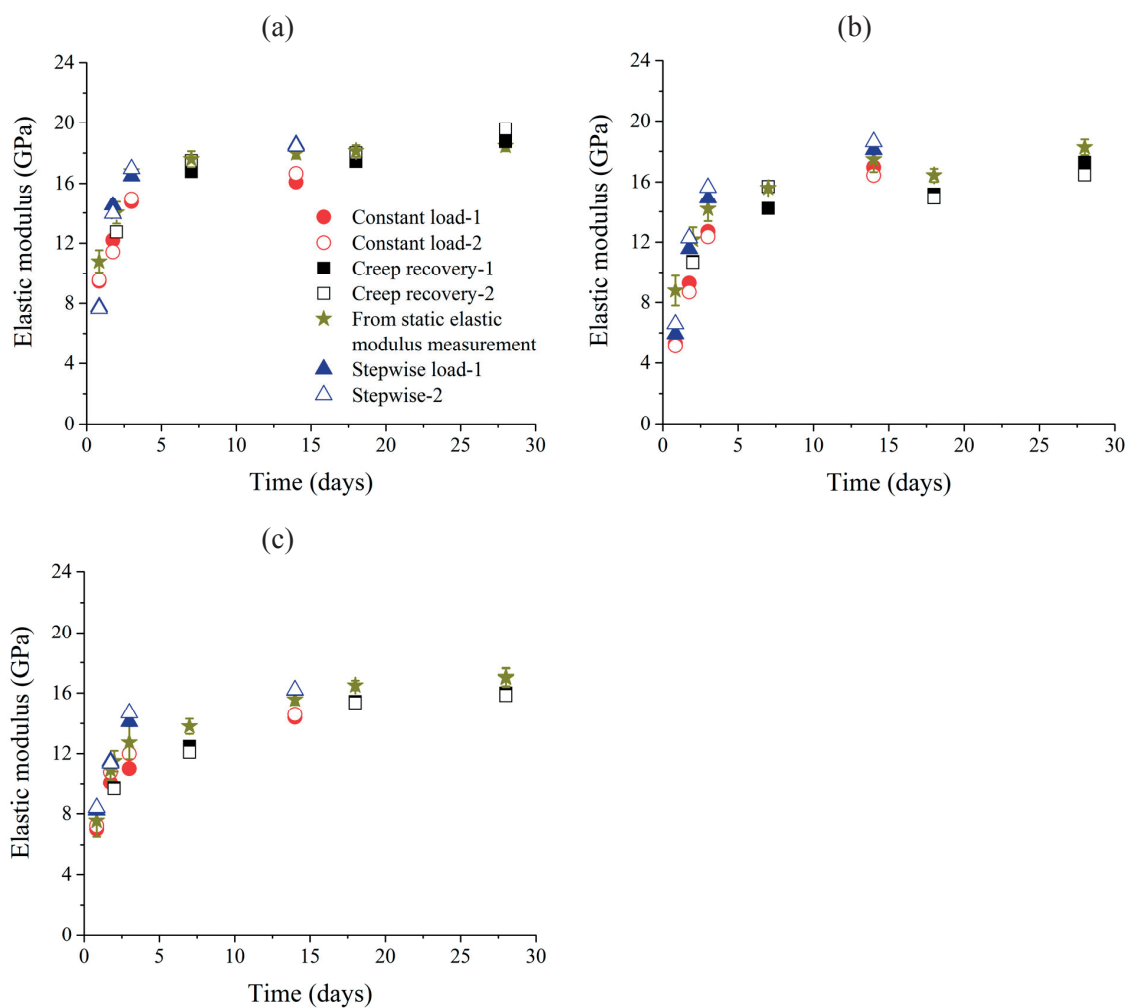


Figure 5.17 Comparison between elastic modulus measured from instantaneous strain and quasi-static elastic modulus measurement ((a) Cement-0.35; (b) CFA40-0.35; (c) CQZ40-0.35)

5.3.4 Basic creep compliance at different loading ages

The subtraction of autogenous shrinkage from apparent creep strain was done using the conventional approach to obtain the basic creep compliance (see *Equation 5.3*). At different loading ages, the average autogenous shrinkage data was zeroed from the time of loading (raw autogenous shrinkage results were shown in *Chapter 3*). After removing the instantaneous strain part, the specific basic creep compliance was calculated by subtracting the free strain (autogenous shrinkage) from the creep strain.

Equation 5.3

$$J_{basic} = \frac{\varepsilon_{bc} - \varepsilon_{as}}{\sigma}$$

in which J_{basic} is the specific basic creep compliance of the sample, ε_{bc} and ε_{as} are the basic creep strain and the autogenous deformation.

The problem of the coupling between autogenous shrinkage and basic creep has been discussed in *section 5.1.2*. It should be noted that, if the coupling exists, a simple subtraction of the measured autogenous shrinkage from the total deformation may introduce an error. If the coupling is an additional creep caused by the capillary pressure or an additional shrinkage caused by the creep, after subtracting, the basic creep compliance will be overestimated in both cases.

The results of the specimens both under constant and stepwise loading are shown in *Figure 5.18*. From the curves, the rate of basic creep compliance decreases with age and cement hydration, obviously for all systems both under stepwise loading and constant loading. At 20 h, all three systems had similar specific basic creep. The results of CQZ40-0.35 were also visibly higher than that of the cement paste before 14 d, while after that age the basic creep compliance of both systems became closer. However, in CFA40-0.35, higher basic creep compliance and higher rate of specific basic creep are evident at later loading ages.

Comparing the results under stepwise loading with those under constant loading at the same loading time, the rate of the specific basic creep compliance was lower in the former loading condition because of the loading history. The difference may be due to the fact that the C-S-H was already under stress (albeit at a lower level) in the stepwise loading regime, while it was unstressed before the only loading step in the constant loading regime. The difference between the two loading regimes was larger for CQZ40-0.35.

Creep was not totally reversible until the end of the experiments. For some systems, it is apparent that the creep recovery reached the end of the evolution and the residual creep would not be any more recovered. From the figure, the recovery percentage depends on the loading ages and on the duration of loading: the earlier the loading ages, the higher is the recovery percentage.

The effect of fillers on the creep compliance can be the result of basically three aspects of the different pastes at different loading ages: the evolution of the elastic modulus, the amount of creeping (C-S-H) and non-creeping (all the rest) phases in the pastes and the porosity [80]. However, it is very challenge to quantify the impact of each factor, since they are interlinked. In the following parts, a qualitative understanding of the dominating or important aspects associated with the effect of loading time and type of fillers on creep compliance will be presented.

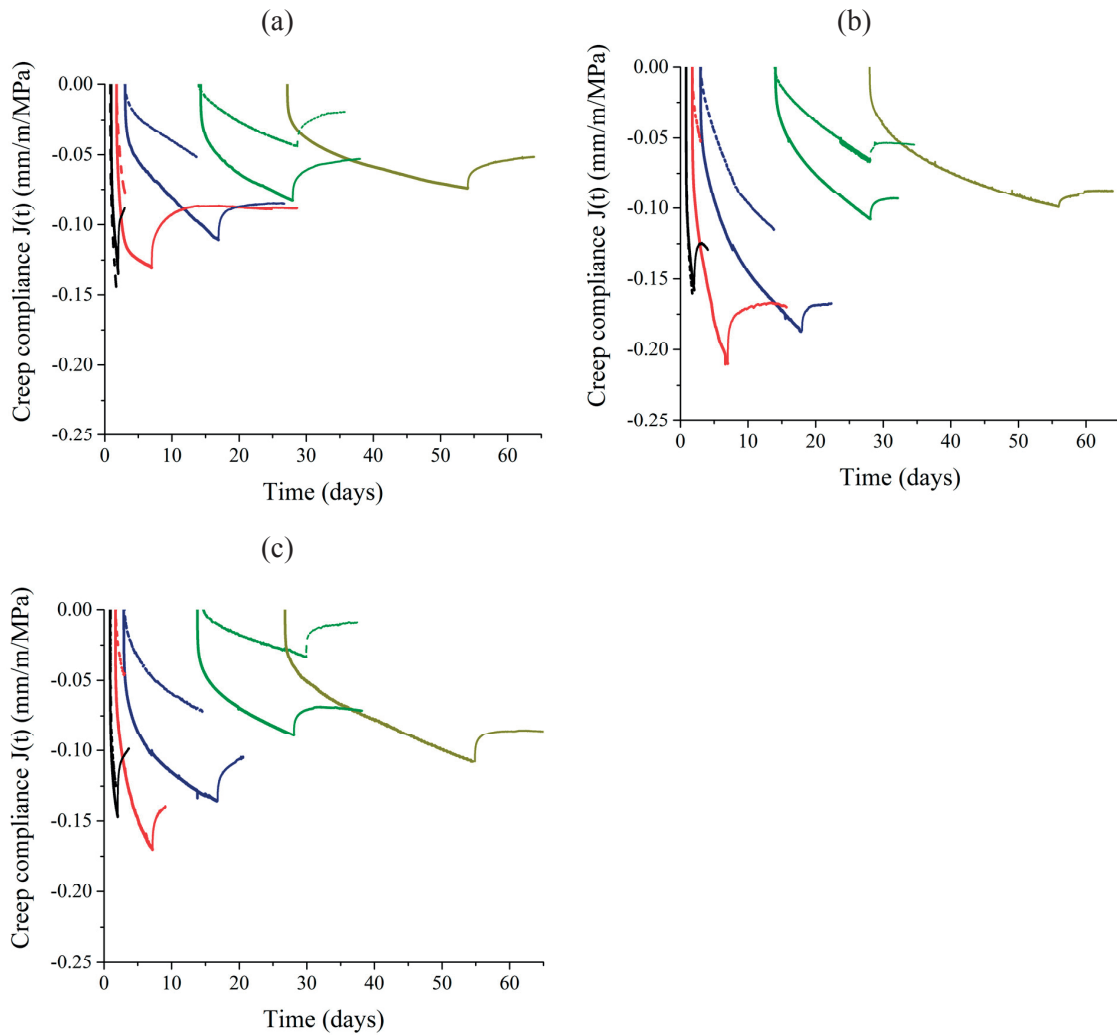


Figure 5.18 Comparison between specific basic creep compliance of the three pastes under two kinds of loading processes (solid line: constant loading; dash line: stepwise loading; (a) Cement-0.35; (b) CFA40-0.35; (c) CQZ40-0.35)

Effect of hydration of cement and reaction of fly ash

In the literature, two main factors linked with the degree of hydration were considered to govern the magnitude of the creep compliance, namely the amount of C-S-H and the porosity.

Up to 7 d, the total heat release is much higher in blended systems, while the total heat at 7 d was similar for CFA40-0.35 and CQZ40-0.35 (see *Chapter 2 and Chapter 7*, same trend as CFA40-0.3 and CQZ40-0.3, continues up to 28 d). According to the evolution of the curves, the evolution in CFA40 and CQZ40 are very similar, while the cement system reached a plateau much faster, which the rate of heat liberation slowing down after 1 d and almost stagnating after 2.5-3 d. Thus in the curve, a clear turning point happened at this age, which seems to correspond to the transition period observed in the creep compliance, see next sections. The degree of hydration evolved slowly after the

initial period (after about 3 d) in the pure cement system, resulting in slow enough formation of C-S-H gel to have a small effect on the kinetics of creep compliance. It is noted that the decreasing hydration speed may be caused by either lack of water, lack of space, or both [96].

For details on the increase of the degree of hydration, the amount of C-S-H and portlandite present in the hydrating pastes, see *section 2.5.3*. Due to the filler effect, in CQZ40-0.35, cement hydration was accelerated with more C-S-H nucleation sites in the system and higher effective w/c. However, comparing the volume fraction of C-S-H in the system, CQZ40-0.35 contained less total C-S-H by volume and thus less creeping phases.

The reaction of fly ash resulted in a decrease of the portlandite. About the effect of fly ash on creep compliance, previous studies show that at later ages, the creep compliance of fly-ash-blended concrete was lower than that of Portland cement concrete, but at early ages the situation is unclear [97,98]. Theoretically, the reaction of fly ash under stress may contribute to the increase of the creep compliance due to removing of some stressed restraints (the fly ash particles themselves). Additionally, the reaction of fly ash will result in more C-S-H (creeping phases) and also dissolve stressed portlandite crystals [99]. These mechanisms could potentially increase the creep compliance, even though the degree of reaction of the fly ash may be limited.

Another factor associated with the degree of hydration is the porosity. Many papers mentioned the effect of porosity on the creep compliance evolution, however without proposing a clear mechanism and without providing convincing evidence. In *Figure 5.19*, the total porosity (from MIP) as a function of hydration time is presented. A valuable piece of information from the figure is that in the pure cement paste, the porosity is decreasing only very slowly after 3 d, which corresponds well with the transition period in both creep compliance and elastic modulus mentioned before.

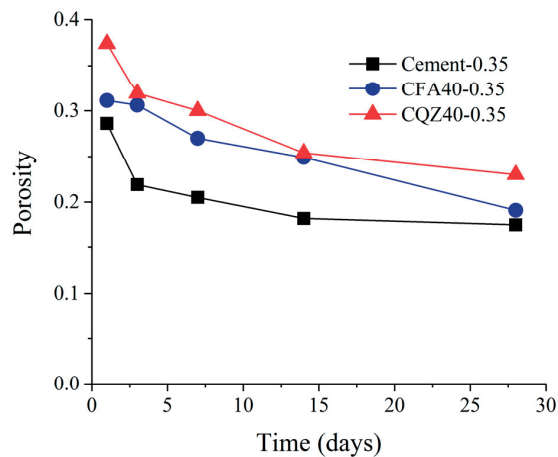


Figure 5.19 Porosity evolution of both systems measured by MIP as a function of time

Effect of the evolution of elastic modulus

From the mechanical point of view, the elastic properties will affect the total visco-elastic behavior. The elastic modulus evolution of the systems by EMM-ARM was plotted in *Figure 5.20 (a)*. The

results from EMM-ARM were close to quasi-static elastic modulus (see *section 5.3.3*) as presented in [93]. In Cement-0.35, the elastic modulus increased faster at early ages and reached a stable or final value earlier. Comparing to the development of elastic modulus of CFA40-0.35 and CQZ40-0.35, Cement-0.35 had similar elastic modulus at 11 d but with a completely different process. At the same time, the elastic modulus of CFA40-0.35 and CQZ40-0.35 was increasing gradually within the first two weeks and there was not much difference between them. Interestingly, quartz and fly ash, despite having different stiffness, turned out to have the same effect on the overall elastic modulus. Also in [100,101], equivalent systems containing quartz filler had the similar elastic modulus as mortars with unhydrated cement.

An explanation for the lower creep compliance observed at later loading ages could be the stress distribution between creeping (visco-elastic) and non-creeping (elastic) phases in a cement paste. When the load is applied, the load is distributed between these phases. When the dashpot creeps, the load will be distributed back to the elastic phases, with the global effect that the creeping phases will be subjected to a lower stress within the microstructure and ultimately show less creep if the elastic phases are stiffer [102].

For the effect of fillers, theoretically, the restraint effect of quartz in the cement paste is expected to be higher than that of fly ash and also hydrated phases with only pure cement. This issue should however not be considered without the contribution of other factors, e.g., of the porosity. Apparently, however, the restraint effect of quartz should not be the dominating reason for the variation of the creep compliance, since the elastic modulus of quartz-blended and fly-ash-blended systems was similar (see *section 5.3.3*). Because of the lower elastic modulus of the blended systems compared to the system with pure cement, the creep is more pronounced, as shown in the experimental data.

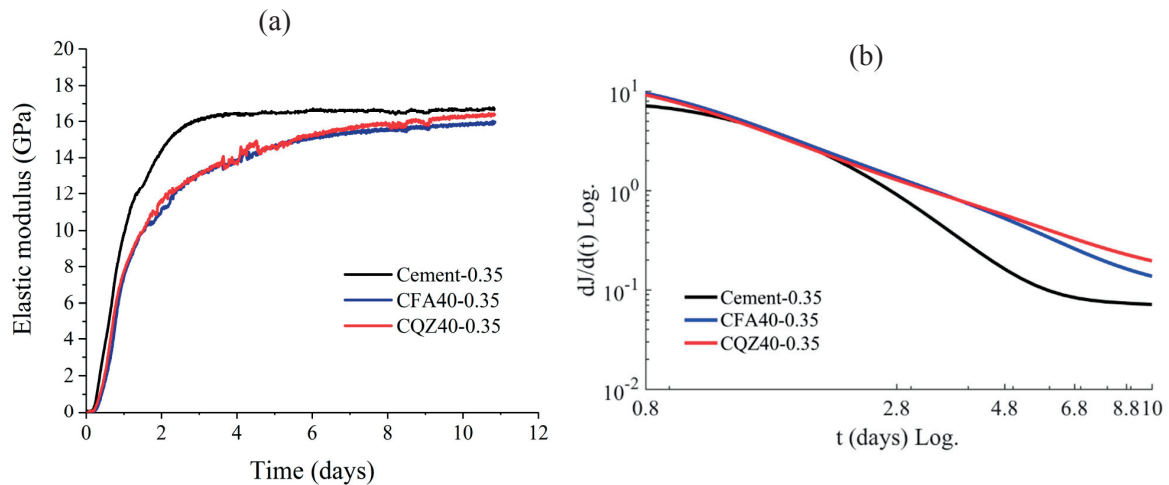


Figure 5.20 The evolution of elastic modulus of the three systems based on EMM-ARM ((a) is the elastic modulus evolution of the three systems; (b) is the analyzed kinetics of the elastic modulus)

In Figure 5.20 (b), using the Tikhonov regularization method [103] to analyze the kinetics of the elastic modulus development, a similar transition period was evident during the same ages (2.5 to 4

d) as for the kinetics of the basic creep compliance. It can be hypothesized that the evolution in the elastic modulus during this period may be also the cause of the changes in visco-elastic behavior observed during this transition. Apparently, since the system became stiffer quickly between 2.5 and 4 d, the rate of creep compliance decreased also rapidly due to the higher elastic modulus of the solid skeleton (see the argument about redistribution of the stresses in the specimen presented above). When the elastic modulus was plotted as a function of cumulative heat release in the three systems (see *Figure 5.21*), a turning point can also be seen in the cement system, which cannot be detected easily in CQZ40-0.35 and CFA40-0.35.

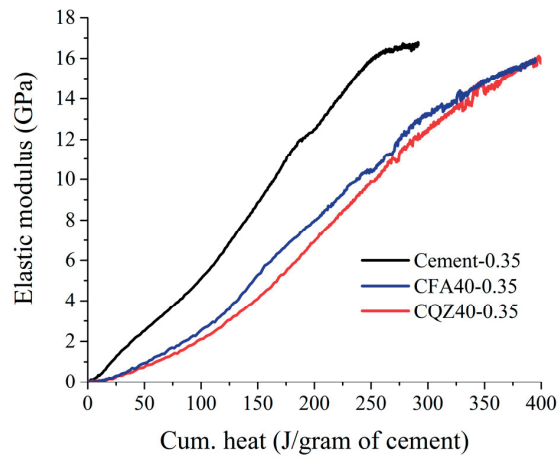


Figure 5.21 The relationship between cumulative heat and elastic modulus in the three systems

5.4 Power law expression

5.4.1 Kinetics of creep compliance

Tikhonov regularization with 10-fold technique was used to trace the kinetics of the basic creep compliance based on the average of two basic creep compliance results. This approach yields smooth and clean curves compared to direct derivation. The reason for using $t-t_0$ rather than t is because it is advantageous to trace the creep variation during the first very short time under load. The kinetics (or rate) of creep compliance under constant loading are almost linear with time in a log-log plot (see *Figure 5.22*).

Compared to the linear trend of the kinetics of creep compliance obtained in the literature by fitting discrete points [80], the method used here is much more precise and clear. As is also shown in *Figure 5.22*, the kinetics of creep compliance in the samples under stepwise loading also show linear dependence on time in a log-log plot. For different loading times, the kinetics evidence the same trend, which indicates similar basic creep behavior as reported in the literature for both cement paste and concrete [37,42,43]. The small variations and inconsistencies observed immediately after loading are likely due to unstable loading or imprecise deformation measurements at the beginning of each loading step.

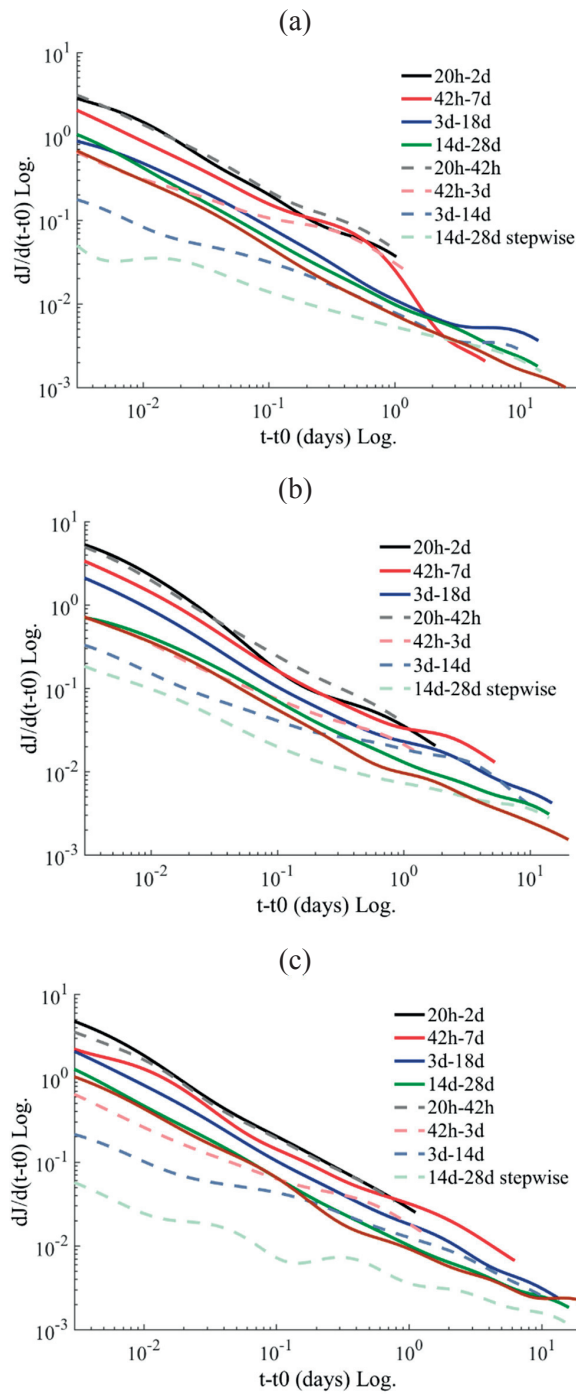


Figure 5.22 Kinetics of creep compliance of pastes under constant and stepwise loading (solid lines are results from samples under constant loading regime while dashed lines are results from samples under stepwise loading regime, (a) Cement-0.35, (b) CFA40-0.35; (c) CQZ40-0.35)

As evident from the results shown in Figure 5.22, the same equation can be used to express the loading time and the kinetics of creep compliance for samples both under stepwise and constant loading

regime. The only notable exception is observed for the kinetics of creep compliance of the pure cement paste loaded constantly at 42 h to 7 d. A clear transition period was observed when the load was kept constant between 42 h and 7 d. The slope of the curve within this interval was close to that of samples loaded earlier. In a first stage (from loading to around 2.5 d), the rate of creep compliance decreased linearly as a function of loading time ($t-t_0$). In a second stage (from 2.5 d to 4 d), the kinetics decreased sharply with loading time. In a final stage (after 4 d), the decrease of the rate of creep compliance slowed down, similarly to samples loaded later. In other words, to characterize the visco-elastic behavior (short-term or long-term behavior): before the observed transition period, the creep compliance is strongly affected by aging; after this critical period, the visco-elastic behavior is much less dependent on aging.

The amplitude of the rate of creep compliance decreased with later loading ages in all systems, indicating a close relationship between amplitude, loading ages (effect of hydration degree) and history. The effect of loading history becomes clear when comparing data from samples under constant and stepwise loading. Comparing the slopes of creep compliance at different loading time, the slopes are visibly similar. The rate of creep compliance for loads imposed at the same ages in the stepwise and constant loading regimes tended to reach the same value. The time for reaching the same rate of creep compliance is different depending on the age of loading as well, which means that cement hydration does have an important influence.

5.4.2 Power law expression

Based on the shape of the experimental curves, a power law can be conveniently used to fit the evolution of the kinetics of the basic creep compliance for most of the systems. When the amplitude and the slope are determined by best fit of the experimental results, a simple equation (*Equation 5.4*) with limited parameters can be established. By solving *Equation 5.4*, *Equation 5.5* gives an expression for the kinetics of creep compliance. In order to determine the trend of parameters A and C , the data calculated from the previous section will be used.

Equation 5.4

$$\ln J'(t-t_0) = C \cdot \ln(t-t_0) + k$$

Equation 5.5

$$J'(t-t_0) = A \frac{1}{(t-t_0)^{-C}}$$

in which A [$\text{mm/m/MPa} \cdot \text{d}^{C-1}$], C [-] and k are constant, $A = e^k$.

The amplitude A is representing J_0' , which is the creep compliance rate at t_0 . Note that before using the expression for obtaining the fitting parameters, the first 14.4 minutes ($t-t_0 \geq 0.01$ d) of each experiment were excluded to avoid the effect of the error from determination of starting point of creep compliance. According to *Figure 5.22*, A was smaller for later loading times, especially at early ages. For instance, A of Cement-0.35 loaded at 20 h was much larger than that at 3 d (0.035 vs. 0.015). After 3 d, the amplitude was stabilizing until it became about 0.01 at 28 d. This evolution of the

amplitude appeared to parallel the evolution of the degree of hydration. Furthermore, the loading history appeared to have some impact on the value of A : samples under stepwise loading regime systematically showed lower amplitude. In order to quantify the effect of loading history, the amplitude A is listed in *Table 5.2* at different loading ages.

Table 5.2 Amplitude value of the linear relationship between the rate of creep compliance and time

A value	20h-2d	42h-7d (1) *	42h-7d (2) *	3d-18d	14d-28d	28d-56d
Cement-0.35	0.035	0.037	0.015	0.015	0.011	0.009
CQZ40-0.35	0.028	0.020	-	0.018	0.011	0.011
CFA40-0.35	0.033	0.038	-	0.023	0.014	0.010

* For the Cement system, the kinetics of creep between 42 h and 7 d need to be fitted in two parts because of the previously-mentioned transition.

The slope C was fitted by the least squares method after the first 14.4 minutes after loading were removed. The slope values for all the loading time were listed in *Table 5.3*. For the cement system, the slope of the kinetics does not change significantly for different loading ages and the value is always around 0.7. For the quartz-blended system, the slope can be seen decreasing (in absolute value), from 0.87 to 0.67. In the literature, slopes around -0.82 to -0.85 were generally found for concrete. According to Tamtsia et al. [80], the slope of the creep compliance rate was influenced by the w/c through the degree of hydration. Normally, when considering t instead of $t-t_0$, also for cement concrete, creep compliance rates around -1 can be found [9].

As shown in *Table 5.3*, results in this thesis demonstrate that the loading history has a significant influence on the kinetics of creep compliance, especially on the amplitude. This different amplitude is a possible reason for the overestimation of creep compliance in the literature at short-term, which is caused by the higher amplitude in the constant loading. The data obtained in this study suggests that it is possible to establish a relationship between the creep compliance under stepwise and constant loading. The main finding in this respect is that, after a short time, the final rate of creep compliance in both cases reached the same value.

Table 5.3 Slope of the linear relationship between rate of creep compliance and loading time

C value	20h-2d	42h-7d (1) ⁶	42h-7d (2)	3d-18d	14d-28d	28d-56d
Cement-0.35	-0.73	-0.70	-0.75	-0.64	-0.72	-0.75
CQZ40-0.35	-0.87	-0.87	-	-0.78	-0.79	-0.72
CFA40-0.35	-0.72	-0.62	-	-0.63	-0.64	-0.75

⁶ For the Cement system, the kinetics of creep during 42 h to 7 d need to be fitted in two parts because of the previously-mentioned transition.

5.4.3 Back calculation of the creep compliance

This representation of the results in *section 5.4.1* highlights that the kinetics of creep can be modeled by a power-law equation (*Equation 5.5*). In order to verify the accuracy of this power-law expression, the specific basic creep is therefore calculated as follows in *Equation 5.6* and compared with the measured creep compliance in Cement-0.35 (as discussed in the previous section, this system has the largest variation of the kinetics and is more complex, with the presence of a transition period).

Equation 5.6

$$J(t-t_0) = \frac{A}{1+C} \times (t-t_0)^{1+C} + B$$

The constant B [mm/m/MPa] can be determined with the following equation:

Equation 5.7

$$J(t-t_0) = J_{measured}$$

where: $J_{measured}$ is the measured specific basic creep. By using the determined parameters by regression analysis in *section 5.4.2*, the comparison of the measured and calculated creep compliance based on *Equation 5.6* for Cement-0.35 under constant loading was shown in *Figure 5.23*. From the figure, the strain evolution is accurately estimated with the power-law equation for all the loading ages, with B equal to 0. The value of this parameter reflects the degree of inability of the power-law model to describe this part of the creep strain. Two factors can explain it. The first one was already mentioned, it is linked to the duration of the loading process. Another explanation is that the loading process is quasi-instantaneously followed by an increase of the internal relative humidity [27]. This phenomenon induces a swelling. However, this effect is quasi-immediate; therefore, the inadequacy of the power-law for very short-term creep should be mainly linked to the first reason. The transition period was set to start at 2.5 d. This comparison confirms that the largest part of the basic creep strain is governed by a power-law equation during this period of loading.

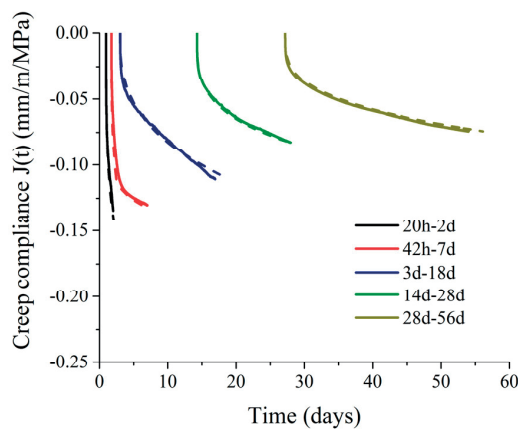


Figure 5.23 Comparison between the back-calculated creep compliance (dashed line) and the measured creep compliance (solid line) under constant loading

5.5 Creep recovery

The creep recovery plot is clearly impacted by the autogenous shrinkage (in these low w/c systems, autogenous shrinkage is particularly pronounced) especially at early ages. For instance, in *Figure 5.15*, the creep recovery of cement paste shows a steeper development with increasing compliance when loaded at 20 h. This behavior is less and less visible at later ages, due to the evolution of self-desiccation. With the replacement of quartz and fly ash, the effect of self-desiccation is less significant as well. Meanwhile, according to the results, the development of creep recovery had similar behavior as the basic creep, showing higher values at early ages. The kinetics of creep recovery for all systems is presented in *Figure 5.24*.

The ratio between the basic creep recovery strains after 1 d (ϵ_r) or 2 d (ϵ_{r2}) at all loading ages and the basic creep strains at loading ages (ϵ_c) at the corresponding ages are shown in *Table 5.4*. From *Figure 5.24*, the creep recovery at some ages reached a sharp decrease of kinetics (in other words, the creep recovery reached a plateau) but this was not observed in all cases. Therefore, the comparison in *Table 5.4* cannot be shown as the ratio of total irreversible creep and the final basic creep strain but can still give an idea of the speed of the recovery and the irreversible part of creep evolving. Cement-0.35 and CQZ40-0.35 had similar ϵ_r / ϵ_c and $\epsilon_{r2} / \epsilon_c$, while CFA40-0.35 showed lower values. There was no clear trend for creep recovery with hydration time. Nevertheless, these results show the dependence on creep strain under loading, loading duration and microstructure differences [64,92,106]. In this study, the ratio ϵ_r / ϵ_c decreased as a power law with time. But it should be noted that, when the loading time is 20 h, the loading duration is perhaps too short, which can also be a factor for creep recovery.

The slope of the rate of creep recovery was calculated based only on the data before the sharp decrease, as shown in *Table 5.5*. Generally, the creep recovery is thought to have similar development as the creep evolution under loading, but it has a much lower value and stabilizes quickly [91,106]. The evolution is also plotted in *Figure 5.25*. Here, different aspects can be identified: 1) the slope C was rather stable for the systems at different loading ages (the variation is below ± 0.05); 2) the slope of the creep recovery was higher than the slope in creep, which may possibly indicate that different mechanisms are acting during creep and creep recovery; 3) the slopes for all systems were close to -0.8.

Note that the creep compliance calculated based on the creep recovery is using the same stress as the load applied before unloading. A linear equation can also be used to link the time and kinetics of creep recovery for samples both under stepwise and simple loading process. Moreover, the slope of the creep recovery was always around -0.75 to -0.85, which is not far from that of creep under load. Upon closer examination, two stages can be identified in the curves. In a first stage, the kinetics of creep recovery decreased with a constant slope of about -0.8. This slope was slightly different from system to system; for instance, for CFA40-0.35 the slope was larger. However, in a second stage, the kinetics of creep recovery decreased sharply with time. At this stage, the creep recovery reached a plateau with a very small rate of change. In *Table 5.5*, the calculation was made based on the first stage.

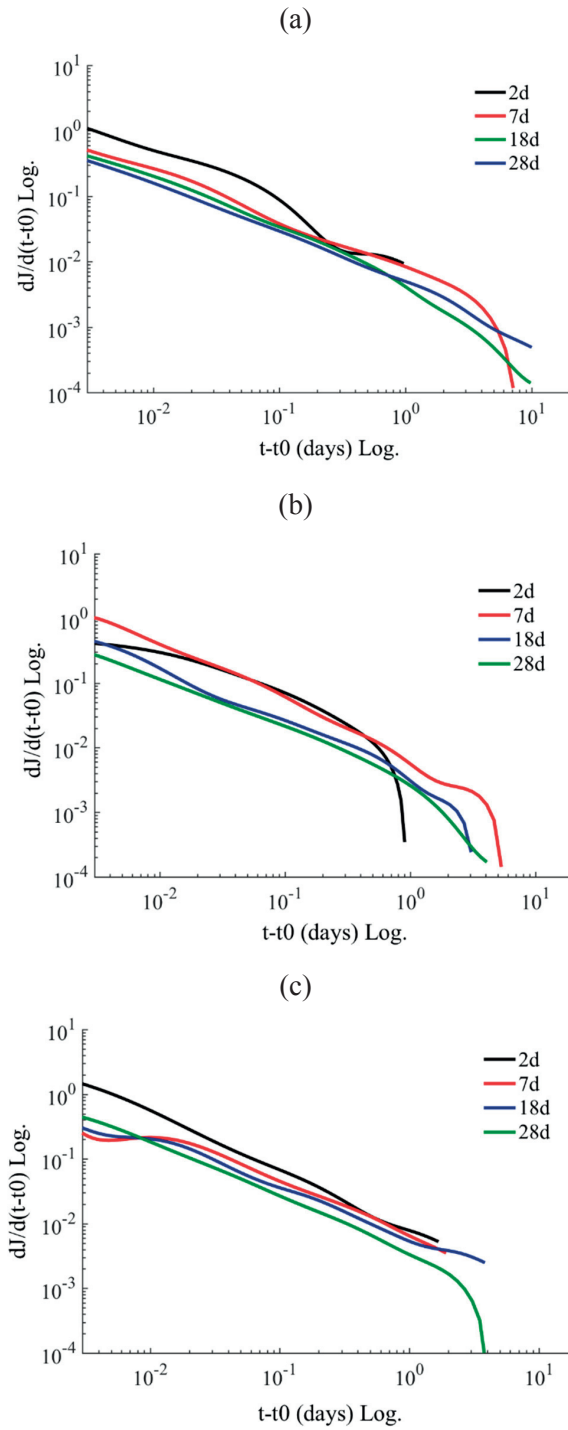


Figure 5.24 Kinetics of creep recovery of the three pastes ((a) Cement-0.35; (b) CFA40-0.35; (c) CQZA0-0.35)

Because of the increase in degree of hydration and the reduction of porosity during the creep tests, the modulus of elasticity is greater during creep recovery than at loading. The elastic recovery was

74 % to 93 % of the elastic deformation at loading. In the literature, it was observed that the type and quantity of fly ash had no appreciable effect on creep recovery [107].

Table 5.4 Strain ratio between creep and creep recovery

Loading time	Cement	CQZ40	CFA40	Cement	CQZ40	CFA40
	$\varepsilon_r / \varepsilon_c$	$\varepsilon_r / \varepsilon_c$	$\varepsilon_r / \varepsilon_c$	$\varepsilon_{r2} / \varepsilon_c$	$\varepsilon_{r2} / \varepsilon_c$	$\varepsilon_{r2} / \varepsilon_c$
20 h	0.34	0.30	0.17	-	-	-
42 h	0.20	0.16	0.22	0.25	0.18	0.24
3 d	0.18	0.15	0.09	0.20	0.18	0.09
14 d	0.21	0.17	0.11	0.25	0.20	0.13

Table 5.5 Slope of the linear relationship between the rates of creep recovery compliance vs. time

Slope value	2 d	7 d	18 d	28 d	56d
Cement	-0.84	-0.79	-0.93	-0.76	-0.81
CQZ40	-0.88	-0.84	-0.69	-0.80	-0.86
CFA40	-0.72	-0.91	-0.87	-0.85	-0.67

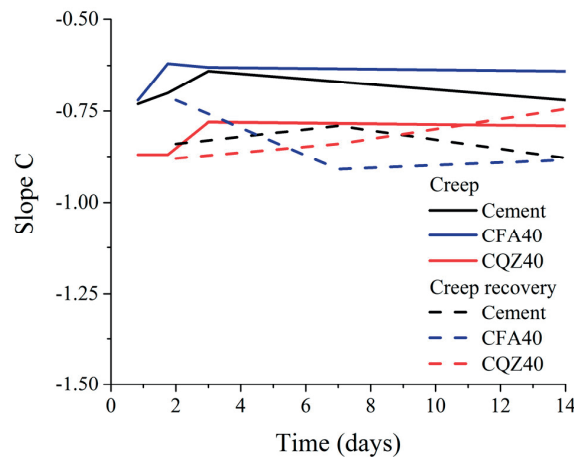


Figure 5.25 Evolution of the slope C as a function of time

5.6 Rheology modeling

A generalized Kelvin-Voigt model, which is constructed with a number n of Kelvin-Voigt units in series, was used to represent the visco-elastic behavior of the pastes. n equals 3 in this chapter, in order to be able to represent both short-term and long-term creep. Each Kelvin-Voigt unit can be de-assembled into a spring and a dashpot. In particular, the model employed in this section was a time-dependent (or degree of hydration-dependent) generalized Kelvin-Voigt model with three units and an additional dashpot. A similar solving method as detailed in [64,65] was used (see Figure 5.26).

The Kelvin-Voigt units can be used to model the short-term mechanism, e.g., micro-diffusion; the additional dashpot can represent the sliding of the C-S-H in the long term, which is proportional to time (or degree of hydration) in the model. The differences between the dashpot and the Kelvin-Voigt units are that the former is totally irreversible, while the latter are totally reversible. Theoretically, the accuracy will be increased when introducing a dashpot, especially for the recovery prediction and the long-term creep prediction. The description of the coefficients in the models are identified as follows:

$E(1, 2...n)(t)$ [MPa] is the aging moduli of the springs in individual Kelvin-Voigt unit. t is the characterization time. $\eta(1, 2...n)(t)$ is the viscosities of the dashpot in the corresponding Kelvin-Voigt unit. The additional dashpot has viscosity η_0 . As the property of the Kelvin-Voigt chain, the stress in each Kelvin-Voigt unit is the same as the total stress, in symbols $\sigma = \sigma_1 = \sigma_2 = \dots = \sigma_n$ [MPa]. In the creep case, the principle of the modeling procedure is approximating the resulting strain with constant stress at each time step (i) based on the *a priori* choice of the number of n and the retardation (or the relaxation time in relaxation) $\tau(1, 2...n)$ [d]. The strain in the Kelvin-Voigt unit is represented as $\varepsilon_{kv}(1, 2...n)(t)$ and the strain in the additional dashpot is shown as ε_{am} . In next part, more on the relationship between the coefficients (with the solution of the stress and strain, the creep compliance can be calculated) and the evolution of the coefficients with time or degree of hydration will both be presented.

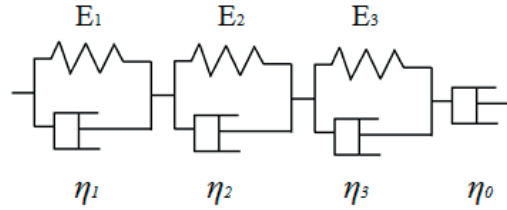


Figure 5.26 Kelvin-Voigt model used in this thesis, 3 units generalized Kelvin-Voigt with an extra dashpot

For each Kelvin-Voigt unit, a set of governing equations are presented as follows [65]:

Equation 5.8

$$\dot{\varepsilon}_{kv} = \frac{\sigma_{n\eta}}{\eta_n(t)}$$

Equation 5.9

$$\dot{\varepsilon}_{kv} = \frac{\dot{\sigma}_n - \dot{\sigma}_{m\eta}}{E_n(t)}$$

With the relationship between the viscosity of the dashpot and the stiffness of the spring: $\eta_n(t) = E_n(t) \times \tau_n$ and the constant retardation time τ_n for each Kelvin-Voigt unit, the two equations can be transformed into a second-order differential equation as follows:

Equation 5.10

$$\tau_n \cdot \ddot{\varepsilon}_{kv} + \left(1 + \frac{\dot{E}_n(t)}{E_n(t)} \cdot \tau_n \right) \cdot \dot{\varepsilon}_{kv} = \frac{\dot{\sigma}_n}{E_n(t)}$$

With this equation, the stress and strain in each individual Kelvin-Voigt unit at each time step was linked together. The extension of the relationship to solve the 3-dimensional (3D) problem can be seen in [65], where the visco-elastic Poisson's ratio is introduced. The detailed numerical algorithm for the strain increment for each Kelvin-Voigt unit is shown in [65], resulting in Equation 5.11, see the formula derivation in Appendix B. The stress in the dashpot $\eta(1, 2...n)(t)$ needs also to be updated in each discretized time step, see Equation 5.12. The whole numerical scheme flow chart for individual Kelvin-Voigt unit is presented in Figure 5.27. The deformation of the additional dashpot was added to the first Kelvin-Voigt unit and the total strain was calculated based on Equation 5.13. The ε_{am} is numerically determined with a log expression.

Equation 5.11

$$\Delta \varepsilon_{nkv}^i = \frac{\sigma_{\eta}^i}{k_{nkv}^i} \cdot \left(1 - e^{-\frac{-\Delta t_i}{\bar{\tau}_n^i}} \right) + \left(\sigma_n^{i+1} - \sigma_n^i \right) \cdot \frac{1}{k_{nkv}^i} \cdot \left(1 - \frac{\eta_n^i}{k_{kv}^i \cdot \Delta t_i} \cdot \left(1 - e^{-\frac{-\Delta t_i}{\bar{\tau}_n^i}} \right) \right)$$

where k_{nkv} is equal to $E_n + \dot{E}_n \times \tau_n$ and $\bar{\tau}_n$ is equal to $\tau_n / (1 + \dot{E}_n / E_n \cdot \tau_n)$

Equation 5.12

$$\sigma_{n\eta}^{i+1} = \eta_n^{i+1} \cdot \left(\frac{\sigma_{n\eta}^i}{\eta_n^i} \cdot \left(1 - \frac{k_{nkv}^i \cdot \Delta t_i}{E_n^i \cdot \tau^i} \right) + \frac{\dot{\sigma}_n^i}{\eta_n^i} \cdot \Delta t_i \right)$$

Equation 5.13

$$\varepsilon_{bc} = \sum_1^n \varepsilon_{nkv} + \varepsilon_{am}$$

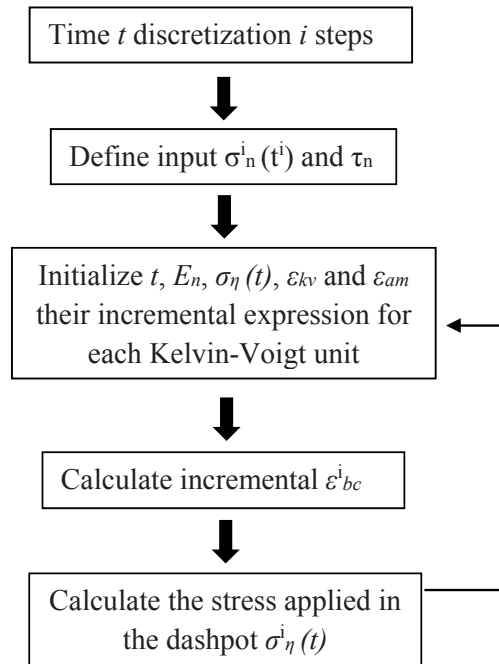


Figure 5.27 Numerical scheme for the strain increment

Fitting parameters

A dashpot and three Kelvin-Voigt units with three constant retardation time τ_n and $E(I, 2\dots n)(t)$ values that were evolving with the relationship with $E(I, 2\dots n)(t=\infty)$ which was determined based on the creep of the specimens loaded at 28 d. The reason for using data at 28 d for the final values (at time infinite) is because the hydration of the specimen after 28 d was really small and the creep evolution was also much more stable (the difference between the kinetics of creep compliance of the specimens loaded at 14 d and 28 d were not very significant). Only the final prediction results are shown for the other two systems. Next, the least squares method was used to determine the fitting parameters $(E(I, 2\dots n)(t)$ for different loading ages).

The expressions used for ϵ_{am} in the model were as follows, as the function of the degree of hydration and initial porosity according to [108]:

Equation 5.14

$$\Delta\epsilon_{am} = \frac{\sigma_n^i + \sigma_n^{i+1}}{2} \times \ln\left(\frac{t_{i+1}}{t_i}\right) \div \eta_0$$

$$\eta_0 = \frac{\eta_\infty \cdot t}{1 - \sqrt{(1-p_0) \cdot (1-\alpha)}}$$

where: p_0 is the initial porosity, α is the degree of hydration.

The selected τ_n , $E(I, 2\dots n)(t=\infty)$ and η_∞ for Cement-0.35 are presented in Table 5.6.

Table 5.6 Fitting parameters for Cement-0.35 in the Kelvin-Voigt model

Unit number	Chain 1	Chain 2	Chain 3
τ_n (days)	0.01	0.1	1.0
$E(1, 2\dots n)(t=\infty)$ (MPa)	99	93	85
η_∞ (MPa)	20.0		

In Figure 5.28, the evolution of E_n in the modeling of creep of Cement-0.35 is demonstrated. The important goal is to make the evolution of the value smooth and continuous. With the parameters presented in the Table 5.6 and Figure 5.28 (for the other two systems as well), the results of fitting creep compliance under constant loading for three systems are shown in Figure 5.29, Figure 5.30 and Figure 5.31, respectively. The degree of hydration was obtained from Chapter 2 by isothermal calorimetry. As shown in the figures, the results from the generalized Kelvin-Voigt chain give a reasonably good fit of the experimental data. A significant difference is observed in Cement-0.35 at loading age of 3 d. In this test, a transition happens which cannot be fitted with a continuous change of E_n .

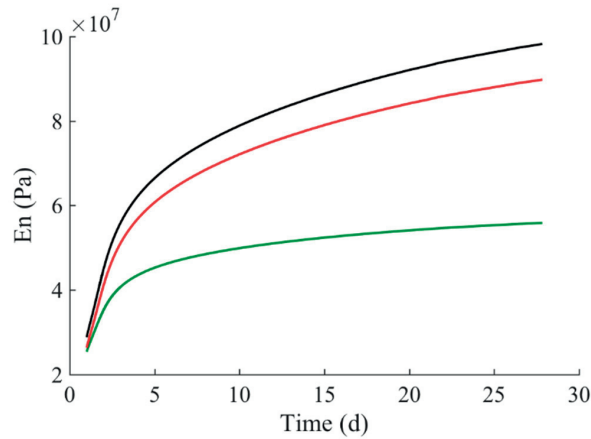
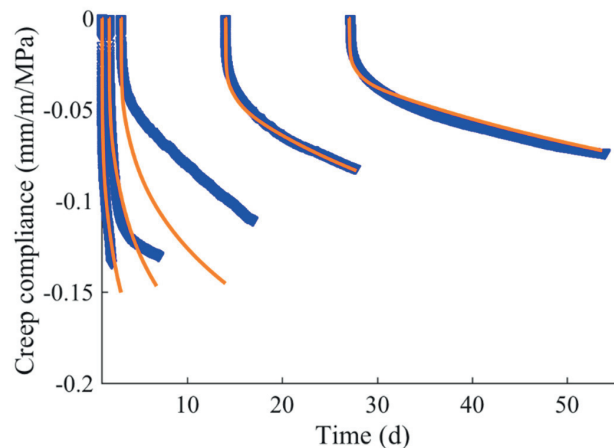
Figure 5.28 Evolution of E_n in the prediction of Cement-0.35, green is E_1 ; black is E_2 ; red is E_3 

Figure 5.29 Comparison of the predicted and measured creep compliance in Cement-0.35 (orange are predictions, blue are measured results)

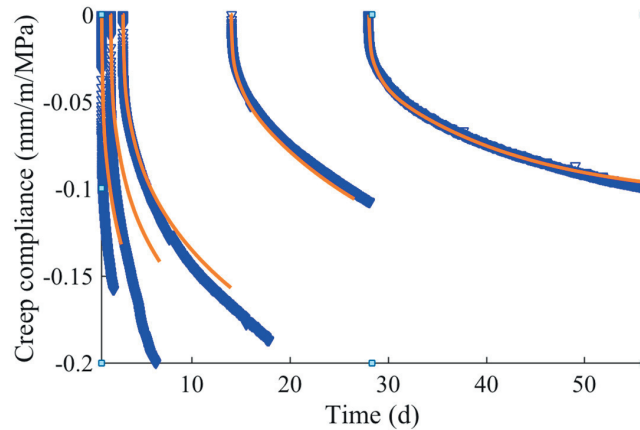


Figure 5.30 Comparison of the predicted and measured creep compliance in CFA40-0.35 (orange are predictions, blue are measured results)

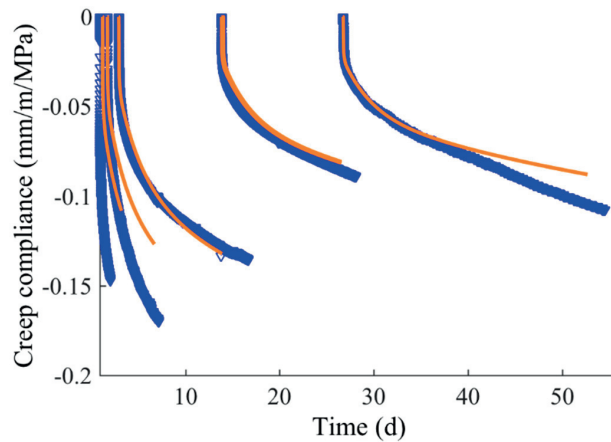


Figure 5.31 Comparison of the predicted and measured creep compliance in CQZ40-0.35 (orange are prediction, blue are measured results)

5.7 Conclusions

In this chapter, a quantitative study about the visco-elastic behavior of Cement-0.35, CFA40-0.35 and CQZ40-0.35 was carried out. A power law expression was fitted to the experimental data to express the basic creep behavior of the pastes. For the time-dependent visco-elastic response, a generalized Kelvin-Voigt chain was used for the prediction. The main conclusions from this study are:

1. By using metal creep frames with lever mechanism, the creep compliance of the three systems was measured. While both blended systems showed lower creep compliance than Cement-0.35 at early

ages, CFA40-0.34 showed the highest creep compliance at later ages. The whole entire visco-elastic response depended on loading levels and loading time.

2. The elastic modulus calculated from the instantaneous strain in the creep frames was close to the quasi-static elastic modulus, indicating the feasibility and accuracy of this experimental method for creep. The links between the elastic and visco-elastic behavior in the cementitious systems are strong, as shown by a transition period that is evident in both. This transition period is likely the result of both hydration and microstructure being nearly constant after this point in time.

3. A power law can be used to fit creep compliance and creep recovery of cementitious materials. The amplitude is related to the type of samples, loading time and history of loading, while the slope is influenced by the w/c through the degree of hydration. The expression agrees well with the experimental data and can be successfully applied for the prediction of creep compliance. The slope was found to be almost constant, around -0.8, for different materials. The samples under stepwise loading and constant loading have different amplitudes; however, after a time interval that depends on loading, the creep compliance rates at later ages are similar.

4. When comparing the creep compliance under loading and unloading, their coefficient is found to be similar. This is not affected by the SCMs and fillers in the systems. However, the creep recovery can be seen to vary between systems.

5. The hydration-dependent, generalized Kelvin-Voigt model was able to fit the creep of cementitious materials under constant loading, which can be later used for the prediction of the autogenous shrinkage.

5.8 References

- [1] Z. P. Bažant, M. H. Hubler, Q. Yu, Pervasiveness of excessive segmental bridge deflections: wake-up call for creep, *ACI Struct. J.* 108 (2011).
- [2] C. Burgoyne, R. Scantlebury, Why did Palau Bridge collapse?, *Struct. Eng.* 84 (2006) 30–37.
- [3] Z. P. Bažant, L. Panula, Creep and shrinkage characterization for analyzing prestressed concrete structures, *Prestress. Concr. Inst.* 25 (1980) 86–122.
- [4] F. Benboudjema, F. Meftah, J.M. Torrenti, A viscoelastic approach for the assessment of the drying shrinkage behaviour of cementitious materials, *Mater. Struct.* 40 (2006) 163–174.
- [5] T. C. Hansen, A. H. Mattock, Influence of size and shape of member on the shrinkage and creep of concrete, *ACI J. Proc.* 63 (1966) 267–290.
- [6] G. De Schutter, Applicability of degree of hydration concept and maturity method for thermo-visco-elastic behaviour of early age concrete, *Cem. Concr. Compos.* 26 (2004) 437–443.
- [7] P. Acker, F. -J. Ulm, Creep and shrinkage of concrete: physical origins and practical measurements, *Nucl. Eng. Des.* 203 (2001) 143–158.
- [8] Z. P. Bažant, Prediction of concrete creep and shrinkage: Past, present and future, *Nucl. Eng. Des.* 203 (2001) 27–38.
- [9] M. Vandamme, F. -J. Ulm, Nanogranular origin of concrete creep., *Proc. Natl. Acad. Sci. U.*

- S. A. 106 (2009) 10552–10557.
- [10] M. Vandamme, F. J. Ulm, Nanoindentation investigation of creep properties of calcium silicate hydrates, *Cem. Concr. Res.* 52 (2013) 38–52.
- [11] I. Pignatelli, A. Kumar, R. Alizadeh, Y. Le Pape, M. Bauchy, G. Sant, I. Pignatelli, A. Kumar, R. Alizadeh, Y. Le Pape, A dissolution-precipitation mechanism is at the origin of concrete creep in moist environments, 54701 (2016) 0–10.
- [12] M. Wyrzykowski, P. Lura, The effect of external load on internal relative humidity in concrete, *Cem. Concr. Res.* 65 (2014) 58–63.
- [13] R. Alizadeh, J. J. Beaudoin, L. Raki, Viscoelastic nature of calcium silicate hydrate, *Cem. Concr. Compos.* 32 (2010) 369–376.
- [14] M. Irfan-ul-Hassan, B. Pichler, R. Reihnsner, C. Hellmich, Elastic and creep properties of young cement paste, as determined from hourly repeated minute-long quasi-static tests, *Cem. Concr. Res.* 82 (2016) 36–49.
- [15] J. Beaudoin, B. Tamtsia, J. Marchand, M. Science, C. Workshop, A re-examination of creep mechanisms in hydrated cement systems, *Ind. Ital. Del Cem.* (2000).
- [16] P. Pourbeik, J. J. Beaudoin, R. Alizadeh, L. Raki, Creep of 45 year old cement paste: the role of structural water, *Mater. Struct.* (2015) 739–750.
- [17] Z. P. Bažant, J. C. Chern, Concrete at variable humidity: constitutive law and mechanisms, *Mater. Struct.* 18 (1985) 1–20.
- [18] B. T. Tamtsia, J. J. Beaudoin, Basic creep of hardened cement paste. A re-examination of the role of water, *Cem. Concr. Res.* 30 (2000) 1465–1475.
- [19] J. Glucklich, O. Ishai, Creep mechanism in cement mortar, *ACI J. Proc.* 59 (1962) 923–948.
- [20] N. H. Brown, B. B. Hope, The creep of hydrated cement paste, *Cem. Concr. Res.* 6 (1976) 475–485.
- [21] H. Ye, Creep Mechanisms of Calcium–Silicate–Hydrate: An overview of recent advances and challenges, *Int. J. Concr. Struct. Mater.* 9 (2015) 453–462.
- [22] T. C. Powers, Mechanisms of shrinkage and reversible creep of hardened cement paste, in: *Int. Conf. Struct. Concr. Sect. G*, 1965: pp. 319–344.
- [23] T. C. Powers, The thermodynamics of volume change and creep, *Matériaux Constr.* 1 (1968) 487–507.
- [24] R. L’Hermite, M. Mamillan, retrait et fluage des plaque, *An. ITBTP.* 21 (1968) 1319–1337.
- [25] M. Wyrzykowski, P. Lura, RH dependence upon applied load: experimental study on water redistribution in the microstructure at loading, in: *CONCREEP 10*, American Society of Civil Engineers, Reston, VA, 2015: pp. 339–347.
- [26] Z. P. Bažant, Theory of creep and shrinkage in concrete structures: a précis of recent developments, *Mech. Today*, Pergamon Press. (1975) 1–93.
- [27] Z. C. Grasley, D. A. Lange, Constitutive modeling of the aging viscoelastic properties of portland cement paste, *Mech. Time-Dependent Mater.* 11 (2007) 175–198.
- [28] E. A. Pachon-Rodriguez, E. Guillon, G. Houvenaghel, J. Colombani, Wet creep of hardened hydraulic cements - Example of gypsum plaster and implication for hydrated Portland cement, *Cem. Concr. Res.* 63 (2014) 67–74.

- [29] M. Suter, G. S. Benipal, Time-dependent behaviour of reacting concrete I: Mechanism and theory, *Mech Time-Depend Mater.* 10 (2006) 51–62.
- [30] V. S. Ramachandran, R. F. Feldman, J. J. Beaudoin, *Concrete science : treatise on current research*, Heyden, 1981.
- [31] A. Bazzoni, *Study of early hydration mechanisms of cement by means of electron microscopy*, EPFL, 2014.
- [32] K. L. Scrivener, P. Juilland, P. J. M. Monteiro, Advances in understanding hydration of Portland cement, *Cem. Concr. Res.* 78 (2015) 38–56.
- [33] T. C. Powers, T. L. Brownyard, Studies of the physical properties of hardened Portland cement paste, *J. Am. Concr. Inst.* 43 (1946) 101–132.
- [34] A. C. A. Muller, *Characterization of porosity & C-S-H in cement pastes by ¹H NMR*, EPFL, 2014.
- [35] R. F. Feldman, P. J. Sereda, A new model for hydrated Portland cement and its practical implications, *Repr. from Eng. J.* 53 (1970) 53–59.
- [36] F. H. Wittmann, *Grundlage eines modells zur beschreibung charakteristischer Eigenschaften des betons*, Ernst, 1977.
- [37] H. M. Jennings, A model for the microstructure of calcium silicate hydrate in cement paste, *Cem. Concr. Res.* 30 (2000) 101–116.
- [38] H. M. Jennings, Refinements to colloid model of C-S-H in cement: CM-II, *Cem. Concr. Res.* 38 (2008) 275–289.
- [39] A. M. Neville, Creep of concrete; plain, reinforced, and prestressed, in: *Mech. Creep Creep Hypotheses*, 1971: pp. 258–309.
- [40] F. J. Ulm, F. Le Maou, C. Boulay, Creep and shrinkage coupling : New review of some evidence, *Rev. Française Génie Civ.* 3 (1999) 21–37.
- [41] B. P. Bazant, A. B. Hauggaard, S. Baweja, Microprestress-solidification theory for concrete creep., (1997) 1195–1201.
- [42] H. M. Jennings, Colloid model of C-S-H and implications to the problem of creep and shrinkage, *Mater. Struct.* 37 (2003) 59–70.
- [43] B. Mather, Session G: Mechanisms of shrinkage and creep, in: *Cem. Concr. Assoc.*, 1968.
- [44] A. Bentur, R. L. Berger, F. V. Lawrence, N.B. Milestone, S. Mindess, J.F. Young, Creep and drying shrinkage of calcium silicate pastes III. A hypothesis of irreversible strains, *Cem. Concr. Res.* 9 (1979) 83–95.
- [45] H. M. Jennings, J. J. Thomas, D. Rothstein, J. J. Chen, Chapter 6.11: Cements as porous materials, in: *Handb. Porous Solids*, 2008.
- [46] R. F. Feldman, Mechanism of creep of hydrated Portland cement paste, *Cem. Concr. Res.* 2 (1972) 521–540.
- [47] P. Trtik, B. Münch, P. Lura, A critical examination of statistical nanoindentation on model materials and hardened cement pastes based on virtual experiments, *Cem. Concr. Compos.* 31 (2009) 705–714.
- [48] P. Lura, P. Trtik, B. Münch, Validity of recent approaches for statistical nanoindentation of cement pastes, *Cem. Concr. Compos.* 33 (2011) 457–465.

- [49] W. Li, S. Kawashima, J. Xiao, D.J. Corr, C. Shi, S. P. Shah, Comparative investigation on nanomechanical properties of hardened cement paste, *Mater. Struct.* 49 (2016) 1591–1604.
- [50] D. Mc Henry, A new aspect of creep in concrete and its application to design, in: ASTM, 1943.
- [51] Y. Lee, S. T. Yi, M. S. Kim, J. K. Kim, Evaluation of a basic creep model with respect to autogenous shrinkage, *Cem. Concr. Res.* 36 (2006) 1268–1278.
- [52] L. Taerwe, G. De Schutter, Towards a more fundamental non-linear basic creep model for early age concrete, *Mag. Concr. Res.* 49 (1997) 195–200.
- [53] F. J. Ulm, P. Acker, *Le point sur le fluage et la recouvrance des betons*, 1998.
- [54] M. Vandamme, F. J. Ulm, P. Fonollosa, Nanogranular packing of C-S-H at substoichiometric conditions, *Cem. Concr. Res.* 40 (2010) 14–26.
- [55] Z. P. Bažant, J. K. Kim, L. Panula, Improved prediction model for time-dependent deformations of concrete: Part 1-Shrinkage, *Mater. Struct.* 24 (1991) 327–345.
- [56] W. Hermerschmidt, H. Budelmann, Creep of early age concrete under variable stress, in: *Con-creep 10*, 2013: pp. 929–937.
- [57] I. Pane, W. Hansen, Early age creep and stress relaxation of concrete containing blended cements, *Mater. Struct.* 35 (2002) 92–96.
- [58] P. Ghodousi, M. H. Afshar, H. Ketabchi, E. Rasa, Study of early-age creep and shrinkage of concrete containing Iranian Pozzolans: an experimental comparative study, *Trans. A Civ. Eng.* 16 (2009) 126–137.
- [59] B. Delsaute, C. Boulay, S. Staquet, Creep testing of concrete since setting by means of permanent and cyclic loadings, *Cem. Concr. Compos.* (2016) 75–88.
- [60] O. Bernard, F. J. Ulm, J. T. Germaine, Volume and deviator creep of calcium-leached cement-based materials, *Cem. Concr. Res.* 33 (2003) 1127–1136.
- [61] C. A. Jones, Z. C. Grasley, Short-term creep of cement paste during nanoindentation, *Cem. Concr. Compos.* 33 (2011) 12–18.
- [62] Z. P. Bažant, A. B. Haugegaard, S. Baweja, F. Ulm, Creep . I : aging and drying effects, *J. Eng. Mech.* 123 (1997) 1188–1194.
- [63] M. Königsberger, M. Irfan-ul-Hassan, B. Pichler, C. Hellmich, Downscaling based identification of nonaging power-law creep of cement hydrates, *J. Eng. Mech.* 142 (2016) 4016106.
- [64] M. Briffaut, F. Benboudjema, J. M. Torrenti, G. Nahas, Concrete early age basic creep: Experiments and test of rheological modelling approaches, *Constr. Build. Mater.* 36 (2012) 373–380.
- [65] A. Hilaire, F. Benboudjema, A. Darquennes, Y. Berthaud, G. Nahas, Modeling basic creep in concrete at early-age under compressive and tensile loading, *Nucl. Eng. Des.* 269 (2014) 222–230.
- [66] C. Hua, P. Acker, A. Ehlacher, Analyses and models of the autogenous hardening cement paste shrinkage, 25 (1995) 1457–1468.
- [67] P. Lura, O. M. Jensen, K. van Breugel, Autogenous shrinkage in high-performance cement paste: An evaluation of basic mechanisms, *Cem. Concr. Res.* 33 (2003) 223–232.
- [68] Z. C. Grasley, C. K. Leung, Desiccation shrinkage of cementitious materials as an aging, poroviscoelastic response, *Cem. Concr. Res.* 41 (2011) 77–89.

- [69] K. M. Lee, H. K. Lee, S. H. Lee, G. Y. Kim, Autogenous shrinkage of concrete containing granulated blast-furnace slag, *Cem. Concr. Res.* 36 (2006) 1279–1285.
- [70] Z. C. Grasley, D. A. Lange, The viscoelastic response of cement paste to three-dimensional loading, *Mech Time-Depend Mater.* 11 (2007) 27–46.
- [71] Y. Lee, S. -T. Yi, M. -S. Kim, J. -K. Kim, Evaluation of a basic creep model with respect to autogenous shrinkage, *Cem. Concr. Res.* 36 (2006) 1268–1278.
- [72] D. Gawin, M. Wyrzykowski, F. Pesavento, Modeling hygro-thermal performance and strains of cementitious building materials maturing in variable conditions, *J. Build. Phys.* 31 (2008) 301–318.
- [73] D. Gawin, F. Pesavento, B. A. Schrefler, Modelling creep and shrinkage of concrete by means of effective stresses, *Mater. Struct.* 40 (2007) 579–591.
- [74] N. Ranaivomanana, S. Multon, A. Turatsinze, Basic creep of concrete under compression, tension and bending, *Constr. Build. Mater.* 38 (2013) 173–180.
- [75] N. Ranaivomanana, S. Multon, A. Turatsinze, Tensile, compressive and flexural basic creep of concrete at different stress levels, *Cem. Concr. Res.* 52 (2013) 1–10.
- [76] P. Rossi, J. -L. Tailhan, F. Le Maou, L. Gaillet, E. Martin, Basic creep behavior of concretes investigation of the physical mechanisms by using acoustic emission, *Cem. Concr. Res.* 42 (2012) 61–73.
- [77] Y. Wei, S. Liang, W. Guo, Decoupling of autogenous shrinkage and tensile creep strain in high strength concrete at early ages, *Exp. Mech.* 57 (2017) 475–485.
- [78] G. M. Ji, T. Kanstad, Ø. Bjøntegaard, E. J. Sellevold, Tensile and compressive creep deformations of hardening concrete containing mineral additives, *Mater. Struct.* 46 (2013) 1167–1182.
- [79] I. Pane, W. Hansen, Investigation on key properties controlling early-age stress development of blended cement concrete, *Cem. Concr. Res.* 38 (2008) 1325–1335.
- [80] B. T. Tamsia, J. J. Beaudoin, J. Marchand, The early age short-term creep of hardening cement paste: load-induced hydration effects, *Cem. Concr. Compos.* 26 (2004) 481–489.
- [81] G. De Schutter, Degree of hydration based Kelvin model for the basic creep of early age concrete, *Mater. Struct.* 32 (1999) 260–265.
- [82] Z. P. Bažant, J. C. Chern, Double-power logarithmic law for concrete creep, *Cem. Concr. Res.* 14 (1984) 793–806.
- [83] Z. P. Bažant, J. C. Chern, Log double power law for concrete creep, *ACI J.* 82 (1985) 665–675.
- [84] M. Larson, J. -E. Jonasson, Linear logarithmic model for concrete creep, *J. Adv. Concr. Technol.* 1 (2003) 188–200.
- [85] A. B. Giorla, Modelling of alkali-silica reaction under multi-axial load, EPFL, 2013.
- [86] M. Shahidi, B. Pichler, C. Hellmich, Interfacial micromechanics assessment of classical rheological models. I: single interface size and viscosity, *J. Eng. Mech.* 142 (2016) 4015092.
- [87] Z. P. Bažant, P. Santosh, Solidification theory for concrete creep, *J. Eng. Mech.* 115 (1989) 1691–1703.

- [88] D. Gawin, F. Pesavento, B. A. Schrefler, Hygro-thermo-chemo-mechanical modelling of concrete at early ages and beyond. Part II: shrinkage and creep of concrete, *Int. J. Numer. Methods Eng.* 67 (2006) 332–363.
- [89] S. A. Altoubat, D. A. Lange, Tensile Basic Creep: Measurements and Behavior At Early Age, *ACI Mater. J.* 98 (2001).
- [90] Z. P. Bažant, Material models for structural creep analysis, in: *Math. Model. Creep Shrinkage Concr.*, 1988: p. 459.
- [91] G. Schutter, L. Taerwe, Fictitious degree of hydration method for the basic creep of early age concrete, *Mater. Struct.* 33 (2000) 370–380.
- [92] W. Jiang, G. De Schutter, Y. Yuan, Degree of hydration based prediction of early age basic creep and creep recovery of blended concrete, *Cem. Concr. Compos.* 48 (2014) 83–90.
- [93] M. Azenha, F. Magalhães, R. Faria, Á. Cunha, Measurement of concrete E-modulus evolution since casting: A novel method based on ambient vibration, *Cem. Concr. Res.* 40 (2010) 1096–1105.
- [94] S. Norm, *Construction en bois – Spécifications complémentaires*, (2003) 1–28.
- [95] M. Shahidi, B. Pichler, C. Hellmich, How interface size, density, and viscosity affect creep and relaxation functions of matrix-interface composites: a micromechanical study, *Acta Mech.* 227 (2016) 229–252.
- [96] E. M. J. Berodier, Impact of the supplementary cementitious materials on the kinetics and microstructural development of cement hydration, *Ecole Polytechnique Federale De Lausanne*, 2015.
- [97] N. Bouzoubaâ, S. Foo, *Use of fly ash and slag in concrete: A Best Practice Guide*, (2005).
- [98] B. A. Gedam, A. M. Asce, N. M. Bhandari, A. Upadhyay, Influence of supplementary cementitious materials on shrinkage, creep, and durability of high-performance concrete, *J. Mater. Civ. Eng.* 28 (2015) 1–11.
- [99] O. M. Jensen, P. F. Hansen, Autogenous deformation and change of the relative humidity in silica fume-modified cement paste, *ACI Mater. J.* 93 (1996) 539–543.
- [100] C. Di Bella, A. Michel, H. Stang, P. Lura, Early age fracture properties of microstructurally-designed mortars, *Cem. Concr. Compos.* 75 (2017) 62–73.
- [101] C. Di Bella, M. Wyrzykowski, M. Griffa, P. Termkhajornkit, G. Chanvillard, H. Stang, A. Eberhardt, P. Lura, Application of microstructurally-designed mortars for studying early-age properties: Microstructure and mechanical properties, *Cem. Concr. Res.* 78 (2015) 234–244.
- [102] S. J. Lokhorst, K. van Breugel, Simulation of the effect of geometrical changes of the microstructure on the deformational behaviour of hardening concrete, *Cem. Concr. Res.* 27 (1997) 1465–1479.
- [103] A. S. Lubansky, Y. L. Yeow, Y.-K. Leong, S.R. Wickramasinghe, B. Han, A general method of computing the derivative of experimental data, *AIChE J.* 52 (2006) 323–332.
- [104] Z. P. Bažant, S. S. Kim, S. Meiri, Triaxial moisture-controlled creep tests of hardened cement paste at high temperature, *Mater. Constr.* 12 (1979) 447–456.
- [105] A. Sellier, S. Multon, L. Buffo-Lacarrière, T. Vidal, X. Bourbon, G. Camps, Concrete creep modelling for structural applications: Non-linearity, multi-axiality, hydration, temperature and

- drying effects, *Cem. Concr. Res.* 79 (2016) 301–315.
- [106] A. M. Neville, Creep recovery of mortars made with different cements, *J. Am. Concr. Inst.* (n.d.) 167–174.
- [107] K. Wesche, *Fly ash in concrete : properties and performance*, E & FN Spon, 1991.
- [108] A. Hilaire, *Etude des déformations différées des bétons en compression et en traction, du jeune au long terme : application aux enceintes de confinement*, UniverSud Paris, 2015.
- [109] A. Korpa, R. Trettin, The influence of different drying methods on cement paste microstructures as reflected by gas adsorption: Comparison between freeze-drying (F-drying), D-drying, P-drying and oven-drying methods, *Cem. Concr. Res.* 36 (2006) 634–649.

Chapter 6 Prediction of autogenous shrinkage as poro-visco-elastic deformation

This chapter presents the prediction of autogenous shrinkage of three systems first by considering only the poro-elastic deformation and then including the poro-visco-elastic response. Predictions of elastic deformation from different poromechanical models were compared. Different factors impacting the predictions were investigated. The prediction of the poro-visco-elastic response of the material to the internal stress was performed based on generalized Kelvin-Voigt models with parameters linked with the degree of hydration and the initial porosity (determined from *Chapter 5*).

Contents

6.1	Literature review.....	122
6.1.1	Empirical and semi-empirical models.....	122
6.1.2	Mechanistic prediction methods	124
6.2	Prediction Methods.....	132
6.2.1	Poro-elastic prediction	132
6.2.2	Poro-visco-elastic prediction.....	135
6.3	Parameters from experiments	136
6.3.1	Saturation degree.....	136
6.3.2	Average pore pressure.....	138
6.3.3	Other parameters	138
6.4	Prediction results	141
6.4.1	Prediction of elastic response.....	141
6.4.2	Prediction of the visco-elastic component	144
6.4.3	Prediction of overall autogenous shrinkage	146
6.5	Conclusions	147
6.6	References	148

6.1 Literature review

Investigations on the autogenous shrinkage of cementitious materials have been carried out for many years and considerable efforts have been made to formulate reliable models for prediction of autogenous shrinkage (e.g., [1–3]). However, no complete prediction of autogenous shrinkage by using either analytical or numerical methods has been achieved so far [4,5]. A problem was identified by some researchers who found a mismatch between the poro-elastic predictions and the measured results at lower RH [4,5]. Therefore, attention has been paid to identify the reason for these discrepancies.

Since the cement paste displays visco-elastic behavior under stress, such behavior should likely also manifest itself under the action of internal stress due to capillary pressure [5–8]. Therefore, assuming the validity of the superposition principle, autogenous shrinkage (neglecting thermal dilation because of the isothermal conditions and possible damage, e.g., micro-cracks) can be expressed as:

Equation 6.1

$$\varepsilon = \varepsilon_e + \varepsilon_c$$

where: ε [$\mu\text{m}/\text{m}$] is the total autogenous shrinkage occurring after setting (in the solid material), ε_e [$\mu\text{m}/\text{m}$] is the (poro) elastic deformation and ε_c [$\mu\text{m}/\text{m}$] is the contribution of the creep deformation.

The visco-elastic response of cementitious materials at very early age is extremely complex, both to measure and to predict. This complexity arises from the fact that the measurement takes place over a period of time, and during this time properties of the system change due to hydration. Thus both the stresses exerted on the porous body due to (self-) desiccation of pores and the material properties (e.g., microstructural and mechanical characteristics) are changing at the same time.

In addition, the contribution of the visco-elastic component to the total measured autogenous deformation is not completely understood. There is a major debate about the existence of couplings between the autogenous deformation and creep, see discussion in *section 5.1.2*. Numerical models are the most common approaches to deal with this visco-elastic response [7,9]. However, these models often lack verification from reliable experimental results.

In this state of the art, existing prediction methods of autogenous shrinkage are reviewed. The models are divided into two categories based on their specific principles: (1) empirical and semi-empirical models; (2) mechanistic models.

6.1.1 Empirical and semi-empirical models

Empirical or semi-empirical models refer to models obtained via regressive analyses on a certain amount of experimental data about specific materials [10–12]. The parameters usually studied are the mixture properties, e.g., w/c, mineral compositions of cement and aggregates and compressive strength. Generally, in this sort of models, some other parameters have to be determined by fitting the specific experimental curves or statistically from a large sampling database.

Tazawa and Miyazawa [13,14] carried out some studies about the impact of cement compositions and admixture on autogenous shrinkage of cement pastes. Based on least square analysis, autogenous shrinkage was linked to the mineral compositions (clinker phases) for one w/c:

Equation 6.2

$$\varepsilon(t) = -0.012 \cdot \alpha_{C_3S}(t) \cdot (C_3S\%) - 0.070 \cdot \alpha_{C_2S}(t) \cdot (C_2S\%) \\ + 2.256 \cdot \alpha_{C_3A}(t) \cdot (C_3A\%) + 0.859 \cdot \alpha_{C_4AF}(t) \cdot (C_4AF\%)$$

where: $\alpha(t)$ is the degree of hydration of a certain phase at time t [d], $C_3S\%$, $C_2S\%$, $C_3A\%$ and $C_4AF\%$ are mass percentages of four main clinker phases in the raw materials. For engineering applications, this model is not practical since the determination of the reaction of different mineral phases increases the complexity of the final prediction. Moreover, the applications of the model are strongly limited since the fillers and other components are not considered.

Later, the JCI committee recommends the following equation for predicting autogenous shrinkage of concrete [15]:

Equation 6.3

$$\varepsilon(t) = \kappa \cdot \varepsilon_{\infty} \cdot \beta(t)$$

where: κ [-] is a coefficient to express effects of types of cement and mineral admixture (κ equals 1 for pure Portland cement). ε_{∞} [$\mu\text{m}/\text{m}$] is the infinite autogenous shrinkage strain which depends on w/c ($\varepsilon_{\infty} = 3070 \cdot \exp(-7.2 \cdot w/c)$). $\beta(t)$ [-] is a parameter related to time t [d] and initial set time t_{in} [d]: ($\beta(t) = 1 - \exp(-a \cdot (t - t_{in})^b)$). t_{in} is a temperature-dependent parameter: $t_{in} = \Sigma \Delta t_i \cdot \exp(13.65 - 4000/(273 + T(\Delta t_i)))$, where Δt_i is the time after which concrete temperature is T [$^{\circ}\text{C}$]. a and b are two material-dependent constants which are determined by fitting the experimental results.

Yoo et al. [16] modified this formula by regression analysis of autogenous shrinkage of HPC to extend the application of the model. They suggested that the two constants, a and b , should be fixed as 0.375 and 0.500. They also used a κ that depended on the initial set time instead of a constant κ value.

CEB-FIP [17] recommends to predict autogenous shrinkage based on compressive strength:

Equation 6.4

$$\varepsilon(t) = \varepsilon_{caso}(f_{cm}) \cdot \beta_{as}(t)$$

where: $\varepsilon_{caso}(f_{cm})$ [$\mu\text{m}/\text{m}$] is the autogenous shrinkage coefficient which depends on compressive strength f_{cm} [MPa]: ($\varepsilon_{caso}(f_{cm}) = -\alpha_{as} \cdot (f_{cm}/10 / (6 + f_{cm}/10)^{2.5})$) and $\beta_{as}(t)$ [-] is a time-dependent coefficient. The suggested value for coefficient α_{as} [-] depends on the type of cement used (800 for slowly hardening cement, 700 for normal- or rapid-hardening cement and 600 for rapid, high strength cement [17]). The equation used for calculating $\beta_{as}(t)$ is $\beta_{as}(t) = 1 - \exp(-0.2t^{0.5})$.

Another well-known empirical model for predicting autogenous shrinkage of concrete is the B4 model [10,18] (extension of the B3 model established by Bažant in 1995 [19] and recommended by RILEM). In this model, autogenous shrinkage is predicted based on *Equation 6.5*. This approach introduced the concept of autogenous shrinkage half-time τ_{au} (relating to τ_{au0} and w/c):

Equation 6.5

$$\varepsilon(t) = \varepsilon_{au0} \cdot \left(\frac{ag/c}{6}\right)^{r_5} \cdot \left(\frac{w/c}{0.38}\right)^{r_4} \cdot \left(1 + \left(\tau_{au0} \cdot \left(\frac{w/c}{0.38}\right)^{r_1} / t\right)^\alpha\right)^{r_2}$$

where: ε_{au0} is the final autogenous shrinkage (assumed to be negative), ag/c is the mass ratio of the aggregate and cement, α is a w/c -dependent component ($\alpha=r_3 \cdot (w/c/0.38)$). As shown in the equation, the model is quite complicated, with seven independent constants (ε_{au0} , τ_{au0} , r_1 , r_2 , r_3 , r_4 and r_5) to be determined. These constants can be obtained by fitting the experimental curves.

Two machine-learning methods for the prediction of autogenous shrinkage have been published in the literature: an artificial intelligence model [20] and a support vector machine [21]. These two methods are of limited application as they cannot be extrapolated beyond the domain of the training data and have a large set of controlling parameters [20]. In terms of the lower number of parameters needed for the prediction, the support vector machine method might be preferred [21].

In summary, these models can be applied quickly in concrete design for an approximated calculation of autogenous shrinkage of concrete with (in the best cases) a limited number of parameters, especially in the field. However, they are phenomenological approaches not accounting for the real physical mechanisms, and therefore of very limited applicability for a wide range of mix compositions and environmental conditions.

6.1.2 Mechanistic prediction methods

Autogenous shrinkage is a phenomenon taking place in a material point, since its definition assumes no temperature or moisture gradients (sealed samples at isothermal conditions) [22]. Therefore, autogenous shrinkage at the macroscopic level can be in principle calculated using only analytical models. However, there exist also multi-scale models, in which autogenous shrinkage is calculated based on homogenization from the microstructural scale [4,23]. At the macroscopic level, calculations of autogenous shrinkage can be next incorporated in the structural models of hardening concrete, e.g., [24–26].

Poromechanical approaches for unsaturated porous materials based on changes of pore fluid pressure as the main driving force are commonly used to predict autogenous shrinkage (e.g., [4,5,9]). Most of the models for predicting the pore fluid pressure are based on the Kelvin-Laplace law, which gives the pressure difference between liquid and gas phases in a capillary pore structure, see *Chapter 3* and *Chapter 4* [27,28]. After obtaining the pore fluid pressure, the resulting strain is calculated either by analytical models (e.g., multi-scale modeling with self-consistent scheme homogenization and Mori-Tanaka homogenization [23]) or by numerical models (e.g., FEM homogenization [29]), with or without considering creep.

In this section, different methods for calculating changes of pore fluid pressure and models of considering these changes in prediction of autogenous shrinkage are reviewed. Capillary pressure is assumed here as an approximation of pore fluid pressure [30].

Basically, there are three approaches in literature for obtaining the capillary pressure evolution in hardening cement paste:

1) Calculation based on Kelvin-Laplace equation directly from measured RH

Lura et al. [5] modeled the autogenous shrinkage based on the measured RH, considering additionally the RH_s caused by the dissolved ions in the pore fluid. In their study, RH_s was approximated using Raoult's law [31], see *Chapter 3*. The prediction of autogenous shrinkage was found satisfactory when the RH was high (higher than 97 %). At lower RH (down to about 94 %) an underestimation of the autogenous shrinkage was attributed to the visco-elastic part not considered in the prediction, see *Figure 6.1*. Grasley and Leung [6] also considered changing concentrations of dissolved ions in the pore solution in their prediction with not only Raoult's law [31] but also Pitzer's equation [32]. It was found that, in the case of self-desiccation, Raoult's law gave rather accurate prediction of RH_s for high saturation degree above 0.5 [6]. Zhang et al. [33], Lu and Koenders [34] and Gawin et al. [24] used the same approach, the former one considering also the effect of temperature in their model, while the latter two added a creep component to the simulation (in a later section, the methods used for considering creep will be discussed).

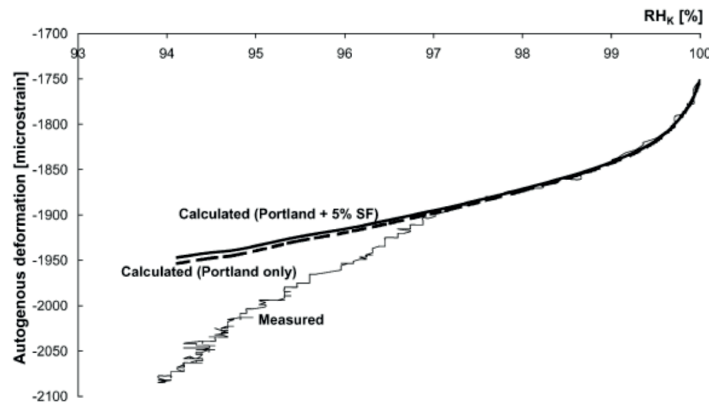


Figure 6.1 Measured and calculated autogenous shrinkage as a function of RH_k . The difference between the measured curve and the calculated ones is thought to be linked with the visco-elastic response of cementitious materials (from [5])

2) Calculation based on the Young-Laplace equation by determining the Kelvin radius

Pore pressure can be determined using the Young-Laplace equation as a function of meniscus radius in the largest pores still filled with water. This size, referred to as the Kelvin radius, was basically determined in the literature following the following three approaches.

Chemical shrinkage and MIP

This method, first proposed by Hua et al. [9], has been already discussed in *Chapter 4*. The principle is that the Kelvin radius corresponding to the emptied pore volume by chemical shrinkage is the same

as the volume intruded by mercury through pores of the same size as those corresponding to the Kelvin radius. Since the chemical shrinkage is a function of the degree of hydration, the emptied pore volume can also be estimated directly from the degree of hydration. An extended method was developed by Chen et al. [27], where they discussed in detail the associated error and uncertainties with also taking the absorbed water layer into account. In addition, they provided an approximation of the difference by using the saturated samples in chemical shrinkage and dried samples in MIP, resulting in an overestimation of RH by around 1.4%. The overall uncertainty of this method from experimental error was found to be around 1-2% [27].

The novel method proposed in *Chapter 4* based on ^1H NMR and MIP, which measures water-filled pores instead of emptied pore volume, offers another possibility for predicting the Kelvin radius and then later the capillary pressure.

MIP (critical pore size or threshold pore size)

From MIP measurements alone, Li and Li [35] took the critical pore size as the Kelvin radius, but gave no justification for this choice. As shown in *Chapter 4*, the Kelvin radius is larger than the critical pore size at one day but smaller after the first day in the systems studied in this thesis.

Link to degree of hydration and w/c

Pichler et al. [23] proposed an equation for predicting the capillary pressure from specific values of w/c and degree of hydration α . Based on an extension [23] of their multiscale micromechanics-hydration model [36] (the structure of the model is shown in *Figure 6.2*), the volume fraction of liquid and gas phases at the cement-paste scale (the scale II) could be obtained. The capillary pressure then can be calculated based on the combination of the pore size distribution determined from the experiments and the volume fractions of liquid and gas phases.

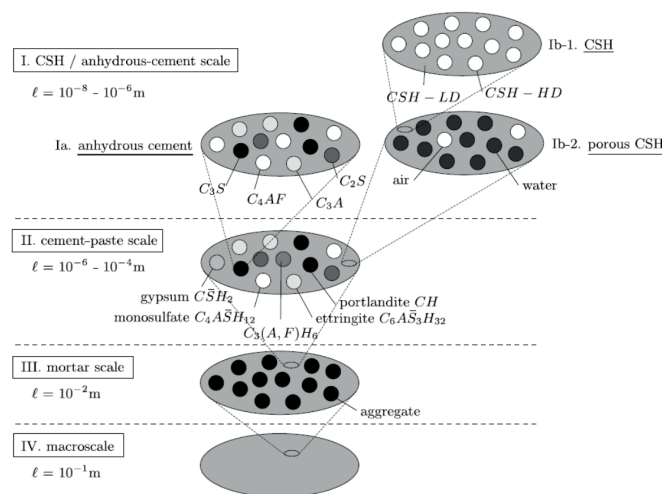


Figure 6.2 Multi-scale structure of the simulation from Pichler et al. [23]

A linear relationship between the pore volume and pore radius obtained from MIP and SEM images analysis were used in the investigation. The idea for combining MIP and SEM is to overcome the underestimation of larger pores in the MIP measurements [37]. Afterwards, a regression analysis was performed, based on which a linear relationship between the \log_{10} based Kelvin radius and the volume fraction of liquid and gas phases was established. The predicted capillary pressure therefore can be plotted as a function of degree of hydration and w/c , as shown in *Figure 6.3*.

This method is semi-empirical, since the simulation of the hydration was based on experimentally-determined kinetics and the pore size distribution was not simulated directly. The principle behind this approach is similar to Hua's method. They used experimental data from literature. One issue in this model is the reliability of the linear relationship established between the pore volume and the pore size.

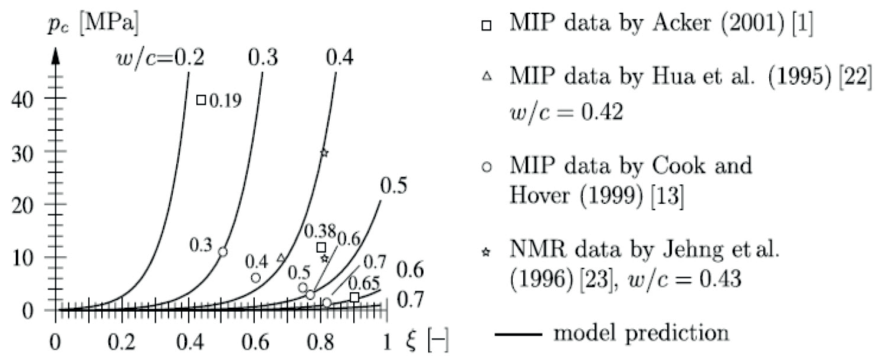


Figure 6.3 Relationship between capillary pressure and w/c and degree of hydration from [23]

After determining the internal stress (capillary pressure), models linking autogenous shrinkage and capillary pressure are needed. There are also various approaches for achieving this:

1) Elastic deformation

Poro-elastic methods

Poro-elastic modeling has been widely used in predictions of autogenous shrinkage (e.g., [2,5,33,38]). The basis of most poromechanical models, the *Biot-Bishop approach* [39] has already been discussed in *Chapter 3*. In this part, a more detailed discussion on the determination of parameters and modified equations according to *Coussy* [40] and *Vlahinić* [41] is presented.

In the *Biot-Bishop approach* [39], three parameters need to be determined: saturation degree S , bulk modulus K of the porous material and bulk modulus of the solid body K_s .

The saturation degree is the volume fraction of the evaporable water (V_{ew}) in the total porosity (V_p), see *Equation 6.6* [5,42]. As discussed in *Chapter 3*, the use of S is a simplification of Bishop's parameter χ . However, this simplification has been questioned by Gawin et al. [7] for cementitious systems, which have considerable internal surface area. Gawin et al. [7] obtained the product $b\chi$ (b is

the Biot coefficient) as a function of S by fitting experimental data on drying shrinkage and sorption isotherms of concrete and cement paste reported in [28], see *Figure 6.4*, adapted from [7]. It should be however noted that the determination of the Bishop's parameter to be used for estimating poro-elastic deformations by simply fitting experimental deformations is necessarily invalid, since the latter is most likely an effect of both elastic and creep deformations (as will be shown later in this chapter).

Equation 6.6

$$S = \frac{V_{ew}}{V_p}$$

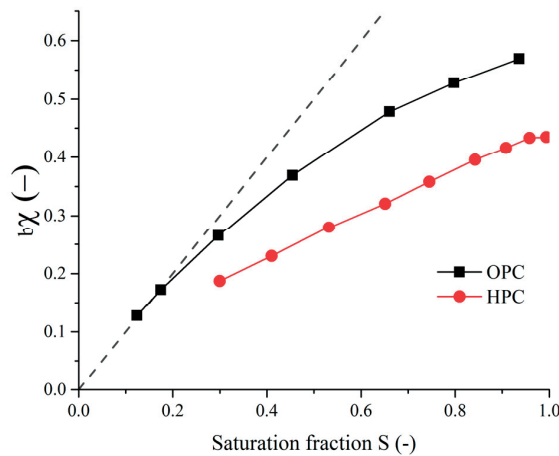


Figure 6.4 Experimental data for $b\chi$ as a function of S in Portland cement paste and HPC, adapted from [7]. The Biot coefficient would be above 0.8, depending on elastic modulus and Poisson's ratio

To find the saturation degree S , the porosity and the water content or the emptied pores volume need to be known. Conventionally, there are two classes of experimental methods for determining S : destructive and non-destructive. The destructive approach requires to remove water and to determine a dry reference state, e.g., water vapor sorption isotherms measurement [23]. Non-destructive approaches, e.g., ^1H NMR [43], are not dependent on the arbitrarily-defined reference state. Nevertheless, it is still necessary to define which population of water occupying different size classes of pores is considered as relevant for the averaging of pressure and therefore for the applied saturation degree.

The estimation of S can be also done with Powers' model combined with either experimental data on mineralogy or with the phase assemblage calculated from Gibbs Energy Minimization (GEMs) [5]. With water vapor sorption isotherms, it is not possible to determine the S of an early-age sample that undergoes hydration. This method is affected by the reference state assumed, which means different results will be obtained with different drying approaches. Another problem is that it takes some time (generally, hours to days, depending on pore structure, sample size, RH level and the way in which it is controlled) to reach relative humidity equilibrium and to finish the whole desorption ramp, while

the microstructure is rapidly changing in the early-age samples. A possible solution for this is using an equivalent system [44] without evolution of hydration during the test to monitor the early-age system. In this chapter, the method based on Powers' model will be used and compared with the estimation based on ^1H NMR and chemical shrinkage [45].

The bulk moduli of the porous material and of the solid skeleton, K and K_S , describe the compressibility of the porous material and of the solids, respectively. The hydration-dependent K can be determined from the Young's modulus E and the Poisson's ratio ν , see *Equation 6.7*, in which the Poisson's ratio decreases from 0.5 (Poisson's ratio of an incompressible fluid [46]) and stabilizes at about 0.18-0.25 after about 1 day of hydration [5,47].

Equation 6.7

$$K = \frac{E}{3 \cdot (1 - 2 \cdot \nu)}$$

For cement paste, K_S is reported to be in the range between 38 and 55 GPa, depending on the bulk modulus of all the solid phases in the system, among which the largest uncertainty is the bulk modulus of the intrinsically-porous C-S-H [48]. In principle, K_S should be approximately constant or should slightly decrease at early ages due to the lower Young's modulus of hydrated phases compared to the anhydrous phases [48]. In the prediction, for simplicity, a constant K_S is very often used [49]. In *Vlahinić's method* [41], they considered the weakening of the solid caused by desaturation of the pores in the prediction, thus using \bar{K}_S decreasing with S instead of K_S , see *Equation 6.8*. On the other hand, no Bishop's parameter is used in this approach, since saturation was already accounted in \bar{K}_S .

Equation 6.8

$$\bar{K}_S = K_S - \frac{(K_S - K) \cdot (1 - S)}{(1 - S \cdot V_p)}$$

Calculation of \bar{K}_S with *Equation 6.8* for the exemplary input yields 36.7 GPa for mature cement paste (calculated with $S = 0.8$, $K_S = 44$ GPa, $K = 13.5$ GPa and $V_p = 0.2$) and 39 GPa for early-age cement paste ($S = 0.9$, $K_S = 44$ GPa, $K = 6.9$ GPa and $V_p = 0.3$). This difference between early-age and mature pastes has a negligible effect on the shrinkage, also because K_S is much larger than K and therefore K dominates the term $(1/K - 1/K_S)$.

In *Coussy's method* [40], the equivalent pore pressure is introduced to replace the average capillary pressure in the *Biot-Bishop approach* [39], which takes the contribution of the interface energy into account. The resulting equation is as follows, if the gas pressure is ignored (similarly as in the *Biot-Bishop approach*):

Equation 6.9

$$\varepsilon = -\frac{1}{3}(Sp_c + U) \cdot \left(\frac{1}{K} - \frac{1}{K_S} \right) = -\frac{1}{3} \left(Sp_c + \int_s^1 p_c(S) dS \right) \cdot \left(\frac{1}{K} - \frac{1}{K_S} \right)$$

where: U [Pa] is the interface energy. For drying shrinkage, this modification may change substantially the final results but in the self-desiccation case, again, the differences should not be significant since the term due to interface energy is relatively low at high saturation degrees.

Analytical self-consistent scheme methods

The multi-scale model by Pichler et al. [23], see *Figure 6.2*, used the analytical homogenization method at different scales and upscaling from cement paste to concrete was performed. They simulated the average strain and stress in the system by analytical self-consistent and Mori-Tanaka scheme homogenization methods at different scales, see *Figure 6.2*. Moreover, at the scale II, they considered also the crystallization pressure caused by ettringite formation (see suggested reasons for the expansion that often occurs in the measured autogenous deformation explained in *Chapter 3*) [23].

Zhang et al. [33] proposed the multiple hole model with a self-consistent scheme for simulating the elastic deformation of autogenous shrinkage without considering creep. In their work, the pore size distribution used in the model was obtained by a Raleigh distribution function with accumulated pore volume from experiments. The principle of the modeling is the classical poro-mechanics approach, *Biot-Bishop approach* using S multiply by a pore structure influencing factor as the Bishop's parameter.

2) Visco-elastic deformation

Empirical method

Hua et al. [50] considered volumetric and deviatoric components of creep under hydrostatic internal stress caused by capillary pressure in the simulation. The reason for considering also the deviatoric components under hydrostatic stress is due to the non-hydrostatic local stress state caused by the heterogeneous microstructure. The linear autogenous shrinkage including both an elastic and a visco-elastic part was then calculated based on Boltzmann's superposition, see *Equation 6.10*. The one-dimensional creep ($J(t, t')$ including the elastic part, t is the current time, t' is the stress acting time) is determined from experiments, see *Equation 6.11*.

Equation 6.10

$$\varepsilon(t) = \int_{t_0}^t (1 - 2 \cdot \nu) \cdot J(t, t') \cdot d\Sigma(t')$$

in which, $\Sigma(t')$ [MPa] is the macroscopic compression of the skeleton.

Equation 6.11

$$J(t, t') = \frac{1}{E(t')} + \varepsilon_{\infty}(t') \cdot \frac{(t - t')^{\alpha(t')}}{(t - t')^{\alpha(t')} + b(t')}$$

in which, $E(t')$ [GPa] is the elastic modulus of the system at t' [d], other functions ($\alpha(t')$ and $b(t')$) are determined by the comparison with the experimental curves (minimizing the error). This simulation

was based only on few empirical data, which ignored aging of the creep compliance, and resulted in an overestimation of the overall autogenous shrinkage.

Solidification method

Gawin et al. [7] incorporated the microprestress-solidification theory by Bažant et al. [51,52] in their model of shrinkage as an effect of effective stress and demonstrated that creep caused by effective stresses was of the same order of magnitude as the shrinkage strains. They used an analytical expression of microprestress from Bažant et al. [51,52] and numerically solved the constitutive equations linked with the creep function. Compared to the simulation and measurements, they concluded that coupling autogenous shrinkage and creep is necessary for a complete prediction. However, the details of the coupling proposed in their work lacked experimental verification.

A microstructural modeling approach based on *μic* was used together with the FEM method for predicting the autogenous shrinkage of cement pastes [4,53]. The microstructure is modeled based on a vector approach, which allows avoiding limitation of the resolution at the hydration stage [54]. The prediction of the elastic part was based also on poro-elasticity. However, the visco-elastic response was based on solidification and the aging of the visco-elastic creep was considered with densifying and space filling. They used the logarithmic law for the visco-elastic behavior of C-S-H obtained from nanoindentation experiments [55] and simulated the time-dependent Maxwell chains on individual elements of the FEM element mesh of the simulated microstructures from *μic*.

Based on aging poro-visco-elasticity, Grasley and Leung [6] presented a new model for predicting either autogenous shrinkage or drying shrinkage. They combined solidification theory and a time-shift approach and applied Laplace transformation (complex integrations and derivations in the time domain become much simpler multiplication expressions in the Laplace domain) in their simulation. In the time-shift approach, the shape of the creep compliance curve is kept by the solidification of C-S-H gel on the log-time scale, which means that the aging of the visco-elastic compliance may be calculated by shifting the real time along the log axis being pseudo-time (ξ'), see *Equation 6.12*. The proposed equation for linear autogenous shrinkage accounting also for the aforementioned interfacial pressure can be seen in *Equation 6.13*.

Equation 6.12

$$J(t, t') = \frac{1}{E_p \cdot \nu(t')} + \int_{t'}^t \frac{1}{\nu(\theta)} \cdot \frac{\partial J_s \{ \xi'(\theta) - \xi'(t') \}}{\partial \theta} d\theta$$

where: E_p [GPa] is the elastic modulus, ν [-] is the Poisson's ratio, θ is the dummy time variable of integration, J_s is the non-aging creep compliance.

Equation 6.13

$$\varepsilon(t) = \frac{\partial (P_c(t') - U(t'))}{\partial t'} \cdot \left\{ (1 - 2\nu) \cdot J(t, t') - \frac{1}{3K_s} \right\} dt'$$

Grasley and Leung [6] came to the conclusion that the poro-elastic model significantly underestimated the autogenous shrinkage, unless ageing of the C-S-H gel being included.

In addition to these various models considering the capillary pressure as driving force, Koenders and van Breugel [56] calculated autogenous shrinkage based on changes of surface tension as a function of RH decrease. In their calculation, the surface tension was obtained according to *Gibbs-Bangham approach*, where the surface tension was determined based on the number of moles of water per unit area which are adsorbed to the pore wall, see *Equation 6.14*. To link the macroscale deformation and the evolution of surface tension, *Equation 6.15* was used for calculating the increment of the autogenous shrinkage.

Equation 6.14

$$\gamma = R \cdot T \cdot \int \Gamma d \ln(p) = R \cdot T \cdot \int \frac{n - n_{liquid} - n_{gas}}{A_{por}(\alpha(t))} d \ln(p)$$

where: R and T are the same as the definition in *Chapter 3*, n is the total number of moles of molecules in the system; n_{liquid} is the number of moles of molecules in the liquid phase, n_{gas} is the number of moles of molecules in the gas phases. A_{por} [m^2] is total area of the pore wall. Γ is the number of moles per unit area which are adsorbed to the pore wall area depending on the pore constant k . Since the original HYMOSTRUC model was not able to predict pore size distribution, they used the relationship between pore volume and pore size, where k is the constant linking them. k is ranging from 0.05 to 0.11 for coarse cement and fine cement, respectively.

Equation 6.15

$$\frac{\partial \varepsilon}{\partial t} = \lambda \cdot \frac{\partial \gamma}{\partial t} = \frac{\Sigma \cdot \rho_{pa}}{3E} \cdot \frac{\partial \gamma}{\partial t}$$

where: Σ [m^2] ($\Sigma = A_{por} - A_{water}$) is the area of the pore wall of the empty pores; ρ_{pa} [kg/m^3] is the specific mass of the cement paste; λ [-] is the proportionality factor or compliance modulus of hardening cement paste.

With the HYMOSTRUC model (the microstructure is modeled by random particle structures generated from HYMOSTRUC together with the A_{por} and total pore volume together), they finally drew the conclusion that the prediction agreed well with the experimental results. However, the validity of the method for predicting autogenous shrinkage when the RH is higher than 75% is still questionable.

6.2 Prediction Methods

6.2.1 Poro-elastic prediction

The *Biot-Bishop approach* [39], *Coussy's method* [40] and *Vlahinić's method* [41] were used in the poro-elastic predictions in this chapter based on the equations shown in the literature review section. The *Biot-Bishop approach* [39] was used as a reference method for studying the effect of associated parameters. The parameters were all determined from experiments, except K_s . Comparisons were made with three poro-elastic approaches and additionally the effect of the following parameters was studied with the *Biot-Bishop approach* only:

- 1) Poisson's ratio determined experimentally or with an assumed constant value of 0.22;
- 2) saturation degree either determined based on ^1H NMR and chemical shrinkage or using Powers' model;
- 3) constant K_s of 44 GPa or upper and lower value in the range of K_s , 38 GPa and 55 GPa [48].

The approaches for determining different parameters in the calculation were as follows:

Capillary pressure

The capillary pressure used in the model evolves according to the Kelvin-Laplace equation based on the measured RH. $R = 8.314 \text{ J}/(\text{mol}\cdot\text{K})$, $T = 293.15 \text{ K}$, $M_w = 0.01802 \text{ kg}/\text{mol}$ and $\rho_w = 1000 \text{ kg}/\text{m}^3$. RH and RH_s were determined by water activity sensors for both the cement paste sample and the extracted pore solution, see *Chapter 4*.

Saturation degree

The volume of evaporable water is according to [57] composed of physical bound water and free water that is lost after drying at $105 \text{ }^\circ\text{C}$. A different classification is possible with a non-destructive method like ^1H NMR, where evaporable water is considered as the sum of gel water, interlayer water and capillary water [58]. In Powers' model, however, the 'gel water' has a different meaning as the gel water defined in this chapter [59]. Therefore, in Powers' model, the evaporable water was calculated by combining only 'gel water' and capillary water. In the method based on ^1H NMR, the volume of evaporable water came from the sum of the detected gel water, interlayer water and capillary water. The total porosity in the denominator of the right side of *Equation 6.6* should be the sum of both the gel pores and the capillary pores, see *Equation 6.16*.

Equation 6.16

$$S = \frac{V_{ew}(\alpha)}{V_p(\alpha)} = \frac{V_{cw}(\alpha) + V_{gw}(\alpha) + V_{inter}(\alpha)}{V_{cw}(\alpha) + V_{gw}(\alpha) + V_{inter}(\alpha) + V_{cs}(\alpha)}$$

where: V_{cw} [ml/ml], V_{gw} [ml/ml] and V_{inter} [ml/ml] are the volume fraction of the capillary water, gel water and interlayer water, respectively. V_{cs} [ml/ml] is the chemical shrinkage or the emptied pore volume fraction. All of them depend on the degree of hydration of the system α and the dependence is unique only in sealed conditions. In order to compare two methods for calculating S , the porosity in *Equation 6.6* is considered as the volume of all evaporable water and the chemical shrinkage.

To obtain the volume fraction of capillary water, gel water and interlayer water from ^1H NMR, signal fractions of different types of water obtained from ^1H NMR (*Chapter 4*) were transformed to the volume fractions of the different water populations in the systems with the assumption of the same density of $1 \text{ g}/\text{cm}^3$ for all types of water.

According to Powers' model, the volume of evaporable water of Cement-0.35, CQZ40-0.35 and CFA40-0.35 up to 28 d can be determined by assuming: non-evaporable water equal to $0.23 \text{ g}/\text{g}$ of

reacted cement and 0 g/g of reacted fly ash, chemical shrinkage equal to 6.4 ml/100 g of reacted cement and 10 ml/g of reacted fly ash [5,60]:

$$V_{cs} = 0.2 \cdot (1 - p_0) \cdot \alpha$$

$$V_{cw} = p_0 - 1.3 \cdot (1 - p_0) \cdot \alpha$$

$$V_{gw} = 0.6 \cdot (1 - p_0) \cdot \alpha$$

where: the initial porosity of three systems p_0 and the degree of reaction of fly ash were calculated in *Chapter 2*. The degree of hydration of the cement α is determined from the cumulative heat release measured by isothermal calorimetry, also in *Chapter 2* with the following equation:

$$\alpha = \frac{Q(t)}{Q_\infty}$$

where: $Q(t)$ is the cumulative heat released at time t which can be obtained from calorimetry. Q_∞ is the potential heat of the cement at complete hydration, which can be determined from the mineral phases composition of the cement from knowledge of the enthalpy of complete hydration of each phase ΔH [61].

$$Q_\infty = \Delta H_{C_3S} \cdot C_3S\% + \Delta H_{C_2S} \cdot C_2S\% + \Delta H_{C_3A} \cdot C_3A\% + \Delta H_{C_4AF} \cdot C_4AF\%$$

where: ΔH of C_3S , C_2S , C_3A and C_4AF are equal to 517 J/g, 262 J/g, 1144 J/g⁷ or 1672 J/g⁸, 418 J/g⁹, respectively. $C_3S\%$, $C_2S\%$, $C_3A\%$ and $C_4AF\%$ are the percentages of the four main clinker phases in the cement.

The most common methods used for obtaining the porosity are water absorption [62], MIP and nitrogen adsorption and desorption isotherms [63]. The water absorption is simple to operate but the porosity obtained from it has been found to be much higher than the one from MIP [64]. The MIP and nitrogen adsorption methods require drying the samples prior to the measurements, which may induce some damage to the sample. On the other hand, as already mentioned, traditional gravimetric methods (by weighing a sample at a certain state and next after drying) are not applicable for the systems that undergo hydration process due to the time necessary for drying of the samples while they still hydrate¹⁰. Secondly, neither MIP nor nitrogen adsorption desorption isotherms are able to quantify the total amount of gel pores, since mercury and nitrogen cannot enter all the pores (i.e., the minimum entry pore diameter of MIP is around 2.4 nm assuming a contact angle of 120°) [65–67]. To avoid these limitations, in this chapter, the total porosity obtained from ¹H NMR (water-filled pores) and chemical shrinkage (hydration emptied pores with voids) together was used to compare to the estimation from Powers' model.

⁷ Considering the reaction of C_3A with gypsum to produce AFm

⁸ Considering the reaction of C_3A with gypsum to produce AFt

⁹ Considering the reaction of C_4AF with portlandite to produce hydrogarnet

¹⁰ Measured results of porosity are influenced by different drying method, for instance, direct drying methods, e.g., freeze-drying, give a bigger peak in measured pore size distribution by MIP compared to the solvent exchange [81].

Elastic modulus and Poisson's ratio

The elastic modulus was based on the results of the static elastic modulus measurement from *Chapter 5*. The Poisson's ratio was determined from the dynamic Young's modulus of elasticity (E [GPa]) and the shear modulus (G [GPa]) according to ASTM C215 [68] by using prismatic samples, see *Equation 6.17*:

Equation 6.17

$$\nu = \frac{E}{2G} - 1$$

where: E and G were calculated based on the equations in the standard. The measured key values in both equations were the fundamental longitudinal frequency and the fundamental torsional frequency. Other parameters used in the calculation are shown in *Table 6.1*. The standard deviations at all ages (measurements performed once per day until 15 d) were lower than 0.02 for the Poisson's ratio.

Table 6.1 Parameters for calculating E and G

Parameters*	L [m]	b [m]	t [m]	R [-]	A [m ²]
Value	0.1	0.025	0.025	1.183	0.000625

* The parameters are the ones used in ASTM C215 [68] for relating the frequency and the moduli. L is the length of the specimen, A is the cross section of the specimen, b and t are width and thickness of the specimen, respectively.

6.2.2 Poro-visco-elastic prediction

From the experimental point of view, the capillary pressure (assumed as the driving force of autogenous shrinkage) is a hydrostatic load, in which the stress state is different than in uniaxial compression or tension tests commonly used to investigate creep of concrete. Due to its relative simplicity and relevance for practice, the uniaxial compressive creep test has been used most widely in studies of visco-elastic deformation of cementitious materials [69,70]. The experimental campaign and a discussion of the visco-elastic response of the cementitious materials studied in this thesis were presented in *Chapter 5*. From the prediction point of view, as stated in *Chapter 5*, the main difficulty comes from the effect of aging at early ages.

In this chapter, the visco-elastic equivalent bulk modulus was calculated from the creep compliance and the visco-elastic Poisson's ratio measured under uniaxial compression conditions. Linear elastic properties were removed from the overall visco-elastic behavior in order to account only for the creep part; the separation was reported and discussed in *section 5.3.3*. The way for predicting the visco-elastic deformation was carried out with the generalized Kelvin-Voigt model and the input stress of the effective pore pressure. The evolution of the parameters (stiffness of the spring and the viscosity of dashpots) in the generalized Kelvin-Voigt chains model were obtained from *Chapter 5*.

The same evolution of all the parameters with the degree of hydration for Cement-0.35, CQZ40-0.35 and CFA40-0.35 were used also in this prediction.

The creep component of the linear autogenous shrinkage was predicted with the following equation:

Equation 6.18

$$\varepsilon_c(t) = \int_{t_0}^t \left\{ (1 - 2 \cdot \nu'(t)) \cdot \frac{\partial J(t, t')}{\partial t} - \frac{1}{3K_S} \right\} \cdot d\sigma = \int_{t_0}^t \left\{ (1 - 2 \cdot \nu'(t)) \cdot \frac{\partial J(t, t')}{\partial t} - \frac{1}{3K_S} \right\} \cdot (dP_{cap} \cdot S + P_{cap} \cdot dS)$$

where: t , t_0 and t' are the current time, reference time and the loading time, respectively; ν' is the visco-elastic Poisson's ratio, $J(t, t')$ is the specific basic creep compliance (uniaxial).

The visco-elastic Poisson's ratio has rarely been measured accurately due to the practical difficulty of this kind of measurements, in particular low resolution of the measurements combined with small deformations. In literature, there is large scatter reported, with contradictory trends (increase and decrease over time), but the mature values reported are around 0.15 to 0.2 [71]. It has been found to be similar to the elastic Poisson's ratio when the stress level is lower than 40 % [72,73]. A prediction of the visco-elastic Poisson's ratio based on microstructural modeling was done by Li et al. [74] assuming the mechanism of relaxation from the time-dependent dissolution of cement grains. In their simulation, the visco-elastic Poisson's ratio was found to depend on the w/c and on the loading time. To evaluate the effect of the visco-elastic Poisson's ratio on the autogenous shrinkage predictions, in this work, two approaches were used in the prediction of visco-elastic response of the autogenous shrinkage: 1) use of the elastic Poisson's ratio; 2) use of the value from the simulation in [74].

6.3 Parameters from experiments

6.3.1 Saturation degree

The saturation degree of three systems measured with ^1H NMR are shown in *Figure 6.5* as a function of time and of degree of hydration of cement together with the estimation using Powers' method. The water fraction in CFA40-0.35 could not be measured with ^1H NMR due to too fast relaxation with high iron content in the system [75].

As expected, Cement-0.35 had the lowest saturation degree compared to that of CQZ40-0.35 and CFA40-0.35 in both approaches. In the ^1H NMR and chemical shrinkage method, the difference between the saturation degree of Cement-0.35 and CQZ40-0.35 was small. More water-filled pores were found in the CQZ40-0.35 paste due to the higher effective water in the system. With Powers' model, the CFA40-0.35 and Cement-0.35 both had saturation degree of about 0.86 at 28 d.

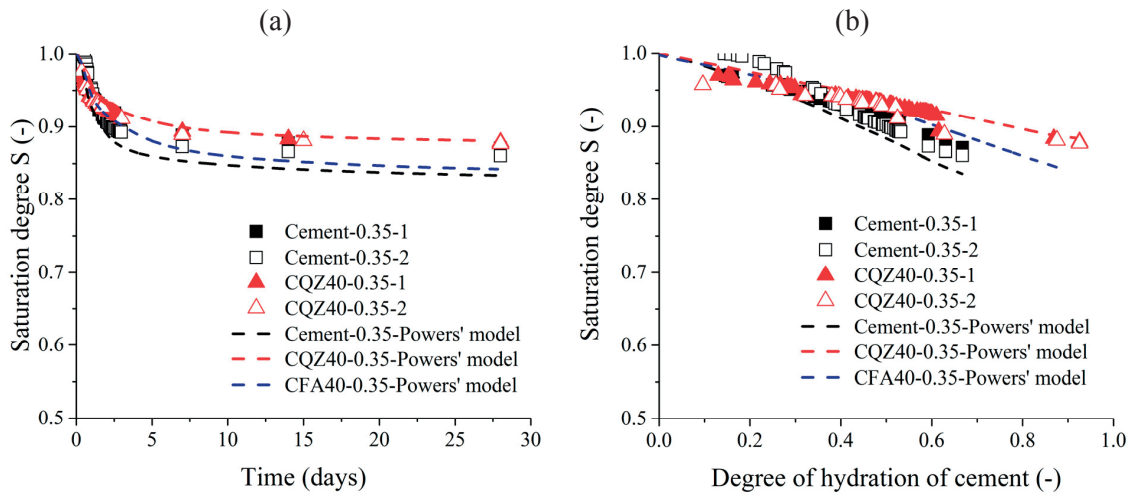


Figure 6.5 Saturation degrees of both systems calculated either with Powers' model or based on ^1H NMR results: (a) saturation degree as a function of time; (b) saturation degree as a function of degree of hydration

Comparing the saturation degree obtained from Powers' model and the method combining ^1H NMR and chemical shrinkage, Powers' model seemed to overestimate the change of the degree of saturation in Cement-0.35. In CQZ40-0.35, the saturation degree from two approaches matched well considering both the trend and the absolute value. As shown in *Figure 6.5*, the prediction of saturation degree agreed very well for both methods until 2-3 days and then they diverged. The maximum difference of the saturation degree from Powers' model and the measurements was around 0.05. According to *Figure 6.5(b)*, the trend of the evolution of the saturation degree with the degree of hydration in Cement-0.35 and CQZ40-0.35 from two approaches had high similarity.

In [76], Powers and Brownyard carefully executed measurements and proposed a model for the solid and liquid compositions in the hydrated cement and the mechanical properties. Their work is fundamental but the model obtained inevitably may have the limitations of the materials used at that time (almost 70 years ago). The cement mineralogy difference can be part of the reason for the different results from the two approaches.

In a recent review by Brouwers [67], he claimed that Powers and Brownyard overestimated the volume of the gel water because they disregarded the higher density of the gel water. The question of gel water being compressed was discussed for long time and the temporary conclusion was the density of gel water to be 1.11 g/cm^3 instead of 1 g/cm^3 [77]. However, this could be partly due to different cement mineralogy as well. This overestimation happened also in the prediction with ^1H NMR (assuming a same density for both gel and capillary water).

Another recent finding from ^1H NMR shows that the linear growth or variation of the volume fraction of different types of water from Powers' model was not valid at early ages [65]. ^1H NMR experiments showed a steep desaturation of capillary pores at the initial stage of hydration (before about 1 d) [65]. However, this difference in the volume fraction of different water populations can be also partly due to the aforementioned different cement composition.

6.3.2 Average pore pressure

The average pore pressure ($S \cdot P_c$) is assumed as the driving force both for the elastic response and the visco-elastic response of the materials, as shown in *Figure 6.6*. For ease of representation, the effective pore pressure (negative) calculated from the average RH was plotted as a positive value in *Figure 6.6*. As cement hydration goes on, the pressure increases, following the Kelvin equation. The maximum capillary pressure reaches around 14 MPa, considerably less than the uniaxial compressive strength (see *Chapter 5*), therefore it can be assumed that the material remains in the linear elastic regime.

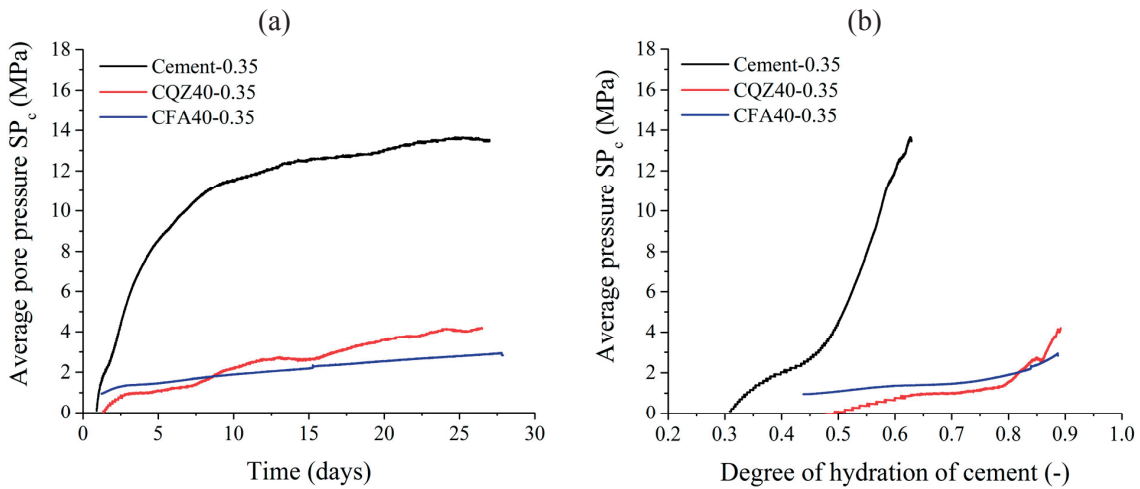


Figure 6.6 Average pore pressure in two systems: (a) as a function of time; (b) as a function of degree of hydration (with S from Powers' model)

6.3.3 Other parameters

Poisson's ratio

The calculated dynamic elastic modulus, the shear modulus and the corresponding Poisson's ratio of cement paste up to 10 d are plotted in *Figure 6.7*. Note that the Poisson's ratio was adopted from [47], where it was determined experimentally with resonance ultrasound spectroscopy (i.e. dynamic measurements) on an ordinary Portland cement paste with w/c of 0.30. The Poisson's ratio decreased sharply during the first day, from about 0.32 to 0.24. After 2 days, the evolution of the Poisson's ratio was much slower; the value decreased asymptotically to a constant Poisson's value close to 0.22. The development of Poisson's ratio at early ages is found to be dominated by a fluid phase response when the water phase is continuous, and then by a solid phase response when the solid phases start to percolate [78]. An exponential equation was used to fit the experimental data, which was later used in the prediction of autogenous shrinkage.

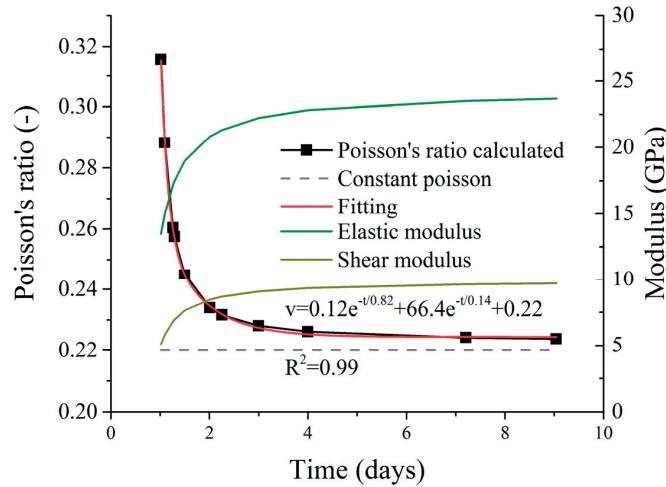


Figure 6.7 Poisson's ratio calculated from the Young's modulus and the shear modulus and comparison with the constant Poisson's ratio from literature

Visco-elastic 'Poisson's' ratio

The visco-elastic 'Poisson's' ratio is considered here as the ratio between transversal to longitudinal visco-elastic deformation. In [74], it was obtained from FEM simulations on evolving microstructures considering the cement particles dissolution/precipitation and C-S-H intrinsic visco-elasticity during hydration. The simulated visco-elastic Poisson's ratio was shown in *Figure 6.8* for loading at 1 d and 7 d with either constant elastic Poisson's ratio or constant bulk modulus, adapted from [74]. For a constant Poisson's ratio of C-S-H (0.25), the expression for the Young's modulus used in the prediction was: $E(t) = 11.2 + 11.2 \cdot \exp(-0.2t)$ GPa. For a constant bulk modulus of C-S-H (14.9 GPa), the expression for the shear modulus applied in the simulation was: $G(t) = 4.5 + 4.5 \cdot \exp(-0.2t)$ GPa.

In the first case, the visco-elastic Poisson's ratio of both loading ages was decreasing with the increase of the hydration time. The visco-elastic Poisson's ratio of samples loaded at 7 d was 0.02 higher than the one loaded at 1 d. In the second case, with a constant bulk modulus, the higher visco-elastic Poisson's ratio was found also in the sample loaded at 7 d with an even larger difference (0.03). With constant Poisson's ratio of the C-S-H, the visco-elastic Poisson's ratio was evolving slowly, almost remaining at a constant value (0.25 for load at 1 d, 0.27 for load at 7 d). However, with constant bulk modulus, the variation of the visco-elastic Poisson's ratio was much larger. In both loading conditions, the value increased faster in the first 15 d and reached a plateau later on. In the comparison of the prediction with the *Biot-Bishop approach*, four simulated visco-elastic Poisson's ratio will be used. For the results of specimens being loaded at 7 d, the same evolution of the Poisson's ratio was assumed to start at the time for simulation instead of 7 d, meaning the curve was shifted as started from 0 d for the prediction.

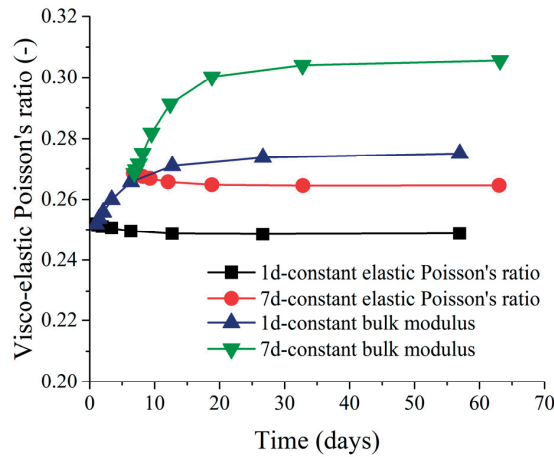


Figure 6.8 Visco-elastic Poisson's ratio, adapted from [74]

Total porosity

In *Vlahinić's method*, the total porosity of the samples was needed for calculating \bar{K}_s . The total porosity both from MIP and from ^1H NMR and chemical shrinkage explained in *Equation 6.16* (here interlayer water was not considered in the calculation), is plotted in *Figure 6.9*.

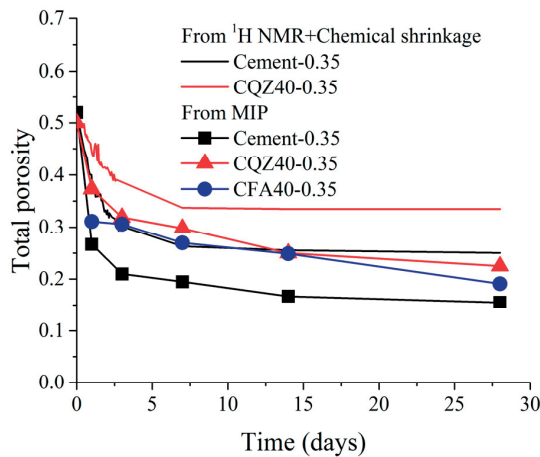


Figure 6.9 Total porosity of both systems (porosity at 0 d was the calculated initial porosity)

As expected, the total porosity of Cement-0.35 and CQZ40-0.35 from ^1H NMR and chemical shrinkage is higher than the one from MIP. The porosity measured from the former method is almost 10 % higher than the one measured from the latter method at 28 d. In the figure, it is evident that the total porosity of Cement-0.35 and CFA40-0.35 decreased much faster than that of CQZ40-0.35 during the first day, starting at similar initial porosity. From 1 d to 28 d, the porosity was lower in Cement-0.35. CFA40-0.35 had slightly lower porosity than CQZ40-0.35. According to the results from ^1H NMR

and chemical shrinkage, at 28 d, the total porosity of CQZ40-0.35 was 0.33, while the value of Cement-0.35 was around 0.28. The difference in porosity is due to the relatively higher water to cement ratio in CQZ40-0.35. The reaction of cement was faster in the case of CQZ40-0.35 but the total consumed water was more in Cement-0.35. To predict autogenous shrinkage continuously, porosity from both methods are used. Exponential formulae were used for fitting the total porosity.

6.4 Prediction results

6.4.1 Prediction of elastic response

Comparison of the prediction from three different methods

The predicted elastic response of the autogenous shrinkage by three different kinds of models and the measured autogenous shrinkage for three systems are shown in *Figure 6.10*. In *Vlahinić's method*, \overline{K}_s calculated with the porosity determined both from MIP and $^1\text{H NMR}$ and chemical shrinkage was used in the prediction of autogenous shrinkage of Cement-0.35 and CQZ40-0.35.

As already discussed (see *Chapter 3 Figure 3.11*), the autogenous shrinkage of the pure cement paste was almost 5 times higher than that of CQZ40-0.35 and about 3 times higher than that of CFA40-0.35. For CQZ40-0.35, the autogenous deformation showed an expansion after 3 d, which peaked at about 10 d and was followed only by moderated shrinkage afterwards. This behavior is not reflected in internal RH, see *section 3.2.2*, which decreased constantly albeit only moderately. As expected, no poro-elastic approach is able to predict the expansion.

For all prediction methods, the predicted elastic component of the autogenous shrinkage in Cement-0.35 and CFA40-0.35 at 28 d was only about one quarter of the measured autogenous shrinkage. This is in agreement with the results in [5], where the prediction based on the *Biot-Bishop equation* diverged when the RH was lower than 97 %. In Cement-0.35, the RH was lower than 97 % after around 3 d and this time appears also to be the time of divergence between the simulations and the measured autogenous shrinkage. In [5], a constant Poisson's ratio was used, which would cause an even earlier divergence here. As shown in *Figure 6.10*, with a constant Poisson's ratios of 0.22, the predicted poro-elastic deformation was higher than the one with the measured Poisson's ratio and also higher than the prediction by other methods.

The difference of the predicted results by these methods was relatively small. The maximum difference of around 60 $\mu\text{m}/\text{m}$ occurred in Cement-0.35. This was not surprising (see *section 6.1.2*), since these three models gave similar results at high saturation degree. According to [79], in predictions of drying shrinkage also using poro-elasticity approaches, the prediction from different models were similar when the RH was higher than 75 %, which is always the case for self-desiccation. By using *Coussy's method*, the predicted autogenous shrinkage was the highest among all methods with measured Poisson's ratio, due to the consideration of the additional interfacial energy in the partly saturated

porous samples. Moreover, even the porosities determined from the two methods are significant different, the predicted elastic response of the autogenous shrinkage is still similar. This is due to the rather smaller change of \bar{K}_S caused by the different porosities.

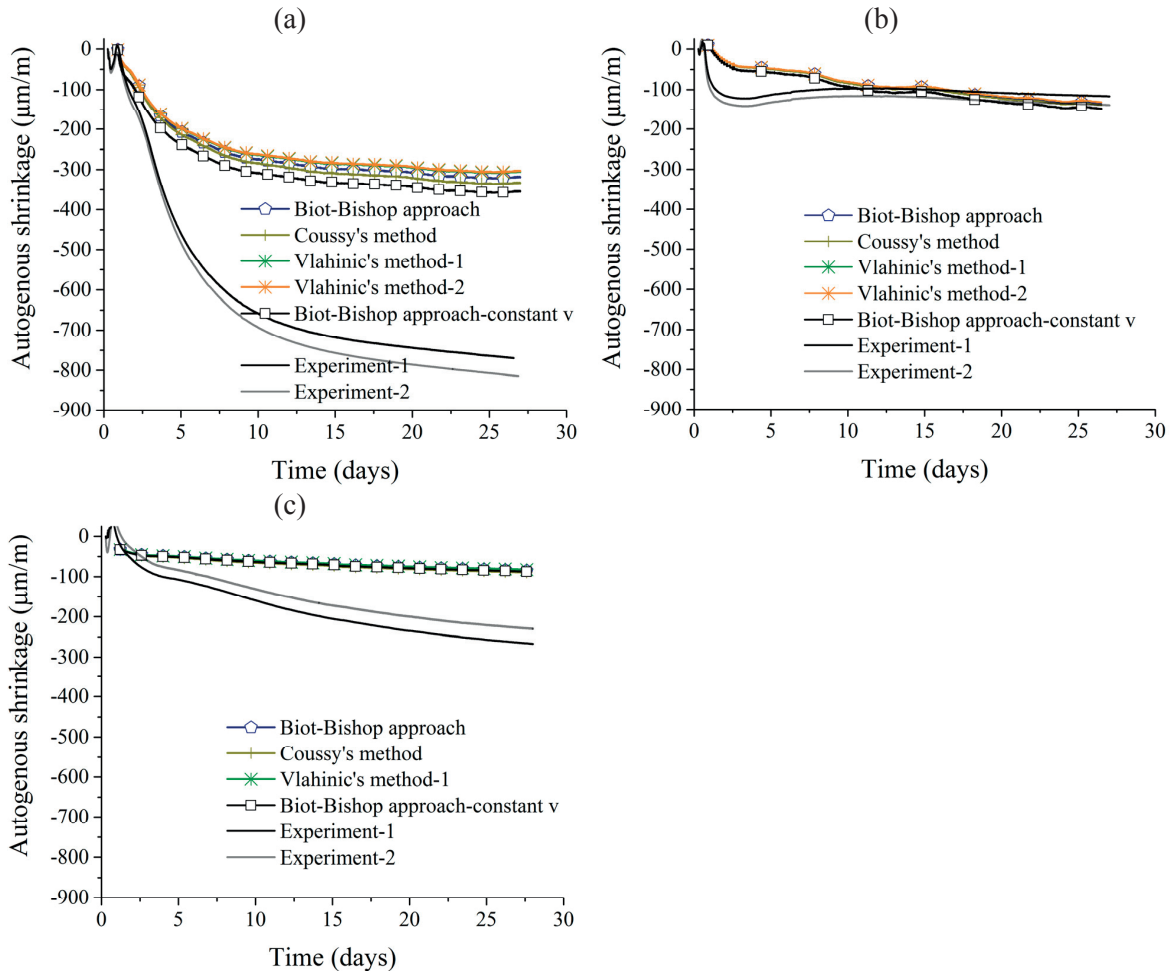


Figure 6.10 Predicted elastic component of autogenous shrinkage with three different models ((a) Cement-0.35; (b) CQZ40-0.35, Vlahinić's method-1 used the porosity from MIP, Vlahinić's method-2 used the porosity from ^1H NMR and chemical shrinkage; (c) CFA40-0.35)

For CQZ40-0.35, the predicted result was very close to the measured autogenous shrinkage at 28 d. However, attention has to be paid to the period before 7 d, where the predictions were much higher than the measured results. The RH of CQZ40-0.35 was above 96 % until 28 d, which could explain the similar results between the prediction and measurements. Another reason is the restraint effect of the quartz fillers, which may have the same function as the fine aggregate in drying shrinkage of mortars [49]. However, since this restraint needs to be considered together with the porosity of the system, as shown in specific basic creep result, CQZ40-0.35 had even a bit higher creep than Cement-0.35. Another possible explanation for the match at later ages is the observed swelling at early ages,

which resulted in lower total shrinkage. As already remarked, the poro-elastic approaches used in this study do not include any mechanism of swelling except for the hygral swelling at increasing RH, which is not the case here. Moreover, it should be noted that the effective capillary pressure is much lower in CQZ40-0.35, which experienced little self-desiccation. At these low capillary pressure levels, expansion due to crystallization/hydration pressure becomes dominant (similar as the case of mixtures with internal curing).

Comparison of the prediction with different saturation degree

By using the *Biot-Bishop approach*, the predicted results with the saturation degree obtained with two different methods are presented in *Figure 6.11*. From *section 6.3.1*, the saturation degree was underestimated by Powers' method; therefore, as shown in the figure, the corresponding autogenous shrinkage was also lower with Powers' method in both samples. However, the difference was only around 15-30 $\mu\text{m}/\text{m}$, which is not significant, even if the difference between the saturation degrees was about 0.05. Therefore, it can be concluded that the saturation degree by using relatively simple Powers' method, is still good enough for the prediction of the poro-elastic deformation of autogenous shrinkage [5].

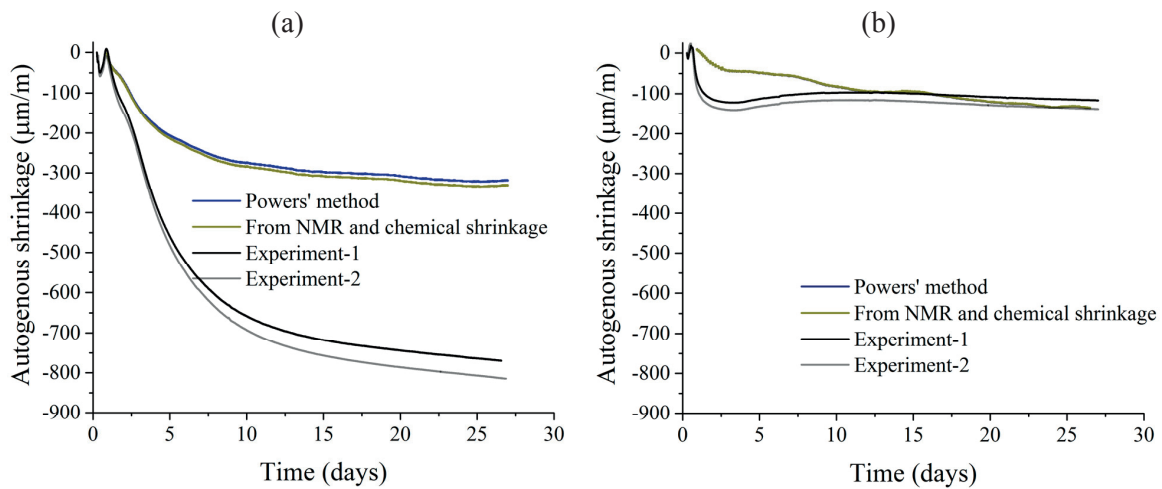


Figure 6.11 Predicted elastic component of autogenous shrinkage with different saturation degrees ((a) Cement-0.35; (b) CQZ40-0.35)

Comparison of the predictions with different bulk moduli

The comparison of the predicted results by using different values for the bulk modulus of the solid skeleton, K_s , is shown in *Figure 6.12*. Again, the impact of the variation in K_s is negligible, with 50 $\mu\text{m}/\text{m}$ difference between the highest bulk modulus and the lowest bulk modulus. The higher the bulk modulus of the solid skeleton was, the higher the predicted elastic component of the autogenous shrinkage. Using a constant value for the bulk modulus of the solid skeleton, the prediction of the

autogenous shrinkage would be underestimated at later ages due to the most likely decreasing of the K_s due to the solidification of C-S-H.

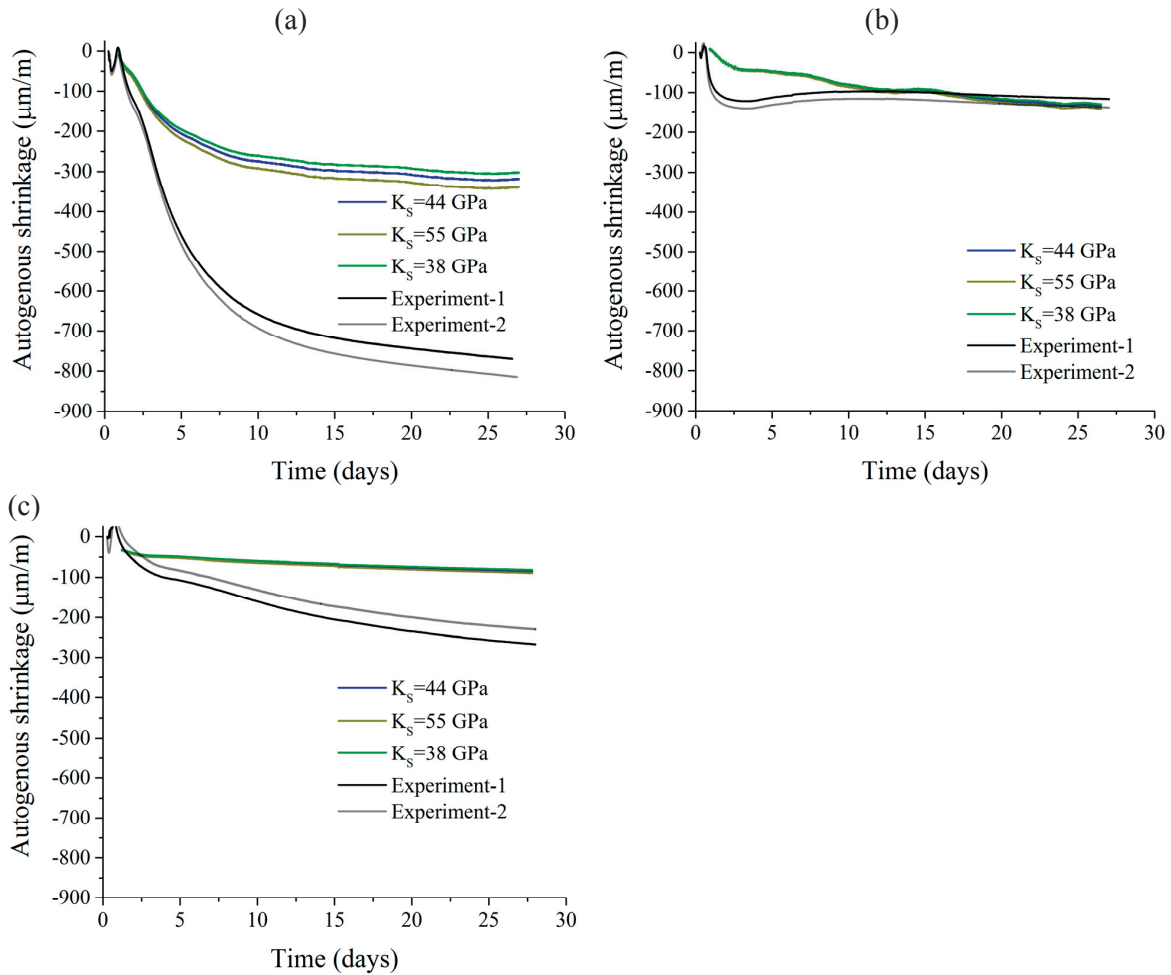


Figure 6.12 Predicted elastic component of autogenous shrinkage with different values for the bulk modulus of the solid skeleton ((a) Cement-0.35; (b) CQZ40-0.35; (c) CFA40-0.35)

6.4.2 Prediction of the visco-elastic component

In Figure 6.13, the predicted visco-elastic component of the autogenous shrinkage based on generalized Kelvin-Voigt chains model is shown, in which the impact of using different visco-elastic Poisson's ratios is shown (see section 6.3.3). In Cement-0.35 and CFA40-0.35, the predicted visco-elastic component is almost 2 times higher than the elastic components. In CQZ40-0.35, the predicted visco-elastic component has the same magnitude as the elastic part.

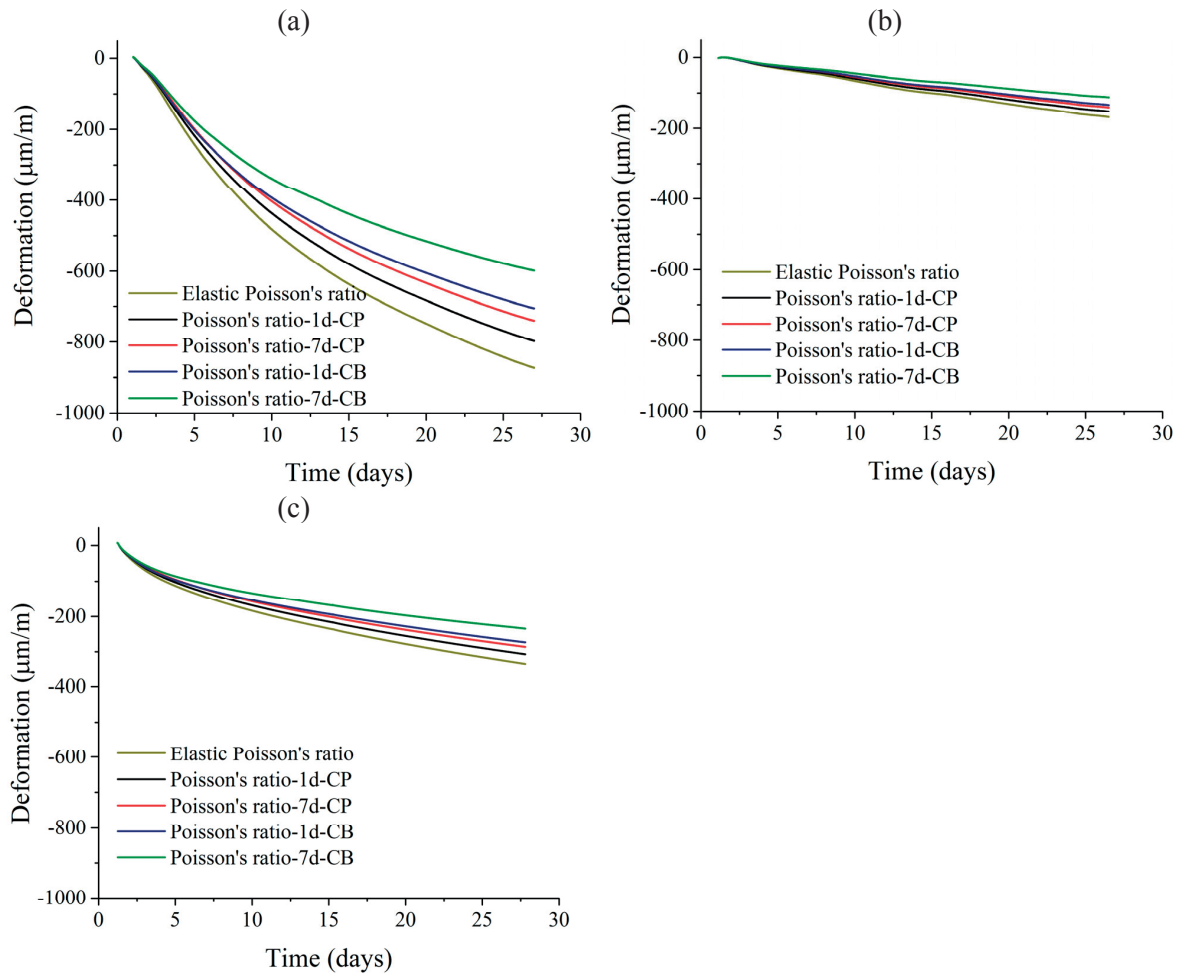


Figure 6.13 Comparison of the predicted visco-elastic component of the autogenous shrinkage with different visco-elastic Poisson's ratio (the visco-elastic Poisson's ratio obtained by assuming constant Poisson's ratio was marked as CP, the one obtained by assuming constant bulk modulus was marked as CB, (a) Cement-0.35; (b) CQZ40-0.35; (c) CFA40-0.35)

Comparing the results of the visco-elastic component of autogenous shrinkage using different visco-elastic Poisson's ratios, it can be concluded that the visco-elastic Poisson's ratio has a rather large effect on the final prediction, especially for Cement-0.35. While the overall trend is not affected by changes in the visco-elastic Poisson's ratio, the difference in the absolute shrinkage values can be as high as $200 \mu\text{m/m}$. The highest predicted visco-elastic component was found when the visco-elastic Poisson's ratio was assumed to be equal to the elastic Poisson's ratio. The lowest predicted visco-elastic component of the autogenous shrinkage was found when the visco-elastic Poisson's ratio was taken from the data from 7 d loading with constant bulk modulus for all systems. There is not much difference between using the visco-elastic Poisson's ratio from under 1 d loading with constant bulk modulus and the one with constant Poisson's ratio under 7 d loading.

6.4.3 Prediction of overall autogenous shrinkage

The prediction of the total autogenous shrinkage, combining the poro-elastic response and the poro-visco-elastic component, is presented in *Figure 6.14*. The prediction took the average value of poro-visco-elastic deformation using different values for the visco-elastic Poisson's ratio. For Cement-0.35, the measured autogenous shrinkage was similar as the prediction before 7 d. After 7 d, the predicted autogenous shrinkage increased faster than the measured deformation. The difference of the autogenous shrinkage at 28 d between prediction and measurement was around 200 $\mu\text{m}/\text{m}$. In CQZ40-0.35, since the capillary pressure was much smaller than the one in Cement-0.35, the corresponding visco-elastic component was not significant. However, at 28 d, the predicted autogenous shrinkage was around 2 times higher than the measurement. In the latter case, the abnormal course of the measured shrinkage should be noted, with a very steep initial shrinkage followed by a moderate expansion; this could have been due to segregation of the mix. In CFA40-0.35, the difference of autogenous shrinkage at 28 d between the measurement and the prediction was lower than other two systems, around 100 $\mu\text{m}/\text{m}$.

The kinetics of the predicted autogenous shrinkage is higher than that of the experiments. In terms of qualitative differences between the three systems, the predicted results are in line with the experimental data, with Cement-0.35 and CQZ40-0.35 systems showing the highest and the lowest autogenous shrinkage, respectively, see *Figure 6.14 (d)*.

There are some possible explanations for the overestimation of autogenous shrinkage from predictions:

- 1) some parts of the discrepancy come from the impact of parameters associated to the prediction of poro-elastic deformation. Even though the effect of each parameter on the prediction was low, the overall influence can be as high as 100 $\mu\text{m}/\text{m}$ (considering the maximum difference in the predictions in this study), see *section 6.4.1*.

- 2) as stated in [80], the uniaxial visco-elastic response of the material is most likely different from the bulk visco-elastic response. The faster relaxation in uniaxial visco-elastic response leads to the higher predicted shrinkage. Grasley and Leung [6] suggested an increasing visco-elastic Poisson's ratio after their prediction. In this chapter, comparison of creep deformation by using different Poisson's ratio confirmed this supposition. It can be seen from this study that the visco-elastic Poisson's ratio may be as high as 0.3 (as the prediction made by using the data from 7 d loading with constant bulk modulus). Since in this study, the same visco-elastic Poisson's ratio was used for all three systems, the difference of the experiments and the prediction was found also different in the three systems.

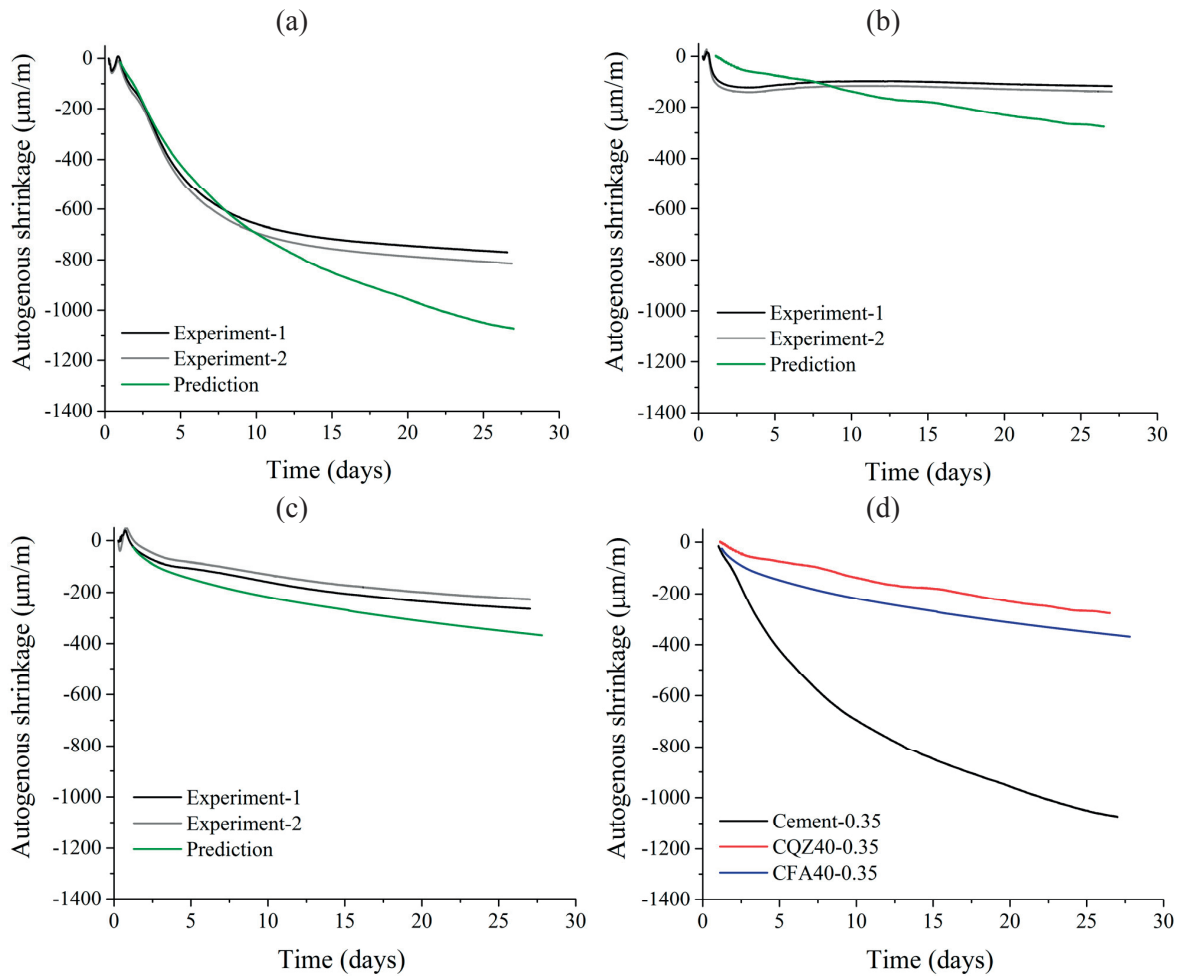


Figure 6.14 Predicted autogenous shrinkage of three systems: (a) Cement-0.35; (b) CQZ40-0.35; (c) CFA40-0.35; (d) Comparison of predictions)

6.5 Conclusions

In this chapter, predictions of autogenous shrinkage until 28 d based on poromechanics and including elastic and visco-elastic response of the materials were presented. The modeling approach was based on a genuine experimental dataset on shrinkage and creep. Different poro-elastic approaches (*Biot-Bishop approach*, *Coussy's method*, and *Vlahinić's method*) were used for the elastic component. The poro-elastic deformation did not require any parameters fitting. A generalized Kelvin-Voigt chains model accounting for aging was used for the prediction of the visco-elastic deformation. The conclusions from this study are as follows:

1. The results presented in this chapter prove the possibility to predict autogenous shrinkage with reasonable accuracy with a limited number of fit parameters (only in generalized Kelvin-Voigt chains model), on the condition that the visco-elastic component is accounted for and its parameters are determined based on experimental creep measurements.

2. The visco-elastic response outweighed the elastic response in the total prediction for the three systems studied in this chapter. The differences depend on the properties of the system, such as w/c and dosage of SCMs.
3. A sensitivity study about the impact on the predicted elastic component of the autogenous shrinkage by using different models, bulk moduli of solid skeleton, Poisson's ratio and saturation degrees was performed. The effect of all these factors are not significant, with a maximum difference around 100 $\mu\text{m}/\text{m}$ found when using different poro-elastic models.
4. The moderate overestimation of the predicted autogenous shrinkage at 28 d is partly due to the uncertainties from the parameters for poro-elastic prediction and partly due to the relatively large impact of the visco-elastic Poisson's ratio on the visco-elastic prediction. An increasing Poisson's ratio is more reasonable for the prediction and the rate of increasing depends on the components of the systems.
5. The reasonably good agreement of the predicted and measured autogenous shrinkage, including the visco-elastic component, proves that the visco-elastic response under the action of hydrostatic pressure (pore fluid pressure) can be assessed based on uniaxial compressive creep measurements.

6.6 References

- [1] C. Pichler, R. Lackner, A multiscale creep model as basis for simulation of early-age concrete behavior, *Comput. Concr.* 5 (2008) 295–328.
- [2] X. Y. Wang, H. S. Lee, S. M. Lim, Numerical simulation of autogenous shrinkage of eco-friendly blended Portland cements using a multi-component hydration model, *Mater. Sci. Forum.* 569 (2008) 261–264.
- [3] Z. Wang, G. Li, Experimental method and prediction model for autogenous shrinkage of high performance concrete, *Constr. Build. Mater.* 49 (2013) 400–406.
- [4] Q. Do, Modelling properties of cement paste from microstructure : porosity, mechanical properties, creep and shrinkage, EPFL, 2013.
- [5] P. Lura, O. M. Jensen, K. van Breugel, Autogenous shrinkage in high-performance cement paste: An evaluation of basic mechanisms, *Cem. Concr. Res.* 33 (2003) 223–232.
- [6] Z. C. Grasley, C. K. Leung, Desiccation shrinkage of cementitious materials as an aging, poroviscoelastic response, *Cem. Concr. Res.* 41 (2011) 77–89.
- [7] D. Gawin, F. Pesavento, B. a. Schrefler, Hygro-thermo-chemo-mechanical modelling of concrete at early ages and beyond. Part II: shrinkage and creep of concrete, *Int. J. Numer. Methods Eng.* 67 (2006) 332–363.
- [8] X. Li, Z. C. Grasley, J. W. Bullard, E. J. Garboczi, Irreversible desiccation shrinkage of cement paste caused by cement grain dissolution and hydrate precipitation, *Mater. Struct.* 50 (2017) 104.
- [9] C. Hua, P. Acker, A. Ehrlacher, Analyses and models of the autogenous shrinkage of hardening cement paste, *Cem. Concr. Res.* 25 (1995) 1457–1468.

- [10] M. H. Hubler, R. Wendner, Z. P. Bažant, Statistical justification of Model B4 for drying and autogenous shrinkage of concrete and comparisons to other models, *Mater. Struct.* 3 (2015) 797–814.
- [11] Y. Li, J. Bao, Y. Guo, The relationship between autogenous shrinkage and pore structure of cement paste with mineral admixtures, *Constr. Build. Mater.* 24 (2010) 1855–1860.
- [12] Z. Wang, G. Li, A prediction model for autogenous shrinkage of high-performance concrete in bridge engineering, *Mag. Concr. Res.* 65 (2013) 1325–1335.
- [13] E. Tazawa, S. Miyazawa, Influence of cement and admixture on autogenous shrinkage of cement paste, *Cem. Concr. Res.* 25 (1995) 281–287.
- [14] E. Tazawa, S. Miyazawa, Influence of constituents and composition on autogenous shrinkage of cementitious materials, *Mag. Concr. Res.* 49 (1997) 15–22.
- [15] Japan Concrete Institute, Technical Committee report on autogenous shrinkage, 2002.
- [16] S. W. Yoo, S. J. Kwon, S. H. Jung, Analysis technique for autogenous shrinkage in high performance concrete with mineral and chemical admixtures, *Constr. Build. Mater.* 34 (2012) 1–10.
- [17] CEB-FIP, CEB-FIP Model Code 1990, Thomas Telford, London, 1994.
- [18] R. Wendner, M. H. Hubler, Z. P. Bažant, The B4 model for multi-decade creep and shrinkage prediction, in: *Mech. Phys. Creep. Shrinkage, Durab. Concr.*, n.d.: pp. 429–436.
- [19] Rilem recommendation: Creep and shrinkage prediction model for analysis and design of concrete structures-model B3, *Mater. Struct.* 3 (1995) 357–365.
- [20] M. L. Nehdi, A. M. Soliman, Artificial Intelligence Model for Early-Age Autogenous Shrinkage of Concrete, *ACI Mater. J.* 109 (2012) 353–362.
- [21] J. Liu, K. Yan, X. Zhao, Y. Hu, Prediction of autogenous shrinkage of concretes by support vector machine, *Int. J. Pavement Res. Technol.* 9 (2016) 169–177.
- [22] O. M. Jensen, P. F. Hansen, Autogenous deformation and RH-change in perspective, *Cem. Concr. Res.* 31 (2001) 1859–1865.
- [23] C. Pichler, R. Lackner, H. A. Mang, A multiscale micromechanics model for the autogenous-shrinkage deformation of early-age cement-based materials, *Eng. Fract. Mech.* 74 (2007) 34–58.
- [24] D. Gawin, F. Pesavento, B. A. Schrefler, Modelling creep and shrinkage of concrete by means of effective stresses, *Mater. Struct.* 40 (2007) 579–591.
- [25] F. Benboudjema, J.M. Torrenti, Early-age behaviour of concrete nuclear containments, *Nucl. Eng. Des.* 238 (2008) 2495–2506.
- [26] V. Gribniak, G. Kaklauskas, R. Kliukas, R. Jakubovskis, Shrinkage effect on short-term deformation behavior of reinforced concrete – When it should not be neglected, *Mater. Des.* 51 (2013) 1060–1070.
- [27] H. Chen, M. Wyrzykowski, K. Scrivener, P. Lura, Prediction of self-desiccation in low water-to-cement ratio pastes based on pore structure evolution, *Cem. Concr. Res.* 49 (2013) 38–47.
- [28] V. Baroghel-Bouny, M. Mainguy, T. Lassabatere, O. Coussy, Characterization and identification of equilibrium and transfer moisture properties for ordinary and high-performance cementitious materials, *Cem. Concr. Res.* 29 (1999) 1225–1238.

- [29] Q. H. Do, S. Bishnoi, K. L. Scrivener, Microstructural Modeling of Early-Age Creep in Hydrating Cement Paste, *J. Eng. Mech.* (2016) 4016086.
- [30] O. Coussy, *Poromechanics*, 2004.
- [31] C. L. Page, Ø. Vennesland, Pore solution composition and chloride binding capacity of silica-fume cement pastes, *Matériaux Constr.* 16 (1983) 19–25.
- [32] K. S. Pitzer, *Activity coefficients in electrolyte solutions*, Kluwer Academic Publishers-Plenum Publishers, Florida, 1974.
- [33] J. Zhang, D. Hou, Y. Han, Micromechanical modeling on autogenous and drying shrinkages of concrete, *Constr. Build. Mater.* 29 (2012) 230–240.
- [34] T. Lu, E. Koenders, Modeling and analyzing autogenous shrinkage of hardening cement paste 1 Introduction 2 Theoretical basis, in: 14 Proc. Int. Conf. Aging Mater. Struct., 2014: pp. 155–162.
- [35] Y. Li, J. Li, Capillary tension theory for prediction of early autogenous shrinkage of self-consolidating concrete, *Constr. Build. Mater.* 53 (2014) 511–516.
- [36] O. Bernard, F. J. Ulm, E. Lemarchand, A multiscale micromechanics-hydration model for the early-age elastic properties of cement-based materials, *Cem. Concr. Res.* 33 (2003) 1293–1309.
- [37] S. Diamond, M. Leeman, Pore size distributions in hardened cement paste by SEM image analysis, in: *MRS Proceeding*, Cambridge University Press, 1994.
- [38] M. Wyrzykowski, P. Lura, F. Pesavento, D. Gawin, Modeling of internal curing in maturing mortar, *Cem. Concr. Res.* 41 (2011) 1349–1356.
- [39] A. W. Bishop, G. E. Blight, Some aspects of effective stress in saturated and partly saturated soils, *Géotechnique*. 13 (1963) 177–197.
- [40] O. Coussy, The equivalent pore pressure and the swelling and shrinkage of cement-based materials, *Mater. Struct.* 37 (2003) 15–20.
- [41] I. Vlahinić, H. M. Jennings, J.J. Thomas, A constitutive model for drying of a partially saturated porous material, *Mech. Mater.* 41 (2009) 319–328.
- [42] T. C. Hansen, Physical structure of hardened cement paste. A classical approach, *Mater. Struct.* 19 (1986) 423–436.
- [43] A. Gajewicz, Characterisation of cement microstructure and pore – water interaction by 1H Nuclear Magnetic Resonance Relaxometry, University of Surrey, 2014.
- [44] C. Di Bella, M. Griffa, T. J. Ulrich, P. Lura, Early-age elastic properties of cement-based materials as a function of decreasing moisture content, *Cem. Concr. Res.* 89 (2016) 87–96.
- [45] J. -Y. Jehng, D. T. Sprague, W. P. Halperin, Pore structure of hydrating cement paste by magnetic resonance relaxation analysis and freezing, *Magn. Reson. Imaging*. 14 (1996) 785–791.
- [46] A. P. Roberts, E. J. Garboczi, Computation of the linear elastic properties of random porous materials with a wide variety of microstructure, *R. Soc.* 458 (2002) 1033–1054.
- [47] M. Wyrzykowski, P. Lura, Moisture dependence of thermal expansion in cement-based materials at early ages, *Cem. Concr. Res.* 53 (2013) 25–35.
- [48] Z. C. Grasley, G. W. Scherer, D. A. Lange, J. J. Valenza, Dynamic pressurization method for measuring permeability and modulus: II. cementitious materials, *Mater. Struct.* 40 (2007) 711–

- 721.
- [49] C. Di Bella, M. Wyrzykowski, P. Lura, Evaluation of the ultimate drying shrinkage of cement-based mortars with poroelastic models, *Mater. Struct.* (2017).
 - [50] C. Hua, P. Acker, A. Ehlacher, Analyses and models of the autogenous hardening cement paste shrinkage, 25 (1995) 1457–1468.
 - [51] Z. P. Bažant, Solidification theory for concrete creep. i: formulation, *Engineering*. 115 (1989) 1691–1703.
 - [52] Z. P. Bažant, A. B. Hauggaard, S. Baweja, Microprestress-solidification theory for concrete creep .2. Algorithm and verification, *J. Eng. Mech.* 123 (1997) 1195–1201.
 - [53] I. Jaouadi, *Etude numerique et experimentale de retrait endogene de la pate de ciment au jeune age*, EPFL, 2008.
 - [54] S. Bishnoi, K.L. Scrivener, Studying nucleation and growth kinetics of alite hydration using μ ic, *Cem. Concr. Res.* 39 (2009) 849–860.
 - [55] M. Vandamme, F.J. Ulm, Nanoindentation investigation of creep properties of calcium silicate hydrates, *Cem. Concr. Res.* 52 (2013) 38–52.
 - [56] E. A. B. Koenders, K. van Breugel, Numerical modelling of autogenous shrinkage of hardening cement paste, *Cem. Concr. Res.* 27 (1997) 1489–1499.
 - [57] T. C. Hansen, Physical Structure of Hardened Cement Paste, *Mater. Struct.* 19 (1986) 423–436.
 - [58] A. C. A. Muller, K. L. Scrivener, A.M. Gajewicz, P.J. McDonald, Use of bench-top NMR to measure the density, composition and desorption isotherm of C-S-H in cement paste, *Microporous Mesoporous Mater.* 178 (2013) 99–103.
 - [59] T. C. Powers, Mechanisms of shrinkage and reversible creep of hardened cement paste, in: *Int. Conf. Struct. Concr. Sect. G*, 1965: pp. 319–344.
 - [60] H. Justnes, B. Ardoullie, E. Hendrix, E. Sellevold, D. Van Gemert, The Chemical Shrinkage of Pozzolanic Reaction Products, in: *ACI SP 179-11*, 1998: pp. 191–205.
 - [61] H. F. W. Taylor, *Cement chemistry*, Thomas Telford Publishing, 1997.
 - [62] A. Standard, ASTM C 642-13: Standard Test Method for Density, Absorption, and Voids in Hardened Concrete, (2013).
 - [63] E. P. Barrett, L.G. Joyner, P.P. Halenda, The determination of pore volume and area distributions in porous substances. i. computations from nitrogen isotherms, *J. Am. Chem. Soc.* 73 (1951) 373–380.
 - [64] M. Krus, K. K. Hansen, H.M. Künzel, Porosity and liquid absorption of cement paste, *Mater. Struct.* 30 (1997) 394–398.
 - [65] A. C. A. Muller, K. L. Scrivener, A. M. Gajewicz, P. J. McDonald, Densification of C–S–H Measured by ^1H NMR Relaxometry, *J. Phys. Chem.* 117 (2013) 403–412.
 - [66] A. C. A. Muller, K. L. Scrivener, A reassessment of Mercury Intrusion Porosimetry by comparison with ^1H NMR relaxometry, *Cem. Concr. Res.* (2016) submitted.
 - [67] H. J. H. Brouwers, The work of Powers and Brownyard revisited: Part 1, *Cem. Concr. Res.* 34 (2004) 1697–1716.
 - [68] ASTM C215, Standard test method for fundamental transverse , longitudinal , and torsional

- resonant frequencies of concrete specimens 1, *Am. Soc. Test. Mater.* (2014) 1–7.
- [69] M. Briffaut, F. Benboudjema, J.M. Torrenti, G. Nahas, Concrete early age basic creep: Experiments and test of rheological modelling approaches, *Constr. Build. Mater.* 36 (2012) 373–380.
- [70] N. Ranaivomanana, S. Multon, A. Turatsinze, Basic creep of concrete under compression, tension and bending, *Constr. Build. Mater.* 38 (2013) 173–180.
- [71] A. Aili, M. Vandamme, J. -M. Torrenti, B. Masson, J. Sanahuja, Time evolutions of non-aging viscoelastic Poisson’s ratio of concrete and implications for creep of C-S-H, *Cem. Concr. Res.* 90 (2016) 144–161.
- [72] M. Polivka, D. Pirtz, R. F. Adams, Studies of creep in mass concrete, *ACI J.* 6 (1963) 257–286.
- [73] K. S. Gopalakrishnan, A. M. Neville, A. Ghali, Creep Poisson’s ratio of concrete under multi-axial compression, *ACI J.* (1969) 1008–1020.
- [74] X. Li, Z. C. Grasley, J. W. Bullard, E. J. Garboczi, Computing the time evolution of the apparent viscoelastic/viscoplastic Poisson’s ratio of hydrating cement paste, *Cem. Concr. Compos.* 56 (2015) 121–133.
- [75] A. Valori, P. J. McDonald, K. L. Scrivener, The morphology of C-S-H: Lessons from 1H nuclear magnetic resonance relaxometry, *Cem. Concr. Res.* 49 (2013) 65–81.
- [76] T. C. Powers, T. L. Brownyard, Studies of the physical properties of hardened Portland cement paste, *J. Am. Concr. Inst.* 43 (1946) 101–132.
- [77] H. J. H. Brouwers, The work of Power and Brownyard revisited: Part 2, *Cem. Concr. Res.* 35 (2005) 1922–1936.
- [78] O. Bernard, F. J. Ulm, E. Lemarchand, A multiscale micromechanics-hydration model for the early-age elastic properties of cement-based materials, *Cem. Concr. Res.* 33 (2003) 1293–1309.
- [79] M. Wyrzykowski, C. Di Bella, P. Lura, Prediction of drying shrinkage of cement-based mortars with poroelastic approaches – a critical review, in: 6th Biot Conf. Poromechanics, Paris, 2017.
- [80] Z. C. Grasley, D. A. Lange, The viscoelastic response of cement paste to three-dimensional loading, *Mech Time-Depend Mater.* 11 (2007) 27–46.
- [81] K. Scrivener, R. Snellings, B. Lothenbach, A practical guide to microstructural analysis of cementitious materials, 2016.

Chapter 7 Numerical simulation of autogenous shrinkage of cementitious materials

This chapter presents a numerical simulation of autogenous shrinkage. The microstructures of three systems investigated in the previous chapters were simulated with the geometry modeling platform *mic*, starting from the actual PSD and the mixture proportions of the raw materials. The microstructures evolve during time according to predetermined rules that simulate hydration of the cement and reaction of the SCMs. The outputs of *mic*, voxels, nodes and elements of the voxels were used as inputs of an extended FEM platform. In the FEM simulation of both the elastic and visco-elastic response of the materials, the stress calculated from RH_k , S and b was imposed as an external load. The elastic and visco-elastic behavior of the C-S-H were both back-calculated from the macro-scale mechanical properties. The autogenous shrinkage was combined with the elastic and visco-elastic simulations based on FEM method.

Contents

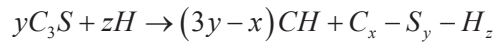
7.1	Literature review	154
7.1.1	Hydration of cement	154
7.1.2	Microstructural modeling of hydration of cement pastes	157
7.2	Simulation methods.....	163
7.2.1	Microstructure simulation with <i>mic</i> platform.....	163
7.2.2	Finite element method for micro-mechanical simulation of elastic deformation under pore fluid pressure	167
7.2.3	Simulation of the visco-elastic behavior of C-S-H based on non-aging creep.....	169
7.2.4	Simulation of aging creep.....	172
7.2.5	Simulation of autogenous shrinkage.....	174
7.3	Prediction results.....	175
7.3.1	Simulation of the elastic response of material under capillary pressure ...	175
7.3.2	Simulation of the non-aging visco-elastic behavior of C-S-H.....	179
7.3.3	Simulation of aging creep.....	181
7.3.4	Simulation of autogenous shrinkage.....	182
7.4	Conclusions	183

7.1 Literature review

7.1.1 Hydration of cement

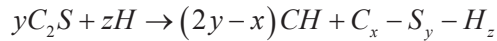
Cement hydration is a complex process with multiple chemical reactions and transformations of solid and liquid phases occurring simultaneously [1]. The PSD and the chemical composition of the cement play a paramount role for the global hydration properties, e.g., hydration kinetics and phase assemblage. The main reactions occurring in cementitious systems are presented in the following equations¹¹ [1]. The primary hydration products of cement clinker forming the solid skeleton are C-S-H and portlandite, as shown in *Equation 7.1* and *Equation 7.2* below. In particular C-S-H is important for the mechanical properties of the hardened cement paste.

Equation 7.1



Normally, the range of x/y is between 1.4 and 1.9 for reaction of pure C_3S . However, in commercial cements, this range can be extremely broad, from 0.4 to 2.3 [2].

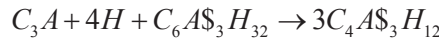
Equation 7.2



Equation 7.3



Equation 7.4



Explicit reaction formulas are critical for modeling the hydration of cement. All stoichiometry appearing in these equations can be determined as long as the composition of C-S-H is fixed. However, the composition of C-S-H varies in different systems and different conditions. In other words, the coefficients x and y (Ca/Si) are not fixed [1,2]. The structure of C-S-H with various Ca/Si can be described as a defective tobermorite structure [3].

According to a model by Jennings, two types of C-S-H have been identified, so-called low density C-S-H (LD C-S-H) or outer-product C-S-H and high density C-S-H (HD C-S-H) or inner-product C-S-H [4,5]. Under TEM, two kinds of C-S-H can also be distinguished: one has compacted and homogenized structure; the other one shows a looser packing and directional morphology [2], see *Figure 7.1*. The C-S-H is seen to be forming around cement grains, with the HD C-S-H adjacent to the clinker grain (within the original volume of the unhydrated cement grains [2]) and the LD C-S-H forming further.

¹¹ The reactions of another main clinker phase in cement, C_4AF , are similar to the reactions of C_3A .

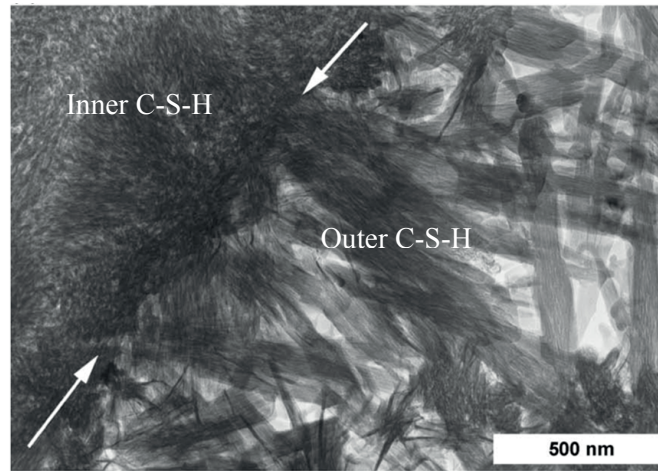


Figure 7.1 A TEM micrograph for inner and outer C-S-H of a C_3S paste with w/c of 0.4 after 8 years of hydration; the white arrows are the boundary between inner and outer C-S-H. From [2]

The LD C-S-H needles form during the first hours of hydration and keep growing until a certain length. The maximum length was found to be 200-400 nm [6]. However, the reasons limiting the length of the C-S-H needles are still under debate.

The average density and average composition of C-S-H can be determined from 1H NMR and chemical shrinkage according to [7]. The calculated density of nanocrystalline, solid C-S-H¹² is 2.68 g/cm³, considering the interlayer water as a part of the C-S-H. In a study of white cement paste with w/c of 0.4 by Muller et al. [7], the density of the solid C-S-H remained constant with the increase of degree of hydration but the density of the bulk C-S-H (including the gel water) increased from 1.8 g/cm³ to about 2.1 g/cm³. The ratio between the amount of interlayer water and gel water varies with hydration time and systems. At around 2 d, this ratio is about 0.5 in the systems studied in [8] (w/c ranged from 0.32 to 0.48). The proposed chemical formulae for the two kinds of compositions of C-S-H, with or without gel water, are (the definition of different types of water is following [8], see Chapter 4): $(CaO)_{1.53}(SiO_2)_{0.96}(Al_2O_3)_{0.02} \cdot 5.25H_2O$ and $(CaO)_{1.53}(SiO_2)_{0.96}(Al_2O_3)_{0.02} \cdot 1.92H_2O$. The study in [8] gave fundamental inputs for microstructural modeling by providing values for the densification of C-S-H as a function of the degree of hydration.

From the modeling point of view, the difference between the two types of C-S-H can be considered as either a density difference or a porosity difference [9]. For example, in the colloid globule type-model by Jennings [10], they proposed to distinguish two types of C-S-H from their packing density. They actually suggested a denser packing of HD C-S-H, see Chapter 5. In addition, the chemical formula of C-S-H from experiments can serve as a reference for hydration modeling.

When quartz powder is included in the system, it promotes the reaction due to the filler effect without changing the composition of the C-S-H [11]. The dilution by quartz can be regarded as the same effect as increasing the w/c in cementitious systems. Consideration of the possible nucleation sites

¹² The so-called solid C-S-H and later bulk C-S-H is based on reference [7].

for C-S-H on the surface of the quartz powders should be taken in the microstructural simulation of hydration with quartz-blended systems. The nucleation effect (C-S-H needles growing on the surface of quartz particles) can be seen directly in SEM pictures, see *Figure 7.2*.

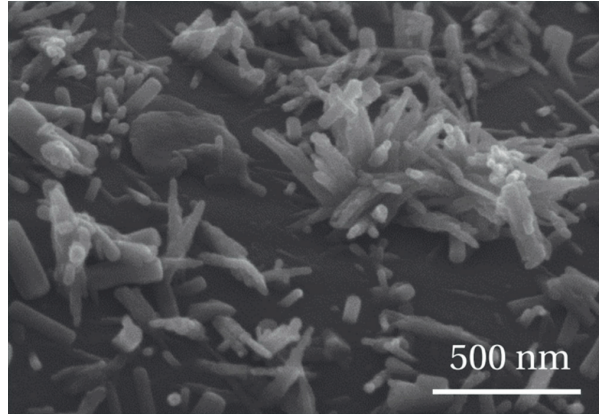


Figure 7.2 Microstructure of C-S-H needles growing on the surface of quartz particle, from [11]

Fly ash, as a SCM used in cement paste, leads to a composition change of the C-S-H due to the pozzolanic reaction. Since only siliceous fly ash (class F) was used in this thesis, the description about the variation of the components was focused on this type of fly ash. A typical siliceous fly ash has a minimum 70 % of $\text{SiO}_2 + \text{Al}_2\text{O}_3 + \text{Fe}_2\text{O}_3$ in the raw material, according to ASTM C 618 [12].

As fly ash is a material with low reactivity, the filler effect of fly ash at early ages should be considered, as addressed in *Chapter 3*. The pozzolanic reaction happens at later ages (usually after several days-weeks), depending on the chemical compositions, the fineness of the particles and the amount of reactive phases (glasses) in the fly ash [13]. The degree of reaction of fly ash is typically around 10-20 % at 28 days. During the reaction, SiO_2 and Al_2O_3 originating from the glass phase of fly ash dissolve due to the high pH of the pore solution and react with portlandite [14]. A SEM image of the reaction of fly ash at 550 days in a fly-ash-blended system is shown in *Figure 7.3*.

Due to the supply of silicon from the fly ash, the Ca/Si of C-S-H in fly-ash-blends is lower than the one in pure cement paste. The ratio in the former is around 1.3-1.4 while in the latter it is around 1.7-1.9, depending on the initial chemical compositions of the raw materials [15]. This ratio does not change significantly during hydration. In addition, the Al/Si in C-S-H is higher in fly-ash-blends than in Portland cement, to the extent that the C-S-H may be rather considered calcium aluminate silicate hydrate (C-A-S-H) [14,16]. For C-A-S-H generated in blended systems, a tobermorite-like structure seems to be maintained [16]. Moreover, fly ash contains significant quantities of Al_2O_3 but little SO_3 , which results in a decrease of ettringite content in the cement pastes [17]. Due to the sulfate to aluminum ratio being lower in fly-ash-blends, the formation of mono-sulfate is promoted instead of ettringite [15].

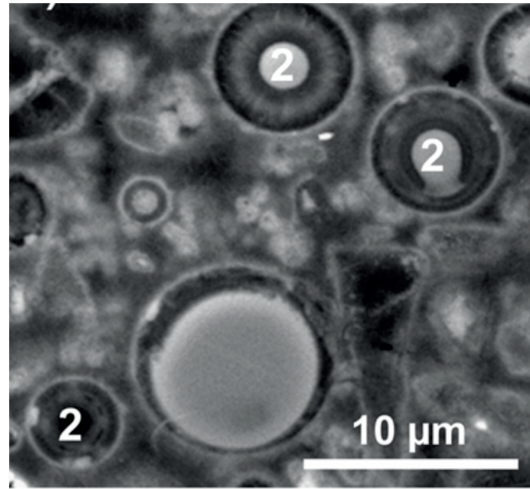


Figure 7.3 SEM micrograph showing reaction of fly ash (partly reacted fly ash marked as 2) in a fly-ash-blended system after 550 d, from [15]

The determination of the amount of phases reacted as a function of time in fly-ash-blended cement systems is a challenging but fundamental task. It helps to link the progress of the reaction of the different components (cement and fly ash) with the subsequent changes of hydration products and other properties. Due to the high heterogeneity (presence of various types of glasses) and the high amount of amorphous material in the fly ash, traditional methods for quantification of the degree of reaction such as XRD, TGA, selective dissolution and spectroscopy backscattered electron image analysis (BSE) are facing different challenges [18,19]. A new quantification method [20] based on SEM and EDS was applied in this thesis, see *Chapter 2*.

7.1.2 Microstructural modeling of hydration of cement pastes

Thanks to the constant improvements in computational power, it became possible to describe and predict hydration and microstructure development of cementitious materials using numerical models. Fundamental models for simulating the kinetics, nucleation and growth of hydration products during cement hydration have a long history. The *Avrami equation* [21] (see *Equation 7.5*) and *boundary nucleation and growth models* (see *Equation 7.8*) [22] are the two most widely used models [9,23]. The conventional *Avrami equation* assumes randomly distributed nucleation in the volume, while the *boundary nucleation and growth model* is based on the assumption that nucleation occurs only on planar grain boundaries [22].

Equation 7.5

$$X(t) = 1 - \exp\left(-(kt)^m\right)$$

where: $X(t)$ is the volume fraction of phases that are transformed at time t ; m is a constant related to three parameters, see *Equation 7.6*; k is a temperature-dependent rate constant that covers the rates of growth and nucleation, which can be determined by *Equation 7.7*.

The effect of different parameters in the *Avrami equation* on the simulation of hydration of cement has been discussed, e.g., in [24,25].

Equation 7.6

$$m = p / s + q$$

where: p is the number of dimensions of the occurring growth, which accounts for the shape of the growth ($p=1$ applies to needles; $p=2$ applies to sheets and $p=3$ applies to spheres); q is the type of nucleation, which is normally chosen to be 0 for site saturation and 1 for continuous nucleation; s is the type of rate control. There are two common types of rate control: phase boundary control ($s=1$) and diffusion control¹³ ($s=2$). As a result, a wide range of values for m have been reported in the literature, from 1 to 3 [25]. From experiments on C_3S hydration, e.g., isothermal calorimetry or small-angle X-ray scattering, m is found to lie between 2 and 3 [21,26].

Equation 7.7

$$k = \frac{\pi \cdot G^3}{3} (I + 4 \cdot N_0)$$

where: G represents the linear growth rate of individual nuclei (growth of radius); I represents the nucleation rate per unit area of boundary; N_0 is the initial number of nuclei per unit volume.

Equation 7.8

$$X(t) = 1 - \exp \left[-2O_v^B \int_0^{Gt} \left(1 - \exp \left(-\frac{\pi I}{3} G^2 t^3 \left(1 - \frac{3y^2}{G^2 t^2} + \frac{2y^3}{G^3 t^3} \right) \right) \right) dy \right]$$

where: O_v^B is the surface area for nucleation per unit volume; y is a dummy variable. This equation is valid when t is smaller than y/G [23].

Both models are able to provide a reasonable good fit of the kinetics of hydration [9,27]. They are the basis of developing complex models in comprehensive hydration simulations. A more detailed discussion about both models can be found in [25].

Single particle models appeared as the pioneers of the numerical models around forty years ago. This type of models, such as the ones proposed by Kondo et al. [28] and Pommersheim and Clifton [29], were based on layers of hydration products forming with uniform thickness around a single particle of cement. This idea was followed later by more complicated models accounting also for the interactions between different particles.

The last 30 years have witnessed a vigorous development of numerical modeling. The publication of the microstructure simulation model by Jennings and Johnson can be considered the start of the numerical microstructure modeling of cement hydration [30]. Some widely used hydration models developed in the last decades are the *HymoStruc model* (TU Delft), the *CemHyd3D model* (NIST) [31], the *integrated particle kinetics model* (IPKM, EPFL) [32], the *HydratiCA model* (NIST) [33], the

¹³ Boundary control means that the reaction is controlled by the boundary of the grains. Diffusion control means that the reaction is controlled by the diffusion coefficient of the ions diffusing through layers of hydrates [9].

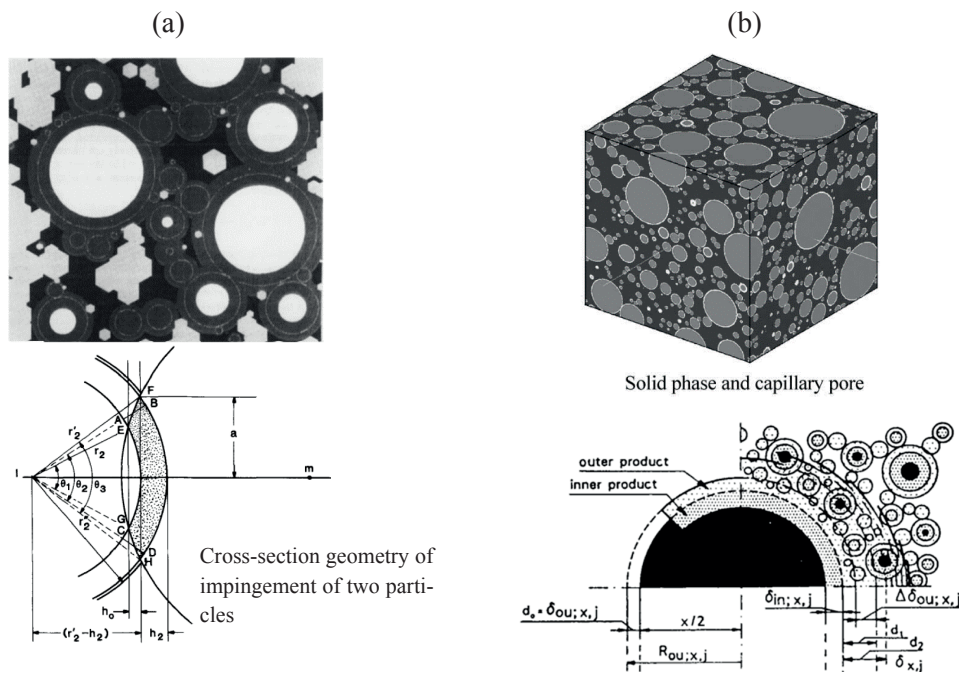
DuCOM model (University of Tokyo) [34,35] and the *mic* modeling platform (EPFL) [9,36]. Based on different types of mathematical methods and on different approaches to describe the physical and chemical phenomena occurring during cement hydration, these models make it possible to simulate the hydration kinetics and the microstructure and further provide the possibility to take the mechanical properties into account. The advantages and disadvantages of some different models have been discussed in detail in, e.g., [25] and [37]. Here, examples of the computational volume elements (CVE) in these models are shown in *Figure 7.4*. The description of the principle of each model shown in *Table 7.1* is primarily focused on how each model deals with the interaction (impingement), the material properties and the kinetics.

Actually, there are three most important concerns in microstructural modeling:

1. How to simulate the microstructure of different systems with reasonable simplifications;
2. How to consider the chemical mechanisms behind the overall reaction;
3. How to increase the speed of the simulation and minimize the resolution limit.

These issues are very important and have not yet been fully solved in existing models. Hydration modeling and its seamless docking with mechanical modeling are receiving considerable attention. Thermodynamic modeling, if can be used to work together with microstructural modeling, can capture all reactions occurring in cementitious systems (however, the kinetics needs to be addressed as well).

A detailed description of *mic* will be presented, since this model is the one used in this thesis. This platform was chosen because compared to other models, the greatest advantage of *mic* is that there is no limitation of resolution, which allows dealing with complex microstructures [44].



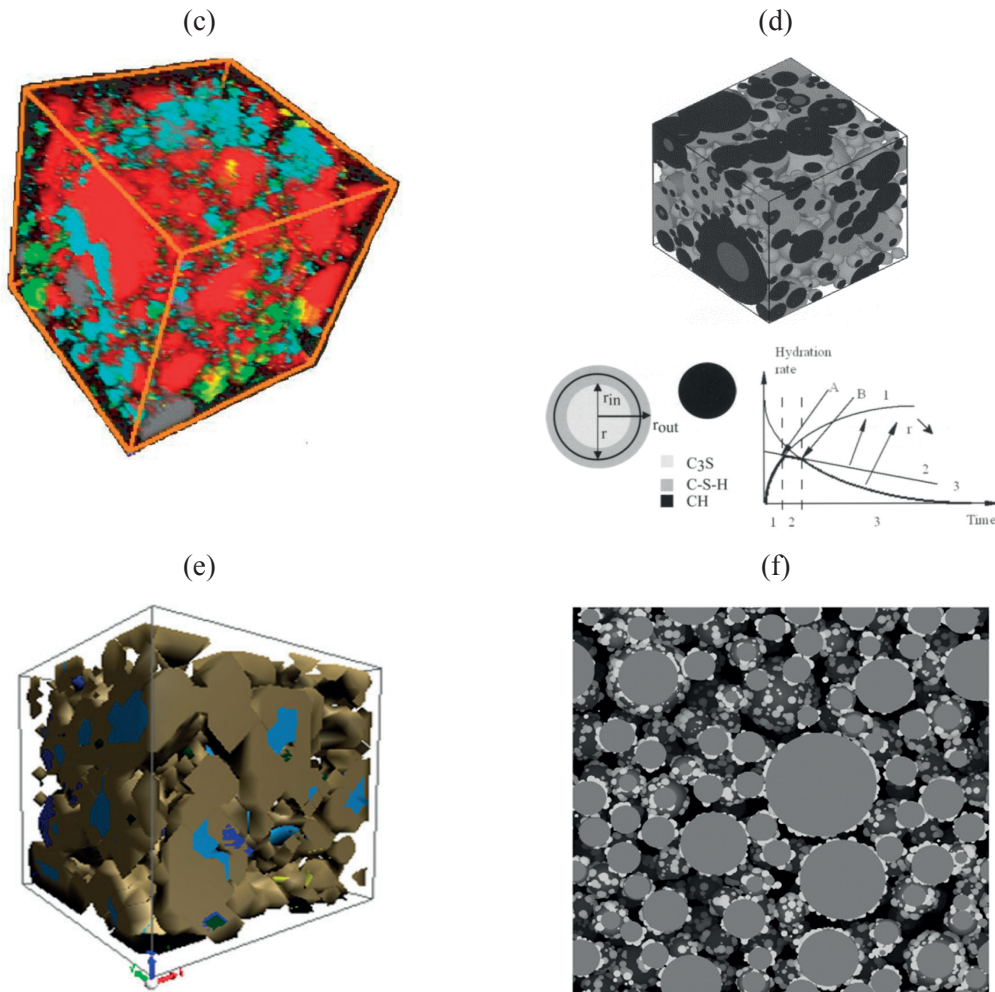


Figure 7.4 CVE of different proposed models: a) Jennings and Johnson model [30]; b) HymoStruc model [38]; c) CemHyd3D model [31]; d) IPKM model [32]; e) HydratiCA model [33]; f) μic modeling platform [36].

μic is a platform that uses the vector approach to characterize the geometry of the microstructure of different materials [39]. In μic , plug-ins are available to formulate different kinetic models (see Figure 7.5), nucleation models, etc., in order to meet the demand for different mechanisms. Materials, reactions and other plugins can be defined by users to simulate different kinetics [24,37]. It also overcomes the computational complexity of IPMK by providing data-structured algorithms [37].

At EPFL, cement hydration, microstructure, porosity and mechanical properties of cement paste have been simulated based on the output of the μic platform, e.g., modeling of autogenous shrinkage of cement paste [39]. However, the most advanced simulation [39] only dealt with short durations (less than 7 d) and the comparison of the simulation with reliable and comprehensive experimental data was lacking.

Table 7.1 Difference of hydration models in literature

Models	<i>Jennings and Johnson</i>	<i>HymoStruc</i>	<i>CemHyd3D</i>	<i>IPKM</i>	<i>HydratiCA</i>	<i>μic</i>
Approach	off-lattice (vector)	Vector	vector	vector	lattice	vector
Elements	spherical particles distributed in a cubic volume	equally-spaced spherical particles distributed in CVE	digitally meshed microstructure of cement paste	3-dimensional (3D) microstructure cube with spherical particles	regular cubic lattice having a lattice space	3D microstructure cube with spherical particles
Advantages	considering hydration products and their positions; considering dissolution and precipitation	user-friendly; successfully used for simulating some mechanical properties	fast, easy to work together with simulation models such as FEM	no resolution limit; allows to represent a wide range of pore sizes	covers most chemical and physical phenomena in hydration	no limit of resolution; allows users to choose independently the models
Disadvantages	lack of implementation of solution chemistry and C-S-H nucleation; no effective algorithm for calculation	needs to calibrate for different mixtures; does not take the impingement and pores into account ¹⁴ ; global reaction only	limitation of resolution; with smaller units (<1 μm), the model cannot converge	high computational complexity; can only simulate a small amount of particles	rather slow speed due to significant parameters that need to be determined	not very user-friendly; no solution chemistry related simulation ¹⁵

¹⁴ with the advanced version of the model, impingement could be considered

¹⁵ can also be linked with thermodynamic models, such as GEMs

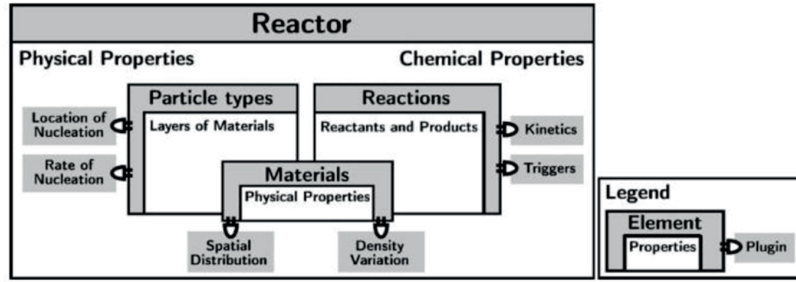


Figure 7.5 Design of structures in *mic* with different plug-ins [36]

To simulate autogenous shrinkage, it is necessary to start from the simulated porosity and pore size distribution, since the pore structure is essential for calculating the driving force of autogenous shrinkage, the pressure in the pore fluid. However, modeling of porosity and water distribution is still a challenging task in all the hydration models. Approaches for simulating the pore network, either by homogenizing the experimental results [40] or generating microstructures with models [27,41], exist in the literature.

In *mic*, as shown in Figure 7.6, the so called *voxel-erosion method* is used to evaluate the pore size distribution. It is a technique based on three-dimensional erosion of pore-space to locate pore-centers. The pore size is determined from the distance of the center reverse to the surface of the solids, called *walk back technique*. Do [37] modified the method by using a new algorithm to calculate the intrusion of mercury and compared the results with MIP. Do concluded that the limitation of simulating pore size distribution is neither due to the resolution (the minimum size used was 5 nm), nor due to the not big enough computational volume [37]. Yet, the porosity simulation is extremely challenging mainly due to the effect of C-S-H shape. When considering a smooth shape of C-S-H (not needle-shaped as in reality), the pores are very different from the real ones (much coarser). Therefore, in this thesis, the average pore pressure has not been calculated based on the simulated pore size distribution, but from the experimental RH_K and S results (P_c - S , calculation see Chapter 6 section 6.2.1).

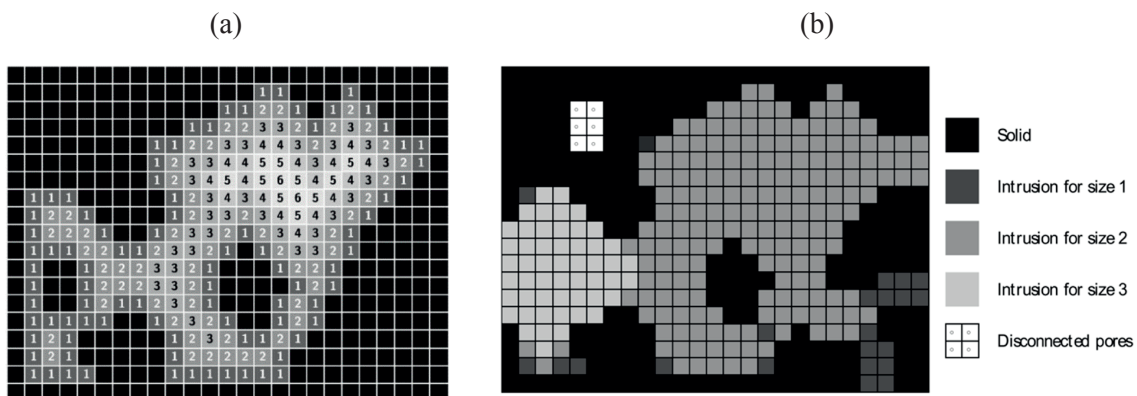


Figure 7.6 Schematic representation of porosity and mercury intrusion simulation in *mic*: (a) the voxel erosion method and the walk back technique [9]; (b) intrusion for voxel connected pores with different size [37]

7.2 Simulation methods

The whole simulation can be separated into a number of sub-simulations from the microstructural simulation to the mechanical simulation. The mechanical simulation combines 2D and 3D simulations. In order to make the procedure of simulation clearer, the sub-simulations and the dimensions used in each simulation are summarized as follows:

- 1) Generation of microstructure with *μic* by fitting experimental degree of hydration of cement and fly ash for three systems: Cement-0.35, CFA40-0.35 and CQZ40-0.35 (3D simulations);
- 2) Back calculate stiffness of outer C-S-H gel (C-S-H + gel water) + capillaries by fitting measured elastic modulus with *AMIE* and link the stiffness with porosity evolution in outer C-S-H gel + capillaries (3D simulation with white cement system with w/c of 0.4, extended simulation in [42]).
- 3) With the relationship between stiffness and porosity of outer C-S-H gel+ capillaries obtained from step 2), stiffness evolution of outer C-S-H gel + capillaries in studied systems was determined by knowing their outer C-S-H porosity. The elastic deformation of studied systems was then simulated with FEM method on FE meshes generated based on *μic* microstructures in *AMIE* framework for two systems: Cement-0.35 and CQZ40-0.35 (2D simulations were possible in *AMIE*, performed on slices from the *μic* microstructures with size of $1 \times 100 \times 100 \mu\text{m}^3$).
- 4) Back calculate visco-elastic behavior of C-S-H with macro-scale experimental results of creep in *AMIE* framework (simulation with regenerated 2D microstructure, volume fraction of different phases obtained from mass balance method).
- 5) Visco-elastic behavior was simulated by FEM method with FE meshes generated based on *μic* microstructures for two systems: Cement-0.35 and CQZ40-0.35 (Do's 3D FEM simulation [39] was used). The visco-elastic behavior of C-S-H gel + capillary obtained from step 4).

7.2.1 Microstructure simulation with *μic* platform

The microstructure evolution of Cement-0.35, CQZ40-0.35 and CFA40-0.35 was simulated with the *μic* platform. In *μic* modeling, the selected computational volume is $100 \times 100 \times 100 \mu\text{m}^3$, with a minimum voxel size of $1 \mu\text{m}$. The duration for the simulation is 680 hours with the time step of 1 h in the first 24 h and with increments of 10 h after 24 h. Sphere sampling points are 92. As shown in [9], simulations with sampling points between 90-100 gives reliable results. Output pixels and element files (containing particles distribution information) are stored for later FEM micro-mechanical modeling.

Materials and particles

In the simulation, four main clinker phases and gypsum are considered in one spherical cement particle. C-S-H is growing outside of cement particles and other hydration products are all defined as newly-created individual particles. The density of each phase used in the simulation is presented in *Table 7.2*. The outer C-S-H is not fixed to a constant density, since densification is considered in the

simulation. The values showed in the table are the minimum and maximum density used for the outer C-S-H. Each reacting phase had its own hydration kinetics and reactions, shown in the next section. In CFA40-0.35 and CQZ40-0.35, fly ash and quartz were presented as individual spherical particles as well. In fly ash particles, two components, reactive phase and unreactive phase, were considered. Water was presented as the background with black color.

Table 7.2 Density of phases considered in the μic simulation

Phases	C ₃ S	C ₂ S	C ₃ A	C ₄ AF	C\$H ₂	inner C-S-H	outer C-S-H	AFt	AFm	CH	FH ₃
Density (g/cm ³)	3.15	3.28	3.03	3.73	2.80	2.25	0.22- 2.25	1.78	2.00	2.24	3.0

The schematic view of particles with different phases is shown in *Figure 7.7*, with the different colors representing the different particles in the image to help distinguishing them. Some minor phases such as gypsum and AFt, AFm and iron hydroxide are not shown in the figure. However, they have basically the same physical appearance as portlandite (independent particles).

The particle size of cement particles was obtained from laser diffraction measurements, see *Chapter 2*. In order to have a representative volume in both the hydration simulation and the micro-mechanical FEM simulation later on, the maximum particle size is controlled to be less than 0.4 of the computational volume [37]. The maximum particle size in the simulations is therefore 40 μm , which means that some larger particles in the real particle size distribution of the cement were assigned to this size. This is not expected to have a significant influence on the results, since particles larger than 40 μm were only around 10 % of the total particles. In addition, the fact that finer particles have higher surface area is more important, especially in the case where the available surface is key for the hydration kinetics and the evolution of the microstructure.

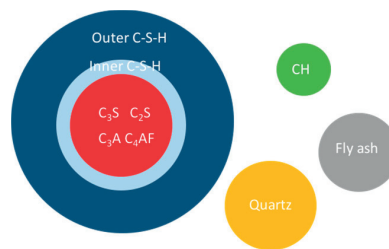


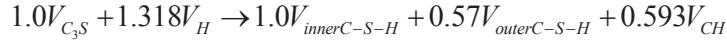
Figure 7.7 Spherical particles in μic simulation

Reactions

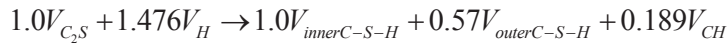
The reactions of the four main clinker phases are included as equations shown in *section 7.1*. Since, in the simulation, the reactions are defined by volume of reactants and hydration products, the equations in *section 7.1* are transformed into the following equations in the volumetric form for the numerical simulation. In the equation, the composition of C-S-H was assumed to be

$(\text{CaO})_{1.7}(\text{SiO}_2)(\text{H}_2\text{O})_4$. This Ca/Si was close to the measurement of the composition of C-S-H in CQZ40-0.35 but 0.2 lower than that in Cement-0.35, see *Chapter 2*. The influence of the Ca/Si on the final volume phase fraction is lower than 2% of the volume of the paste.

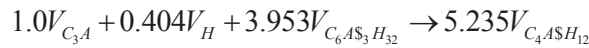
Equation 7.9



Equation 7.10

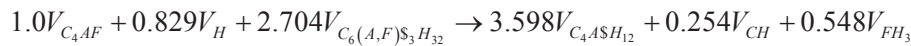
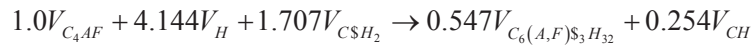


Equation 7.11



Note: the second reaction happens only when there is no C\$H₂ in the system.

Equation 7.12



Note: the second reaction happens only when there is no C\$H₂ in the system.

Models for Hydration kinetics

Three different kinds of kinetics and nucleation models were applied to fit the experimental degree of hydration: *densifying nucleation-growth (NG) kinetics*, *diffusion proportionate kinetics* and *Avrami kinetics*. The densification of C-S-H (typically for outer C-S-H) needs to be taken into consideration [9]. With proper densification, it was observed that the simulation of aging creep was much closer to the experimental results [43]. The densifying kinetics was only used for C₃S but not for other reactions since C₃S had highest amount in the system and therefore dominated the whole reaction. The rate of densifying (k_{en} [g/cm³/h] is a rate constant for describing this effect) has linear relationship with the density, see the following equation [9]:

Equation 7.13

$$\rho = \rho_{\max} - (\rho_{\max} - \rho_{\min}) \cdot \exp(-k_{en} \cdot t / (\rho_{\max} - \rho_{\min}))$$

where: ρ_{\max} [g/cm³] and ρ_{\min} [g/cm³] are the maximum and minimum density of C-S-H, respectively.

The *diffusion kinetics model* attracted considerable attention in recent years. It is believed to be an important mechanism that becomes active after early-age reaction [44]. Therefore, this kinetics is also taken into account in the simulations performed in this thesis. The diffusion kinetics is controlling the

hydration after the main hydration peak. The diffusion-controlled process was simulated based on the equation as follows [9]:

Equation 7.14

$$\frac{dr}{dt} = -k_{diff} / \left(r_{in}^2 \cdot \left(\frac{1}{r_{in}} - \frac{1}{r_{out}} \right) \right)$$

where: r_{in} is the radius of the reactant portion of the particle and r_{out} is the outer radius of the hydration product around the particle; k_{diff} is the composite parameter which is proportional to the diffusion coefficient of the reactive ions through the material.

Parameters in all the kinetics models were obtained by fitting the modeling results with the experimental data. The values for all parameters can be seen in Table 7.3 and Table 7.4.

Table 7.3 Parameters for the densifying NG kinetics model

Parameters	k (h ⁻ⁿ)	k_{en} (g/cm ³ /h)	$t^{16/12}$ (h)	ρ_{max} (g/cm ³)	ρ_{min} (g/cm ³)	m^{17}	vertical growth rate (μ m/h)
C ₃ S	6.7×10^{-4}	0.007	4.9	2.25	0.22	3.0	0.025

Table 7.4 Parameters for Avrami kinetics and diffusion kinetics models

Reactions	C ₃ S	C ₂ S	C ₃ A reaction 1	C ₃ A reaction 2	C ₄ AF reaction 1	C ₄ AF reaction 2
k	diffusion factor 1.0	2.0×10^{-5}	5.0×10^{-3}	2.0×10^{-5}	1.0×10^{-4}	5.0×10^{-5}
m	2.6	2.6	2.6	2.6	2.6	2.6

A dependent exponential nuclei generator was used for generating the grains and the coefficient k is equal to -0.0213, see Equation 7.15.

Equation 7.15

$$N = N_{in} + N_{max} \cdot (1 - \exp(k \cdot t))$$

where: N is the number of nuclei, N_{in} is the initial number of particles, N_{max} is the maximum number of nuclei.

¹⁶ $t_{1/2}$ is the time until 1/2 of the surface becomes covered with a shell of hydrated products.

¹⁷ m has the same meaning as in the Avrami equation.

7.2.2 Finite element method for micro-mechanical simulation of elastic deformation under pore fluid pressure

The FEM simulation in this thesis was performed with a FEM framework *AMIE*. The framework is composed of the necessary elements for microscale FEM simulation, i.e. geometry library, FE library, mesher and solvers [45]. It has been used successfully to simulate the mechanical properties of cement-based materials, e.g., elastic properties, creep and deformation [45,46].

The simulation of elastic deformation of cementitious materials was separated into two steps: 1) simulating the evolution of stiffness of outer C-S-H with porosity; 2) simulating the elastic deformation under capillary pressure (being approximation of the pore fluid pressure).

Simulation of stiffness of outer C-S-H

The first step is based on the work in [42] with two assumptions: 1) the stiffness evolution of the cement paste is associated with the stiffness evolution of the outer C-S-H and the amount of different phases in the system; 2) the densifying of the outer C-S-H is due to the evolution of the volume fraction of porosity (gel water and capillary water) in the outer C-S-H; 3) the outer C-S-H is fast growing outwards to fill the whole space which is not occupied by anhydrites during hydration¹⁸.

This idea comes from the fact that the intrinsic elastic properties of individual phases are given, except for the outer C-S-H, see *Table 7.5*. Actually, the range of stiffness of the outer C-S-H reported in the literature is very broad. In order to determine the stiffness of the outer C-S-H, a back-calculation with trial-and-error was used [47,48] based on the macroscale evolution of the elastic modulus of cement pastes. In this thesis, the back-calculation starts with the same elastic modulus of outer and inner C-S-H.

The back-calculated stiffness from one system was then bridged with the porosity obtained from ¹H NMR. The porosity in the outer C-S-H was determined with *Equation 7.16*. Since the stiffness of the outer C-S-H is thought to change only with porosity, by determining the porosity of the outer C-S-H in other hydrating systems, the stiffness evolution of C-S-H as a function of time in different systems can be calculated.

Equation 7.16

$$P_{outerC-S-H} = \frac{V_{gel} + V_{capillary}}{V_{outerC-S-H}}$$

¹⁸ Instead of bulk C-S-H, C-S-H gel + capillary water (experimental determined) were considered in the mechanical simulation. The experimental porosity will be considered inside of the C-S-H, which leads to the densification of the C-S-H. Note that with this assumption, the heterogeneous of the outer C-S-H was ignored. It also ignores the consistently growing of outer C-S-H for generating the pore network, see [42].

where: $P_{outerC-S-H}$ [-] is the porosity of outer C-S-H; V_{gel} [μm^3] and $V_{capillary}$ are the volume of gel water and capillary water determined from ^1H NMR; $V_{outerC-S-H}$ [μm^3] is the volume of the outer C-S-H, obtained from μic simulation.

In [42], the back calculation of the stiffness evolution of the outer C-S-H was done on white cement with w/c of 0.4 with 15 time points, see *Figure 7.8 (a)*. They correlated the stiffness of outer C-S-H to the measured porosity in the outer C-S-H, see *Figure 7.8 (b)*. The simulated result of stiffness of the outer C-S-H (either needle-shaped or sphere-shaped) based on the self-consistent homogenization was compared to the experimental results. A conclusion that the shape of the outer C-S-H is between needles and spheres was drawn [42].

Table 7.5 Intrinsic stiffness properties of different phases

Phases	Elastic modulus (GPa)	Poisson's ratio (-)	References
H ₂ O	0.001	0.499	
C ₃ S	135	0.3	[49]
C ₂ S	130	0.3	[49]
C ₃ A	145	0.3	[49]
C ₄ AF	125	0.3	[49]
C\$H ₂	30	0.3	[50]
inner C-S-H	29.4	0.24	[51]
outer C-S-H	19-45 ¹⁹	0.24	[52]
CH	38	0.3	[51]
AFt ²⁰	22.4	0.25	[51]
quartz	70	0.15	[53]
fly ash	110	-	[54]

The stiffness simulation based on the C-S-H behavior was then performed on two other systems with w/c of 0.32 and 0.48 [42]. The obtained results agreed well with the experimental data. However, the numerical simulation performed in [43] is only with white cement and until 7 days. In order to obtain the stiffness behavior of the outer C-S-H for a longer duration, the back calculation was extended until 28 d for the same system (the calculation was done by fitting the experimental results of the same white cement with w/c of 0.4) in this thesis. During the back calculation, except for the stiffness of the outer C-S-H, the stiffness of the other phases were needed (values taken from *Table 7.5*). With this approach, the relationship of the stiffness and the porosity for longer time was obtained and was subsequently applied for the systems Cement-0.35 and CQZ40-0.35 up to 28 d.

¹⁹ The elastic modulus of the outer C-S-H has the largest uncertainty, see [52]

²⁰ Other minor phases: e.g., AFm and hydrogarnet are assumed to have the same elastic properties as AFt. Based on [51], their elastic modulus and Poisson's ratios are similar.

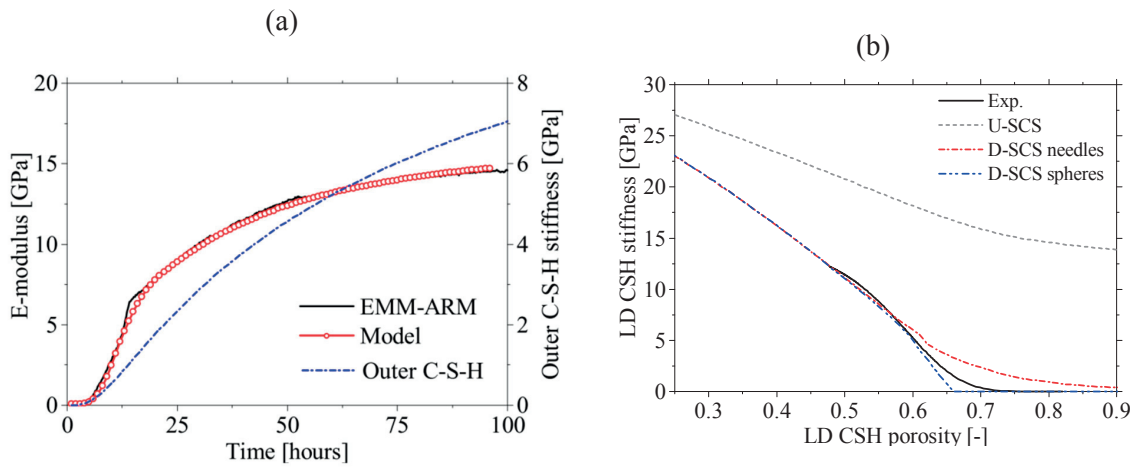


Figure 7.8 Back-calculated stiffness of outer C-S-H (a) and the relationship between stiffness of outer C-S-H and porosity (b), from [42]

Simulation of elastic deformation of cementitious materials under capillary pressure

The stiffness behavior of the outer C-S-H is used in the simulation of the elastic deformation of cementitious systems under a pore pressure load. This part of numerical simulation was done on the generated μic microstructure but the computational volume was assigned to be the slice of $1 \times 100 \times 100 \mu m^3$. The reason is that the 3D model demands higher resolution that could not be reached. With insufficient resolution in 3D, percolation of the solid phases appears too early in the simulations for the systems with low w/c. To overcome this limitation, 2D simulation is used instead at current stage. The load calculated from P_c , S and b ($P_c \cdot S \cdot b$) was applied on the boundaries of the CVE.

Because the stiffness of the outer C-S-H is determined by knowing the porosity from 1H NMR (the correlation between the back-calculated stiffness of the outer C-S-H and the porosity was used), the fly-ash-blended system was not considered in this simulation due to the inability of performing 1H NMR test on fly-ash-blended systems. Another potential issue is that the stiffness of outer C-S-H may change due to different compositions of the C-S-H, e.g., in fly-ash-blended systems, the pozzolanic reaction of the fly ash results in C-A-S-H, see section 7.1.1. It is necessary to verify first the behavior of the C-S-H with different components rather than directly apply the same behavior. The time steps for this simulation were 0, 5, 10, 15, 20, 40, 60, 80, 100, 120, 140, 160, 180, 200, 250, 300, 350, 400, 450, 500, 550, 600, 650 hours.

7.2.3 Simulation of the visco-elastic behavior of C-S-H based on non-aging creep

The principle of the method for simulating the visco-elastic behavior of the C-S-H is similar to the simulation of the stiffness of the outer C-S-H. The difference is that this simulation was performed on a generated 2D microstructure ($100 \times 100 \mu m^2$) in *AMIE* based on volume fractions of different phases obtained from mass balance calculation, see Chapter 2 section 2.5.2. 2D-spherical particles of

different phases with certain volume and assumed PSD were randomly generated in 2D CVE. In this part of simulation, we did not directly use the microstructure simulated from μic due to two reasons: 1) the porosity and water are not simulated from μic , which are critical for the identification of the visco-elastic behavior of C-S-H; 2) the phase fraction simulated from μic was not accurate enough. As long as precise volume fraction of phases and representative microstructure (particle size satisfied the condition that it is not bigger than 0.4 of the size of CVE) are applied, the simulation of visco-elastic deformation will be reliable, e.g., simulation in [55].

The visco-elastic behavior of C-S-H was back-calculated with the experimental data of creep of cement paste at 28 d. The simulated result was used for the simulation of creep for both systems Cement-0.35 and CQZ40-0.35 at early ages. The entire simulation is based on a two-scale homogenization: scale 1 is the scale of C-S-H and water; scale 2 is the scale of cement pastes composed of other elastic phases within a matrix of hydrated gel (or C-S-H gel including C-S-H, water and pores). The elastic properties of the phases are the same as the ones used in *section 7.2.2*.

At the scale of the cement paste, the generated microstructure was then meshed for the *AMIE* simulations; for a schematic representation of the FE mesh, see *Equation 7.9*. This is the scale for performing the back-calculation of the visco-elastic behavior of C-S-H + water. The visco-elastic behavior of C-S-H + water was fitted with 5 Kelvin-Voigt chains. In this simulation, for the sake of simplification, the outer C-S-H and the inner C-S-H are both assumed to show the same visco-elastic behavior.

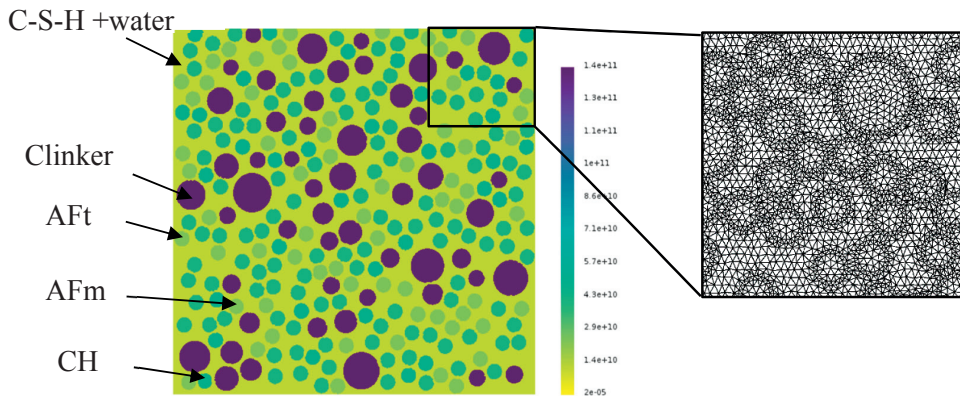


Figure 7.9 Schematic representation of the FEM mesh and the particles generation in *AMIE* (color represents stiffness of different phases, size of $100 \times 100 \mu m^2$)

The reason for using the C-S-H and water scale (see in *Figure 7.10*) is to determine the visco-elastic behavior of C-S-H instead of C-S-H + water. In order to simplify the calculation, on this scale, no numerical simulation has been performed. A scale factor representing the ratio between the visco-elastic behavior of porous body and visco-elastic behavior of solids was used. To obtain the scale factor, the assumption that the visco-elastic properties of the porous medium follow exactly its elastic properties [56,57] was applied (see *Equation 7.17*). Therefore, as long as the ratio of the elastic behavior of the solids (C-S-H) and of the C-S-H+ water (gel water + capillary water) is obtained, the

scale factor can be determined. The ratio of elastic modulus of porous body and that of solids was from the single-cut model (3D Gaussian random field model) in [58]. The single-cut representative computational volume is shown in *Figure 7.11(a)* and the obtained ratio as a function of the volume fraction of solids (C-S-H in this study) are shown in *Figure 7.11(b)*. It means, by knowing the volume fraction of C-S-H in the hydrated gel, the ratio between the elastic behavior of the C-S-H and the elastic behavior of the hydrated gel can be calculated.

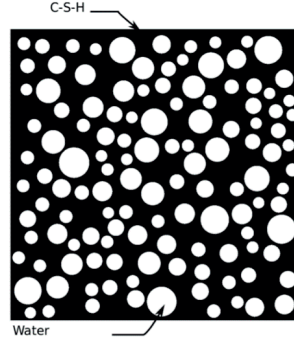


Figure 7.10 Schematic representation of C-S-H and water (hydrated gel) scale in AMIE

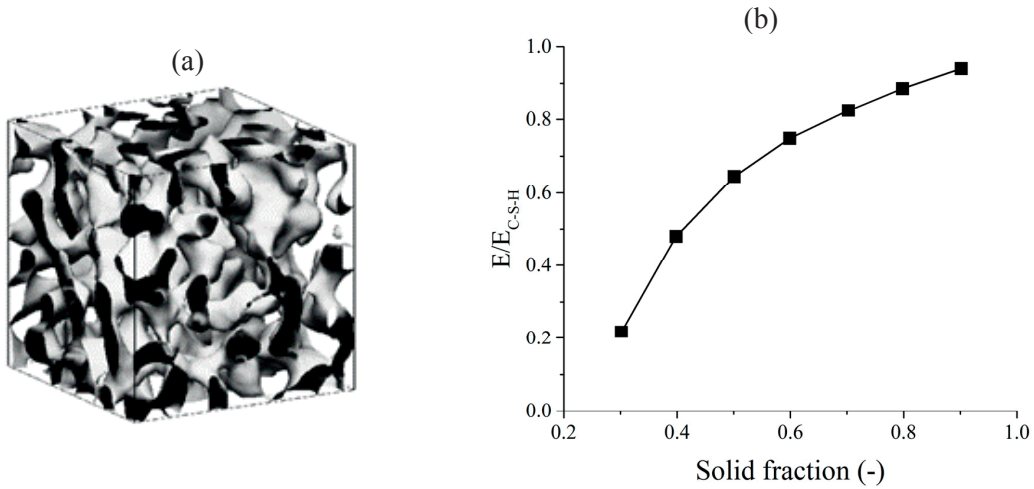


Figure 7.11 Simulated relationship between the ratio of elastic properties of solids and the porous systems: (a) Statistical models of the microstructure, single cut model [58]; (b) relationship of elastic ratio and solid fraction of the system obtained for the single cut model, adapted from [58]

Equation 7.17

$$\varepsilon_{creep}^{C-S-H+water}(\phi) / \varepsilon_{creep}^{C-S-H} = \varepsilon_{elas}^{C-S-H+water}(\phi) / \varepsilon_{elas}^{C-S-H}$$

where: $\varepsilon_{creep}^{C-S-H+water}$ and $\varepsilon_{creep}^{C-S-H}$ are the creep strain in C-S-H + water and C-S-H, respectively; $\varepsilon_{elas}^{C-S-H+water}$ and $\varepsilon_{elas}^{C-S-H}$ are the elastic strain in C-S-H + water and C-S-H, respectively.

7.2.4 Simulation of aging creep

The simulation of macro-scale aging creep is based on the approach developed in [39]. The main principle of the approach is applying a time-dependent generalized Maxwell model for C-S-H in a 3D microstructure generated from *μic* [39]. The time-dependent generalized Maxwell model is describing the visco-elastic behavior of C-S-H.

Some modifications in this thesis, compared to the approach followed in [39], are stated as follows:

The main modification regards the visco-elastic behavior of the C-S-H: in [39], visco-elastic behavior of C-S-H from nanoindentation test was used while in this thesis the back-calculated visco-elastic behavior of C-S-H based on uniaxial compressive creep tests performed on macroscopic cementitious materials (see *Chapter 5*) was used.

From nanoindentation, the relationship between the creep compliance of the C-S-H (J_{C-S-H}) and the elastic modulus of the C-S-H and the creep modulus were proposed by Vandamme and Ulm [59], see *Equation 7.18*.

Equation 7.18

$$J_{C-S-H}(t, t_0) = \frac{1}{E_{C-S-H}} + \frac{1}{C_{uni}} \ln \left(1 + \frac{t - t_0}{\tau} \right)$$

where: E_{C-S-H} [GPa] is the elastic modulus of the C-S-H; C_{uni} [GPa] is the uniaxial creep modulus which can be calculated based on the measured contact creep modulus C [GPa] and the Poisson's ratio of C-S-H (ν_{C-S-H} [-]). The determination of the value for C and C_{uni} is shown in *Equation 7.19* and *Equation 7.20*.

Equation 7.19

$$\frac{C_{uni}}{C} = 1 - \nu_{C-S-H}^2$$

Equation 7.20

$$C = 1588.9(\eta - 0.5)^{1.597}$$

where: η is the packing density of C-S-H and the value used in the simulation in [39] is 0.7.

However, there are several concerns about using the data from nanoindentation directly, as addressed in *Chapter 6*. Besides the problems mentioned, another problem for using the visco-elastic behavior of C-S-H from nanoindentation for early age creep accompanying capillary stresses is the fact that the behavior determined from nanoindentation is associated to the long-term creep, as stated in [60].

Therefore, the visco-elastic behavior obtained from back-calculation based on creep in compression (see *section 7.2.3*) is used for the simulation of aging creep. In order to describe numerically the visco-elastic response of the C-S-H, rheology models need to be used.

In this study, time-varying generalized Kelvin-Voigt chains are used instead of generalized Maxwell chains, which is the second modification compared to [39]. The equivalence of Kelvin-Voigt model and Maxwell model has been proven in [46].

Note that, since the back-calculation was performed with the macro-scale visco-elastic deformation of the cement paste at 28 d, this method is able to retrieve the non-aging visco-elastic behavior of mature C-S-H. Basically, it is equivalent to the method used in [39] without considering the densification. According to *Equation 7.18*, the evolution of creep compliance of the C-S-H is not changing at different loading time (non-aging). The aging of creep is then developing due to the increasing amount of C-S-H present in the system.

In the simulation, spatial solidification was considered [39]. During the solidification process, the visco-elastic behavior of each new C-S-H layer follows its own evolution, see *Figure 7.12*. Different loading histories of each C-S-H layer should be taken into account. Therefore, all the state of the C-S-H phases and the final creep were calculated based on the overall creep results stored in an index array and recalled at each time step. The time steps considered in this simulation are the same as in the stiffness simulation, see *section 7.2.2*.

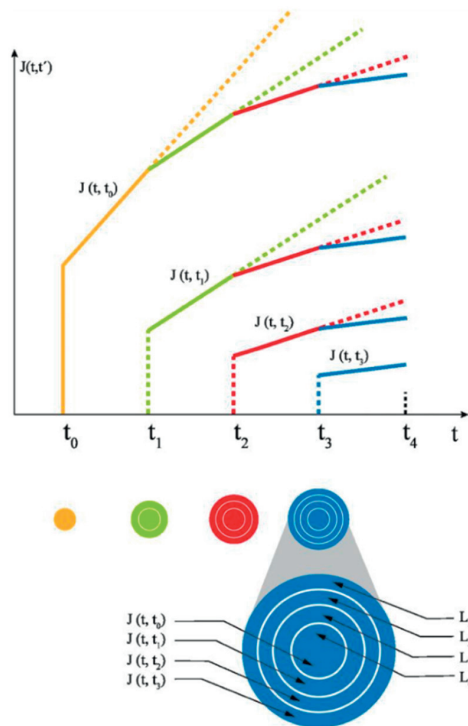


Figure 7.12 Schematic representation of creep behavior ($J(t,t_0)$, $J(t,t_1)$, $J(t,t_2)$ and $J(t,t_3)$) of different layers (L_0 , L_1 , L_2 and L_3) of C-S-H considering densification, with loading starting from t_0 (the different creep curve represents the creep behavior of the layer with the same color), from [39]

A static boundary condition was used in this simulation. In the cubic CVE (from *µic*), a uniform stress is applied on one face and the opposite face of it was fixed. The hydration products are generated in a stress-free field, as addressed explicitly in *Figure 7.13*. In *Figure 7.13*, a schematic representation of the stress and strain state during different processes are shown (in general case only): (I) is adding

an external loading; (II) hydrates formation; (III) increase of the external loading. (II) and (III) occur almost simultaneously. During process (I), in a system with existing phases, the visco-elastic response of the phases is then appearing. The new layer of C-S-H is forming in a stress-free state (II). During processes (II), the newly-formed C-S-H and the existing C-S-H before external loading act together to sustain against the so-called “*differential internal loading*” [37], which results from stress redistribution due to creep of the existing C-S-H under initial loading.

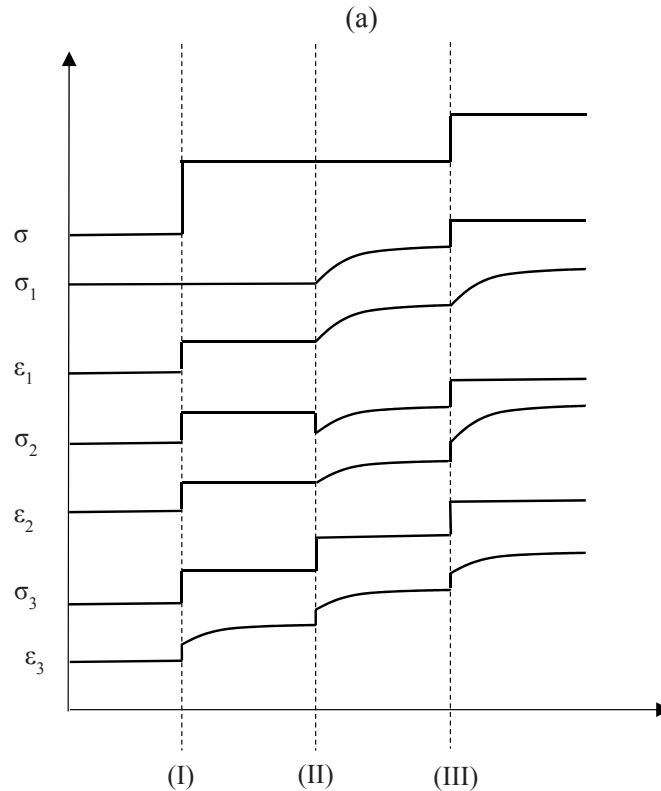


Figure 7.13 Schematic representation of the stress and strain state response of different phases during loading and hydration processes: σ is the external stress; σ_1 and ε_1 are the stress and strain response of water; σ_2 and ε_2 are the stress and strain response of clinker phases; σ_3 and ε_3 are the stress and strain response of hydrates

7.2.5 Simulation of autogenous shrinkage

The autogenous shrinkage simulation combines the simulation of the elastic response and the visco-elastic response of the materials. The simulation is based on the driving mechanism of the capillary pressure evolution. The elastic response of the autogenous shrinkage is calculated directly using the method explained in section 7.2.3. The visco-elastic behavior of C-S-H is the same as discussed in section 7.2.4. The input stress imposed on the C-S-H is the pressure calculated from the measured RH_k , S and b . Finally, the visco-elastic response of the autogenous shrinkage is simulated based on the superposition method. The simulation approach is summarized in the flow chart in Figure 7.14.

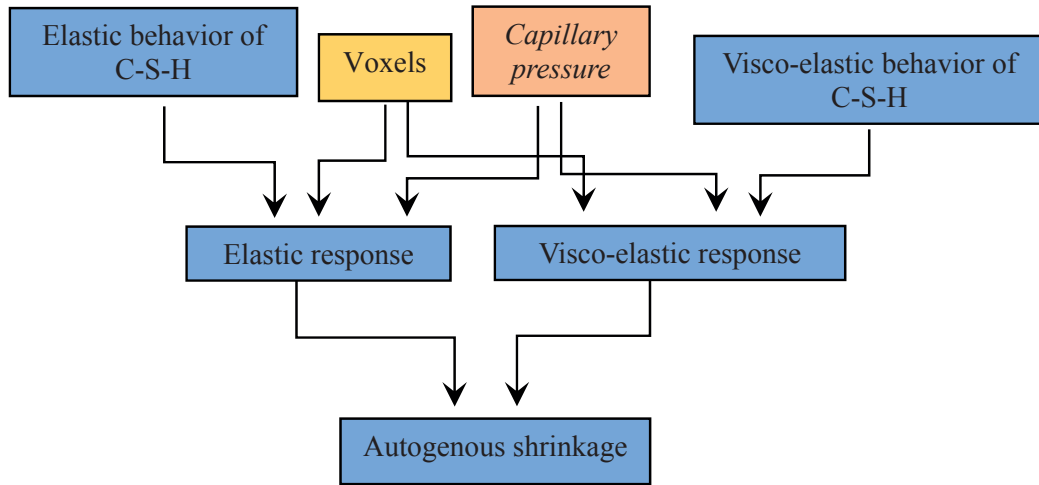


Figure 7.14 Flow chart of the simulation of autogenous shrinkage with FEM modeling

7.3 Prediction results

7.3.1 Simulation of the elastic response of material under capillary pressure

Simulation of hydration and microstructure

The simulated, meshed microstructures of systems Cement-0.35, CQZ40-0.35 and CFA40-0.35 at different ages (from 0 h to 28 d) with μic are shown in *Figure 7.15*. The corresponding simulated degree of hydration of these three systems is also presented on the right side of *Figure 7.15*. According to the meshed microstructures, during hydration, the outer C-S-H was filling the space while the cement particles were dissolved. The evolution of portlandite crystals and inner C-S-H are also visible in the figures. In different systems, the filling volume of the outer C-S-H was not the same. For example, in Cement-0.35, the outer C-S-H was almost filling the whole spaces after 6 hours of hydration, while in CQZ40-0.35, some pores were still visible in the meshed microstructure. Note that this porosity will be taken into account to calculate the porosity in outer C-S-H.

The comparison of the degree of hydration from the model and in the experiments shows that the parameters used for fitting the hydration evolution are appropriate. Some small mismatches appearing during the deceleration period of the hydration curve are possibly due to inadequate kinetics or to the inadequate densifying model for the outer C-S-H. It can also be due to an intrinsic limitation of the simulation with μic : since the chemical potential of ion concentration in the solution is not considered, the starting point of the reaction of C_3A is uncertain.

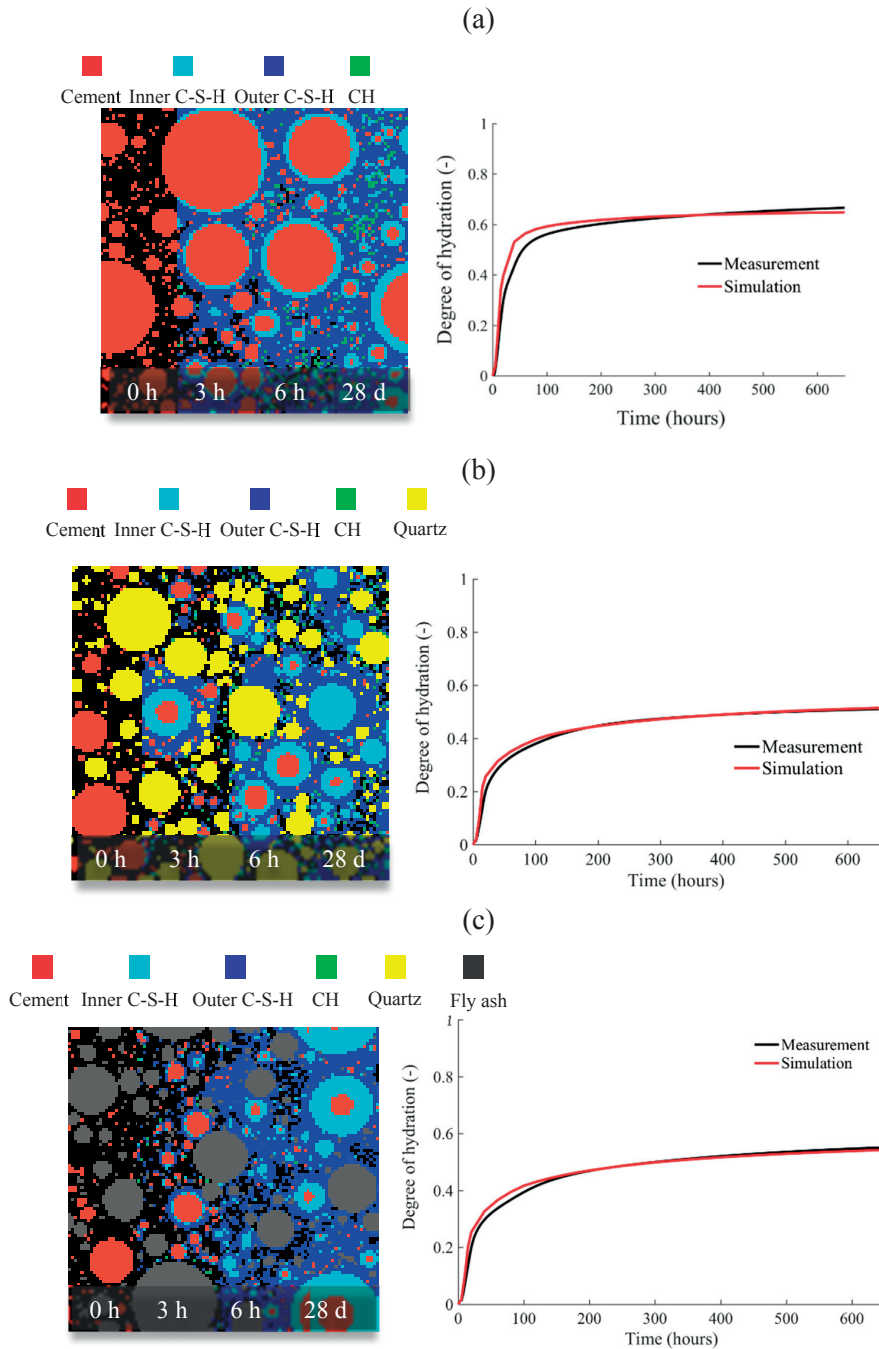


Figure 7.15 Sections of the simulated meshed microstructures for the three systems during hydration (computational cubic volume of $100 \times 100 \times 100 \mu\text{m}^3$), this figure is a 2D view from the x axis, together with the comparison between the simulated and experimental results of degree of hydration of the three systems (degree of hydration is based on total hydrated solids): (a) Cement-0.35; (b) CQZ40-0.35 and (c) CFA40-0.35

Comparison of the volume fraction of different phases from the simulation and mass balance calculation of three systems at 3 d and 28 d are shown in *Figure 7.16*. The volume fraction was normalized per gram of paste. C-S-H and water were not compared because of the assumption of filling outer C-S-H in the system for μic simulation and erroneous volume of C-S-H and water.

From *Figure 7.16*, the volume of anhydrates and fly ash was similar from both mass balance and μic simulation. However, the volumes of portlandite, AFt and AFm showed large differences between the two methods. From the simulation, the volumes of AFt and portlandite were underestimated. For the two systems (Cement-0.35 and CQZ40-0.35) considered in later simulation, the volume of AFt showed the largest difference. However, the influence of AFm should not be critical for the simulations of mechanical properties since the absolute volume of it was not high.

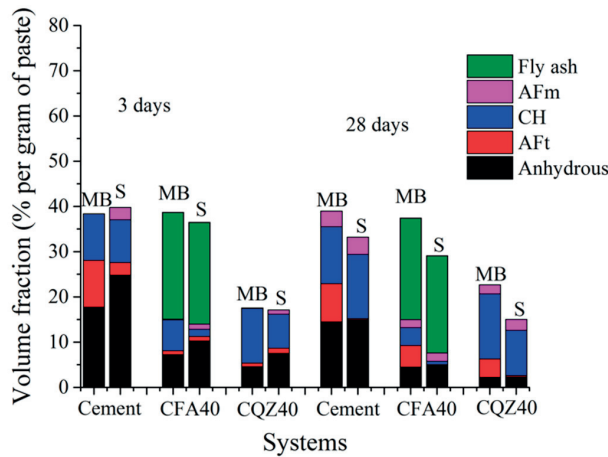


Figure 7.16 Comparison of volume fraction of phases in the system from mass balance calculation and simulation (MB: from mass balance; S: from simulation)

Simulation of stiffness of the outer C-S-H

The simulated evolution of the stiffness of the outer C-S-H as a function of porosity, based on the results with white cement of w/c 0.4 for longer curing periods, is shown in *Figure 7.17 (a)*. As expected, the lower the porosity, the higher the stiffness of the outer C-S-H.

The calculated porosity of the outer C-S-H of Cement-0.35 and CQZ40-0.35 is plotted in *Figure 7.17 (b)*. The porosity of the outer C-S-H in Cement-0.35 and CQZ40-0.35 was calculated based on *Equation 7.16*. The amount of gel water and capillary water was determined from ^1H NMR and the volume fraction of outer C-S-H was obtained from the μic simulation described in the previous subsection. A higher porosity of the outer C-S-H in CQZ40-0.35 should be observed. However, from the figure, the porosity of the outer C-S-H in Cement-0.35 and CQZ40-0.35 was similar, evolving from 0.9 to around 0.5 during the considered period. These results can be interpreted as the lower volume of the solid phases simulated for CQZ40-0.35, corresponding to higher porosity from the μic simulation. As mentioned before, since the outer C-S-H was not able to fill the whole space in CQZ40-0.35, the porosity

from the μic simulation has to be subtracted from the total water obtained from 1H NMR. Thus, the porosity calculated for the outer C-S-H was lower in CQZ40-0.35.

Based on the relationship of the back-calculated stiffness of the outer C-S-H and the porosity of the outer C-S-H, the stiffness evolution of the outer C-S-H as a function of time in Cement-0.35 and CQZ40-0.35 can be both determined. To check the feasibility of the method, the simulated elastic modulus of Cement-0.35 using the stiffness of the outer C-S-H identified is presented in *Figure 7.18*. It can be seen the trend of the elastic modulus followed well the experimental results. The elastic modulus at 28 d from the simulation was around 3 GPa higher than the one from the measurement.

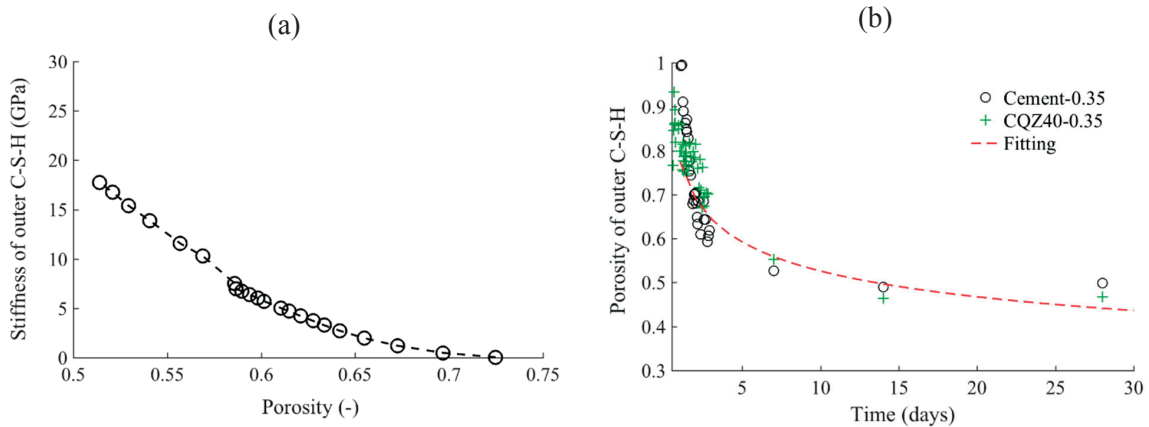


Figure 7.17 Simulated stiffness of outer C-S-H as a function of porosity using the same two systems as in [42] but the duration was extended to 28 days.

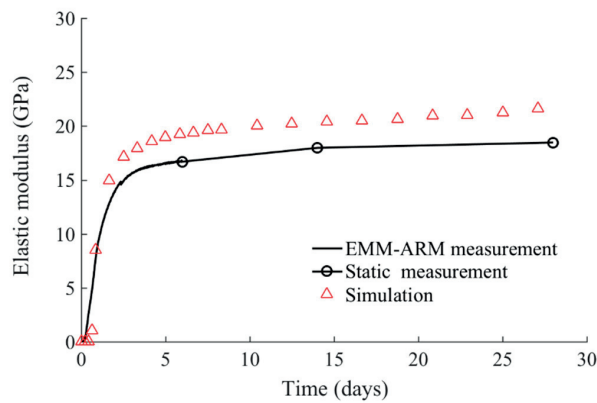


Figure 7.18 Blind simulation of elastic modulus of Cement-0.35

Simulation of elastic response of autogenous shrinkage

The simulated elastic response of Cement-0.35 and CQZ40-0.35 under pore pressure is shown in *Figure 7.19*. The results were compared with the elastic part of the autogenous shrinkage calculated by using poromechanics for both systems (see detailed calculation in *Chapter 6*).

In both Cement-0.35 and CQZ40-0.35, it can be seen that the strain in the FEM was lower than the poromechanics strain, which is consistent with the higher simulated elastic modulus presented in the previous section. At 28 d, the simulated elastic strain was around 70 $\mu\text{m/m}$ lower than the results from the poromechanics.

The difference between the simulated and poromechanics strain can be due to two reasons. First of all, it is because that the simulated elastic response was based on the stiffness of outer C-S-H back-calculated from a white cement system with w/c of 0.40. The properties of outer C-S-H are actually known to be related to the w/c [37]. Another possible reason can be due to the differences from the poromechanics strain calculation when using different parameters, see *Chapter 6*.

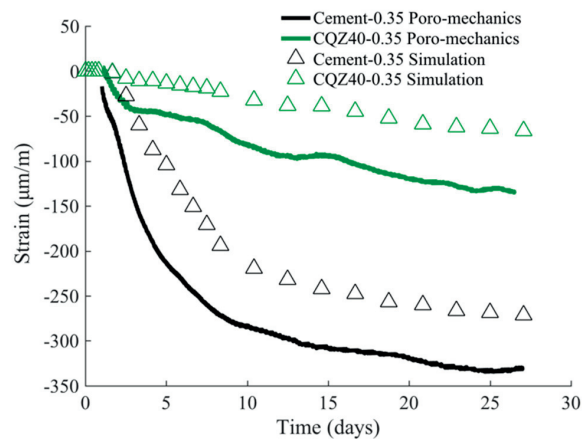


Figure 7.19 Simulated elastic response of autogenous shrinkage and the comparison of it with the analytical calculation from poromechanics

7.3.2 Simulation of the non-aging visco-elastic behavior of C-S-H

The parameters obtained from FEM simulation for the generalized Kelvin-Voigt model by fitting the macro-scale creep data of Cement-0.35 at 28 d are shown in *Table 7.6*. Note that this calculation was performed at the scale of the cement paste (the scale 2). Therefore, the calculated parameters are for the matrix with C-S-H and water together. Next, the relationship between the porous body and the solid was used, as explained in *section 7.2.3*. In the calculation, the solid volume fraction in C-S-H and water matrix was around 0.55, as calculated from the mass balance method. The corresponding ratio between the visco-elastic behavior of the matrix and the C-S-H was around 0.70 (the scale factor), based on *Figure 7.11 (b)*.

One aspect that should be noticed is that the parameters for the generalized Kelvin-Voigt chains for C-S-H and water are proportional to the parameters for cement paste. This is not only an assumption but is due to the fact that the C-S-H is the only phase in the system which exhibits visco-elastic behavior. The study in [61] supports this behavior by indicating that down-scaling from cement paste to C-S-H hydrates does not change the trend of the creep function curve. Therefore, during the fitting process, after fitting the cement paste with generalized Kelvin-Voigt chains (the same process as in *Chapter 5*), the parameters for visco-elastic behavior of C-S-H and water can be simulated by only multiplying with a scale factor. This two-steps process makes the fitting of the visco-elastic behavior much easier.

The fitted creep of cement paste is compared to the measured creep of Cement-0.35 at 28 d, see *Figure 7.20(a)*. With the parameters listed on *Table 7.6*, the simulated creep of cement paste can well capture the evolution of the measured creep. Both the evolution of the visco-elastic response of the sole C-S-H and of the matrix composed of C-S-H and water can be seen in *Figure 7.20(a)*.

Table 7.6 Parameters for the generalized Kelvin-Voigt model for C-S-H and water

τ_1 (day)	τ_2 (day)	τ_3 (day)	τ_4 (day)	τ_5 (day)
0.02	0.2	2	20	200
E_1 (Pa)	E_2 (Pa)	E_3 (Pa)	E_4 (Pa)	E_5 (Pa)
7.0×10^{10}	4.2×10^{10}	3.4×10^{10}	2.59×10^{10}	9.1×10^9

Compared to the creep compliance of C-S-H obtained from nanoindentation, which was also plotted in *Figure 7.20(b)* for comparison, the method applied in this thesis yields smaller deformations, ranging from around 34 $\mu\text{m}/\text{m}/\text{MPa}$ to around 111 $\mu\text{m}/\text{m}/\text{MPa}$. Considering the densification process of the C-S-H, the denser the C-S-H is, the stiffer the C-S-H will be [59]. If the creep response obtained from nanoindentation corresponds to long-term creep manifesting over years, the visco-elastic behavior of C-S-H should be stiffer than the one back-calculated from macro-scale creep experiments at early ages. As presented in *Figure 7.20*, the results agreed with the expectation: the visco-elastic deformation of C-S-H was slightly lower than the one obtained from the back-calculation.

Compared to the visco-elastic behavior of needle-shaped C-S-H [61], obtained from homogenization fitting based on 3-minutes' creep experiments, the visco-elastic behavior of C-S-H was lower in the needle-shaped C-S-H.

In [61], the isochoric creep of needle-shaped hydrates is proposed to have a power-law behavior, see *Equation 7.21*. The parameters were determined from minimizing the error between the simulated visco-elastic response of a multi-scale microstructure model and experimental results.

Equation 7.21

$$\mathbb{J}_{hyd}(t-\tau) = \frac{1}{3K_{hyd}} \mathbb{I}^{vol} + \frac{1}{2} \left[\frac{1}{\mu_{hyd}} + \frac{1}{\mu_{c,hyd}} \left(\frac{t-\tau}{t_{ref}} \right)^{\beta_{hyd}} \right] \mathbb{I}^{dev}$$

where: $\mathbb{J}_{hyd}(t-\tau)$ [$\mu\text{m}/\text{m}/\text{MPa}$] is the creep tensor function of needle-shaped C-S-H; t [seconds] is the current time; τ [seconds] is the loading time, t_{ref} is the reference time (using a fixed value of 86400 seconds after [62]); K_{hyd} and μ_{hyd} are the bulk modulus and the shear modulus of needle-shaped C-S-H; \mathbb{I}^{vol} and \mathbb{I}^{dev} are the volumetric and the deviatoric part of the identity tensor \mathbb{I} , see [61]. $\mu_{c,hyd}$ and β_{hyd} is the shear creep modulus and exponent of needle shape C-S-H. The values for K_{hyd} , μ_{hyd} , $\mu_{c,hyd}$ and β_{hyd} determined from the simulation in [61] are 18.69 GPa, 11.76 GPa, 20.93 GPa and 0.251, respectively. Only linear deformation was considered in the comparison.

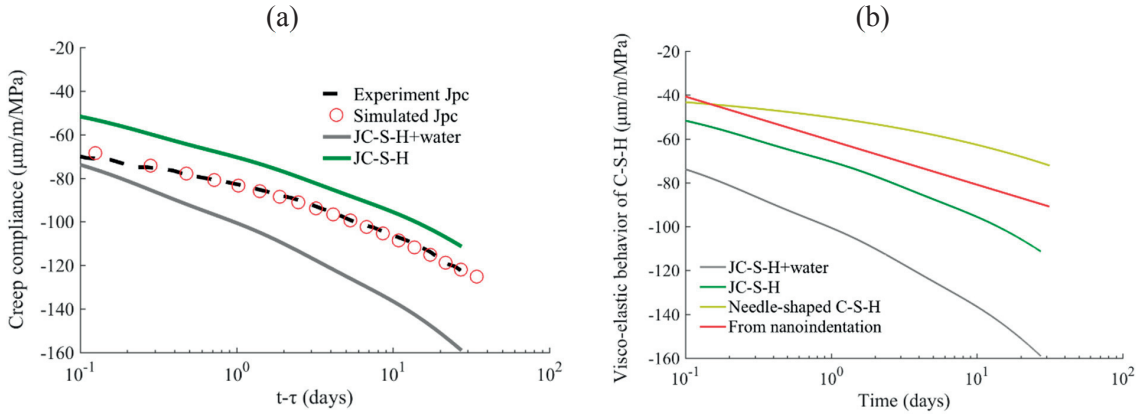


Figure 7.20 Simulated visco-elastic behavior of C-S-H and hydrated gel (C-S-H and water together): (a) comparison between the fitted and the measured creep of cement paste; (b) comparison with the creep of C-S-H from nanoindentation and the simulation in [61]

The reason for the small difference of the visco-elastic behavior of C-S-H is that different shapes of phases in the microstructure modeling were selected. From self-consistent scheme homogenization simulation, the stiffness for needle-shaped C-S-H is higher than the one for a spherical C-S-H [42]. To clarify the exact reason, more studies should be carried out.

7.3.3 Simulation of aging creep

The specific basic creep of Cement-0.35 and CQZ40-0.35 under loading at 3 d and 14 d is simulated. The results are compared with the experimental data (see Chapter 5), see Figure 7.21. The results from these two loading ages were selected due to the stable creep behavior apparent in the experimental data.

For both systems, the simulation underestimates creep at both loading times. The mismatch is more significant at the beginning of the loading. For the long term, the kinetics of the creep evolution was not so different between the simulation and the measurement. Since the same visco-elastic behavior of C-S-H was used for simulation, the differences between the two systems were only due to the amount of C-S-H. One problem is the fact that the visco-elastic behavior of C-S-H was calculated

from Cement-0.35 at 28 d. It should be noted that the density of C-S-H could be different with different w/c, which is not taken into consideration in this thesis. Clearly, the densification makes a huge difference for the simulation.

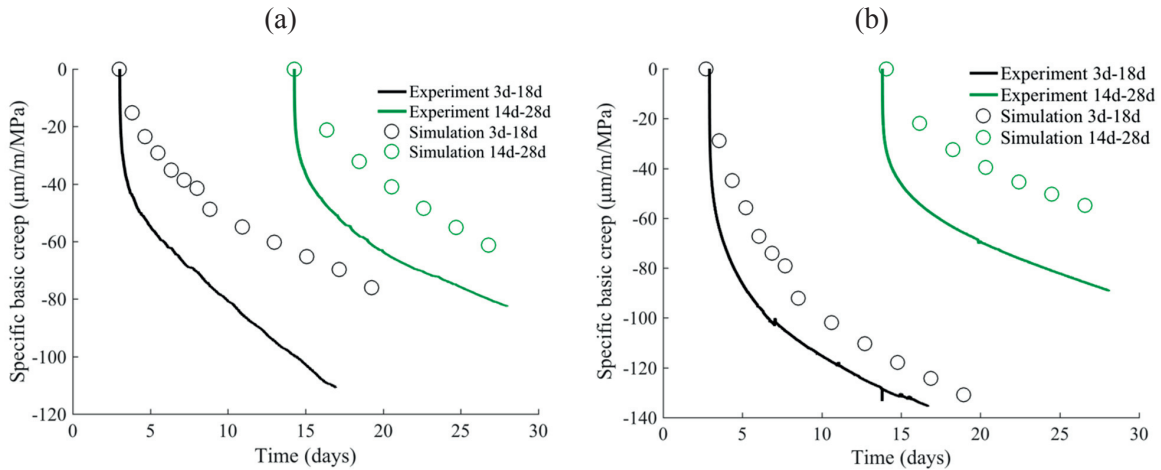


Figure 7.21 Simulated creep of Cement-0.35 and CQZ40-0.35 under loading at 3 d and 14 d

7.3.4 Simulation of autogenous shrinkage

The superposition principle was used for calculating the visco-elastic response of the autogenous shrinkage. Due to high computational cost, only 6 loading steps were selected in the calculation: 20, 60, 100, 140, 200 and 300 hours. The visco-elastic response of the material to effective pore pressure at each loading step was first simulated, see *Figure 7.22*. The same parameters as explained in *section 7.3.3* were used during the simulation. The simulated elastic part of the autogenous shrinkage (see *section 7.3.1*) was also added in the calculation of the final autogenous shrinkage, see *Figure 7.23*.

From the comparison between the simulated visco-elastic response of autogenous shrinkage and the prediction from the generalized Kelvin-Voigt model, the former had lower value than the latter especially at early ages in both systems. In CQZ40-0.35, the simulated visco-elastic response of autogenous shrinkage was closer to the prediction from the generalized Kelvin-Voigt model than that in Cement-0.35.

The simulated autogenous shrinkage in CQZ40-0.35 was much lower than in Cement-0.35 which is consistent with the experimental data. However, in both cases, the simulated autogenous shrinkage was higher than the experimental results, especially at later ages.

Note that the loading steps are not enough to follow the accurate evolution of the capillary pressure and consequently the visco-elastic behavior of the materials. This is for example the reason for the sharp increase of the strain at 14 d in the simulation of autogenous shrinkage of Cement-0.35.

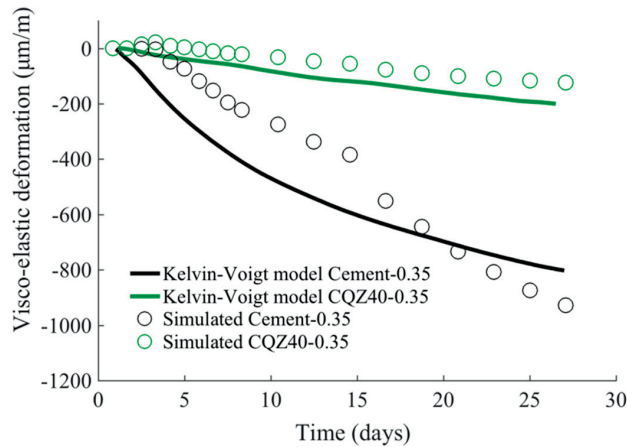


Figure 7.22 Comparison between the simulated visco-elastic deformation of Cement-0.35 and CQZ40-0.35 from FEM method and from generalized Kelvin-Voigt chains model

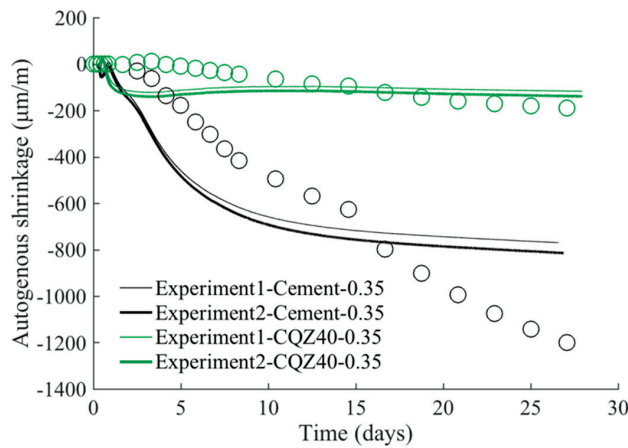


Figure 7.23 Simulated autogenous shrinkage of Cement-0.35 and CQZ40-0.35

7.4 Conclusions

In this chapter, the numerical simulation of autogenous shrinkage until 28 days for Cement-0.35 and CQZ40-0.35 was accomplished. The simulation is organized in the following structure: 1) the microstructure was simulated with the *mic* platform to obtain the representative computational volume, including phases fraction and distribution; 2) the elastic and visco-elastic behavior of the C-S-H were simulated in *AMIE* by using back-calculation from experimental results; 3) the elastic part of the autogenous shrinkage was simulated based on the simulated microstructure, the elastic behavior of the C-S-H and the calculated pore pressure; 4) the visco-elastic response of the autogenous shrinkage was simulated based on the simulated microstructure, the visco-elastic behavior of the C-S-H and the

calculated pore pressure. The autogenous shrinkage was then simulated combining the elastic response and the visco-elastic response: point 3) and point 4).

The main conclusions of this chapter are:

1. Actual particle size distributions of the raw materials were used in the microstructure simulation with the *μic* platform. Using the same kinetics parameters for the same phases in different systems, the degree of hydration of cementitious materials can be accurately fitted. Since the pore size distribution cannot be accurately simulated, the capillary pressure as the driving force of the autogenous shrinkage needs to be calculated from the experimental RH and *RH_s* results and be imposed as a load considering the saturation degree and Biot coefficient on the C-S-H in the FEM simulation.
2. The elastic behavior of the outer C-S-H is highly linked with the porosity in the outer C-S-H. With the back-calculated behavior of the outer C-S-H from one system, the elastic response of autogenous shrinkage in other systems can be simulated. The simulated elastic response was higher than the one analytically calculated with poromechanics method. Possible reasons for this observed difference were that a simulation with size of $1 \times 100 \times 100 \mu\text{m}^3$ was used in the simulation and also that the properties of the C-S-H might vary with cement type.
3. The creep of the C-S-H back-calculated from macroscale creep results of cement paste was slightly higher than the one obtained from nanoindentation. Compared to the results obtained also from back-calculation in multi-scale modeling in the literature, the creep of the C-S-H obtained in this chapter was also higher. This might be due to differences in the shape of the C-S-H between this chapter and the literature.
4. The simulated creep based on the visco-elastic behavior of the C-S-H was lower than in the experiments, especially for CQZ40-0.35. This is mainly because of the inaccurately simulated water amount and wrong pore-network.
5. The final simulation of the autogenous shrinkage was of the same magnitude of the experimental data. With limited loading steps, the autogenous shrinkage was overestimated in both systems. It is remarked that the assumptions and simplifications used in this simulation need further verification.

7.5 References

- [1] H. F. W. Taylor, Cement chemistry, Thomas Telford Publishing, 1997.
- [2] I. G. Richardson, Tobermorite/jennite- and tobermorite/calcium hydroxide-based models for the structure of C-S-H: applicability to hardened pastes of tricalcium silicate, β -dicalcium silicate, Portland cement, and blends of Portland cement with blast-furnace slag, metakaol, Cem. Concr. Res. 34 (2004) 1733–1777.
- [3] X. Cong, R. J. Kirkpatrick, ²⁹Si MAS NMR study of the structure of calcium silicate hydrate, Adv. Cem. Based Mater. 3 (1996) 144–156.
- [4] H. M. Jennings, Refinements to colloid model of C-S-H in cement: CM-II, Cem. Concr. Res. 38 (2008) 275–289.

- [5] H. M. Jennings, Colloid model of C-S-H and implications to the problem of creep and shrinkage, *Mater. Struct.* 37 (2003) 59–70.
- [6] A. Bazzoni, Study of early hydration mechanisms of cement by means of electron microscopy, EPFL, 2014.
- [7] A. C. A. Muller, K.L. Scrivener, A.M. Gajewicz, P.J. McDonald, Use of bench-top NMR to measure the density, composition and desorption isotherm of C-S-H in cement paste, *Microporous Mesoporous Mater.* 178 (2013) 99–103.
- [8] A. C. A. Muller, Characterization of porosity & C-S-H in cement pastes by ^1H NMR, EPFL, 2014.
- [9] S. Bishnoi, K. L. Scrivener, Studying nucleation and growth kinetics of alite hydration using μic , *Cem. Concr. Res.* 39 (2009) 849–860.
- [10] H. M. Jennings, A model for the microstructure of calcium silicate hydrate in cement paste, *Cem. Concr. Res.* 30 (2000) 101–116.
- [11] E. M. J. Berodier, Impact of the Supplementary Cementitious Materials on the kinetics and microstructural development of cement hydration, Ecole Polytechnique Federale De Lausanne, 2015.
- [12] ASTM C618, Standard specification for coal fly ash and raw or calcined natural pozzolona for use in concrete, (2015) 1–5.
- [13] B. W. Langan, K. Weng, M.A. Ward, Effect of silica fume and fly ash on heat of hydration of Portland cement, 32 (2002) 1045–1051.
- [14] M. Narmluk, T. Nawa, Effect of curing temperature on pozzolanic reaction of fly ash in blended cement paste, *Int. J. Chem. Eng. Appl.* 5 (2014) 31–35.
- [15] F. Deschner, F. Winnefeld, B. Lothenbach, S. Seufert, P. Schwesig, S. Dittrich, F. Goetz-Neunhoeffler, J. Neubauer, Hydration of Portland cement with high replacement by siliceous fly ash, *Cem. Concr. Res.* 42 (2012) 1389–1400.
- [16] B. Lothenbach, K. Scrivener, R. D. Hooton, Supplementary cementitious materials, *Cem. Concr. Res.* 41 (2011) 1244–1256.
- [17] I. G. Richardson, G. W. Groves, The incorporation of minor and trace elements into calcium silicate hydrate (CSH) gel in hardened cement pastes, *Cem. Concr. Res.* 23 (1993) 131–138.
- [18] K. L. Scrivener, B. Lothenbach, N. De Belie, E. Gruyaert, J. Skibsted, R. Snellings, A. Vollpracht, TC 238-SCM: hydration and microstructure of concrete with SCMs, *Mater. Struct.* (2015) 835–862.
- [19] P. T. Durdziński, M. Ben Haha, S. A. Bernal, N. De Belie, G. Elke, B. Lothenbach, J. L. Provis, A. Schöler, C. Stabler, Z. Tan, A. Vollpracht, F. Winnefeld, Y. Villagrán Zaccardi, M. Zajac, K. L. Scrivener, Outcomes of the RILEM round robin on degree of reaction of slag and fly ash in blended cements, *Mater. Struct.* 50:135 (2017).
- [20] P. T. Durdziński, C. F. Dunant, M. Ben Haha, K. L. Scrivener, A new quantification method based on SEM-EDS to assess fly ash composition and study the reaction of its individual components in hydrating cement paste, *Cem. Concr. Res.* 73 (2015) 111–122.
- [21] M. Avrami, Melvin, Kinetics of phase change. I general theory, *J. Chem. Phys.* 7 (1939) 1103–1112.

- [22] J. W. Cahn, The kinetics of grain boundary nucleated reactions, *Acta Metall.* 4 (1956) 449–459.
- [23] G.W. Scherer, J. Zhang, J. J. Thomas, Nucleation and growth models for hydration of cement, *Cem. Concr. Res.* 42 (2012) 982–993.
- [24] A. Kumar, S. Bishnoi, K. L. Scrivener, Modelling early age hydration kinetics of alite, *Cem. Concr. Res.* 42 (2012) 903–918.
- [25] J. J. Thomas, J. J. Biernacki, J. W. Bullard, S. Bishnoi, J. S. Dolado, G. W. Scherer, A. Luttge, Modeling and simulation of cement hydration kinetics and microstructure development, *Cem. Concr. Res.* 41 (2011) 1257–1278.
- [26] D. R. Vollet, A. F. Craievich, Effects of temperature and of the addition of accelerating and retarding agents on the kinetics of hydration of tricalcium silicate, *J.Phys.Chem. B.* 104 (2000) 12143–12148.
- [27] P. Navi, C. Pignat, Simulation of cement hydration and the connectivity of the capillary pore space, *Adv. Cem. Based Mater.* 4 (1996) 58–67.
- [28] K. Kondo, S. Ueda, Kinetics and mechanisms of the hydration of cements, in: *Proc. Fifth Int. Symposium Chem. Cem.*, Tokyo, 1968: pp. 203–248.
- [29] J. M. Pommersheim, J. R. Clifton, Mathematical modeling of tricalcium silicate hydration, *Cem. Concr. Res.* 9 (1979) 765–770.
- [30] H. M. Jennings, S. K. Johnson, Simulation of microstructure development during the hydration of a cement compound, *J. Am. Ceram. Soc.* 69 (1986) 790–795.
- [31] D. P. Bentz, Three dimensional computer simulation of Portland cement hydration and microstructure development, *J. Am. Ceram. Soc.* 80 (1997) 3–21.
- [32] C. Pignat, Simulation of cement paste microstructure hydration, pore space characterization and permeability determination, *Mater. Struct.* 38 (2005) 459–466.
- [33] J. W. Bullard, E. Enjolras, W. L. George, S. G. Satterfield, J. E. Terrill, A parallel reaction-transport model applied to cement hydration and microstructure development, *Model. Simul. Mater. Sci. Eng.* 18 (2010) 25007.
- [34] K. Maekawa, R. Chaube, T. Kishi, Modelling of concrete performance : hydration, microstructure formation, and mass transport, E & FN Spon, London ;, 1999.
- [35] K. Maekawa, T. Ishida, T. Kishi, Multi-scale Modeling of Concrete Performance, *J. Adv. Concr. Technol.* 1 (2003) 91–126.
- [36] S. Bishnoi, K. L. Scrivener, uic: A new platform for modelling the hydration of cements, *Cem. Concr. Res.* 39 (2009) 266–274.
- [37] Q. Do, Modelling properties of cement paste from microstructure : porosity, mechanical properties, creep and shrinkage, EPFL, 2013.
- [38] K. van Breugel, Numerical simulation of hydration and microstructural development in hardening cement-based materials. (II) applications, *Cem. Concr. Res.* 25 (1995) 522–530.
- [39] Q. H. Do, S. Bishnoi, K. L. Scrivener, Microstructural modeling of early-age creep in hydrating cement paste, *J. Eng. Mech.* (2016) 4016086.
- [40] J. Marchand, E. Samson, Y. Maltais, R. J. Lee, S. Sahu, Predicting the performance of concrete structures exposed to chemically aggressive environment—Field validation, *Mater. Struct.* 35

- (2002) 623–631.
- [41] B. Münch, L. Holzer, Contradicting geometrical concepts in pore size analysis attained with electron microscopy and mercury intrusion, *J. Am. Ceram. Soc.* 91 (2008) 4059–4067.
- [42] J. L. D. Granja, Continuous characterization of stiffness of cement - based materials: experimental analysis and micro-mechanics modelling, 2016.
- [43] T. Honorio, B. Bary, F. Benboudjema, Multiscale estimation of ageing viscoelastic properties of cement-based materials: A combined analytical and numerical approach to estimate the behaviour at early age, *Cem. Concr. Res.* 85 (2016) 137–155.
- [44] J. W. Bullard, H. M. Jennings, R. A. Livingston, A. Nonat, G. W. Scherer, J. S. Schweitzer, K. L. Scrivener, J. J. Thomas, Mechanisms of cement hydration, *Cem. Concr. Res.* 41 (2011) 1208–1223.
- [45] C. F. Dunant, K.L. Scrivener, Micro-mechanical modelling of alkali–silica-reaction-induced degradation using the AMIE framework, *Cem. Concr. Res.* 40 (2010) 517–525.
- [46] A. B. Giorla, Modelling of Alkali-Silica Reaction under Multi-Axial Load, EPFL, 2013.
- [47] J. Sanahuja, L. Dormieux, G. Chanvillard, Modelling elasticity of a hydrating cement paste, *Cem. Concr. Res.* 37 (2007) 1427–1439.
- [48] C. F. Dunant, A. Hilaire, Dunant 2015 - Fully-coupled creep-damage models for concrete, (2015) 1–8.
- [49] K. Velez, S. Maximilien, D. Damidot, G. Fantozzi, F. Sorrentino, Determination by nanoindentation of elastic modulus and hardness of pure constituents of Portland cement clinker, *Cem. Concr. Res.* 31 (2001) 555–561.
- [50] F. G. Bell, A survey of the engineering properties of some anhydrite and gypsum from the north and midlands of England, *Eng. Geol.* 38 (1994).
- [51] G. Constantinides, F.-J. Ulm, The effect of two types of C-S-H on the elasticity of cement-based materials: Results from nanoindentation and micromechanical modeling, *Cem. Concr. Res.* 34 (2004) 67–80.
- [52] H. Manzano, J. S. Dolado, A. Ayuela, Elastic properties of the main species present in Portland cement pastes, *Acta Mater.* 57 (2009) 1666–1674.
- [53] Quartz | Quartz Grinding | Ceramic Quartz | Quartz Properties, (n.d.). http://www.ferroc ceramic.com/quartz_table.htm.
- [54] T. Matsunaga, J. Kim, S. Hardcastle, P. Rohatgi, Crystallinity and selected properties of fly ash particles, *Mater. Sci. Eng. A.* 325 (2002) 333–343.
- [55] A. B. Giorla, Modelling of alkali-silica reaction under multi-axial load, EPFL, 2013.
- [56] H. S. Tsien, A generalization of Alfrey’s theorem for visco-elastic media, in: *Q. Appl. Math.*, 1950: pp. 104–106.
- [57] T. Alfrey, Non-homogeneous stresses in visco-elastic media, *Q. Appl. Math.* 2 (1944) 113–119.
- [58] A. P. Roberts, E. J. Garboczi, Computation of the linear elastic properties of random porous materials with a wide variety of microstructure, *R. Soc.* 458 (2002) 1033–1054.
- [59] M. Vandamme, F.-J. Ulm, Nanogranular origin of concrete creep, *Proc. Natl. Acad. Sci. U. S. A.* 106 (2009) 10552–10557.

- [60] M. Vandamme, F. J. Ulm, Nanoindentation investigation of creep properties of calcium silicate hydrates, *Cem. Concr. Res.* 52 (2013) 38–52.
- [61] M. Königsberger, M. Irfan-ul-Hassan, B. Pichler, C. Hellmich, Downscaling based identification of nonaging power-law creep of cement hydrates, *J. Eng. Mech.* 142 (2016) 4016106.
- [62] M. Irfan-ul-Hassan, B. Pichler, R. Reihnsner, C. Hellmich, Elastic and creep properties of young cement paste, as determined from hourly repeated minute-long quasi-static tests, *Cem. Concr. Res.* 82 (2016) 36–49.

Chapter 8 Conclusions and perspectives

The main goal of the current work is to predict autogenous shrinkage of cementitious materials at early ages (up to 28 days). Both analytical prediction and numerical simulation methods were developed for capturing the evolution of autogenous shrinkage. The main conclusions and perspectives are presented in this chapter.

Entire conclusions are categorized into two parts: experimental part and simulation part, which is consistent to the structure of this thesis. The experimental part is useful on the one hand for understanding the effect of hydration, microstructure, relative humidity and mechanical properties on the evolution of autogenous shrinkage, and on the other hand for providing chemical and physical related inputs for later simulations. The simulation part proves the possibility of predicting the whole evolution of autogenous shrinkage with experimental determined parameters. Additionally, it helps for better understanding of the behavior and mechanisms of autogenous shrinkage.

Contents

8.1 Experimental part.....	190
8.1.1 Main findings.....	190
8.1.2 Future perspectives.....	191
8.2 Analytical prediction part.....	191
8.2.1 Main findings.....	191
8.2.2 Future perspectives.....	192
8.3 Numerical simulation part.....	192
8.3.1 Main findings.....	192
8.3.2 Future perspectives.....	193
8.4 References.....	193

8.1 Experimental investigations

To understand fundamental behavior of autogenous shrinkage, experiments related to autogenous shrinkage were carried out. This work focused on systems with different w/s (0.35 and 0.3) and substitution levels of quartz filler and fly ash. For visco-elastic behavior, three typical systems were selected (Cement-0.35, CFA40-0.35 and CQZ40-0.35). Autogenous shrinkage was measured by using corrugated tubes; degree of hydration and phases assemblage were followed with isothermal calorimetry and XRD; microstructure was investigated with MIP and ^1H NMR; the reaction of fly ash was determined with SEM-EDS method and visco-elastic tests were carried out with creep frames. Experimental part includes *Chapter 2*, *Chapter 3*, part of *Chapter 4* and *Chapter 5*.

8.1.1 Main findings

Important findings according to this part of work are listed as below:

The autogenous shrinkage of cementitious materials is impacted by the w/c, the amount of substitution fillers and the pozzolanic reaction. The correlation between autogenous shrinkage and RH indicates that autogenous shrinkage is highly linked with but not only with the evolution of RH.

- Systems with lower w/c have higher autogenous shrinkage. The reason can be associated to the less available water and faster hydration (see *Chapter 2*).
- The addition of fly ash and quartz fillers lowers the autogenous shrinkage, especially at early ages. The effect is due to the affected microstructure evolution (higher porosity) and more initial available water at early ages.
- At 28 d, fly-ash-blended system results to almost 100 $\mu\text{m}/\text{m}$ higher than the quartz-blended system with the same substitution level. The reaction of fly ash was around 25% at that time. This higher autogenous shrinkage is due to the rigid solids transformed to the hydrated gel which has higher deformation under same stress.
- The relationship between autogenous shrinkage and RH are approximately linear. The relationship follows the indication of the Kelvin-Laplace equation. The systems with higher amount of quartz fillers show a big expansion at first several days.

Elastic modulus is higher in systems with lower w/c. The effect of fillers on the elastic modulus is not significant. On the one hand, the stiffness of quartz is higher than hydration products and lower than anhydrates (clinker phases). On the other hand, the effect of porosity has to be taken into account. It compensates the influence of replacement of quartz powders on elastic modulus. Actually the effect of porosity is much higher than the effect of stiffness of raw materials.

The visco-elastic behavior of cementitious materials is different with or without fillers inside. The fly-ash-blended systems show highest visco-elastic behavior. It is clear that the effect of porosity, elastic modulus and hydration of fly ash play a big role.

The kinetics of creep compliance is following a power-law expression. The amplitude of the equation

is related to the type of samples, loading time and history of loading while the slope was influenced by the w/c through degree of hydration.

8.1.2 Future perspectives

There are still unclear mechanisms and explanations of some properties in this part of work. Future work for experimental investigations of autogenous shrinkage should focus on quantification of the effect of different factors:

- Clarification of the expansion shown in quartz systems with low w/c at first several days. A quantification of the effect should be properly done.
- Quantification of the effect of pozzolanic reaction of fly ash on autogenous shrinkage evolution. Origins of the impact should be clarified as well.
- The exact reasons for higher visco-elastic behavior on fly-ash-blended systems should be studied more by bridging better the correlation between different properties. Statistical methods or modeling will be helpful tools for the quantification of the links between them.
- The existence of coupling of autogenous shrinkage and creep is still not clear. It would be useful to have an investigation on this problem. First step is to prove the existence of the coupling and the next step is to quantify it.

8.2 Analytical prediction part

8.2.1 Main findings

Two analytical predictions were carried out in this thesis: 1) the prediction of RH based on microstructure evolution of cementitious materials according to Kelvin-Cohan equation, see *Chapter 4*; 2) the prediction of autogenous shrinkage based on poromechanics and experimental results of visco-elastic behavior of the materials, see *Chapter 6*.

Some main findings based on this part of work are listed as follows:

The prediction of RH with the new method based on ^1H NMR and MIP shows a good agreement with the experimental RH. Since the prediction is based on the microstructure evolution, it will be a good sign for later using microstructure modeling for autogenous shrinkage.

The autogenous shrinkage of cementitious materials was predicted from available models with parameters quantified from experimental data. The elastic response was predicted by using poromechanical methods and the visco-elastic behavior was done with the method using generalized Kelvin-Voigt chains.

The prediction of autogenous shrinkage was completed considering both elastic and visco-elastic response based on experimental data. The results agreed reasonably well with the experimental autogenous shrinkage. The prediction well captured the aging visco-elastic behavior, when using generalized Kelvin-Voigt chains.

Within the modeling, the comparison of the saturation fraction and Powers' model and the visco-elastic Poisson's ratio from different models were done. In the case of autogenous shrinkage, no significant difference was found by using different poromechanical models. The saturation fraction from Powers' law was a bit higher than the experimental results. The visco-elastic Poisson's ratio is an important parameter but also the most uncertain one.

8.2.2 Future perspectives

Future work on the prediction of autogenous shrinkage should focus on:

1) adding the simulation of expansion in the total prediction;

In systems with higher w/c, the expansion can be a large portion of the total deformation. However, only few studies considered the expansion caused by ettringite into simulation of autogenous shrinkage [1]. For another source of expansion, the crystallization of portlandite [2] also needs to be considered in the prediction. It will help to complete the prediction of total autogenous deformation.

2) verifying the parameters used in the prediction. For example, more reliable value for visco-elastic Poisson's ratio should be confirmed.

3) considering the possible coupling of creep and autogenous shrinkage.

8.3 Numerical simulation part

8.3.1 Main findings

Numerical simulation of autogenous shrinkage was done in *Chapter 7*, which included the simulation of microstructure of cementitious systems and the simulation of stiffness and visco-elastic behavior of C-S-H. The simulations are based on two simulation platforms: *μic* [3] and *AMIE* [4] FEM modeling.

The algorithms of the simulations are more on the basis of previous work in [5,6]. Some major changes comparing to previous simulations are: 1) the external load based on the calculation of effective capillary pressure was functioned only on C-S-H; 2) the simulation of elastic part was based on back-calculated evolving stiffness of outer C-S-H with the porosity; 3) the visco-elastic behavior of C-S-H was not obtained from nanoindentation as in [7], but back-calculated from the macro-scale experimental data with FEM homogenization.

Some main findings can be seen as below:

- Even though it is not possible to simulate the porosity completely at this stage of the study, it is promising to see a reasonable match between the numerical simulated deformation caused by capillary pressure and the elastic part analytical prediction of the autogenous shrinkage.
- The back-calculated stiffness and visco-elastic behavior of C-S-H are reasonable by having similar results for different systems (Cement-0.35 and CQZ40-0.35). The property is not highly depending on the systems (e.g., with different w/cs).
- The simulation of visco-elastic part of autogenous shrinkage is reasonable good when compared with the experimental data. The simulation of total autogenous shrinkage including elastic and visco-elastic parts is in good agreement with the results at 28 d but the evolution of autogenous shrinkage needs to be simulated better.

8.3.2 Future perspectives

There are still quite some limitations of the current modeling of autogenous shrinkage and more works need to be done:

- In the microstructure simulation, no solution chemistry was considered. The ion concentration and interaction between solution and solids should be also considered which will help for understanding especially the mechanism visco-elastic behavior (e.g., the recent proposed dissolution-precipitation mechanism [8]).
- The simulation of elastic behavior and visco-elastic behavior are both based on $1 \times 100 \times 100 \mu\text{m}^3$. It may have different result for doing the simulation with a real 3-dimensional micro structure. The difference of 2-dimensional case and 3-dimensional case simulation should be studied.
- The visco-elastic simulation is only based on non-aging visco-elastic behavior of C-S-H. The aging effect was considered with the amount C-S-H. Densifying of C-S-H could be also considered with the porosity evolution. Further, more reliably, new implement methods for directly aging visco-elastic behavior of C-S-H should be proposed. Carrying out experimental work on macroscale visco-elastic behavior of C-S-H can be a promising way to help to establish new methods.
- Micro-cracks and crack propagation should be considered in later simulation of autogenous shrinkage. When under capillary stress, the possibility of occurring micro-cracks is high. The presence of micro-cracks leads to expansion and influences the final autogenous shrinkage.

8.4 References

- [1] Z. C. Grasley, C. K. Leung, Desiccation shrinkage of cementitious materials as an aging, poroviscoelastic response, *Cem. Concr. Res.* 41 (2011) 77–89.
- [2] G. Sant, B. Lothenbach, P. Juilland, G. Le Saout, J. Weiss, K. Scrivener, The origin of early

- age expansions induced in cementitious materials containing shrinkage reducing admixtures, *Cem. Concr. Res.* 41 (2011) 218–229.
- [3] S. Bishnoi, K. L. Scrivener, uic: A new platform for modelling the hydration of cements, *Cem. Concr. Res.* 39 (2009) 266–274.
- [4] C. F. Dunant, K. L. Scrivener, Micro-mechanical modelling of alkali–silica-reaction-induced degradation using the AMIE framework, *Cem. Concr. Res.* 40 (2010) 517–525.
- [5] A. B. Giorla, Modelling of alkali-silica reaction under multi-axial load, EPFL, 2013.
- [6] Q. Do, Modelling properties of cement paste from microstructure : porosity, mechanical properties, creep and shrinkage, EPFL, 2013.
- [7] Q. Do, S. Bishnoi, K. L. Scrivener, Microstructural modeling of early-age creep in hydrating cement paste, *J. Eng. Mech.* (2016) 4016086.
- [8] I. Pignatelli, A. Kumar, R. Alizadeh, Y. Le Pape, M. Bauchy, G. Sant, I. Pignatelli, A. Kumar, R. Alizadeh, Y. Le Pape, A dissolution-precipitation mechanism is at the origin of concrete creep in moist environments, 54701 (2016) 0–10.

Appendix A

In the creep setup, the deformations of the specimens itself were not measured directly, rather the displacement between the loading plates was measured. In order to quantify the error induced from this approach, a 2D FEM simulation with CAST 3M was done on the elastic modulus. The simulation was only done on one quarter of the sample, due to the symmetry of the loading specimen and the loading cell. The meshing was denser in the region of contact between the steel ball and the steel plate (see *section 5.2* for a description of the setup). The detailed meshing and the boundary conditions were presented in *Figure A.1*. The results indicate that the elastic modulus of the specimen will be underestimated by measuring the displacement of two loading cells. The degree of underestimation depends on the elastic modulus of the sample. Generally, the higher the elastic modulus of the sample is, the higher the degree of underestimation will be. For example, with the assumption of the elastic modulus of the steel plate being 210 GPa and Poisson ratio of 0.3, the simulated elastic modulus of the measured whole set (steel plate with the sample together) was 11.2 GPa if the real elastic modulus of the sample was 15.21 GPa (Poisson's ratio of 0.25). If the elastic modulus of the sample was changed to 10 GPa (Poisson's ratio was kept the same), the simulated elastic modulus of the whole set was 8.2 GPa.

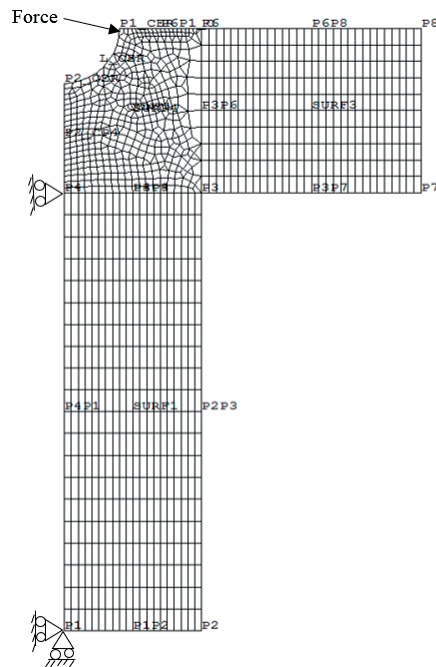


Figure A.1 The meshing and boundary condition in the CAST 3M simulation

Appendix B

The calculation of the increment strain of the Kelvin-Voigt units (from *Equation 5.10* to *Equation 5.11*) with the definition of all the parameters:

The general solution of the derivation strain of the Kelvin-Voigt units for *Equation 5.10* is:

Equation B.1

$$\dot{\varepsilon}_{nkV}^i = \lambda_n \cdot e^{-\frac{t}{\bar{\tau}_n}} + \frac{\dot{\sigma}}{k_{nkV}}$$

The increment strain then would be:

Equation B.2

$$\Delta \varepsilon_{nkV}^i = \int_{t_i}^{t_{i+1}} \lambda_n^i \cdot e^{-\frac{t}{\bar{\tau}_n^i}} + \frac{\dot{\sigma}^i}{k_{nkV}^i} dt$$

From *Equation 5.8*, λ_n can be calculated as follows:

$$\begin{aligned} \sigma_{\eta}^i &= \eta_n^i \cdot \dot{\varepsilon}_{nkV}^i = \eta_n^i \cdot \left(\lambda_n^i \cdot e^{-t_i/\bar{\tau}_n^i} + \frac{\dot{\sigma}^i}{k_{nkV}^i} \right) \\ \lambda_n^i &= \left(\frac{\sigma_{\eta}^i}{\eta_n^i} - \frac{\dot{\sigma}^i}{k_{nkV}^i} \right) \cdot e^{t_i/\bar{\tau}_n^i} \end{aligned}$$

Then, λ_n is replaced by the expression above in to *Equation B.2*, the derivation is solved as follows:

$$\begin{aligned} \int_{t_i}^{t_{i+1}} \left(\lambda_n e^{-t/\bar{\tau}_n} + \frac{\dot{\sigma}_n}{k_{nkV}} \right) dt &= -\bar{\tau}_n \lambda_n e^{-t/\bar{\tau}_n} \Big|_{t_i}^{t_{i+1}} + \frac{\sigma_n^{i+1} - \sigma_n^i}{k_{nkV}} \\ &= -\bar{\tau}_n^i \cdot \left(\frac{\sigma_{\eta}^i}{\eta_n^i} - \frac{\sigma_n^{i+1} - \sigma_n^i}{\Delta t_i k_{nkV}^i} \right) \cdot e^{t_i/\bar{\tau}_n^i} \cdot (e^{-t_{i+1}/\bar{\tau}_n^i} - e^{-t_i/\bar{\tau}_n^i}) + \frac{\sigma_n^{i+1} - \sigma_n^i}{k_{nkV}^i} \\ &= -\bar{\tau}_n^i \cdot \left(\frac{\sigma_{\eta}^i}{\eta_n^i} - \frac{\sigma_n^{i+1} - \sigma_n^i}{\Delta t_i k_{nkV}^i} \right) \cdot (e^{-\Delta t_i/\bar{\tau}_n^i} - 1) + \frac{\sigma_n^{i+1} - \sigma_n^i}{k_{nkV}^i} \\ &= \frac{\sigma_n^{i+1} - \sigma_n^i}{k_{nkV}^i} \cdot \left(1 + \frac{\bar{\tau}_n^i (e^{-\Delta t_i/\bar{\tau}_n^i} - 1)}{\Delta t_i} \right) - \frac{\sigma_{\eta}^i}{\eta_{kv}^i} \cdot \bar{\tau}_n^i \cdot (e^{-\Delta t_i/\bar{\tau}_n^i} - 1) \end{aligned}$$

After inserting $\bar{\tau}_n / (1 + \dot{E}_n / E_n \cdot \tau_n)$ in the calculation, *Equation 5.11* is obtained.

Curriculum Vitae

Name: **Zhangli Hu**

Address: EPFL STI IMX LMC MXG 241 (Bâtiment MXG) Station 12
CH-1015 Lausanne Switzerland

Date of Birth: 11/03/1988

Telephone: [+41 21 69 32852](tel:+41216932852)

E-mail: zhangli.hu@epfl.ch

RESEARCH INTERESTS

- Mechanical properties of cement paste and concrete with SCMs, especially early-age deformation and durability
- Hydration characteristics of cement and mineral chemistry
- Analytical modeling and simulation of mechanical properties of cement-based materials

EDUCATION

- **01/10/2013 -Now** PhD student at the Laboratory of Construction Materials (LMC)
École polytechnique fédérale de Lausanne (EPFL)
Supervisors: Prof. Karen Scrivener, Prof. Pietro Lura
Thesis project: Prediction of autogenous shrinkage of fly ash blended cement
- **09/2011 -09/2013** Master at Hunan University, Hunan, China; Major: Building Materials
Supervisor: Prof. Caijun Shi
Thesis project: Early hydration and shrinkage of alkali-activated slag / fly ash blend cement
- **09/2007-06/2011** Bachelor at Hunan University, Hunan, China; Major: Civil Engineering

INTERNSHIPS, RESEARCH & TEACHING EXPERIENCES

09/2013 -09/2016

- Giving lectures in LC3 school on hydration properties
- Teaching assistant for the course advanced materials class for shrinkage and creep section
- Co-supervise a master student semester project, title: *Visco-elastic behavior of cementitious materials*.

09/2015 -12/2015

- Teaching assistant for the course advanced materials class for shrinkage and creep section

03/2015 -06/2015

- Supervise a bachelor student semester project, title: *Prediction of internal relative humidity in fly-ash blended systems based on pore structure evolution*

03/2014 -06/2014

- Supervise a bachelor student semester project, title: *A comparison study of degree of hydration of blended cement systems measured by different methods*

09/2011 -06/2013

- Research on concrete durability (cooperation with *Lafarge, France*)

- **Research experience:** Subway Project in Changsha: raw materials selection, inspection and durability design of high-performance concrete; assistant researcher.
- **Research experience:** Hunan Highway Administration Office Project - Chishi Bridge: raw materials selection and durability design of concrete; assistant researcher.

PRICES & AWARDS

- **11/2015** Rewarded as Best slam presentation in EPFL EDMX research day
- **9/2010-9/2011** Rewarded as Excellent Student Leader, excellent League member in Hunan University
- **9/2009-9/2010** Awarded **1st** scholarship in Hunan University
- **9/2008-9/2009** Awarded **1st** scholarship in Hunan University
- **9/2007-9/2008** Awarded **2nd** scholarship in Hunan University

PUBLICATIONS

Publications in peer-reviewed scientific journal

- [1] Zhangli Hu, Mateusz Wyrzykowski, Karen Scrivener, Pietro Lura. A novel method to predict internal relative humidity in cementitious materials by ¹H NMR. Cement and Concrete Research, submitted;
- [2] Mateusz Wyrzykowski, Zhangli Hu, Sadegh Ghourchian, Karen Scrivener, Pietro Lura. Corrugated tube protocol for autogenous shrinkage measurements: review and statistical assessment [J], Material and structures, 2017, 50 (1): 50-57;
- [3] Zhangli Hu, Caijun Shi, Jianming Yang, Dehui Wang, Yuan Chang. Factors Influencing setting time of magnesium phosphate cement by Bayesian network [J], Journal of the Chinese Ceramic Society, 2014, 42 (1): 38-44;
- [4] Xiaopeng An, Caijun Shi, Zhang Cao, Dehui Wang, Fuqiang He, Zhangli Hu. Relation between bulk resistance and pore structure of hardened cement [J], Journal of the Chinese Ceramic Society, 2014, 8: 1011-1017;
- [5] Zhangli Hu, Caijun Shi, Zhang Cao, Zhihua Ou, Dehui Wang, Zemei Wu, Liang He. A review on testing methods for autogenous shrinkage measurement of cement-based materials [J], Journal of Sustainable Cement-Based Materials, 2013, 2(2): 161-171;
- [6] Lufeng Jia, Caijun Shi, Zhang Cao, Dehui Wang, Zhangli Hu, Zemei Wu, Zhihua Ou. A review on methods for in-situ concrete permeability testing [J], Materials Review, 2013, 27 (11):106-111

Peer-reviewed conference proceedings

- [1] Zhangli Hu, Adrien Hilaire, Mateusz Wyrzykowski, Karen Scrivener, Pietro Lura. Elastic and visco-elastic behavior of cementitious materials at early ages, 6th Biot Conference on Poromechanics, July 2017.
- [2] Zhangli Hu, Hadi Kazemi-Kamyab, Mateusz Wyrzykowski, Karen Scrivener, Pietro Lura. Experimental investigation of the effect of fly ash on autogenous shrinkage at early ages, 14th ICCO, October 2015;
- [3] Zhangli Hu, Hadi Kazemi-Kamyab, Mateusz Wyrzykowski, Karen Scrivener, Pietro Lura. Autogenous shrinkage in blended cement systems, 34th CCSC, September 2014;

